STUDY OF HFQ FORMING PROCESS ON LIGHTWEIGHT ALLOY COMPONENTS

By

Haoxiang Gao

Department of Mechanical Engineering

South Kensington Campus

Imperial College London

London SW7 2AZ

U.K.

Declaration of originality

This thesis hereby presented is based on research by the author at the Department of Mechanical Engineering of Imperial College London. I declare the work contained in this thesis is only author's own work. Not any part of the present work has been submitted for any other degree or qualification elsewhere.

Haoxiang Gao

July 2017

Copyright declaration

Acknowledgements

Abstract

In order to reduce CO_2 emissions and improve fuel efficiency for the aerospace industry, a leading edge sheet metal forming technology, namely solution heat treatment, forming and in-die quenching (HFQ) was utilised to form lightweight, complex-shaped components, efficiently and cost-effectively.

The work performed in this research project contains two major achievements. The first achievement is successfully forming a complex AA2060 (Al-Li alloy) wing stiffener demonstrator part, and an L-shape AA7075 demonstrator part, without necking or fracture, using HFQ forming technology. The feasibility of forming the aluminium alloys was based on a series of fundamental experimental tests including uniaxial tensile test, isothermal forming limit test and artificial aging test. The second achievement is the development of a novel forming limit prediction model, namely the viscoplastic-Hosford-MK model. This model enables the forming limit prediction of AA2060 and AA7075 alloys under hot stamping conditions, featuring non-isothermal and complex loading conditions. This prediction model fills a significant need in industry for accurately predicting the forming limit of aluminium alloys under such complex forming conditions. The effectiveness of the developed model was analytically verified for AA2060, demonstrating accurate material responses to cold die quenching, strain rate and loading path changes. By applying the developed model to the hot stamping of an AA2060 component, its accuracy was successfully validated. Furthermore, the viscoplastic-Hosford-MK model was also demonstrated for use in industry by determining the optimum initial blank shape of an L-shape AA7075 component. An iterative simulation procedure implementing the forming limit prediction model was used to arrive at an optimum blank shape by the minimisation of the failure criterion. The optimised initial blank shape design was applied in the experimental hot stamping of a demonstrator AA7075 component. The accuracy of the developed model was validated by the successful forming of the component, without necking or fracture.

Nomenclature

English Alphabet

f Imperfection factor

T Temperature (°C)

l Constant in Hosford yield function

R' Isotropic material hardening (MPa)

$R_{1,2}$ Lankford coefficient in Hosford yield function

R Universal gas constant

t Thickness of blank (mm)

A Material constant for dynamic recovery

C Material constant for static recovery

m Material constant for strain rate hardening

n_1 Material constant for strain hardening

d Actual grain size (μm)

$\bar{d}$ Normalized grain size

K Material constant for power law (MPa)

k Initial yield stress (MPa)

B Material constant for isotropic material hardening (MPa)

C Material constant for static recovery

n_2 Material constant for static recovery

E	Young's Modulus (MPa)
Q	Activation energy (J/mol)
M	Mesh Size
F	Fillet radius (mm)
h	Height (mm)
t	Time (s)

Greek Alphabet

$\bar{\sigma}$	Equivalent stress (MPa)
$\bar{\varepsilon}$	Equivalent strain
$\dot{\varepsilon}$	Strain rate (/s)
$\bar{\varepsilon}$	Strain increment
α	Strain ratio
β	Loading path
$\bar{\rho}$	Normalized dislocation density
ρ	Dislocation density
ρ_m	Saturated dislocation density
ψ_0	Material Constant in viscoplastic material model
$\dot{\bar{\rho}}$	Normalized dislocation density rate
γ	Material constant in viscoplastic material model
$\dot{\bar{\varepsilon}}_p$	Equivalent plastic strain rate (/s)
$\bar{\varepsilon}_T$	Total equivalent strain
ϖ	Damage parameter
$\dot{\omega}$	Damage rate parameter
α_1	Material constant for grain growth hardening
β_1	Material constant for grain growth hardening

Superscripts

*   Critical

Subscripts

0, i   Initial

a   Zone a (M-K model)

b   Zone b (M-K model)

1   Major strain direction

2   Minor strain direction

3   Through-thickness direction

Abbreviations

exp   Exponential

f   Function

LP   Loading path

Contents

List of Figures

Chapter 4 FE simulation of HFQ process of AA2060

Chapter 5 Forming limit prediction of AA2060 under hot stamping conditions

Chapter 6 Forming limit prediction of AA7075 alloy under hot stamping conditions

List of Tables

Chapter 5 Forming limit prediction of AA2060 under hot stamping conditions

Chapter 6 Forming limit prediction of AA7075 alloy under hot stamping conditions

List of Publications

Journal articles:

2015

Gao H, Li N, Hou H, Zhang Y, Zhang N, Wang L, Lin L, 2015. Determination of a set of constitutive equations for an Al-Li alloy at SPF conditions, Materials Today: Proceedings, 2S, S408 – S413. https://dx.doi.org/10.1016/j.matpr.2015.05.056

Ji K, **Gao H**, El Fakir O, Wang L, 2015. Determination of heat transfer coefficient for hot stamping process, Materials Today: Proceedings, 2S, S434 – S439. https://dx.doi.org/10.1016/j.matpr.2015.05.059

Ma G, Wang L, **Gao H**, Zhang J, Reddyhoff T, 2015. The Friction Coefficient Evolution of a TiN Coated Contact During Sliding Wear, Applied Surface Science, 345: 109-115. http://dx.doi.org/10.1016/j.apsusc.2015.03.156

2016

Gao H, Weng T, Liu J, Li Z, Wang L, 2016. Hot stamping of an Al-Li alloy: a feasibility study, Manufacturing Review, 3(5).   http://dx.doi.org/10.1051/mfreview/2016006

Zhou D, Yuan X, **Gao H**, Wang A, Liu J, El Fakir O, Politis DJ, Wang L, Lin J, 2016. Knowledge Based Cloud FE Simulation of Sheet Metal Forming Process, Journal of Visualized Experiments. https://dx.doi.org/10.3791/53957

Liu J, **Gao H**, El Fakir O, Lin J, 2016. Hot stamping of AA6082 tailor welded blanks: experiment and FE simulation. Manufacturing Review. 3, 8. https://doi.org/10.1051/mfreview/2016009

Luan X, El Fakir O, **Gao H**, Liu J, 2016. Formability of AA6082-T6 at warm and hot stamping conditions. Key Engineering Materials. 716, 107-113. https://doi.org/10.4028/www.scientific.net/KEM.716.107

2017

Gao H, El Fakir O., Wang L, Politis D.J., Li Z., 2017. Forming limit prediction for hot stamping processes featuring non-isothermal and complex loading conditions. International Journal of Mechanical Sciences. 131-132, 792-810. https://doi.org/10.1016/j.ijmecsci.2017.07.043

Wang A, Liu J, **Gao H**, Wang L, Marc M, 2017. Hot stamping of AA6082 tailor welded blanks: experiments and knowledge-based cloud – finite element (KBC-FE) simulation, Journal of Materials Processing Technology. 250, 228-238. https://doi.org/10.1016/j.jmatprotec.2017.07.025

Conference papers:

2014

Gao H, Li N, Hou H, Zhang Y, Zhang N, Wang L, Lin L, 2014. Determination of a set of constitutive equations for an Al-Li alloy at SPF conditions, Joint 3rd UK-China Steel Research Forum & 15th CMA-UK conference on Materials Science and Engineering, Oxford, UK, 10-11 July, 2014. https://doi.org/10.1016/j.matpr.2015.05.056

2015

Gao H, Weng T, Liu J, Li C, Li Z, Wang L, 2015. Hot stamping of an Al-Li alloy: a feasibility study. ICNFT2015 - Proceedings of the 4th International Conference on New Forming Technology, Scotland, UK, 6-9 August 2015. https://doi.org/10.1051/mfreview/2016006

2017

Gao H, Denis J.P., Luan X, Kang J, Zhang Q, Zheng Y, Mohammad G, Wang L, 2017. Forming limit prediction AA7075 alloys under hot stamping conditions. IDDRG2017 - 36th IDDRG conference Materials Modelling and testing for sheet metal forming, Munich, Germany, July 2017.

Chapter 1

Introduction

1.1 Introduction

The fuel efficiency of aircrafts has long been a critical engineering challenge for manufacturers globally, for economic and environmental reasons. This is driving manufacturers to find cost effective ways of reducing mass by incorporating lightweight materials, and low-cost forming technologies. Aluminium alloys remain the dominant structural material used in aerospace applications (Dorward and Pritchett, 1988), and thus, a high demand for aluminium alloy components remains. In this research, AA2060 (an aluminium lithium alloy) and AA7075 alloys are investigated to produce lightweight and complex-shaped components for the aerospace industry using a developed forming technology.

Current sheet forming technologies are limited in terms of productivity. Parts with complex geometrical features cannot be produced with cold forming technology due to low ductility at room temperature (Gao et al., 2016; Zhang & Ma, 2015). Although superplastic forming (SPF) is a sophisticated process which enables the forming of complex- shaped components by using relatively inexpensive tooling, long processing time and localised thinning remain major issues for SPF. To overcome the problems inherent in cold and SPF forming techniques, the Solution Heat Treatment, Forming and in-die Quenching (HFQ) forming technique has been developed, which effectively combines forming and heat treatment in one operation (Lin et al., 2011). By combining forming and heat treatment, HFQ enables the fast processing of component from high strength aluminium alloy. In recent years, the HFQ technology has been successfully employed for niche and premier car industries. A number of medium and high strength aluminium alloys, such as AA5XXX, AA6XXX (Garrett et al. 2005; Mohamed et al., 2012), AA2XXX (Wang et al., 2011) and AA7XXX were successfully formed into complex-shaped components using HFQ forming technology.

In addition to the feasibility study of using HFQ forming technology on AA2060 and AA7075 alloys, the optimisation of forming parameters for AA2060 and AA7075 formed part under hot stamping conditions was performed using a developed forming limit prediction model. The developed forming limit prediction model was required to capture the intrinsic features of the hot stamping process featuring non-isothermal and non-linear loading conditions.

1.2 Aim and objectives

The main aim of this research is to study HFQ forming technology for forming high strength complex-shaped Al-Li alloy and AA7075 components. To achieve this aim, the following scientific and technological objectives have been met:

- Material characterisation, formability assessment and age hardening analysis of AA2060 through experiments including uniaxial tensile tests, formability tests, forming tests and artificial aging tests
- Development of a viscoplastic material model incorporating the yield function and damage model. Calibration of the model with experimental data for AA2060 and AA7075 alloys
- Numerical analysis of the developed forming limit prediction model by demonstration of the model response to cold die quenching, strain rate and loading path changes for modelling the forming of AA2060 and AA7075 components
- Optimisation of forming parameters and forming limit prediction for AA2060 and AA7075 alloys under HFQ forming conditions

1.3 Major tasks

To achieve the objectives, the research programme has been divided into a number of distinct tasks, which are detailed below:

(1) Review of the state of the art forming technologies for aluminium alloys forming. focusing on (i) superplastic forming; (ii) HFQ forming;

(2) Thermomechanical property determination of AA2060 using uniaxial tensile tests and formability tests. Uniaxial tests are used to determine flow stress and ductility of a given material at temperatures ranging from 350 to 500°C and strain rates ranging from 0.2 to

13/s. Formability tests are used to determine Forming Limit Curve (FLC) diagrams for different forming rates and forming temperatures.

(3) Forming tests to test feasibility of HFQ forming technology with AA2060. The age hardening behaviour of AA2060 are also investigated using artificial aging tests.

(4) Set up FE model of HFQ process. The FE simulation models for AA2060 and AA7075 hot stamping processes are calibrated with experimental results from forming test.

(5) Development of viscoplastic-Hosford-MK model, calibration of the viscoplastic-Hosford-MK model and implementation of the developed model into commercial FE code.

(6) Study of forming limit prediction on AA2060 and AA7075 formed part using viscoplastic-Hosford-MK model. The development of necking in the component is investigated in relation to changes in strain rate, temperature and strain path. Additionally, the numerical optimisation of initial blank shape for the successful forming of an L-shape AA2060 demonstrator part is performed.

1.4 Thesis structure

In this thesis, the introduction of AA7075 and AA2060 alloys, as well as a review of forming technologies for aluminium alloys, and forming limit prediction models are shown in Chapter 2. The material characterisation of AA2060, including tensile tests, formability tests and forming tests are presented in Chapter 3. The FE simulation for the forming of the AA2060 wing stiffener component is shown in Chapter 4. The forming limit analysis of the viscoplastic-Hosford-MK model on the AA2060 wing stiffener component as a small scale component is presented in Chapter 5. Based on the work in Chapter 5, the forming limit prediction of a large L-shape component and determination of its optimal blank shape were performed in Chapter 6. The final conclusions of this research are summarised in Chapter 7.

Chapter 2

Literature review on the sheet metal forming technologies of lightweight alloy

In the present chapter, a literature review is presented discussing the material properties, application and manufacturing technologies used in the production of lightweight sheet Al-Li alloy and AA7075 components in the aerospace industry. Moreover, a review of traditional Superplastic Forming (SPF) technology is compared to novel sheet metal forming technologies such as Solution heat treatment, forming and in-die quenching (HFQ), with their respective benefits and limitations outlined. In addition, the methods of determining forming limit diagrams are reviewed as they are critical in examining the success of a formed component. Finally, a review of Forming Limit Diagram (FLD) prediction models are presented. From the reviewed methods, a novel FLD prediction model is developed as presented in subsequent chapters as an example hot-stamped aluminium component.

2.1 Lightweight Aerospace Alloys

2.1.1 Aluminium-Lithium alloy

In recent years, aluminium-lithium (Al-Li) alloys have become attractive materials for the aerospace industries. With a high specific strength of $151MPa/(g/cm^3)$ (Karabin et al., 2012), high stiffness of $(31.2GPa/(g/cm^3))$ (Battelle Memorial Institute, 2012) and good fatigue strength of 117MPa (Heinimann et al., 2007), aluminium lithium alloys are regarded as promising materials competing with composite materials (Prasad et al., 2014). Al-Li alloys not only provides good mechanical properties that satisfy the requirements of manufacturing an aero-component, but are also lightweight alloy, as Lithium has an extremely low density. It has been stated in the literature that for each 1wt% addition of Li, the density of the Al alloy can be reduced by 3%, and therefore aero-components manufactured from Al-Li alloy offer a significant weight reduction potential for aero-strctural components (Pickens, 1985).

Development of Al-Li alloys

The age-hardening phenomenon of aluminium alloys was first found by Wilm (1911), the commercial aluminium alloys containing lithium, called 'Scleron' with composition $Al_{12}Zn_3Cu_{0.6}Mn_{0.1}Li$, were first explored by Reuleaux (1924). The Al-Li alloy was found to exhibit greater resistance to corrosion and higher tensile strength in comparison to the other types of aluminium alloys present at the time.

The development of modern Al-Li alloys began in the late 1970s and early 1980s. AA2020 was one of the first generation of modern Al-Li alloys, with its successful application on the United States Navy RA 5C Vigilante aircraft (Balmuth and Schmidt 1980). However, although the low density and high Young's modulus encouraged increased adoption of AA2020 in aerospace, the drawback was poor toughness due to planar slip, and large recrystallized grains, forming coarse constituents from un-identified trace elements (Starke, 2013). To overcome the ductility problem of AA2020, second-generation Al-Li alloys, namely AA2090, AA8090 and AA2090 were developed in the mid-1970s by replacing the manganese alloying element with zirconium and decreasing the content of iron and silicon. Due to these composition modifications, AA2090, AA8090 and AA2090 as the second-generation Al-Li alloys were formed with improved ductility and were successfully used on the Airbus A340 (Starke, 2013). However, the disadvantages of second-generation Al-Li alloys were found to include high anisotropy, crack deviation and delamination problems. Moreover, it was found that although a high content of Li improves lightweight and fracture toughness characteristics, these second-generation Al-Li alloys demonstrated extremely poor thermal instability at temperatures below artificial aging temperature. The poor thermal stability was found to be induced by high volume fraction of precipitation of δ' (Al_3Li) due to the high Li content (Starke, 2013; Sugamata et al., 1993). Thereby the development of the third generation of Al-Li alloy become more urgent.

The development of third generation of aluminium lithium alloys was begun in the late 1980s and developed by Pickens et al. (1985) and the Lockheed Martin Corporation. The third generation of Al-Li alloy contained Li content less than 2wt% in comparison with 2-2.4wt% Li content of second generation of Al-Li alloy (Prasad and Ramachandran, 2013). The reduction of Li content in third generation Al-Li alloys gave improved thermal stability. Apart from a large reduction of Li, several trace elements were added into third generation Al-Li alloys. For instance, the corrosion resistance and strength of new material were effectively improved by the addition of Zn (Rioja et al., 1990) and Ag, respectively. Due to those chemical

modifications, third-generation Al-Li alloys were developed to obtain high fracture toughness, low anisotropy and good fatigue strength. The third generation AA2195 Al-Li alloy was successfully used in the Super Lightweight Tank of the Space Shuttle in 1998, demonstrating its excellent performance by reducing empty weight by 12% (Lockheed Martin, 2012) due to Al-Li alloy and modification of design in comparison to the previous tank (Starke, 2013). Apart from fracture toughness, anisotropy and fatigue strength, the specific strength of AA2XXX sheet product has been reviewed and compared with other AA2XXX as demonstrated in Figure 2-1. In Figure 2-1, third-generation Al-Li alloys (AA2060 and AA2199) show excellent specific strength. This is particularly the case for AA2060-T8E30, which shows the highest of specific strength of all AA2XXX alloys. In addition to specific strength, AA2060 has an excellent combination of ductility and fracture toughness which was extensively used in aircraft fuselage skins. The strengthening mechanisms and ductility of AA2060 are discussed as follows.
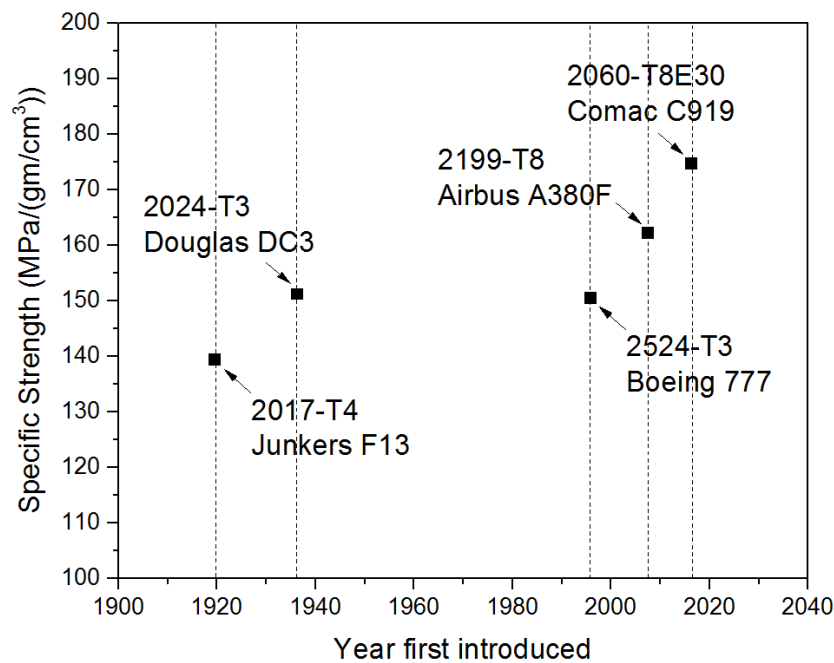
Figure 2-1. Development history of AA2XXX plate products for lower wing covers with improvements of specific strength (Karabin et al., 2012).

Strengthening mechanism and ductility of Al-Li alloy

The AA2060 is categorized as an quaternary Al-Cu-Mg-Li alloy (Prasad et al., 2014; Rioja and Liu, 2012). The associated main strengthening precipitate phases include: "δ' (Al$_3$Li)", "T$_1$ (Al$_2$CuLi)" and "β' (AlZr$_3$)". The δ' (Al$_3$Li) is the most common strengthening phase in Al-Li alloys. The alloy was hardened by solid solution strengthening due to the solution of lithium

atoms. The general strength in Al-Li alloys is obtained from the formation of a large volume fraction of the δ' (Al$_3$Li) phase (Srivatsan et al.,1994). Additionally, AA2060 is a copper-rich content alloy, the T$_1$ (Al$_2$CuLi) plays a significant role in the strengthening mechanism. This is because the new formation of T$_1$ phases eliminates the GP zones at grain boundary (GB) and applies resistance to GB sliding. As the volume fraction of T$_1$ increases, the resistance to grain boundary sliding become larger and finally enhances the strength of the material. Furthermore, β' (AlZr$_3$) is a metastable phase, and the recrystallization is inhibited due to the addition of zirconium elements (Nes et al., 1971), which improves resistance to stress corrosion cracking (Di Russo, 1964). The morphology of the precipitates (δ' (Al$_3$Li), T$_1$ (Al$_2$CuLi) and β' (AlZr$_3$)) are illustrated in Figure 2-2.
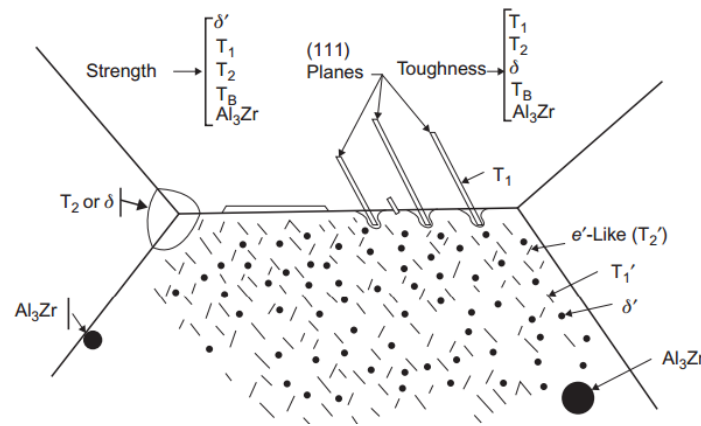
Figure 2-2. Schematic diagram of precipitates present in Al-Li-Cu alloy (Rioja and Liu, 2012)

In quaternary Al-Li-Cu-Mg alloys, the improvement of ductility focuses on the prevention of void nucleation. The nucleation of voids tends to occur at Grain Boundary (GB) precipitates, because the intensive stress concentrations are easily localised near Precipitate Free Zones (PFZ) and coarse GB precipitates. To minimise the formation of PFZs, S' and S'' phases are formed by the addition of magnesium (Gregson et al., 1988; Gregson and Flower, 1985). As less PFZs are generated, the stress concentration hardly localizes at PFZs and GB precipitates (Vasudévan and Doherty, 1987). The nucleation of voids at GB precipitates is delayed and hence ductility of material can be improved. The morphology of void nucleation in aluminium alloy is illustrated in Figure 2-3.
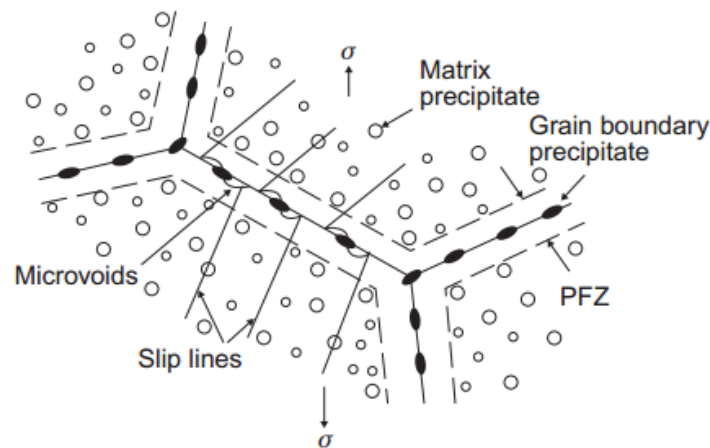
Figure 2-3. Schematic diagram of PFZs and void nucleation at grain boundaries (Vasudévan and Doherty, 1987).

2.1.2 Introduction of AA7XXX alloys

AA7XXX are Al-Zn-Mg-Cu based alloys consisting of 4–8 wt% zinc, 1–3 wt% magnesium, 1–2 wt% copper and 0.3 wt% chromium. The compositions of AA7XXX are listed in Table 2-1. By the addition of copper, magnesium and zinc, AA7XXX alloys, such as AA7049, AA7050, AA7175, AA7178 and AA7475 (Campbell, 2006), obtain excellent corrosion resistance, good specific strength, machinability and fracture toughness (Ram Prabhu, 2015; Heinz et al., 2000). Due to their outstanding material properties, AA7XXX alloys have become extremely attractive materials that are used in the landing gear, engine ribs and fuselage frames for aerospace applications (Dursun and Soutis, 2014; Poole et al., 2006; Ram Prabhu, 2015).

Development history of AA7XXX alloys

In AA7XXX alloy, AA7075 alloy is one of the most common materials used in aircraft, such as for upper wing panel applications (Prasad et al., 2014). Since World War II, the introduction of AA7075 alloy has aided in boosting the performance of AA7XXX alloys in aircraft applications competing with aluminium lithium and other AA2XXX alloys. AA7075 alloy with its high strength leads to the dominance of Al-Zn-Mg-Cu alloys for high-strength applications (Prasad et al., 2014). However, the poor stress corrosion cracking (SCC) resistance of this alloy is one of the main drawbacks for widespread use of AA7075 alloy. In order to overcome poor SCC resistance, new types of material in Al-Zn-Mg-Cu systems were developed based on AA7075 alloy. One of substitutes for AA7075 alloy is the AA7085 alloy (Ram Prabhu, 2015). Apart from enhancement of SCC resistance, the specific strength of the AA7XXX alloys was improved, with the history of development shown in Figure 2-4.

Table 2-1. Composition of 7XXX series alloys (Campbell, 2006)

Alloy	Si	Fe	Cu	Mn	Mg	Cr	Zn	Ti	Zr
AA7020	0.35	0.40	0.20	0.05–0.50	1.0–1.4	0.10–0.35	4.0–5.0	-	0.08–0.20
AA7022	0.50	0.50	0.50–1.0	0.10–0.40	2.6–3.7	0.10–0.30	4.3–5.2	-	-
AA7075	0.40	0.50	1.2–2.0	0.30	2.1–2.9	0.18–0.28	5.1–6.1	0.20	-
AA7079	0.30	0.40	0.40–0.8	0.10–0.30	2.9–3.7	0.10–0.25	3.8–4.8	0.10	-
AA7050	0.12	0.15	2.0–2.6	0.10	1.9–2.6	0.04	5.7–6.7	0.06	0.08–0.15
AA7150	0.12	0.15	1.9–2.5	0.10	2.0–2.7	0.04	5.9–6.9	0.06	0.08–0.15
AA7055	0.10	0.15	2.0–2.6	0.05	1.8–2.3	0.04	7.6–8.4	0.06	0.08–0.25
AA7085	0.06	0.08	1.3–2.0	0.04	1.2–1.8	0.04	7.0–8.0	0.06	0.08–0.15
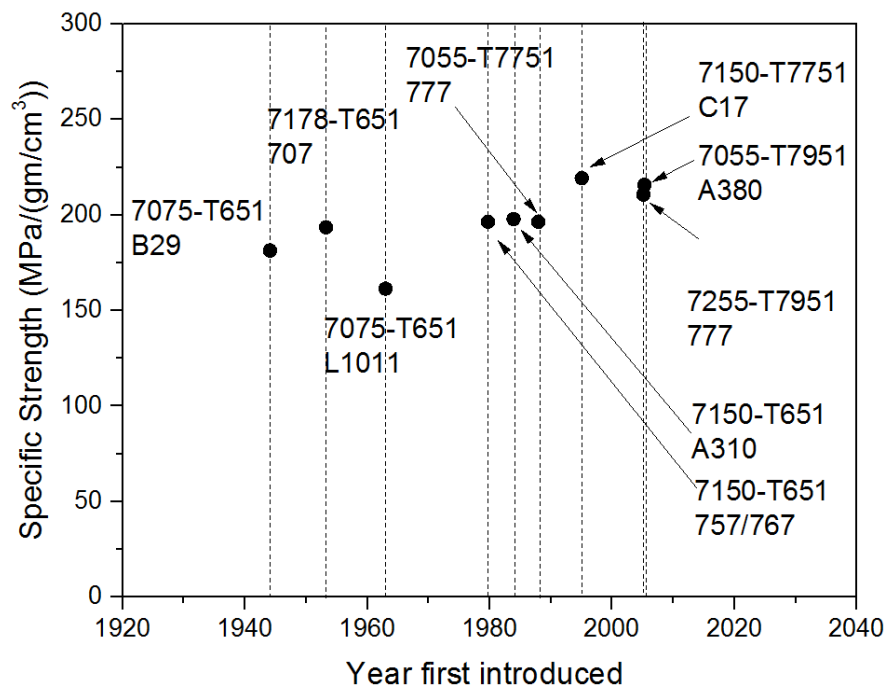
Figure 2-4. Development history of AA7XXX plate products for upper wing panel applications with its improvements of specific strength (Denzer et al., 2012).

Strengthening mechanism of AA7075 alloy and ductility

AA7075 alloy contains a high content of Zn (5.1-6.1wt%), and a low content of Mg (2.1-2.9wt%) and Cu (1.2-2wt%)(The Aluminum Association, 2001). The main strengthening precipitate phases in the Al-Zn-Mg-Cu–based alloy relies on the precipitations of η' (MgZn)

and η'' (MgZn$_2$). The generally accepted strengthening precipitation sequence is summarised as follows (Emani et al., 2009):

$$SS \rightarrow GPZ \rightarrow \eta' \rightarrow \eta''$$
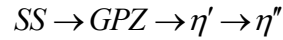
As the Al-Zn-Mg alloy is solution heat-treated, all the precipitates are dissolved into the Al-matrix, the supersaturated solid solution (SS) phase is formed and accompanied by the generation of GP zones (GPZ). As the aging process is applied to solution heat-treated Al-Zn-Mg alloys, spherical GPZ increase in size and subsequently transform into η'. With increasing aging temperature and aging time, the η' phase converts into the η'' phase, and the further improvement in strength of alloy is obtained (Emani et al., 2009).

In addition to strengthening mechanisms of AA7075 alloy, the fracture behaviour of AA7075 alloy has been investigated considering void nucleation and growth. A number of potential causes could lead to fracture of AA7075 alloy under loading conditions, such as the nucleation of voids occurring along the grain boundaries, precipitation-free zones and formation of coarse precipitation-free zones and grains (Pedersen et al., 2011).

2.1.3 Introduction of AA2060 and AA7075 alloy into the aerospace industry

The properties of AA2060 and AA7075 alloys are comprehensively reviewed in this section and compared to other AA2XXX and AA7XXX alloys. In Figure 2-5, the tensile strength, yield strength, density, FCGR (fatigue crack growth resistance), fracture toughness, E (elastic modulus) of aluminium lithium alloys (AA2060-T8E30 and AA2199-T8E74) and other AA2XXX alloys are demonstrated and compared. It can be seen that the Al-Li alloys AA2060-T8E30 and AA2199-T8E74 offer improved material performance compared to AA2524. Additionally, the highest fracture toughness and yield strength is found in AA2060-T8E30 out of all three of the alloys.
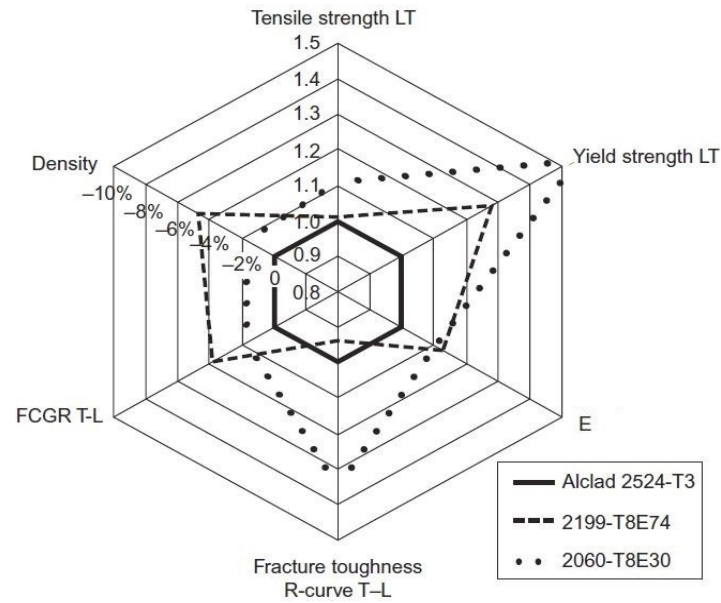
Figure 2-5. Comparison of tensile strength, yield strength, elastic modulus, fracture toughness, fatigue crack growth resistance and density of AA2060-T8E30, AA2199-T8E74 and Alclad 2524-T3 (Magnusen et al., 2012).

The tensile strength, the compressive yield strength in the longitudinal loading direction (CYS L), density, FCGR (fatigue crack growth resistance), fracture toughness, compressive E (elastic modulus) of aluminium alloys (AA7075-T7651, AA7055-T7751, AA7255-T7751 and AA2055-T8X) are compared in Figure 2-6. In comparison to modern Al-Li alloys (AA2055-T8X), AA7075-T7651 alloy has a relatively higher weight, but higher fracture toughness than that of AA2055-T8X.
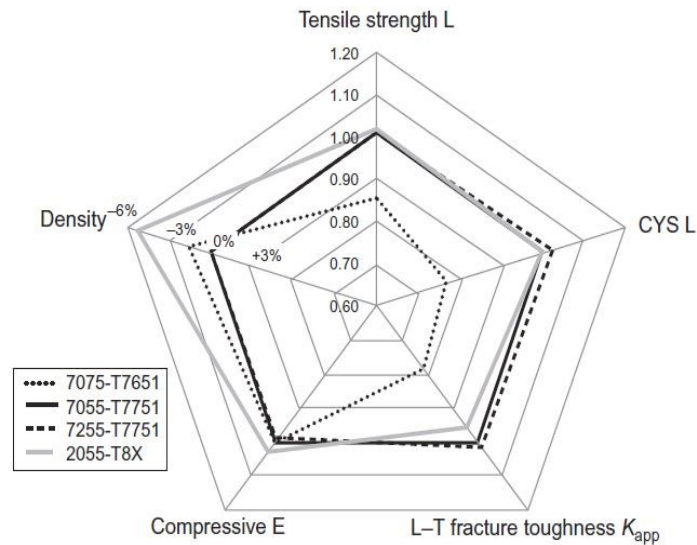
Figure 2-6. Comparison of material properties of aluminium lithium alloy 2055 and AA7XXX alloys such as AA7075-T7651, AA7055-T7751, AA7255-T7751 in the concern of CYS (compressive yield strength), tensile strength, density, fracture toughness, compressive elastic modulus (Denzer et al., 2012)

2.2 A review on SPF and HFQ forming technologies

The poor ductility at room temperature for alloys such as AA2XXX (Wang et al., 2011) and AA7XXX (Zhang and Ma, 2015), means that cold forming techniques are not feasible for forming complex geometrical features. Significant research programs have been undertaken to develop novel manufacturing technologies to process these lightweight materials into complex-shaped components to reduce expensive manufacturing costs and enhance productivity. In this section, Superplastic forming and HFQ forming technologies for processing lightweight materials have been reviewed.

2.2.1 Superplastic forming (SPF)

Superplasticity is the ability to sustain extensive elongation (more than 200%) without necking or fracture in the fine-grained material (Grimes, 1988). The superplastic phenomenon only occurs in a certain range of temperatures and strain rates, which are characterised by low flow stress and high sensitivity of flow stress to strain rate (Mohamed, 2011). The mechanism of superplastic deformation includes the grain rotation, grain boundary sliding and the fine dispersion of thermally stable particles by pinning the grain boundary within the fine structure (Mukherjee, 1979). In the manufacturing of aero-components, Superplastic forming (SPF) is an effective forming technique which is used to produce lightweight structural components with complex geometries. SPF requires low forming pressure but offers superior capability in forming large-scale complex-shaped components with excellent flexibility in the design as well as low tool costs. A schematic diagram of the SPF process is shown in Figure 2-7.
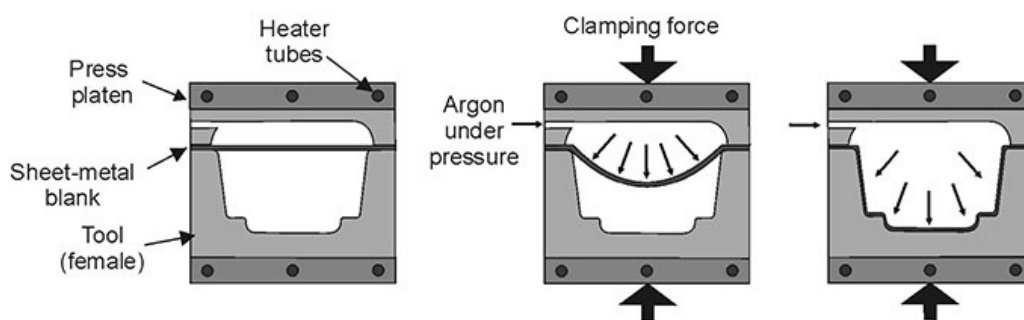
Figure 2-7. Schematic diagram of the superplastic forming process (Mechanicatech, 2014).

From a review of the literature, the limitations of superplastic forming include the development of non-uniform thinning due to localized necking and low production rate. The inhomogeneity of the microstructure and the stress concentration induced from the geometric features of complex-shaped components are the main reasons causing localised necking (Kim and Dunne,

1999; Science et al., 1997; Kim, 1996). Additionally, the low production rate is one of the most serious technical limitations for SPF, which has limited the adoption of SPF in high-volume industrial applications (Barnes, 2007).

2.2.2 Solution heat treatment, forming and in-die quenching (HFQ)

The HFQ^{TM} (Solution heat treatment, Forming and in-die Quenching) process is a hybrid forming process that combines both forming and heat treatment into a single operation. This enables complex-shaped sheet components to be formed whilst retaining the full mechanical strength of the original alloy material (El Fakir et al., 2014). In the HFQ process, the blank is first heated up to its solution heat treatment (SHT) temperature. The solution heat treatment is used to dissolve the alloying elements into the Al-matrix, which forms a supersaturated solid solution (SSSS), thus obtaining high ductility (Ashby, 2006). After solution heat treatment, the blank is transferred to a cold die. The stamping process is activated when the blank is positioned onto the die. During the stamping process, the blank is quenched between two cold dies. The quenching process is applied to freeze the microstructure and maintain the SSSS phase, enabling more complex shapes to be formed. Finally, the post-form strength of formed parts is achieved by conducting artificial aging. A schematic diagram of the HFQ process is shown in Figure 2-8.
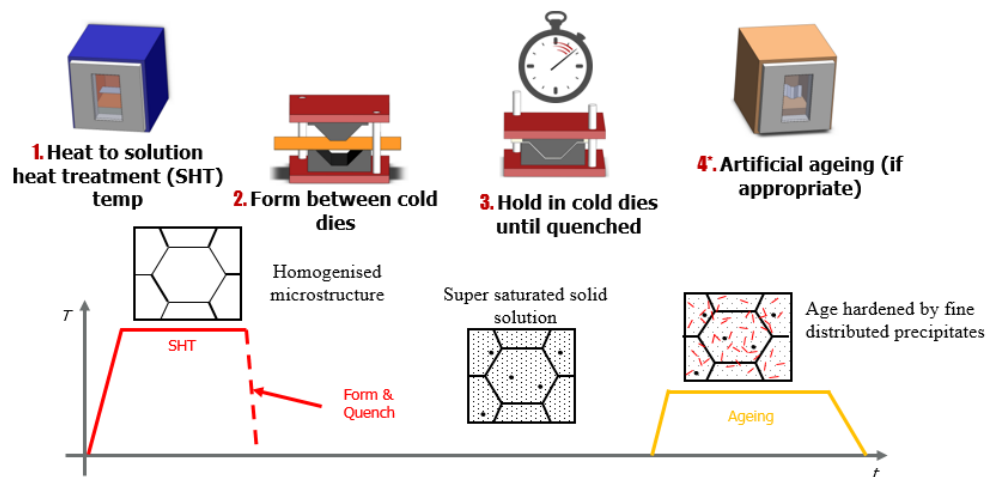
Figure 2-8. Schematic diagram of the HFQ forming process (Imperial College London, 2017).

In recent years, HFQ technology has been applied to a number of alloys including AA5XXX (El Fakir et al., 2014) and AA6XXX (Mohamed et al., 2012; Garrett et al., 2005). Investigations on a similar alloy, AA2024, under HFQ conditions have found that the optimum temperature to obtain high ductility is below the SHT temperature (Wang et al., 2011) due to the presence of low eutectic melting phase. After this first-stage forming process, a second forming stage is

conducted with cold die quenching and artificial aging to obtain the optimum strength of the part (Lin et al., 2009).

2.3 Introduction to forming limit diagrams (FLDs)

In order to form a range of complex-shaped components without localized necking and failure, the most useful tool to assess the sheet-metal formability is a forming limit diagram (FLD). The FLD concept was first introduced by Keeler (1961). A FLD is used to identify the limit of deforming a material without necking or fracture. FLDs consist of a series of forming limit curves (FLCs) representing different forming conditions such as temperature, strain rate and loading path. The FLC can be separated into two sides, a 'left-hand side' and a 'right-hand side'. Based on Keeler's pioneering work, the positive major and minor strains on the left-hand side of the FLD were proved. Subsequent research by Goodwin (1968) completed the FLD on the right-hand side of the diagram. Along an FLC curve, the major and minor strain limits are generated due to various loading paths applied for example, pure shear on the left, plane strain down the centre or biaxial tension on the right-hand side. FLCs enable the definition of acceptable forming zones in a sheet metal–forming process as shown in Figure 2-9. In this figure, above the FLC, failure criteria are identified, such as occurrence of localised necking. Below the FLC, excessive thinning, safe forming region, wrinkling tendency and insufficient stretch are identified.
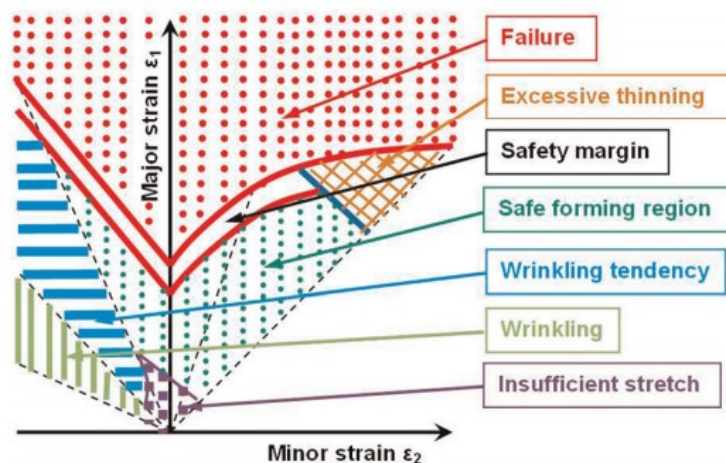
Figure 2-9. Schematic diagram of forming limit diagram with different identified forming zones (Paul, 2013).

2.4 Determination of the Forming Limit Diagram

2.4.1 Determination of the FLD using experimental methods

In order to determine the FLD at room temperature, standard forming limit tests, such as British Standard (BSI, 2008) ISO 12004-2: 2008 and American Society of Testing Materials (ASTM-E2218-02) have been developed. The main equipment used for both standard tests include the punch, hydraulic press machine and blank holder. Two major types of test methods to determine the FLD have been reviewed, which are the Marciniak in-plane test and Nakazima out-plane test (Nakazima et al., 1968) as shown in Figure 2-10(a) and (b), repectively. In the Marciniak in-plane test, a test-piece is stretched by a flat-bottomed cylindrical punch. A steel driver with a hole in the centre is applied between the punch and test-piece in order to minimize the effect of friction on the formability results. In comparison to the Marciniak test, a hemispherical punch is used instead of flat-bottomed cylindrical punch in the Nakazima (Dome) test. The friction effect in Nakajima test is minimised by the application of lubricant. Both the Marciniak in plane test and Nakazima out-plane test are conducted at room temperature which limits conventional FLDs to room temperature.
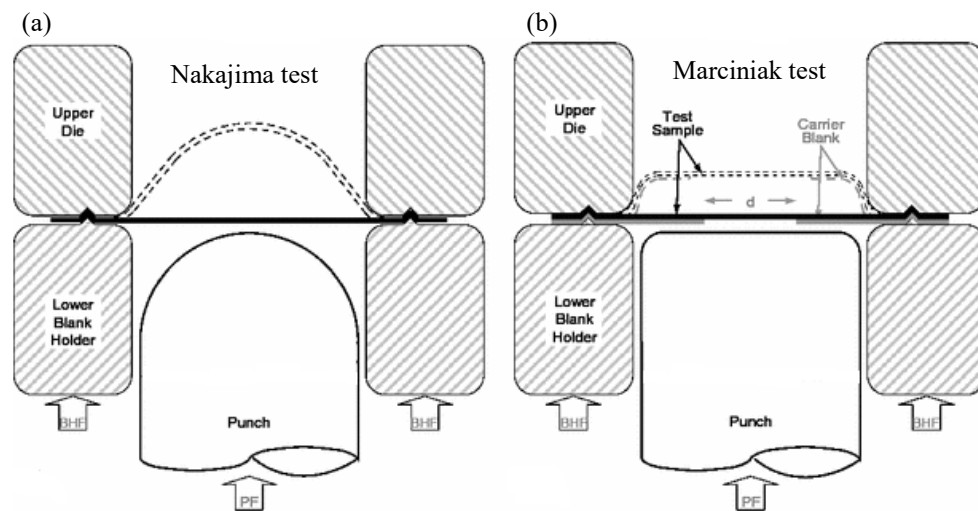
Figure 2-10. Experimental set-up of (a) Nakajima test and (b) Marciniak test (Maier, 2013).

In order to determine the FLDs at elevated temperature, the test-rig and corresponding test procedures were designed and have been successfully conducted by El Fakir et al. (2014b) and Luan et al. (2016). The test rigid design used in their tests is shown in Figure 2-11. Further details on the operation and design of the test rig can be found in El Fakir (2015).
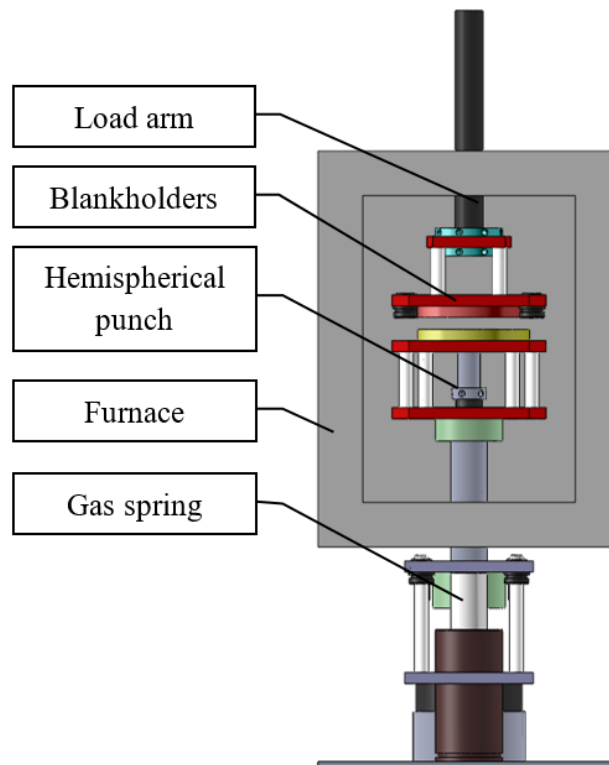
Figure 2-11. A model of an isothermal dome test tool (Luan et al., 2016; El Fakir, 2015)

The experimental methods to determine FLD involve an extremely time consuming process, requiring a great number of tests at different strain rates, temperatures and strain paths. In order to avoid this complex, time-consuming process, the numerical methods to predict FLD have been used by developing the FLD prediction models.

2.4.2 Determination of FLD using theoretical and numerical methods

Theoretical FLD prediction models have been reviewed previously by Banabic (2010) and Schwindt et al. (2015). Classical FLD-prediction models are typically used to predict failure in sheet-metal forming: the Swift model (Swift, 1952), Hill model (Hill, 1952), bifurcation analysis–based models (StÖren and Rice, 1975), the ductile fracture models, and the Marciniak-Kuczynski (M-K) model (Marciniak and Kuczyński, 1967).

The first two approaches utilize instability criteria by introducing diffuse necking and localized necking, as proposed by Swift (1952) and Hill (1952) with the assumption of homogenous sheet metals. The third approach was based on Hill's pioneering work; StÖren and Rice (1975) incorporated deformation plasticity theory into a classical bifurcation analysis in their approach, and indicated that the development of a vertex on the yield locus plays a dominant role on the

onset of localized necking from a state of uniform deformation in thin sheets. The fourth approach concerns the process of failure under various loading conditions, caused by microcracks formed by the nucleation, growth and coalescence of defects (Ran and Fu, 2014). Continuum damage mechanics (CDM) models (Brünig and Gerke, 2011; Chaboche, 2008; Lemaitre, 1985) introduce damage variables to reflect the material structure degradation at the micromechanics scale, with the assumption that failure takes place once specified damage parameters approach a certain value, such as 0.7 (Mohamed et al., 2012). In the CDM models, the specified damage variable is expressed as an effective surface density of cavity or void intersections within a plane (Zhai et al., 2016; Mohamed et al., 2012). Eq. (2.1) shows the power-law viscoplastic constitutive equation as an example:

$$\dot{\varepsilon}_p = \left(\frac{\sigma - R' - k}{K} \right)^{n_1} \tag{2.1}$$

Lin and Mohamad (Lin et al., 2013) generalized viscoplastic-damage constitutive equation to describe the overall damage effects of the material in warm/hot forming conditions. By introducing a damage specified variable into the power-law viscoplastic constitutive equation, the equation is expressed by Eq. (2.2):

$$\dot{\varepsilon}_p = \left(\frac{\sigma / (1 - f_d) - R' - k}{K} \right)^{n_1} \tag{2.2}$$

where f_d is the damage factor.

The final approach concerns the development of necking based on the hypothesis of an initial non-uniformity at local regions, as proposed by Marciniak and Kuczynski. The Marciniak-Kuczynski (M-K) model (Marciniak and Kuczyński, 1967) is one of the most commonly used methods to predict the sheet metal forming limits or instability (Chiba et al., 2013; Eyckens et al., 2011; Signorelli et al., 2009; Allwood and Shouler, 2009). In the model, it is hypothesized that there is a thickness variation at a local region of the specimen, and this initial geometrical non-homogeneity is represented by the variable f_0, known as the 'imperfection factor'. The local region where the imperfection exists is defined as Zone *b*, and the rest of the material as Zone *a*, and the onset of necking is defined when the strain rate ratio in the through-thickness direction or the major strain direction between Zone *b* and Zone *a* reaches a critical value.

Apart from the classical prediction models outlined above, other FLD prediction models have also contributed significantly to the modelling of the formability of sheet metals such as the modified maximum force criterion model, the stress-based criterion model and the through-thickness shear instability criterion model (Hora and Tong, 2008; Stoughton, 2000; Bressan and Williams, 1983).

Several studies in the literature have applied a range of models to predict the forming limit of aluminium alloys (Abovyan et al., 2014; Li et al., 2013; Zhang and Wang, 2012; Khan and Baig, 2011; Stoughton and Yoon, 2011; Abedrabbo et al., 2007; Abedrabbo et al., 2006a, 2006b). Khan and Baig (2011) used the Khan-Huang-Liang (KHL) model to successfully predict the forming limit curves for AA5182-O under warm forming conditions by considering the effects of temperature, strain rate, strain rate sensitivity and anisotropic material behaviour. Abedrabbo et al. (2007; 2006a; 2006b) demonstrated good agreement between their developed model and experimental tests by evaluating the effects of temperature and anisotropy on the failure location. However, the model only considered the effect of temperature; the strain rate and loading path effects required further study. Stoughton and Yoon (2011) assessed the formability of an aluminium alloy under non-proportional loading and triaxial stress loading conditions, emphasizing the importance of a stress-based FLD, and the developed model was validated by a real forming process. Additionally, a stress-based FLD prediction model for a two-stage forming technique was developed in Li et al. (2013). Zhang and Wang (2012) utilized a strain-based FLD to indicate that the occurrence of localized necking is mainly due to the localized geometric softening at a particular level of deformation for anisotropy material.

More importantly, two aspects of constitutive equations used for FLD prediction must be taken into account. One aspect is to predict the mechanical behaviour of the material by developing a material model. The development of material constitutive equations used in FLD prediction models tend to consider multiple physical aspects as discussed as below (Mabuchi and Higashi, 2001; Kim and Dunne, 1999; Lin and Yang, 1999; Zhou, M. and Dunne, 1996).

Material model

The simplest material model to demonstrate the mechanical property of aluminium alloys under different forming conditions uses the stress-strain relationships of Eqs. (2.3) and (2.4):

$$\varepsilon^T = \varepsilon^p + \varepsilon^e \tag{2.3}$$

$$\sigma = E(\varepsilon^T - \varepsilon^p) \tag{2.4}$$

where ε^T is the total true strain, ε^p and ε^e are the plastic strains respectively, E is the Young's modulus and σ is the stress.

During the deformation of a ductile alloy, dislocation controlled deformation dominates when the temperature is below 0.4 T_m (T_m is the melting temperature of the alloy) (Lin et al., 2002; Cheong et al., 2000). The strain hardening plays a dominant role during the deformation of a ductile alloy. The material hardening induced by plastic strain can be represented by power law (Eq. 2.5):

$$\sigma = K\varepsilon^n \tag{2.5}$$

where σ is the true flow stress, ε is the true strain, K is a material constant and n is the strain hardening exponent.

When the temperature is above 0.5 T_m, the overall mechanism for plastic deformation is thermally activated and thus the viscoplastic behaviours became more pronounced. Thus, when including strain and strain rate hardening effects Eq. (2.6):

$$\sigma = K\varepsilon^n \dot{\varepsilon}^m \tag{2.6}$$

where is the $\dot{\varepsilon}$ strain rate and m is the index value of strain rate sensitivity.

Based on literature reviews of constitutive laws in recent years, the research on microstructural evolution of a material has mostly considered material deformation. Material hardening behaviour, on the other hand, can be described by considering the quantified microstructural features: dislocation density, proportion of phase etc. For instance, the dislocation-based and grain-based material hardening equations were introduced to model this behaviour.

Dislocation-based hardening law

In warm/hot forming processes, Lin et al. indicated that the viscoplastic material response can be expressed by developing a dislocation-based hardening material model (Lin et al., 2005). The dislocation density was regarded as one of the important physical aspects in the material model. During the material deformation at elevated temperature, the pre-existing and newly generated dislocations become active. In the activated slip plane, grain boundary sliding occurs (Messerschmidt and Bartsch, 2003). The isotropic hardening effects have been quantified by

the dislocation density evolution (Lin et al., 2013), which is expressed by Eq. (2.7). However, the material deformation at elevated temperatures is complicated. Therefore, in this model, the effects of grain orientation and grain boundary networks are neglected.

$$R' = B\sqrt{\rho}$$

(2.7)

where R' is isotropic material hardening, and B is the material constant.

$$\bar{\rho} = \frac{\rho - \rho_i}{\rho_m - \rho_i}$$

(2.8)

In Eq. (2.8), $\bar{\rho}$ is the normalised dislocation density, ρ_i is the pre-existing dislocation density of a material before deformation, and ρ_m is the saturated dislocation density. ρ is the actual dislocation density, while $\rho - \rho_i$ is the newly generated mobile dislocation density induced by material deformation. $\rho_m - \rho_i$ is the maximum dislocation density that can be generated due to material deformation. The normalized dislocation density $\bar{\rho}$ is the ratio between the newly generated dislocation density and the maximum dislocation density that can be generated by deformation. At the beginning of deformation, $\rho - \rho_i$, the initial normalised dislocation density is 0. When the dislocations are saturated, the normalized dislocation density is 1. The overall dislocation rate can be summarised by Eq. (2.9).

$$\dot{\bar{\rho}} = A(1 - \bar{\rho})\dot{\varepsilon}_p - C\bar{\rho}^{n_2}$$

(2.9)

where $\dot{\bar{\rho}}$ is the rate of overall dislocation density generated, and A, C and n_2 are material constants.

Material hardening due to grain growth

Equations to model grain growth are expressed in Eq. (2.10) and (2.11) (Kim and Dunne, 1999):

$$\dot{\bar{d}} = \alpha_1 \cdot \bar{d}^{-\gamma_0} + \beta_1 \cdot \bar{d}^{-\gamma_1} \cdot \left| \dot{\varepsilon}^P \right|$$

(2.10)

$$\bar{d} = \frac{d}{d_i}$$

(2.11)

where $\bar{d}$ is the normalised average grain size, d is the average grain size and d_i is the initial average grain size, $\dot{\varepsilon}^P$ is the plastic strain rate and α_1, β_1, γ_0 and γ_1 are material constants. In Eq. (2.7), when t = 0, d is equal to d_i, and $\bar{d}$ is 1. In Eq. (2.8), $\alpha_1 \cdot \bar{d}^{-\gamma_0}$ represents the static

grain growth effect on average grain size and $\beta_1 \cdot \bar{d}^{-\gamma_1} \cdot |\dot{\varepsilon}^P|$ is the dynamic grain growth effect on average grain size induced by plastic deformation.

Yield criterion function

Apart from developing constitutive equations for material models, the predictions of FLD also rely on the selection of an appropriate yield function. A yield function was used to establish a relationship for all stress states when yielding occurs in the material (Banabic, 2010). Yield functions are usually classified as two major types, which are isotropic and anisotropic yield functions. Recent research has focused on the development of anisotropic yield functions, with good agreement generally achieved between simulation and experimental results using this criterion (Banabic, 2010). It was found that the isotropic yield function may lead to inaccurate prediction results, especially for the case of a non-linear loading path (Cao et al., 2000; Hiwatashi et al., 1998).

The development of anisotropic yield functions is based on the isotropic yield functions. von-Mises and Tresca are two classic isotropic yield criterions, which are expressed by Eqs. (2.12) and (2.13), respectively:

$$\bar{\sigma} = \left[\frac{\left(\sigma_1 - \sigma_2\right)^2 + \left(\sigma_2 - \sigma_3\right)^2 + \left(\sigma_3 - \sigma_1\right)^2}{2} \right]^{1/2} \tag{2.12}$$

$$\bar{\sigma} = \left|\sigma_1 - \sigma_3\right| \text{ or } \left|\sigma_1 - \sigma_2\right| \text{ or } \left|\sigma_2 - \sigma_3\right| \tag{2.13}$$

where σ_1, σ_2 and σ_3 are the principal stresses and $\bar{\sigma}$ is the yield stress.

The 2-D space yield surfaces of von-Mises yield criterion and Tresca yield criterion are plotted in Figure 2-12; the von-Mises yield criterion is demonstrated by the ellipse shape, whereas the Tresca yield criterion shows a hexagonal prism in principal stress space.
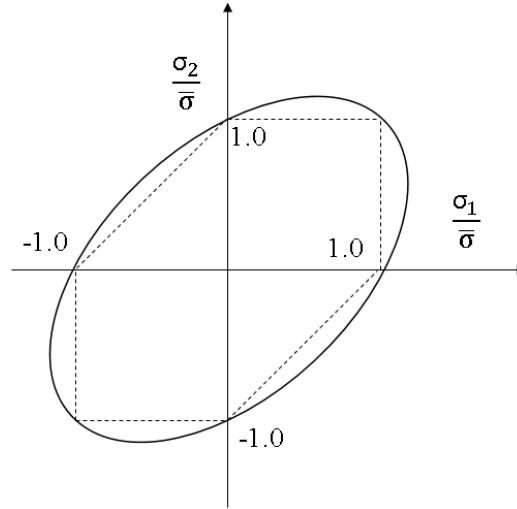
Figure 2-12. Schematic diagram of von Mises criteria and Tresca yield criteria (Adeeb, 2017).

However, Hosford (1972) indicated that the von Mises and Tresca criterion might not fit well for some experimental results, especially for randomly oriented FCC (Bishop et al., 1951) and BCC (Hutchinson, 1968) metals. To overcome this issue, a simplified Hosford's generalized isotropic yield criterion (Hosford, 1972) was developed with good agreement between experimental and theoretical results and is expressed as below:

$$\sigma_0 = \left[\frac{\left(\sigma_1 - \sigma_2\right)^a + \left(\sigma_2 - \sigma_3\right)^a + \left(\sigma_3 - \sigma_1\right)^a}{2} \right]^{\frac{1}{a}} \tag{2.14}$$

where a is not necessarily an integer (Hosford, 1972).

Apart from isotropic yield functions, great efforts have been made to develop yield functions representing the anisotropic behaviour of sheet metals (Barlat et al., 2005; Barlat et al., 2003; Karafillis and Boyce, 1993; Hill, 1993, 1990; Graf and Hosford, 1990; Barlat and Lian, 1989; Hosford, 1985). Three classic types of anisotropic yield functions are reviewed below including Hill (1948)'s yield function, Barlat's yield function and Hosford's yield function.

The first approach is the Hill's yield criterion. The Hill (1948) yield criterion is regarded as the milestone in the development of the theory of anisotropic plasticity. The Hill (1948) model is a classic anisotropic yield function, which has been developed from Huber-Mises criterion by introducing anisotropic coefficients. The Hill (1948) model is expressed in Eq.(2.15):

$$2f_{(\sigma_{ij})} = F\left(\sigma_{yy} - \sigma_{zz}\right)^2 + G\left(\sigma_{zz} - \sigma_{xx}\right)^2 + H\left(\sigma_{xx} - \sigma_{yy}\right)^2 + 2L\sigma_{yz}^2 + 2M\sigma_{zx}^2 + 2N\sigma_{xy}^2 = 1 \quad (2.15)$$

where f is the yield function, and F, G, H, L, M and N are anisotropic constants. The subscripts x, y and z represent the principal axes. Axis x is parallel to the rolling direction, y is the transverse direction and z is the through-thickness direction.

The anisotropic coefficients G, H and F are expressed as:

$$\frac{1}{\sigma_{xx}^2} = G + H, \quad 2F = \frac{1}{\sigma_{yy}^2} + \frac{1}{\sigma_{zz}^2} - \frac{1}{\sigma_{xx}^2}, \quad (2.16)$$

$$\frac{1}{\sigma_{yy}^2} = H + F, \quad 2G = \frac{1}{\sigma_{zz}^2} + \frac{1}{\sigma_{xx}^2} - \frac{1}{\sigma_{yy}^2}, \quad (2.17)$$

$$\frac{1}{\sigma_{zz}^2} = F + G, \quad 2H = \frac{1}{\sigma_{xx}^2} + \frac{1}{\sigma_{yy}^2} - \frac{1}{\sigma_{zz}^2}. \quad (2.18)$$

The anisotropic coefficients L, M and N were calculated as:

$$2L = \frac{1}{\tau_{xx}^2}, \quad 2L = \frac{1}{\tau_{yy}^2}, \quad 2L = \frac{1}{\tau_{zz}^2}. \quad (2.19)$$

For a thin sheet, the plane stress in through-thickness direction is expressed as:

$$(G+H)\sigma_{xx}^2 - 2H\sigma_{xx}\sigma_{yy} + (H+F)\sigma_{yy}^2 + 2N\sigma_{xy}^2 = 1 \quad (2.20)$$

The advantage of the Hill (1948) yield criterion is its simplicity of yield function, which only needs a small number of experimental tests to determine its parameters. However, the most important drawback of the Hill (1948) model is the poor estimation of predictions associated with the variability of the anisotropic coefficients (Banabic, 2010).

Barlat et.al. (1989) have also made a great contribution to the development of the anisotropic yield function including Barlat and Lian's (1994) and (1996) (YLD94; YLD96) yield criteria (Barlat et al., 1997a; Barlat et al., 1997b). The generalized form of YLD94 & 96 is expressed as:

$$\phi = \alpha_x \left| S_y - S_z \right|^m + \alpha_y \left| S_z - S_x \right|^m + \alpha_z \left| S_x - S_y \right|^m = 2\bar{\sigma}_e^m \quad (2.21)$$

where α_x, α_y and α_z are coefficients related to the anisotropic materials. S_x, S_y and S_z are stress tensors in three normal direction defined by Eqs. (2.22 to 2.25):

$$S_{11} = \frac{c_3(\sigma_{11} - \sigma_{22}) + c_2\sigma_{11}}{3} \tag{2.22}$$

$$S_{22} = \frac{c_1\sigma_{22} + c_3(\sigma_{11} - c_2\sigma_{22})}{3} \tag{2.23}$$

$$S_{33} = \frac{-c_2\sigma_{11} - c_1\sigma_{11}}{3} \tag{2.24}$$

$$S_{12} = c_6\sigma_{12} \tag{2.25}$$

where c_1, c_2, c_3 and c_6 are the coefficients of anistropy.

Based on the simulation of circular cup drawing tests using the YLD94 & 96 criteria, it was found that a good agreement was obtained between simulation results and experimental results (Yoon et al., 1999). However, the YLD94 & 96 criteria were computationally expensive. Those yield functions are too complex to calculate the full stress states and derivatives of their equivalent stress (Banabic, 2010).

The third approach is the Hosford's yield criterion, which was proposed in 1979 (Hosford, 1979). In the Hosford (1979) yield function, the determination of "*a*" is strongly dependent on the crystallographic structure of the material. Hosford stated that the best approximation of anisotropic behaviour can be achieved when *a*=6 for BCC materials and *a*=8 for FCC materials.

The generalized form of Hosford (1979) yield function was expressed as:

$$F|\sigma_{22} - \sigma_{11}|^a + G|\sigma_{33} - \sigma_{11}|^a + H|\sigma_{11} - \sigma_{22}|^a = \bar{\sigma}^a \tag{2.26}$$

where *F, G, H* are anisotropic coefficients, and *a* is a constant. σ_{11}, σ_{22} and σ_{33} are the principal stresses and $\bar{\sigma}$ is the equivalent stress.

Considering sheet-metal forming, the Hosford (1979) anisotropic yield function was expressed in Eq. 2.27:

$$R_1\sigma_{11}{}^a + R_2\sigma_{22}{}^a + R_1R_2(\sigma_{11} - \sigma_{22})^a = R_2(R_1 + 1)Y_1{}^a \tag{2.27}$$

where R_1 and R_2 are the strain ratios determined from experiment data, and Y_1 is the tensile yield stress.

The plane stress in sheet metal is expressed using Hosford (1979) as:

$$r_{90}\left|\sigma_{11}\right|^a + r_0\left|\sigma_{22}\right|^a + r_{90}r_0\left|\sigma_{11} - \sigma_{22}\right|^a = r_{90}(r_0 + 1)\bar{\sigma}_0{}^a \qquad (2.28)$$

where $\bar{\sigma}_0$ is the equivalent stress in unaxial tensile direction. r_0 and r_{90} are the strain ratios measured in the major and minor strain directions.

The main benefits of using Hosford's (1979) yield criterion is the ability to obtain a good estimation of the yield locus by fitting the value of exponent value ("a"). In this model, the R_1 and R_2 coefficients are associated with anisotropy, which can be determined from uniaxial tensile tests. Although Hill (1948) and the YLD94 & 96 yield criteria are still widely used, the Hosford (1979) yield criterion shows a good estimation of anisotropic behaviour for FLD prediction results as demonstrated by El Fakir et al. (2014), Li et al. (2012), Friedman and Pan (2000) and Padwal and Chaturvedi (1992).

2.5 Conclusion

In the present chapter, AA2060 and AA7075 lightweight alloys have been reviewed and compared with other AA2XXX and AA7XXX alloys. The limitations identified in AA7075 and AA2060 alloys are their poor ductilities at room temperature. To overcome this issue, the application of SPF and HFQ technologies were reviewed with HFQ being a highly efficient alternative to SPF. Finally, the necking and failure FLD prediction models in the literature have been reviewed, with the limitation of existing models being their inability to predict non-isothermal and complex loading conditions as is present in the HFQ process. In this thesis, an alternative model is proposed to address the limitations of traditional models.

Chapter 3

Material characterisation and forming tests of AA2060[1]

This chapter presents the experimental work conducted on Al-Li alloy (AA2060). Firstly, the mechanical properties of AA2060 were determined through uniaxial tensile tests. The formability of AA2060 under warm and hot stamping conditions was evaluated by conducting formability tests at the appropriate elevated temperatures. Based on the uniaxial tensile and formability test results, the feasibility of forming AA2060 alloy into a complex-shaped component (wing stiffener component) using the two-stage HFQ forming technology was studied. Moreover, the effects of age hardening on the behaviour of AA2060 was studied by performing multi-stage artificial aging tests. From these tests, the optimum aging conditions for AA2060 were determined.

3.1 Test-piece material

The material used for all the tests was 2mm thick AA2060 blanks, which was supplied by Beijing Aeronautical Manufacturing Technology Research Institute (BAMTRI), in the T8 condition (Solution heat treated, cold worked and artificially aged). The chemical composition of AA2060 is shown in Table 3-1.

Table 3-1. Composition of AA2060 blank

Composition	Li	Mg	Cu	Ag	Mn	Zn	Al
(wt%)	0.6-0.9	0.6-1.1	3.4-3.5	0.05-0.5	0.1-0.5	0.3-0.5	Bal.

---

[1] Chapter 3 is based on paper work "Gao, H., Weng, T., Liu, J., Li, C., Li., Z, Wang, L., Hot stamping of an Al-Li alloy: A feasibility study, Manufacturing Review, 3, 2016"

3.2 Uniaxial tensile test

The viscoplastic material response of the alloy over the range of strain rates and temperatures corresponding to warm and hot sheet metal forming was evaluated through the performance of the uniaxial tensile test. Dog-bone-shaped specimens were designed, and laser cut with the gauge length parallel to the rolling direction. The test-piece with its dimensions are shown in Figure 3-1.

(a)   (b)
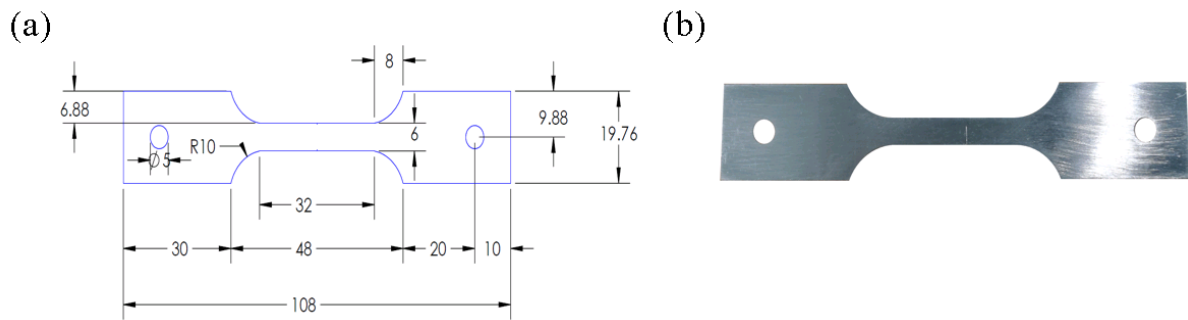
Figure 3-1. (a) Geometry design (in mm) of specimen for uniaxial tensile test (b) Photo of a sample for uniaxial tensile tests

3.2.1 Experiment set-up

The uniaxial tensile tests were conducted on a Gleeble 3800 thermo-mechanical testing machine as shown in Figure 3-2. The Gleeble system uses direct resistance heating to heat the specimen, which is clamped between two continuously cooled jaws. The heating rate can reach up to 10,000°C/s. Thermocouples were spot welded (spot welding voltage 30V) and positioned at the centre of the specimen, providing temperature feedback to the system. The applied load, measured by a load cell, and the strains measured using a C-Gauge transducer positioned at the centre of the specimen (Figure 3-2), were recorded simultaneously. The tensile tests were conducted to failure at various temperatures and strain rates. The test temperatures ranged between 350°C (above the recrystallization temperature) and 520°C (SHT temperature) to model the hot forming conditions of AA2060 (Prasad et al., 2014). The test matrix for the uniaxial tensile tests is shown in Table 3-2.

Table 3-2. Test matrix for uniaxial tensile tests on AA2060

Strain rate / Temperature	350°C	400°C	450°C	470°C	500°C	520°C
0.2/s				✓		
2/s				✓		
6/s	✓	✓	✓	✓	✓	✓
11/s				✓		

(a) (b)

(c)
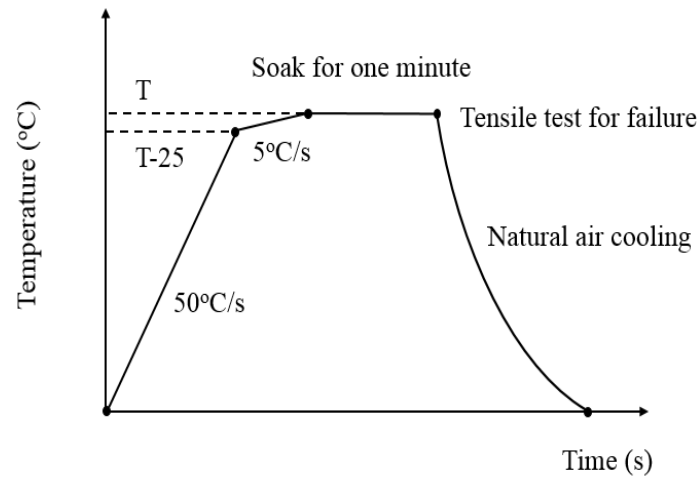
Figure 3-2. (a) The Gleeble 3800 thermal-mechanical testing system and (b) the test specimen setup (c) programmed heating evolution against time

The temperature profile (El Fakir et al., 2014) was defined using the control software of the Gleeble 3800 simulator. The heating rate was set to 50°C/s until the temperature reached 25°C below the target temperature, after which the heating rate was decreased to 5°C/s, to avoid overheating. The specimen was then held at the target temperature for 1 minute to ensure that the temperature was homogenous in the deformation region prior to HFQ forming. The

identification of isothermal zone was shown in Appendix 3A. The temperature profile against time used for these tests is shown in Figure 3-2(c).

Practical complex-shaped components may contain structural features, such as local recessed areas to enhance the stiffness, which inevitably causes step-changes in the strain rate and loading path. As an intrinsic feature of hot stamping processes, severe temperature reductions take place as soon as the hot blank begins to contact the cold forming tools (typically water cooled). Therefore, in addition to the tensile tests outlined above, a test programme was prepared to reproduce these features on the Gleeble 3800, the results of which were used to validate the material model developed in Chapter 5. In the strain rate variation tests, a sharp change in the strain rate was applied within the time range from t=1.2s to t=1.5s. In the temperature variation tests, an abrupt change in the temperature was applied at times t=3.7s and t=9.6s within a second to simulate the cold die quenching effect of the HFQ process. As the temperature change occurred over such a short period (1 seconds) using the Gleeble simulator, the strain induced due to changes in temperature was assumed to be negligible. The test profiles used for the strain rate and temperature variation tests are shown in Figure 3-3(a) and (b).
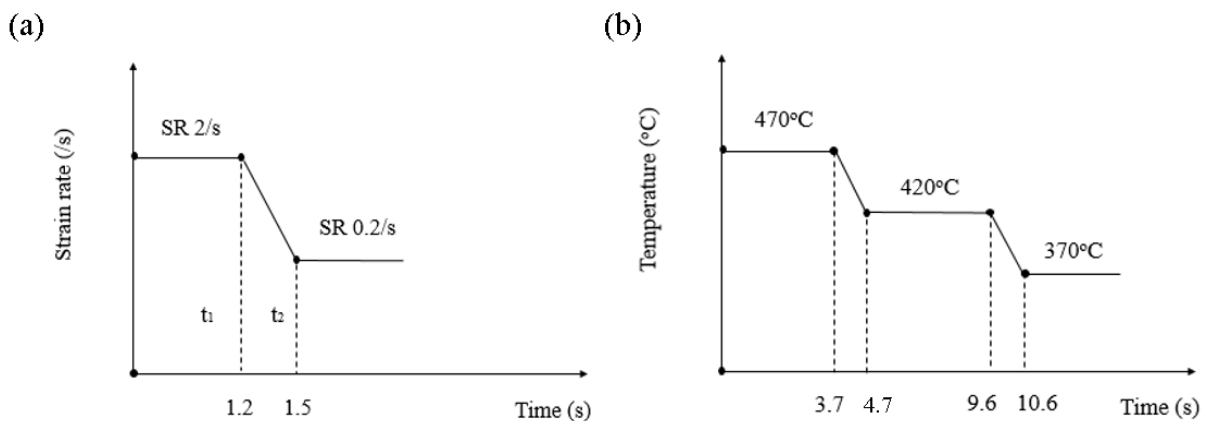
Figure 3-3. (a) Strain rate profile in strain-rate variation test at constant temperature of 470 °C and (b) temperature profile in temperature variation test at constant strain rate of 0.02/s

3.2.2 Flow stress curves with different strain rates and temperatures

The thermal-mechanical properties of AA2060 were obtained by a series of uniaxial tensile tests. Figure 3-4 shows the flow stress curves of AA2060 obtained at different temperatures ranging from 350°C to 520°C, with a strain rate of $2s^{-1}$.
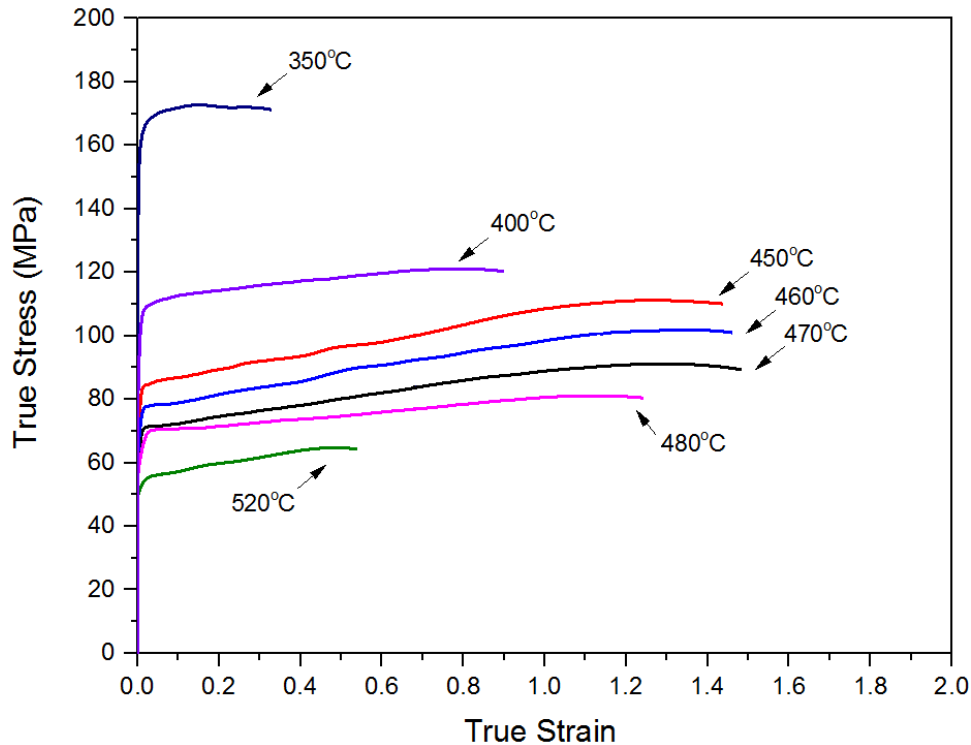
Figure 3-4. Flow stress curves of AA2060 at different temperatures with a constant strain rate of $2s^{-1}$

In Figure 3-4, from 350°C to 470°C, the flow stress decreases with increasing temperature, whereas the failure strains of AA2060 increase with increasing temperature. The reduction in flow stress and increase in failure strain can be explained by thermally activated deformation mechanisms. As the temperature increases, it enhances the mobility of the atoms and dislocations. Hence the material becomes softer and more ductile. However, in Figure 3-4, the ductility decreased remarkably as the temperature was above 470°C. The failure strain at 520°C is about one-third of its peak value, and a similar trend was found for AA2024 (Prasad et al., 2014; Wang et al., 2011). For the typical heat-treatable aluminium alloys used in the automotive industry (e.g. AA6XXX), the soluble precipitates and inclusions dissolve into the matrix at SHT temperature. Thus, the ductility of the alloys attains a higher level than that at lower temperatures due to less obstacle barriers to the dislocation motion during deformation (Davis, 2004). However, it has been deduced that the reduced ductility in AA2024 is due to the presence of low eutectic melting phase at the SHT temperature (Wang et al., 2011). It was found that the intergranular fracture plays a dominant role in failure mechanism of AA2024

due to the presence of low strength phases at grain boundaries. Other Al-Li alloys, such as Weldalite (049) (Prasad and Ramachandran, 2013), have also been hypothesised to exhibit the same behaviour due to low-melting eutectics (Cu and Mg enrichment). As AA2060, AA2024 and Weldalite (049) are all Al-Cu based alloys, the melt of low eutectic melting phase could be one of the reasons to explain the poor ductility over solution heat treatment temperature (Wang et al., 2011).

As can be seen from Figure 3-5, the failure strain of AA2060 increases linearly up until 450℃, where the failure strain reaches a peak before declining with increased temperature. Therefore, to avoid premature fracture and maintain good ductility of the material, subsequent forming tests were conducted at temperatures between 450°C to 470°C.
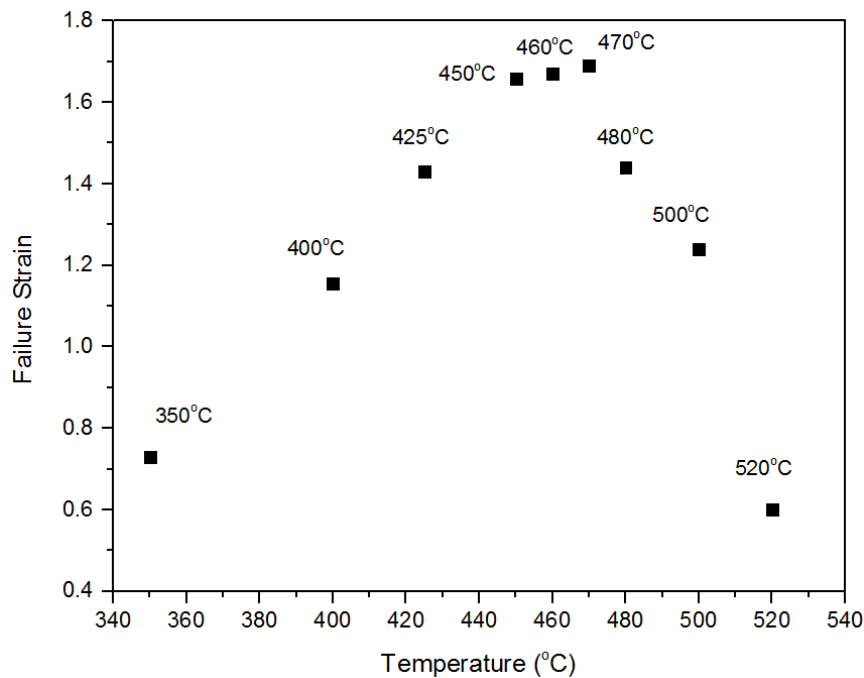
Figure 3-5. Failure strains of AA2060 with different temperatures at a constant strain rate of $2s^{-1}$

The effect of strain rate on the flow stresses of AA2060 is shown in Figure 3-5. It can be seen that the flow stress of AA2060 increases with increasing strain rate due to the strain rate hardening effect. On the other hand, the application of higher strain rates results in lower ductility of AA2060. Thus, it has been found that the increasing strain rate has a negative effect on the ductility of AA2060.
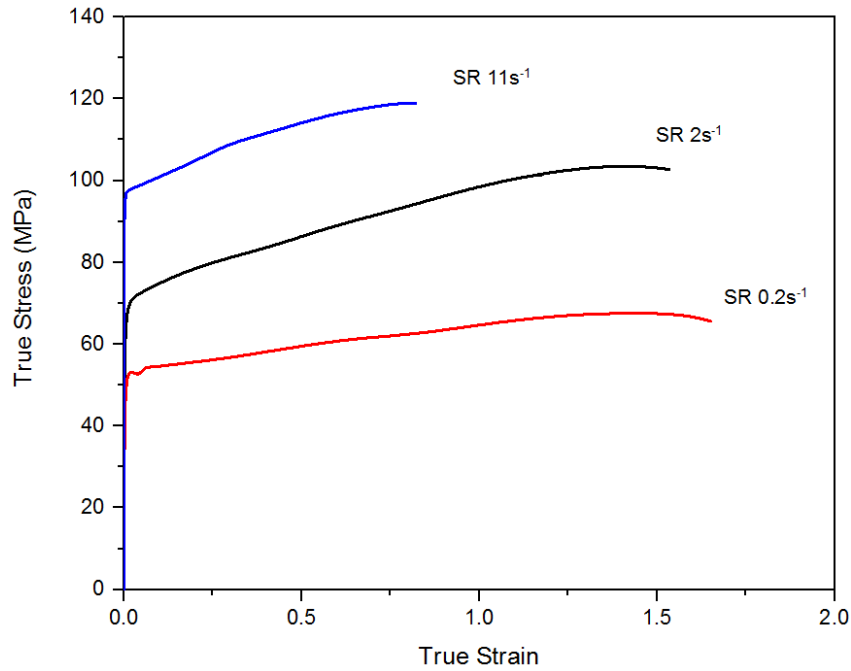
Figure 3-6. Flow stress curves of AA2060 at 470°C with different strain rates (SR: major strain rates)

The trials presented in this section for a variation in strain rate and temperature are used to validate a viscoplastic material model presented in Chapter 5. The experimental results from the strain rate and temperature variation tests are used to access the effectiveness of the viscoplastic material model, which are presented as symbols in Figure 3-7 and Figure 3-8, respectively.
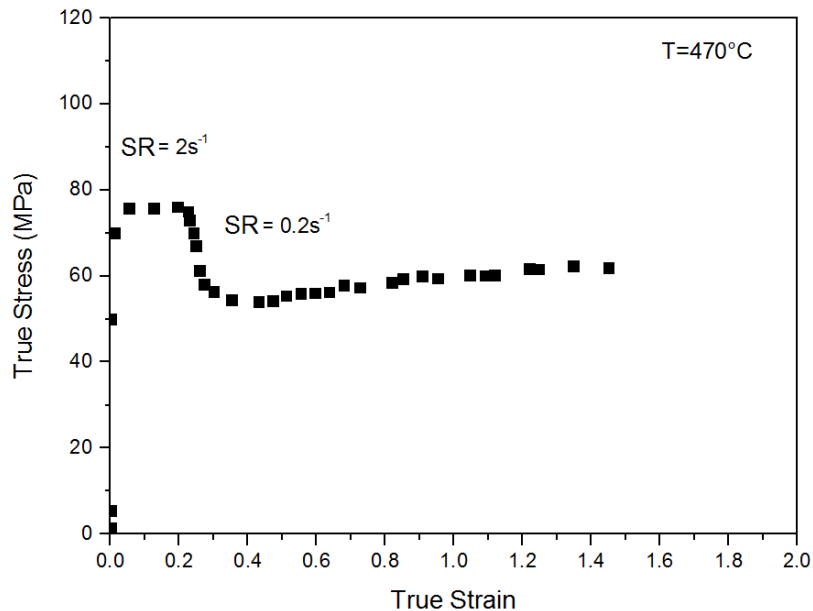
Figure 3-7. Strain-rate jump test at a constant temperature of 470°C.
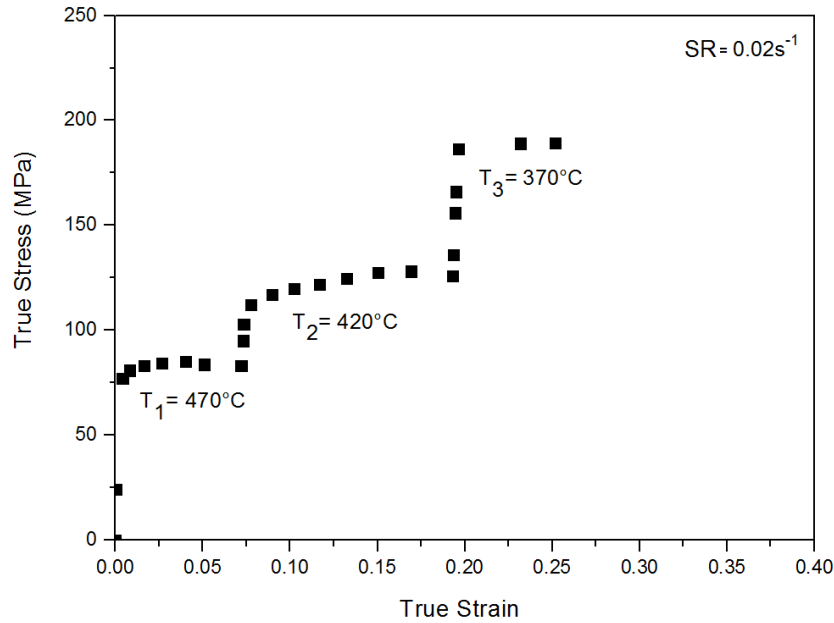
Figure 3-8. Temperature-jump test at a constant strain rate of 0.02/s

In the strain rate variation tests, a sudden drop of strain rate was applied during the uniaxial tensile test as shown in Figure 3-7, resulting in the instantaneous reduction of flow stress due to the reduction of strain rate hardening. In the temperature variation test of Figure 3-8, a constant strain rate of $0.02s^{-1}$ was applied with three sharp reductions in temperature introduced during the uniaxial tensile test, which resulted in corresponding sudden increase in flow stress.

3.3 Forming limit test

3.3.1 Specimen preparation for isothermal forming limit test

The geometry of the test-pieces used in forming limit tests of AA2060 was that of a circular blank with a central parallel shaft, as shown in Figure 3-9(a). Different widths of the parallel shaft (W) were used to obtain different loading paths, as shown by the numbers 1, 2 and 3 on the schematic FLC of Figure 3-9(b). Table 3-3 lists the widths of the parallel shafts of the blanks required to achieve the various loading paths. In Table 3-3, W is the width of the specimen (Figure 3-9(a)), and D the diameter of specimen.

(a)

(b)
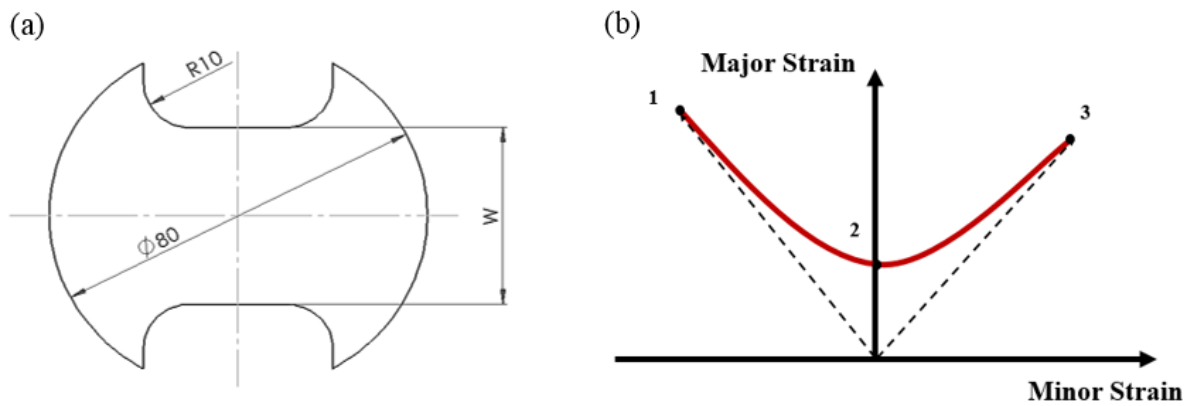
Figure 3-9. Formability test: (a) blank geometry and (b) schematic drawing of the test points for the FLC

Table 3-3. Dimensions of the test-pieces for isothermal forming limit tests

Geometry No.	Test Type	W (mm)	W/D
1	Uniaxial tension	12	0.15
2	Plane strain	40	0.5
3	Biaxial strain	80	1

Electrochemical etching

Electrolytic etching is used in order to measure the strain field of the deformed specimen via the GOM-ARGUS system. All the specimens were electrolytically etched to create a regular grid pattern of 1mm diameter with 1mm spacing on the surfaces of the sample before conducting the formability test. To obtain a clear regular grid pattern, the test-pieces were grinded and polished before conducting the etching process. The electrolytic etching process can be seen in Figure 3-10, with the electrochemical etching process shown in Figure 3-11.

As can be seen from Figure 3-10, a roller was dipped into the etching solution. A test piece was placed and positioned between the metallic plate and grid etching pattern. Afterwards, the roller with a charged etching solution made close contact with the surface of the test-piece and was rolled along the sample in a single direction. At this stage, a chemical reaction occurred at the contact area between the roller and test-piece enabling the grid pattern to be created. In the final stage, the etched specimen was then rinsed by water and dried.
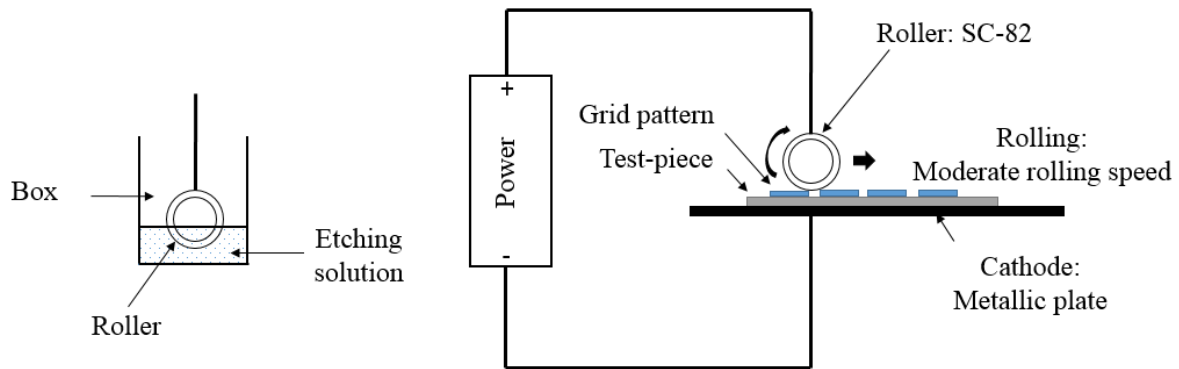
Figure 3-10. Demonstration of the electrochemical etching process
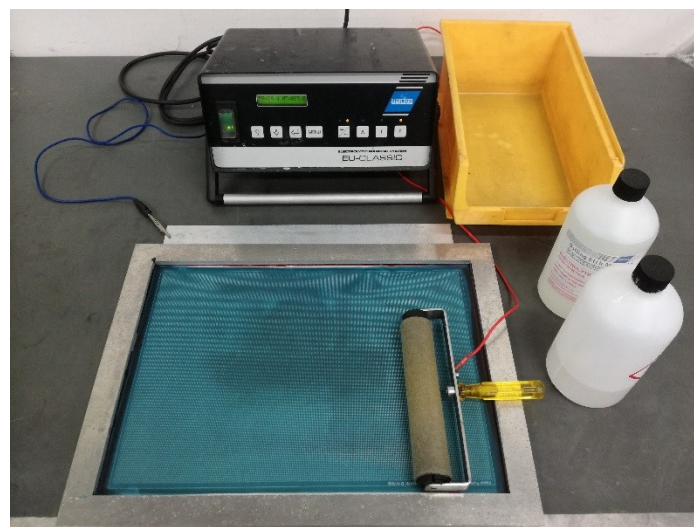
Figure 3-11. The set-up for the electrochemical etching process

3.3.2 Experiment set-up for isothermal forming limit test

Test rig for isothermal forming limit test

An isothermal dome test tool was designed, manufactured and assembled to conduct high temperature forming limit tests. The test rig was designed and integrated within a furnace and mounted on a 250kN ESH press to perform isothermal forming limit tests. Details of the designed tool can be found in the works of El Fakir (2015) and Luan et al. (2016).

The formability test setup is demonstrated in Figure 3-12. The experimental procedure to conduct the isothermal forming limit test is as follows: In the first stage, the target temperature, forming stroke and forming speed were assigned. The forming tools were heated by the Lenton furnace until the target temperature was reached. In the heating stage, the temperature of the

forming tool was monitored by thermocouples positioned on the bottom blankholder. The target forming stroke was set by adjusting the position of the top blankholder. The target forming speed was obtained by adjusting the parameters in the 25kN ESH press via feedback control of displacement against time from the oscilloscope. The displacement was manually measured and the forming time is measured by oscilloscope. In the second stage, a graphite based lubricant, Omega 35 (Sovereign, 2017) was applied to the bottom surface of the specimen by a brush and it was positioned into the test rig. The test piece was placed onto the bottom blank holder and positioned in the desired position by resting against the alignment pins. By adjusting the height of the top blank holder, the specimen was clamped between the top and bottom blank holders. After the furnace was closed, the forming tools and specimen were heated until the target temperature was reached. Test-pieces were soaked for 60 seconds to ensure homogeneous temperature distribution and were subsequently stamped. Formability of the blank was determined by running a series of tests with different punch stroke increments applied in each test until necking started to occur.
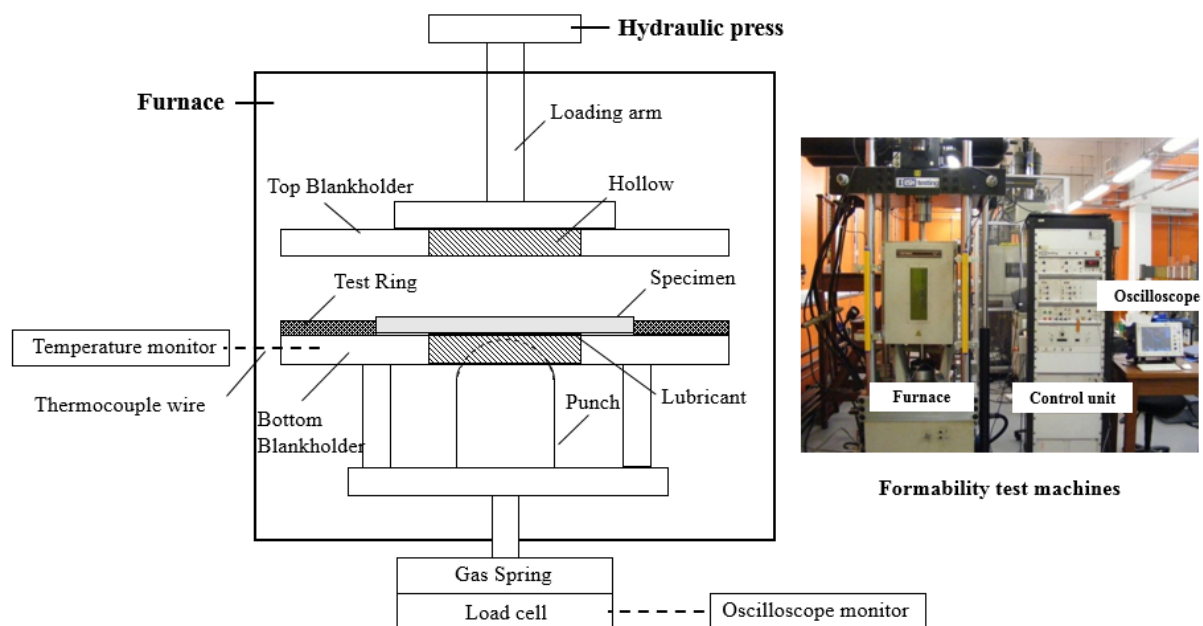
Figure 3-12. The set-up of forming limit test

In each formability test, test-pieces with different geometrical shapes (representing different strain paths) were investigated under different forming temperatures and forming speeds. The test matrix of the formability tests is listed in Table 3-4. In each testing condition, the forming

limit of AA2060 was determined until localised necking occurred. The localised necking on the formed parts with different strain paths is shown in Figure 3-13.
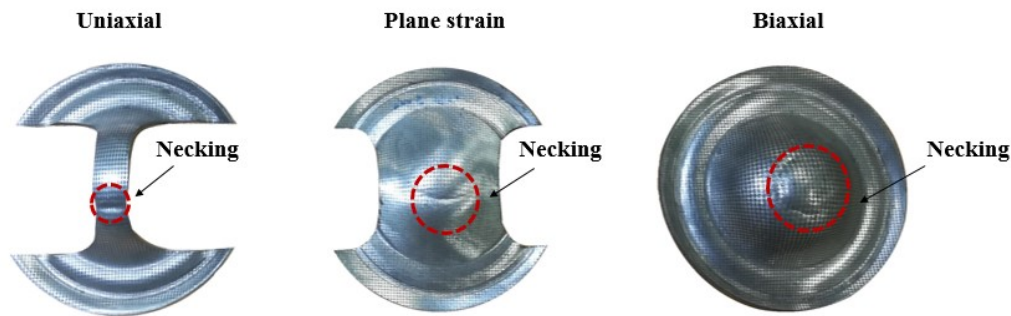
Figure 3-13. Localised necking on formed parts with different strain paths

Three repeat tests in each forming conditions were conducted to limit the effect of unexpected fracture of the deformed specimen. In total, 120 formability tests were conducted for the AA2060.

Table 3-4. Test matrix of forming limit tests

Forming speed \ Temperature (°C)	300	400	450
75 mm/s		✓	
250 mm/s	✓	✓	✓
400 mm/s		✓	

Surface strain measurement for formability test specimens

The full strain field of the formed test pieces was measured using GOM-ARGUS photogrammetry system by taking a series of images (approximately 200 images for each specimen). Those images were taken at different positions by changing the height of the camera and rotating turntable until a 360° map of the test piece was constructed as demonstrated in Figure 3-14(a). The strain measurement setup is presented in Figure 3-14(b). During the mapping process, the stationary camera was positioned in front of the turntable. The turntable was placed in a photo light tent to ensure good visibility of the test-piece. The formed test piece was located in the centre of a turntable enclosed with four rectangular scale bars with coded-mark cubes.
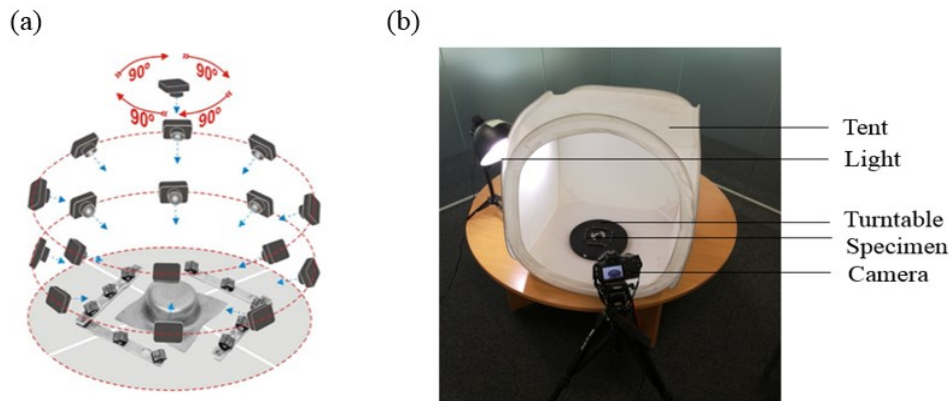
Figure 3-14. (a) Schematic diagram of GOM-ARGUS system (b) GOM-ARGUS system setup for strain measurement

Once the images of formed specimen were taken, the images were imported into the GOM-ARGUS system. By calibrating the system to the rectangular scale bars, the dimensions of the distorted grid pattern on the test-piece surface were recognised and measured, as shown in Figure 3-15.
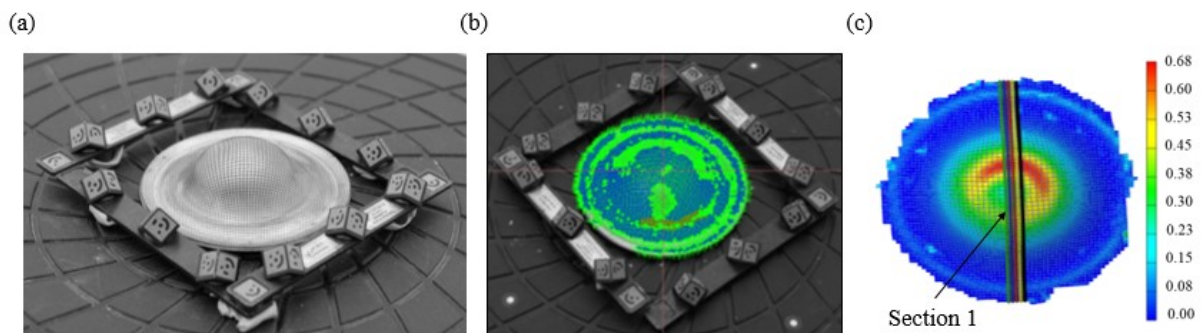
Figure 3-15. (a) Photo of image taken for Argus system (b) Identification of grid of formed part (c) Major strain distribution of formed part

From the ARGUS system, the localised necking was found as indicated by the red regions in Figure 3-15(c). To obtain the forming limit strain, the major and minor strain values on five equal-spaced cross-sections perpendicular to the localised necking region were measured according to the test standard (BIS, 2008) ISO 12004-2: 2008. The solid symbols in Figure 3-16 show the experimental major and minor strain distributions of one section (Section 1 shown as an example) from ARGUS. It can be seen in the figure that there is no clear experimental measurement at the apex of the major and minor strains curves, due to unclear distorted mark by ARGUS systems. Thus, the maximum limit major and minor strains were evaluated using numerical fitting methods according to formability test standards (BIS, 2008) ISO 12004-2:

2008 and procedures described by El Fakir (2015). In Figure 3-16, the numerically fitted major and minor strain curves are represented by a dashed line.
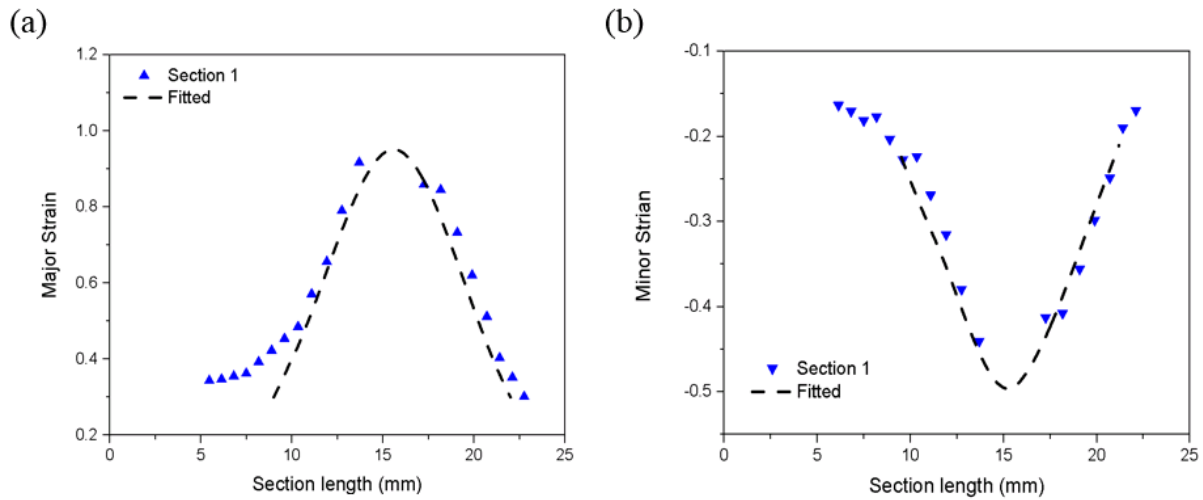
Figure 3-16. Distributions of (a) major and (b) minor strains on a selected section for AA2060 uniaxial specimen at a forming temperature of 400°C and forming speed of 75mm/s. Symbols: Experimental results; Dashed line: Numerical fitting results

Determination of forming limit diagrams of AA2060 at warm and hot stamping conditions

In the formability tests, the limit dome heights were determined under a range of strain rates and temperatures. An example of the limit dome heights for AA2060 at forming speeds ranging from 75mm/s to 400mm/s and temperatures ranging from 300°C to 450°C is shown in Figure 3-17 and Figure 3-18, respectively.

Limit dome heights of the deformed specimens were measured using a height gauge. The measurements of limit dome height can be found in Table 3-7 and Table 3-8 in Appendix 3B. In Figure 3-17 and Figure 3-18, it was found that the limit dome heights of AA2060 increased with temperature and decreased with forming speeds. The forming limit diagrams (FLDs) of AA2060 as a function of forming speeds and temperature were plotted as shown in Figure 3-19 and Figure 3-20, respectively.

Figure 3-19 shows the forming limit diagrams (FLDs) of AA2060 as a function of forming speeds. It was found that the formability of AA2060 decreased with increasing forming speeds. At 400°C, the major deformation mechanism is strain rate hardening. More strain hardening may have a negative effect on the formability of AA2060. Figure 3-20 shows the FLD of AA2060 as a function of forming temperature. It was found that the formability of AA2060

increased with increasing forming temperature. The effect of temperature on the formability is mainly due to the thermal-activated mechanism (Gao *et al.*, 2016). The effect of forming speeds and temperatures on formability of AA2060 are further explained in Chapter 5.
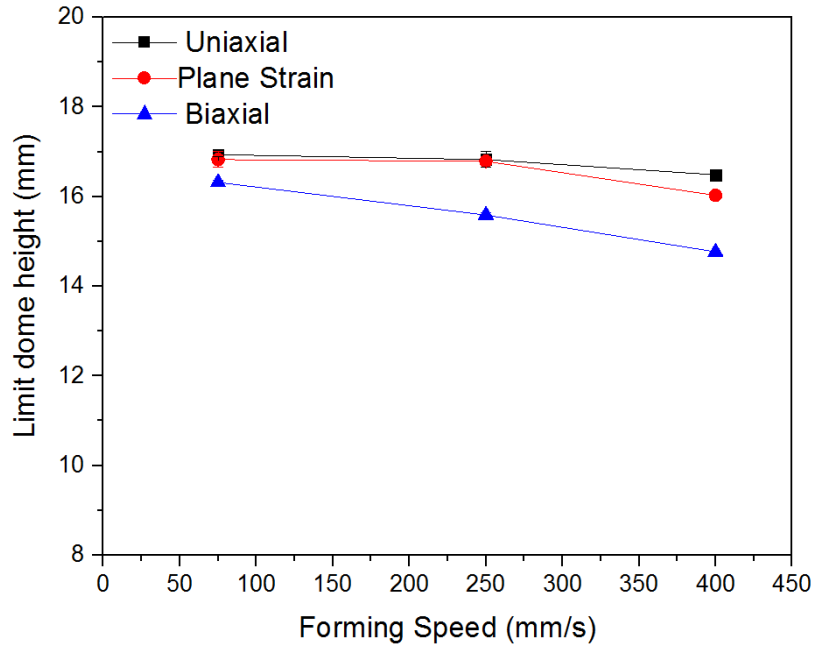
Figure 3-17. Limit dome height of AA2060 at different forming speeds
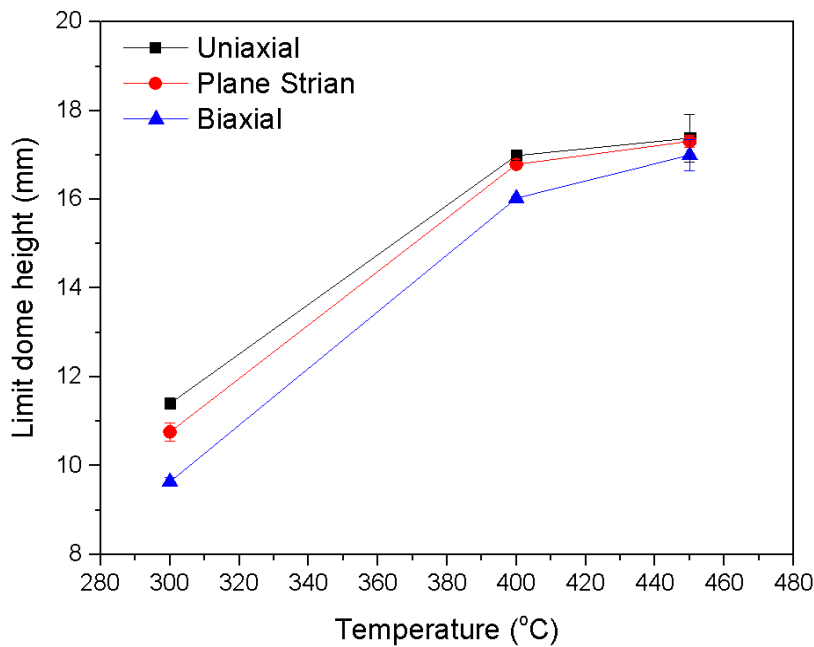
Figure 3-18. Limit dome height of AA2060 at different forming temperatures
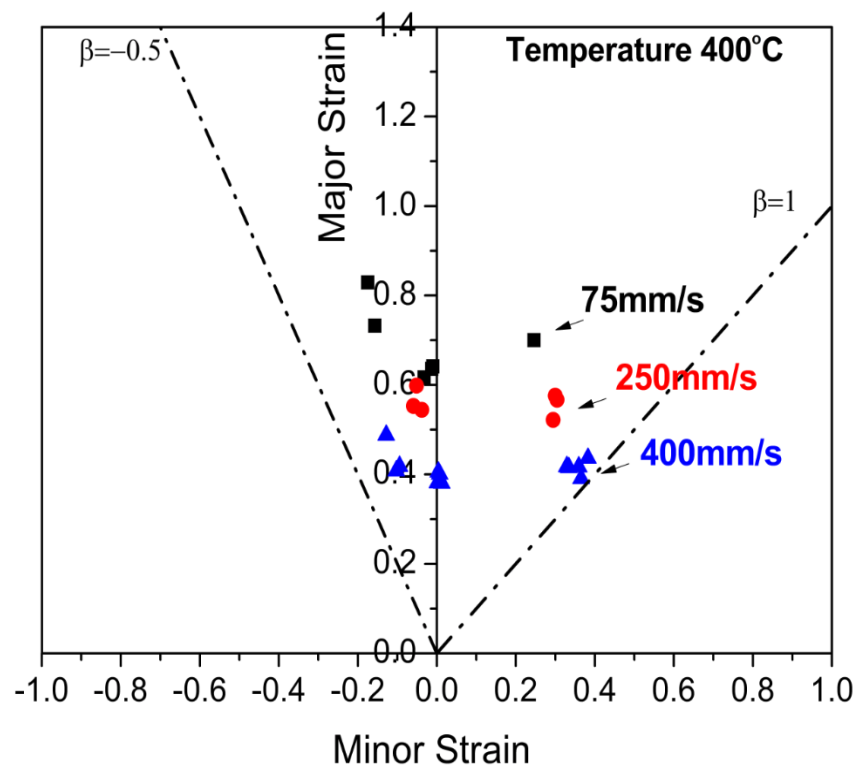
Figure 3-19. Effects of forming speed on the formability of AA2060 at a constant forming temperature of 400°C. β is the ratio between minor strain and major strain.
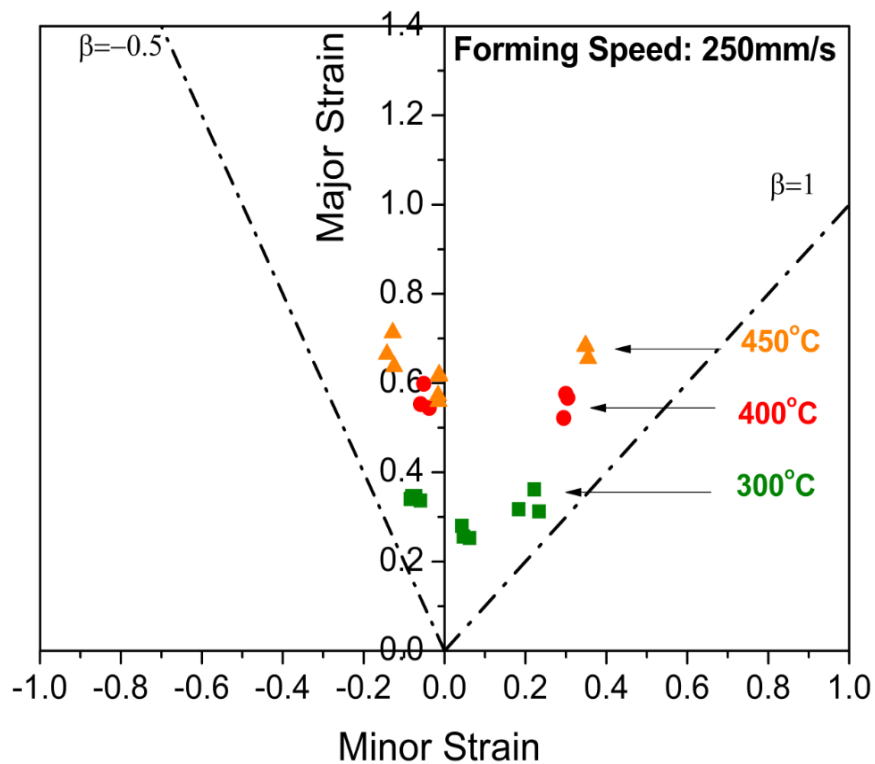
Figure 3-20. Effects of forming temperature on the formability of AA2060 at a constant forming speed of 250mm/s

3.4 HFQ forming of a wing stiffener panel component featuring non-isothermal and complex loading conditions

Forming tests were conducted on a wing stiffener component to satisfy the objectives of Table 3-5. The first objective was to form a complex-shaped component from AA2060 using two-stage HFQ forming technology without experiencing necking or fracture. The second was to form a complex-shaped component of AA2060 with localised necking. This would verify the forming limit prediction model proposed in Chapter 5.

Table 3-5. Experimental objectives for forming tests

Forming tests	Experimental objectives
Forming test A	Form a wing stiffener component without localised necking
Forming test B	Form a wing stiffener component with localised necking

To perform the tests, AA2060 blanks were formed under HFQ forming conditions using an existing wing stiffener forming tool as shown in Figure 3-21.
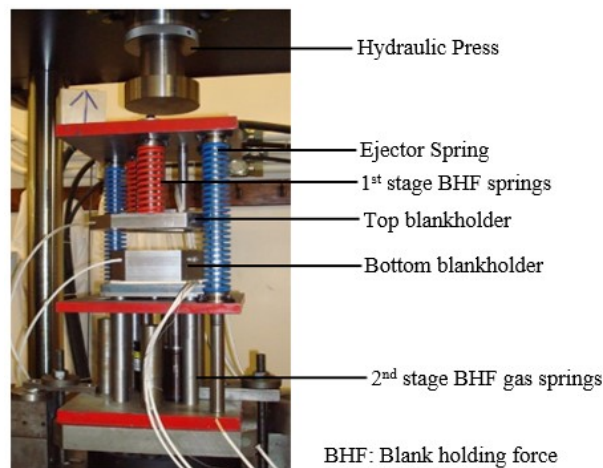
Figure 3-21. Stamping tool used to form wing stiffener component

3.4.1 Specimen preparation for forming test

Rectangular shaped specimens in the size of 200 mm×65mm×2mm were used in the forming tests. Each specimen was prepared using a laser cutting machine with its longitudinal direction parallel to the rolling direction. The specimen surface was electro-etched to measure final strain. Lubricant was applied to the forming die and punch before testing to minimise the friction

during the forming process. The temperature of the test-piece was monitored by thermocouple attached to its edge.

3.4.2 Experiment set-up for forming test

In forming test A (forming wing stiffener component) and B (forming wing stiffener component with limits), the heating profile against time under two-stage HFQ forming process was applied as shown in Figure 3-22. The two-stage HFQ is developed for ultra-high strength aluminium alloys, e.g. AA7XXX and AA2XXX, in which peak ductility occurs at a temperature below SHT temperature. The 1st stage forming is conducted at a temperature where the peak ductility occurs to enable complex shapes to be formed. In the 2nd stage forming, the formed pressing is re-heated to SHT temperature, followed by a subsequent cold die quenching in the same cold dies, with minor plastic deformation applied.
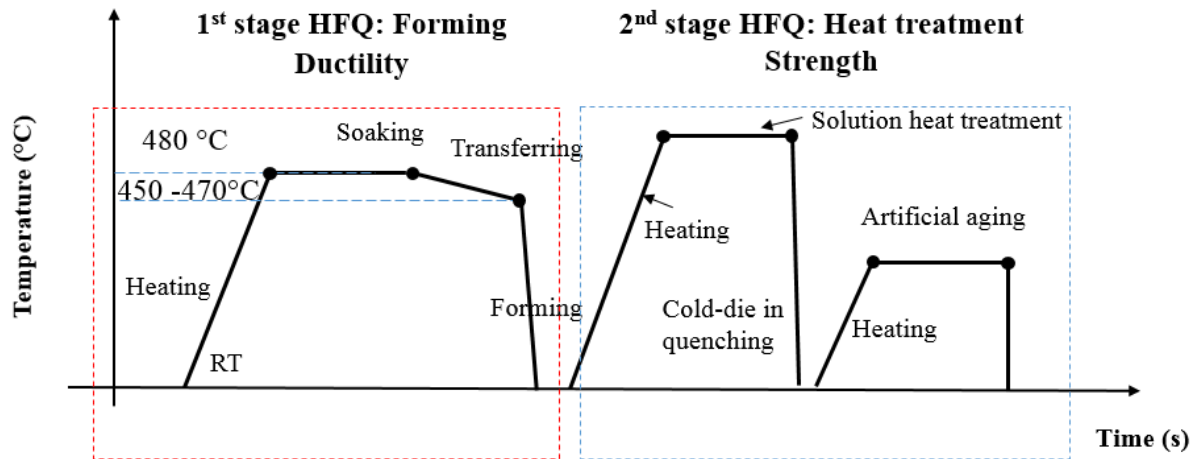
Figure 3-22. Temperature profile used to form AA2060 wing stiffener component under two-stage HFQ forming conditions

In forming test A, the wing stiffener component was formed at a speed of 250 mm/s and temperatures ranging from 450 to 470°C by the two-stage HFQ forming process. The specimen in the size of 200×65×2 mm^3 was prepared. For the first stage, the specimen was heated up to the forming temperature (480°C) which is below the SHT temperature (typically around 520°C) of AA2060 (Starke, 2013). After the hot blank was transferred to the cold tool, the stamping process was activated immediately. The transfer time from the furnace to the cold die was controlled to be around 10 seconds. The aim of first-stage forming is to form the Al-Li alloy with optimum geometrical features. In the second stage, the formed specimen was transferred to the furnace and re-heated up to its SHT temperature (520°C). After soaking at the SHT temperature for 1 min, the specimen was placed back into the cold die and subsequently

quenched to room temperature by the cold dies. The objective of the second stage is to achieve high post-form strength of the alloy. The forming temperature was monitored by thermocouples, recording the temperature history during the whole process. Finally, the formed part was artificially aged. In Section 3.5, the age hardening behaviour of AA2060 was investigated.

Furthermore, forming test B was conducted by running a series of forming trials of increasing punch stroke, until necking started to occur in the central features of the wing stiffener. After localised necking occurred in the formed part, the strain distributions were measured by the ARGUS system as presented in Figure 3-23.
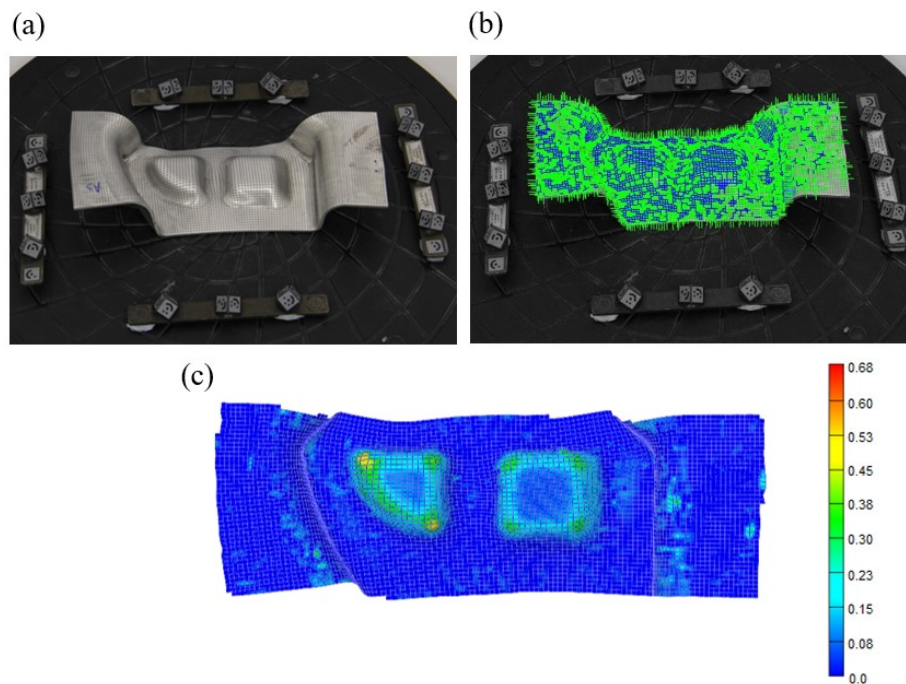
Figure 3-23. Wing stiffener component a) photo of image taken from camera b) identification of grid of formed part using ARGUS system and c) thinning distribution of formed part

3.4.3 Analysis of forming test results

In forming test A, complex-shaped wing stiffener components were successfully formed using two-stage HFQ forming technique without any fracture as presented in Figure 3-24(a) and (b). The part was formed at a forming speed of 250mm/s and forming temperature of 450-470°C.
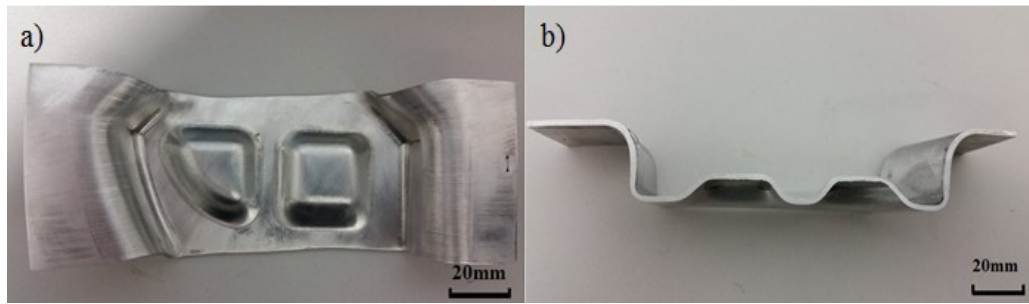
Figure 3-24. A wing stiffener component formed by two-stage HFQ forming process: (a) top view), (b) cross section view, and

In forming test B, by increasing the forming stroke, a wing stiffener component with localised necking was formed using HFQ forming process under the same forming conditions in forming test A as shown in Figure 3-25. The aim of forming test B was to calibrate the forming limit prediction model for AA2060 developed in Chapter 5. According to forming limit test B, the localised necking occurred at the "side wall" of the formed part rather than the "corner region". It was found that the localised necking did not occur in the heavily strained region, which is a counterintuitive result explained later.
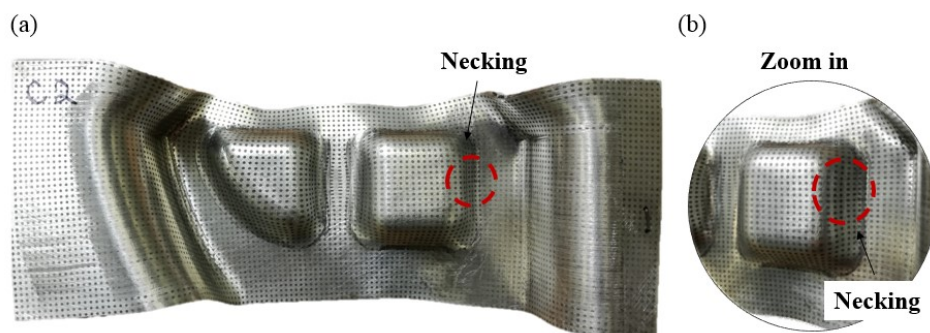
Figure 3-25. A wing stiffener component with localised necking at a limit forming stroke of 29.2 mm under the same forming conditions used in forming test A

3.5 Age hardening of AA2060

In this section, age hardening behaviours of AA2060 were studied by conducting three heat treatment experiments. For the two-stage HFQ conditions, the processing routes of SHT, cold die quenching and artificial aging were conducted to obtain the optimum post-form strength of the part. The effects of solution heat treatment conditions (Experiment 1), natural age hardening behaviour (Experiment 2), and age hardening behaviour under one-stage and two-stage aging tests (Experiment 3) were conducted. The experimental objectives were shown in Table 3-5. In experiment 1, the soaking time for solution heat treatment of AA2060 was determined. In

experiment 2, the hardness of solution heat-treated AA2060 with different natural aging time was measured. In experiment 3, the optimum age hardening temperature and aging time for AA2060 was determined in one-stage and two-stage artificial aging tests. The detailed hardness measurements of age hardening behaviour for AA2060 were taken as listed in Table 3-9 to Table 3-18 (Appendix 3B).

Table 3-6. Experimental objectives for heat treatment tests

Experiment	Experimental objectives
Experiment 1	Effect of SHT of AA2060
Experiment 2	Effect of natural aging
Experiment 3	Effect of age hardening behaviour on one- and two-stage artificial aging tests

3.5.1 Experimental procedure of heat treatment tests

Test pieces were prepared in the dimensions of 20mm×20mm×2mm. The furnace was heated up to the solution heat treatment temperature (AA2060: 520°C) in the first step. A dummy sample was placed into the furnace with thermocouple attached at the same time as the test-piece in order to monitor representative specimen temperature. After heat treatment, the test piece was quenched in water. After the sample was dried, the sample was mounted and its surface was ground. Finally, the hardness measurements were taken on each sample using Vickers hardness machine with 5kg load and 10-second dwell time (HV5/10). The hardness results in each forming conditions were recorded.

In experiment 1 (Determination of SHT minimum soaking time), the AA2060 test-pieces were solution heat treated at 520°C (SHT temperature of AA2060) with different soaking times. After the SHT process, the hot test-piece was then quenched in water. The heat treatment profiles of experiment 1 is shown in Figure 3-26.
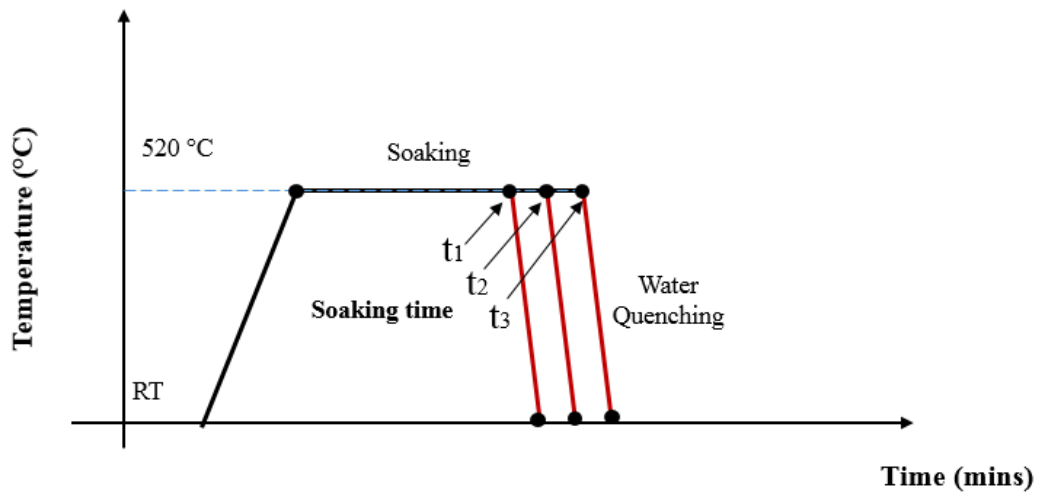
Figure 3-26. Heat treatment profiles of solution heat treatment

In experiment 2 (Natural age effect), the solution-heat-treated and water-quenched AA2060 test-pieces were placed in the open air with different natural aging time. The hardness of sample with different natural aging time was measured. The heat treatment profiles of experiment 2 was shown in Figure 3-27.
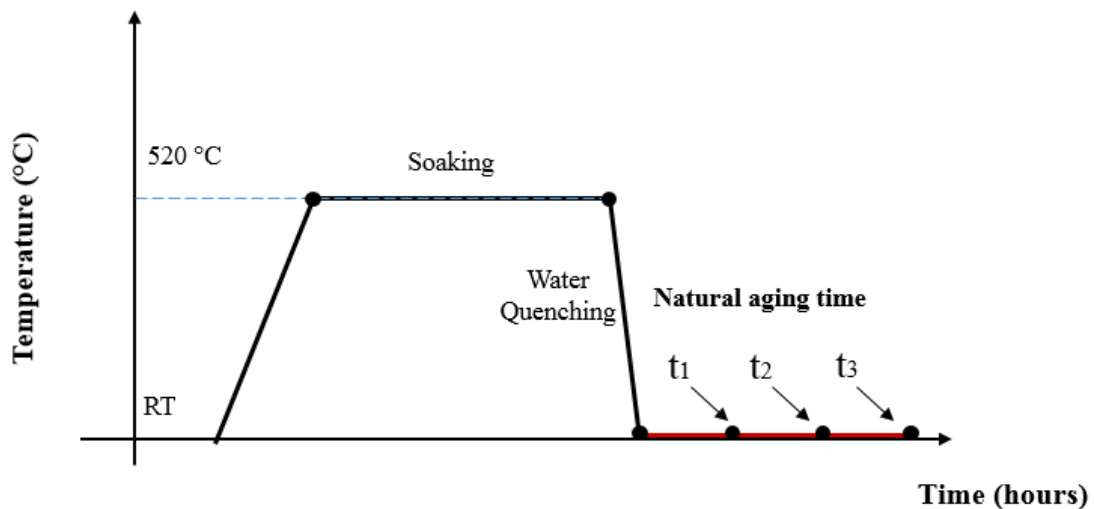
Figure 3-27. Heat treatment profiles of natural aging test

In experiment 3 (Age hardening at one- and two-stage artificial aging tests), the age hardening behaviour of AA2060 was investigated by conducting one-stage aging and two-stage aging tests. The heat treatment profiles of one-stage and two-stage aging tests are shown in Figure 3-28 and Figure 3-29, respectively.
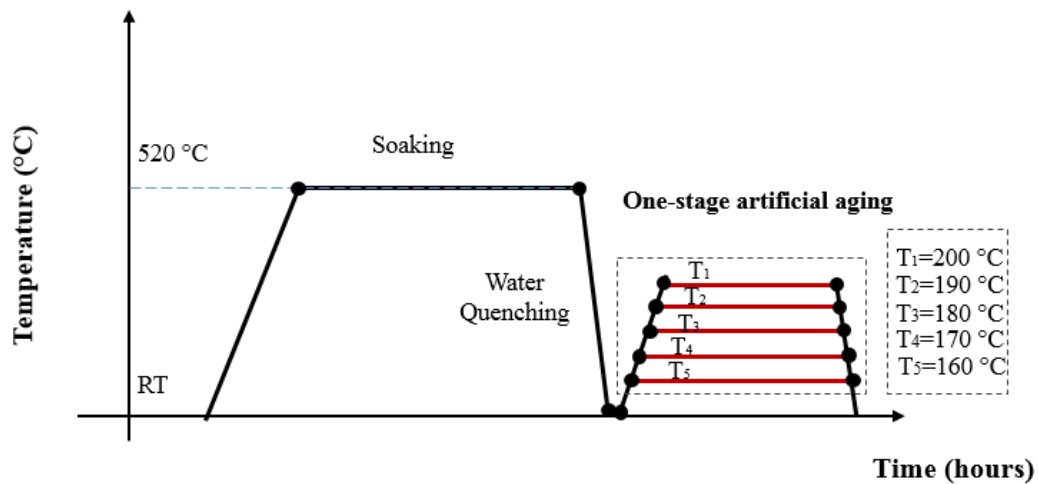
Figure 3-28. Heat treatment profiles of one-stage artificial aging test
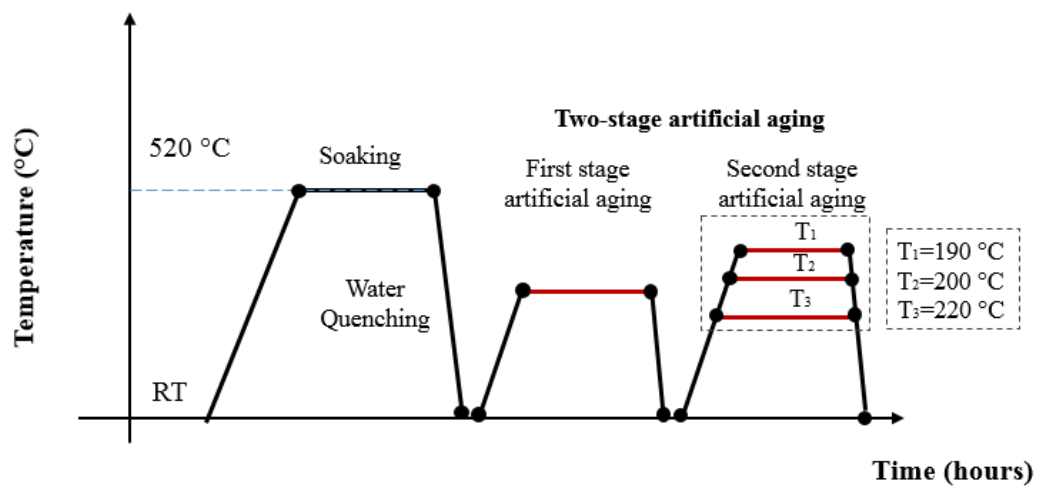
Figure 3-29. Heat treatment profiles of two-stage artifical aging test

3.5.2 Age hardening behaviour of AA2060

Determination of the minimum SHT soaking time for AA2060

The hardness results of experiment 1, where the AA2060 test-piece was solution-heat-treated with different soaking times at 520°C are presented in Figure 3-30. When samples were soaked for one minute, the hardness was approximately 80HV. In comparison to the as-received material, the hardness of the sample dropped from 166.5HV to 80HV during the solution heat treatment.
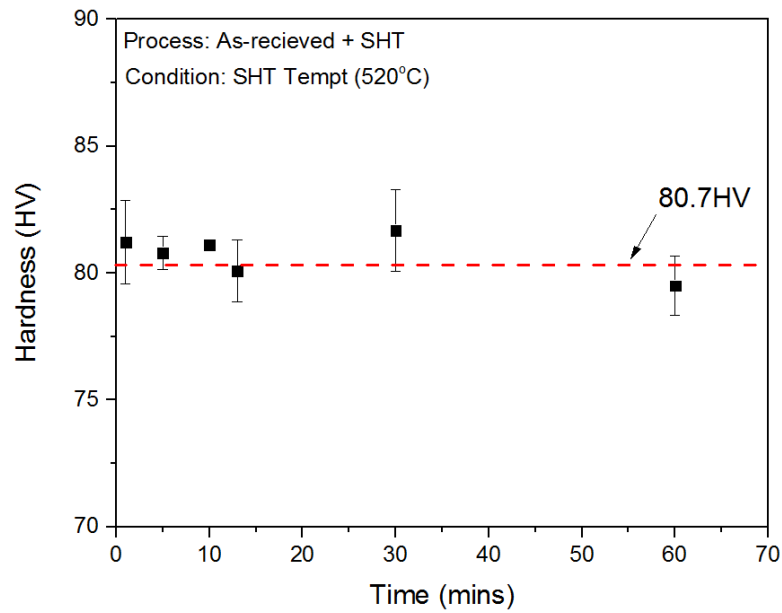
Figure 3-30. Soaking time effects on the hardness of as-quenched specimens

Effect of natural aging on the strength of AA2060

According to experiment 2, the hardness results of solution-heat-treated sample (520°C, soaked 1 minute) with different natural aging times are presented in Figure 3-31.
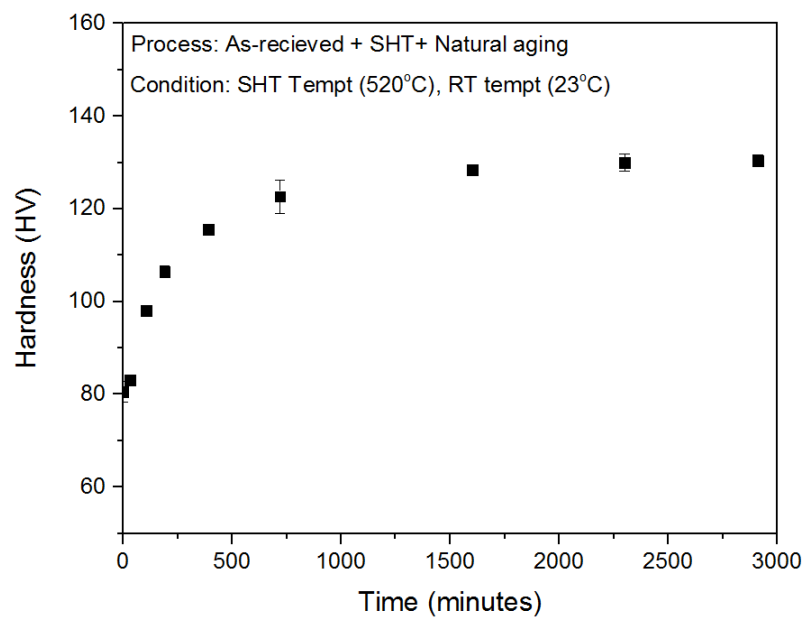
Figure 3-31. Natural age hardening curve of as-quenched AA2060

In Figure 3-31, it was found that natural aging played a significant role on the hardness of AA2060 samples that were solution-heat-treated and water-quenched. As the natural aging

time increased, the hardness of AA2060 increased dramatically and gradually stabilized. For instance, the hardness of sample increase by 20% within 1.5 hours. After 48 hours, the hardness increased by 43.7% and reached 130HV, suggesting that the transfer time for solution-heat-treated and water-quenched AA2060 blanks should be minimised before subsequent artificial aging processes.

One-stage artificial aging tests

After performing the SHT process (520°C, soaked for 1 minute) on the test-pieces, the effects of artificial ageing time and temperature were evaluated, with the results presented in Figure 3-32.
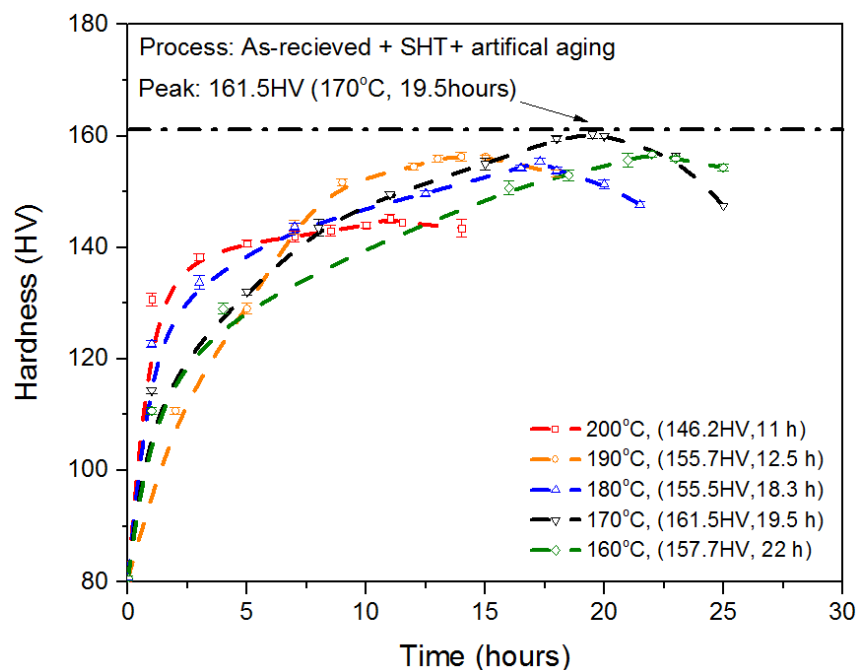
Figure 3-32. Artificial aging of AA2060 with different aging temperature and aging time

In Figure 3-32, the peak hardness of one-stage-artificial-ageing was achieved by artificial aging at 170°C temperature and aging for 19.5 hours. This enabled 97% of the mechanical strength of the as-received material to be maintained.

Two-stage artificial ageing tests

The two-stage artificial aging was also evaluated experimentally, with age hardening curves at different aging conditions presented in Figure 3-33, Figure 3-34 and Figure 3-35. In those three figures, the aging temperature in the first-stage aging was set at 170°C as determined from the one-stage artificial aging test results.
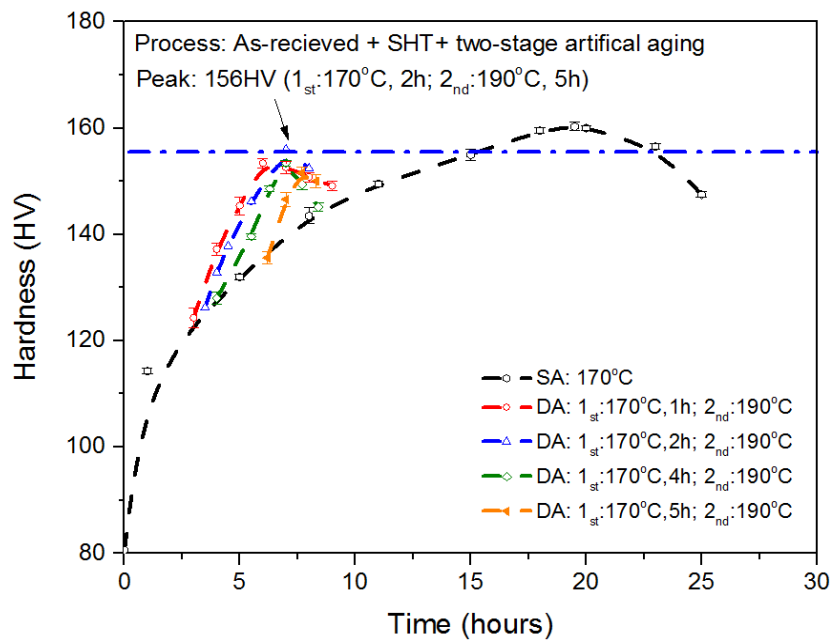
Figure 3-33. The first aging time effect on the two-stage aging of AA2060: first aging at 170°C and second ageing at 190°C (SA: single aging process, DA: double aging process)
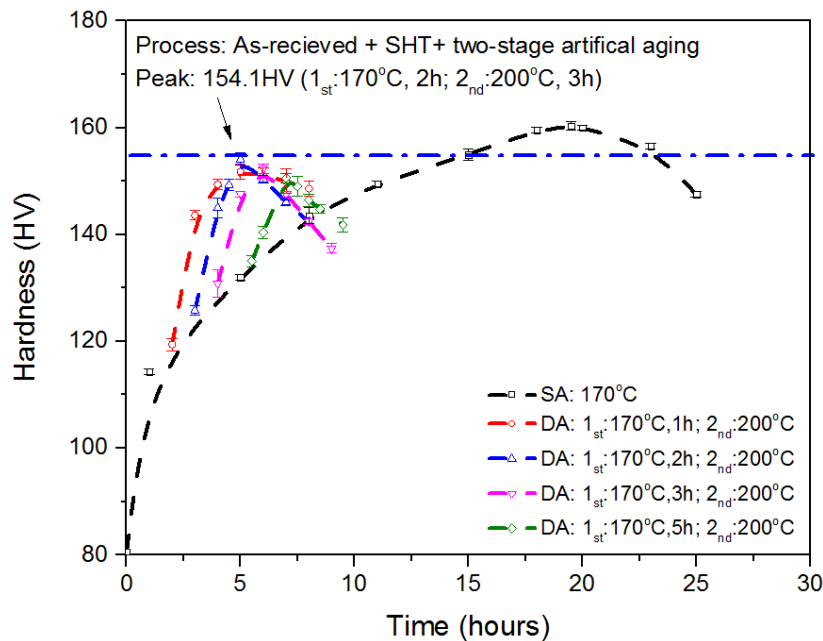
Figure 3-34. Effect of time of first aging on double aging of AA2060: first ageing at 170°C and second ageing at 200°C

In Figure 3-33, peak hardness (156HV) was found at aging conditions: 170°C for 2 hours in the first stage aging and at 190°C for 5 hours in the second ageing. By using the two-stage artificial ageing route (First-stage aging: 170°C, second-stage aging: 190°C), 97% of the full

mechanical strength (AA2060-T6) was retained with the total time for artificial aging shortened by 65%. In Figure 3-34, peak hardness (154.1HV) was found at 170°C for 2 hours in the first-stage aging process and at 200°C for 3 hours in the second-stage ageing process. By using the two-stage artificial ageing route (First-stage aging: 170°C, second-stage aging: 200°C), 95% of the full mechanical strength (AA2060-T6) was retained with the total time for artificial ageing shortened by 74%.
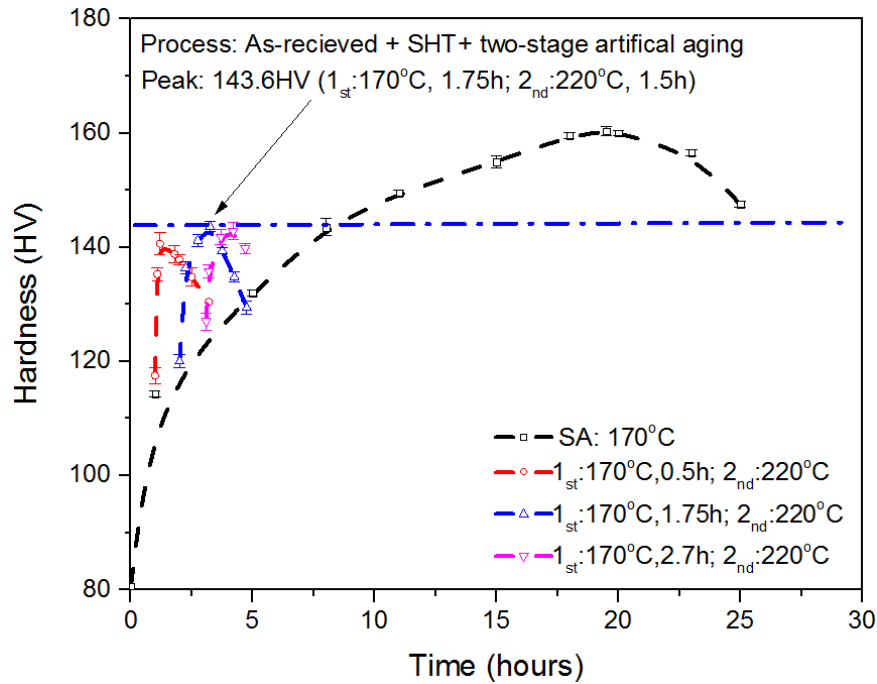
Figure 3-35. Effect of time of first aging on double aging of AA2060: first ageing at 170°C and second ageing at 220°C

In Figure 3-35, peak hardness (143.6HV) was found at 170°C for 1.75 hours in the first-stage aging process and at 220°C for 1.5 hours in the second-stage ageing process. By using the two-stage artificial ageing route (First-stage aging: 170°C, second-stage aging: 220°C), 89% of the full mechanical strength was retained with the total time for artificial ageing shortened by 83%.

Based on experimental results from Figure 3-33, Figure 3-34 and Figure 3-35, the optimum heat treatment conditions for each figures were summarised as presented in Figure 3-36.
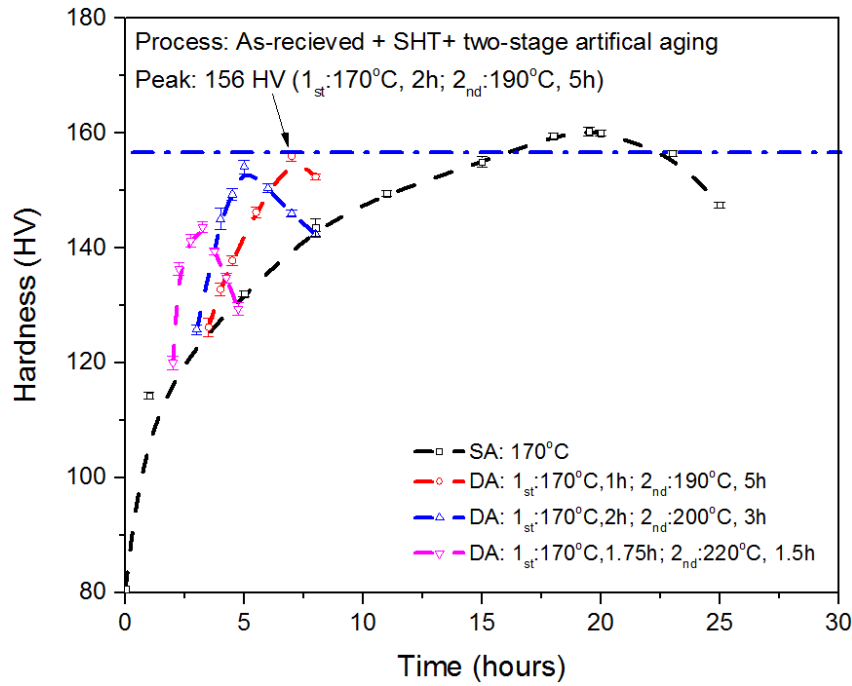
Figure 3-36. Summary of double aging results on AA2060

In Figure 3-36, it was found that the highest hardness was 156HV, with two-stage artificial aging route: aging temperature (170°C) for 2 hours in the first-stage aging process and aging temperature (190°C) for 5 hours in the second-stage aging process.

3.6 Conclusion

The thermo-mechanical properties and formability of AA2060 were characterised by uniaxial tensile test and isothermal forming limit tests under different temperatures and forming speeds. Good ductility of AA2060 was found at the temperature of 450-470°C with a strain rate of 1/s, whereas poor ductility was found at solution heat treatment temperature of AA2060 (520°C). The formability of AA2060 was found to increase with increasing temperature and decreasing with forming speeds. Based on the fundamental results from uniaxial and formability tests, the AA2060 component was successfully formed using HFQ forming technology at 450-470°C without any failure or necking. The age hardening of AA2060 was also considered by a series of heat treatment tests including solution heat treatment tests, natural aging tests, one-stage and two-stage artificial aging tests. By using first-stage artificial aging route (aging temperature: 170°C, aging time: 19.5 hours), the peak hardness of material (161.5HV) was obtained. Additionally, using two-stage artificial aging route (First-stage aging: 170°C, second-stage aging: 190°C), 97% of the full mechanical strength (AA2060-T6) was maintained with the total aging time for artificial ageing shortened by 65%.

Chapter 4

FE simulation of HFQ process on AA2060

In this chapter, the hot stamping process for an AA2060 wing stiffener component is simulated using the FE commercial software PAM-STAMP. The FE simulation results were validated with experimental results obtained from forming tests. Based on the FE simulation, the changes in loading path, temperature and strain rate for AA2060 were analyzed in detail. This chapter includes an introduction to the PAM-STAMP software, a description of FE simulation setup, verification of FE simulation and a discussion of FE simulation results.

4.1 PAM-STAMP simulation setup for the AA2060 wing stiffener forming process

The PAM-STAMP commercial software is a sheet metal forming simulation package that allows the numerical evaluation of cold and warm sheet metal forming and tube-forming processes, and is widely used in the automotive and aerospace industries (ESI, 2015). PAM-STAMP was used in this work to simulate the hot stamping of a wing stiffener component. To simulate this forming process, the 'PAM-STAMP hot-forming module' was selected to enable thermal and mechanical effects to be modeled. The procedure of establishing the PAM-STAMP FE simulation for forming AA2060 wing stiffener component is listed below:

(1) Import the CAD geometrical forming tool into PAM-STAMP

(2) Check and Auto-Mesh the forming tools using the DeltaMesh tool

(3) Define the material properties of forming tools

(4) Assemble the forming tools, import blank shape and position blank

(5) Mesh blank and define properties of blank including thickness, mechanical properties and contact properties (i.e., heat transfer coefficient, friction) between forming tools and the blank

(6) Choose process macro as forming process and define each forming sub-stages

(7) Set boundary conditions of process simulation, input forming parameters in each forming sub-stage and check kinematic process of entire process simulation

(8) Select PAM-STAMP solver mode and run the simulation

In Step (1), the CAD models of forming tools with their geometries were created by the commercial software Solidworks, from which files were exported in the form of IGES. In Step (2), the CAD models of forming tools were imported into PAM-STAMP and meshed automatically using the DeltaMesh tool, which enables the meshing of forming tools of complex geometrical features without requiring any specific knowledge of meshing elements in FE simulation. The 'automatic correction and automatic merging' features were used to eliminate gaps or overlaps. In Step (3), the material properties of forming tools were defined to be Hill 48 standard tool steel in order to keep them consistent with the forming test. The 'Lookup Table' was used to implement forming limit distributions, which were calculated from the developed forming limit prediction model (as described from Chapter 5). This enables the failure criteria of the formed part to be accurately predicted. The material properties of tool steel in the FE simulation are listed in Table 4-1.

Table 4-1. Definition of material properties of forming tools in PAM-STAMP FE simulation

Property	Tool steel
Thermal conductivity (kW/ (mm K))	20
Specific heat (mJ/(kg K))	6.5×10^{11}
Density (kg/m^3)	7.8×10^3
Poisson's ratio	0.3
Young's modulus (GPa)	210

In Step (4), the blank and forming tools including top punch, top blankholder, bottom punch, bottom die, bottom blankholder and gas spring were assembled and positioned as demonstrated in Figure 4-1. All the forming tools were set to be rigid body without considering any mechanical behaviors of deformation. To maintain consistency, the imported blanks from the

CAD model were the same size as in the real forming tests. Moreover, the forming tools and blank were positioned at the same location as the forming tests as demonstrated in Figure 4-2.
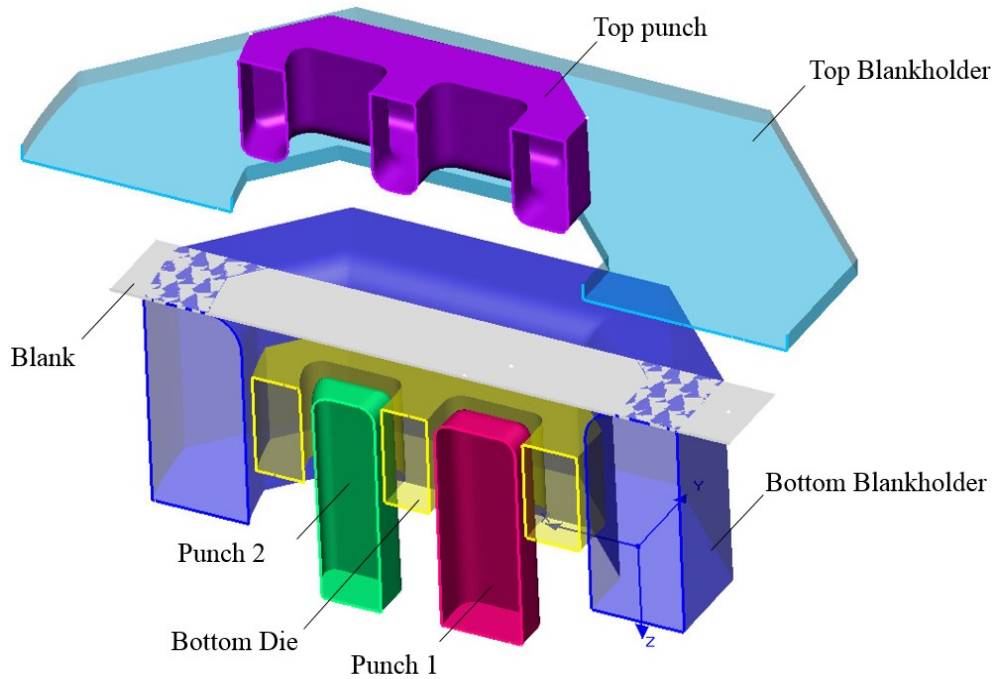
Figure 4-1. Section view of assembled forming tools for forming AA2060 wing stiffener component.
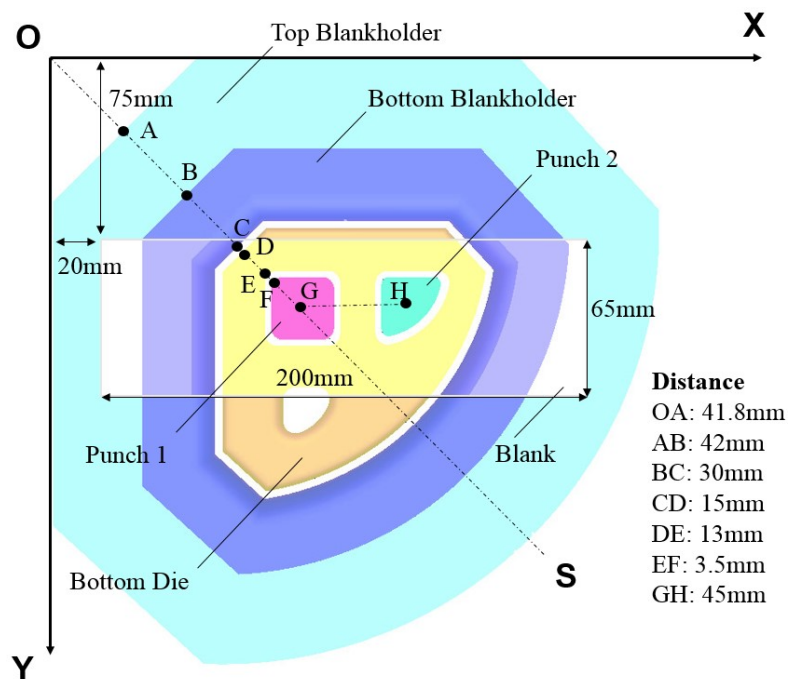
Figure 4-2. Positions of bottom blankholder, bottom die, punch, blank and top blankholder

In Step (5), the blank was meshed automatically to refine the element in PAMSTAMP FE simulation using DeltaMesh, the initial mesh size was used to be 2 mm. The chosen mesh size for the blank obeyed the mesh-size rule from PAM-STAMP software, which is calculated by:

$$M = 0.5 \times (0.5T + F) \tag{4.1}$$

Where M is the mesh size, T is the blank thickness, F is the smallest fillet radius in all imported CAD models of the forming tools.

In this simulation, according to Eq. (4.1), the adequate blank mesh size was 2 mm due to the smallest fillet radius (3 mm) and blank thickness (2 mm) in the models. The material properties of the blank were defined as listed in Table 4-2. Additionally, the rolling direction of blank was defined to be parallel to the longitudinal direction of the blank and Lankford's coefficients defining plastic anisotropy were set to be R_0=0.73 and R_{90}=0.69. The values of R_0 and R_{90} were obtained by uniaxial tensile test.

Table 4-2. Material properties of blank defined in FE simulation

Blank	Young's Modulus (GPa)	Poisson Ratio	Density (kgm^{-3})	Thermal Expansion Coefficient (K^{-1})	Specific heat capacity (J·K^{-1})
Parameter	70	0.33	2.7×10^3	2.4×10^{-5}	890

In order to simulate the viscoplastic material response of AA2060 during deformation, the flow stress curves were imported to PAM-STAMP defining the stress response as a function of strain rate and temperature. To simulate hot stamping conditions, the forming temperatures were set to range from 300 °C to 520 °C and strain rates from 0.1 s^{-1} to 50 s^{-1} shown in Appendix 4A. The matrix of PAM-STAMP material package defined for Al-Li alloy were shown in Appendix 4B. The flow stress curves with different strain rates and temperatures were produced from the developed viscoplastic material model presented in Chapter 5. The procedure to generate flow stress curves is shown in Figure 4-3.

```
┌─────────────────────────────────┐
│   Experimental flow stress      │
│            curves               │
└─────────────────────────────────┘
            ⇩        **Validate**
┌─────────────────────────────────┐
│   Viscoplastic material model   │
└─────────────────────────────────┘
            ⇩         **Predict**
┌─────────────────────────────────┐
│      Flow stress curves         │
└─────────────────────────────────┘
            ⇩         **Import**
┌─────────────────────────────────┐
│      PAM-STAMP software         │
└─────────────────────────────────┘
```
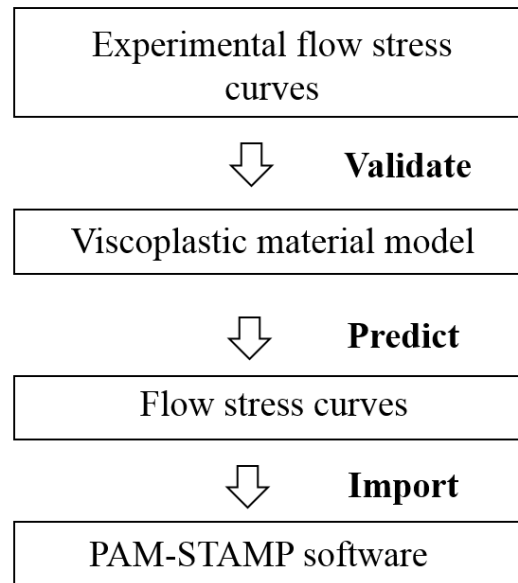
Figure 4-3. Procedures to generate flow stress data in PAM-STAMP material package

In addition to the definition of the material properties of the blank, the contact properties between the blank and forming tools were also required, including friction and heat transfer coefficient. A constant friction coefficient ($f_0 = 0.2$) was applied between forming tools and blank for all the forming stages. The value of friction coefficient was determined by calibrating simulation results to experimental results. In PAMSTAMP software, there was a limitation to model the coefficient of friction with the combined effect of contact pressure (between punch and blank), sliding speed (between punch and blank) and temperature. Furthermore, the interfacial heat transfer coefficient (IHTC) was expressed as functions of the gap between the blank and tool parts (before contact) and pressure (after contact). Those functions were developed and presented by Liu et al. (2015).

In Step (6), the hot forming Process Macro was selected from Process Macro database directory in PAM-STAMP. This Macro is used to define each stage of the forming process. The forming stages used in the simulation include gravity (initial placing of blank on tools), holding (clamping the blank between the tools) and stamping. It should be noted that the quenching stage of the HFQ process was not simulated as this would only affect the microstructure of the component. In Step (7), the boundary conditions used in gravity, holding and stamping stages for all the forming tools and blank (as shown in Figure 4-4) are listed in Table 4-3.
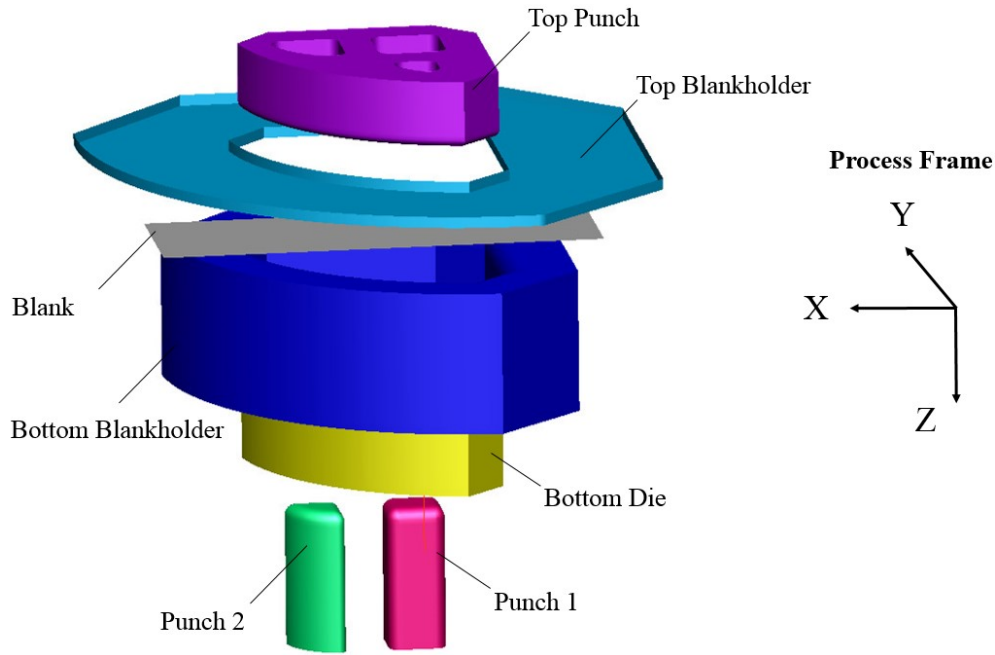
Figure 4-4. Demonstration of forming tools, blank and their coordination frame set up.

Table 4-3. Boundary conditions of forming tools and blank in all the forming stages.

Items / Stages	Gravity	Holding	Stamping
Top Punch			Translation: X, Y Rotation: X, Y, Z
Top Blankholder		Translation: X, Y Rotation: X, Y, Z	Translation: X, Y Rotation: X, Y, Z
Blank	Translation: un-Locked Rotation: un-Locked	Translation: un-Locked Rotation: un-Locked	Translation: un-Locked Rotation: un-Locked
Bottom Blankholder	Translation: X, Y, Z Rotation: X, Y, Z	Translation: X, Y, Z Rotation: X, Y, Z	Translation: X, Y, Z Rotation: X, Y, Z
Bottom Die			Translation: X, Y Rotation: X, Y, Z
Punch 1&2			Translation: X, Y, Z Rotation: X, Y, Z

(Translation/Rotation X, Y indicates the freedom of the element was locked in the X, Y direction)

After defining the boundary conditions for the hot stamping process of AA2060, the forming parameters in each stage were set. In the gravity stage, the blank was positioned on the bottom blank holder. The gravity acceleration was set to be 9.81 m·s^{-2}. In the holding stage, the top blank holder was activated to close down onto the bottom blank holder; the clamping speed of top blank holder was 250 mm/s and the blank holding force was 15 kN. The holding stage FE simulation was terminated as a result of the 'pinch test'. The 'pinch test' is defined as the automatic termination of simulation when a node of a blank is pinched between forming tools. In the stamping stage, the blank was deformed by two continuous pressing stages. The first pressing stage was to deform the blank using the top punch. The second pressing stage deformed the material with two central punches positioned under the bottom die. Termination of the stamping stage relied on the stroke-control process. The stamping speed of top punch was 250 mm/s. The forming parameters of three stages used in FE simulation are summarized and listed in Table 4-4.

Table 4-4. Parameters used for forming wing stiffener component on AA2060

Process parameter	Value
Initial blank temperature (°C)	450
Initial tooling temperature (°C)	20
Forming speed (mm/s)	250
Friction coefficient	0.2
Blankholding force (kN)	15
Gas spring stiffness (kN/mm)	1
Acceleration of gravity (m·s^{-2})	9.81

In Step (8), a double-precision solver, called DMP (Distributed Memory Process) was selected, and the PAM-STAMP FE simulation for hot stamping process of AA2060 was conducted. The DMP method enables parallel computation across multiple several processors as opposed to SMP (Single Memory Process) which can only run on a single processor.

4.2 FE simulation results of HFQ-formed wing stiffener component

The forming of AA2060 wing stiffener component simulated using PAM-STAMP software, with a forming speed of 250 mm/s and forming temperature of 450°C is presented in Figure 4-5. This study focused on the successful forming of the central parts of the wing stiffener component, which include "triangular"- and "rectangular"-shaped parts shown in region A and region B, respectively. To calibrate the FE simulation results, comparisons between simulation results and experimental results were made by selecting data from a cross-section line, as demonstrated in Figure 4-5.
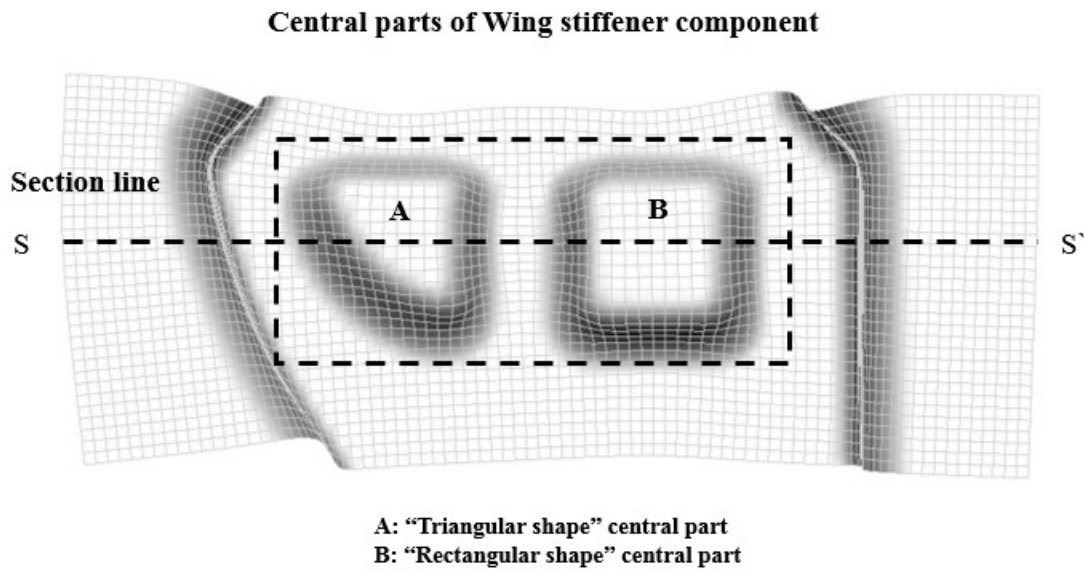
Figure 4-5. FE simulation of wing-stiffener component with a section line S–S′ used for study.

The FE model was verified by comparing the material thinning results from the simulation to the experimental results along the section S–S′ line shown in Figure 4-5. A close agreement was obtained between the experimental and simulation results as shown by Figure 4-6. In Figure 4-6, the normalised thickness is plotted against the distance along the line S-S', with t_0 representing the original blank thickness of 2mm. The thinning is calculated as that:

$$Thinning = (t - t_0)/t_0 \tag{4.2}$$

where t is the thickness, t_0 is the orignal thickness.
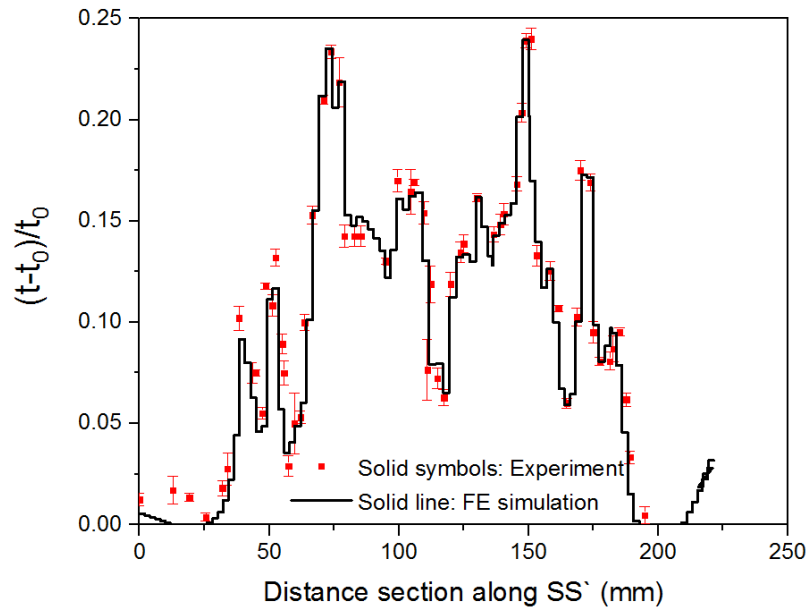
Figure 4-6. Thinning distribution along section SS` on formed wing stiffener component

Based on the FE simulation results, the plastic strain and thinning properties of the blank were predicted. As seen in Figure 4-7(a) and Figure 4-7(b), it was predicted that the largest degree of thinning and plastic deformation would occur at the corner regions as expected.
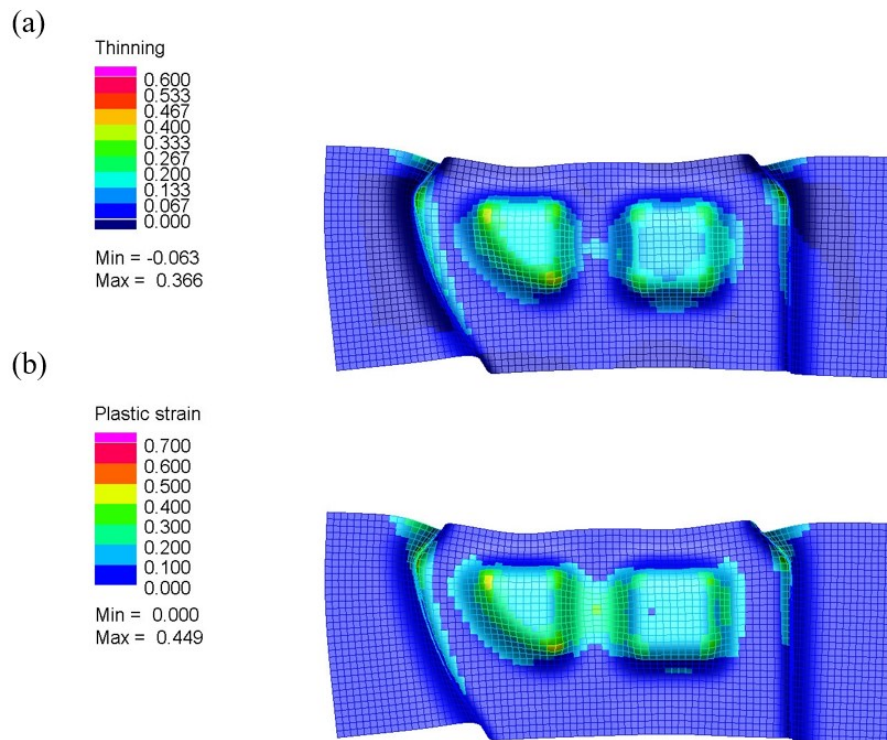
Figure 4-7. (a) Thinning and (b) equivalent plastic strain of distributions of formed component at a forming temperature of 450°C, forming speed of 250 mm/s, and a forming stroke of 25.3 cm.

4.3 Forming limit study of HFQ-formed AA2060 component using FE simulation

4.3.1 Verification of Finite element model

The finite element (FE) software PAM-STAMP was utilized to simulate the stamping of the sheet metal AA2060 wing stiffener component from the corresponding forming test (Chapter 3; forming test B). The model was verified by comparing the material thinning results from the FE simulation with the experimental forming tests. In the experiments, the part was formed at a temperature of 450 ºC and a forming speed of 250 mm/s. In order to study the forming limit of AA2060, the forming stroke was set to 29.2 cm, such that localized necking occurred in the formed part. The thinning distributions of the formed part from the FE simulation and the experiments are shown in Figure 4-8.
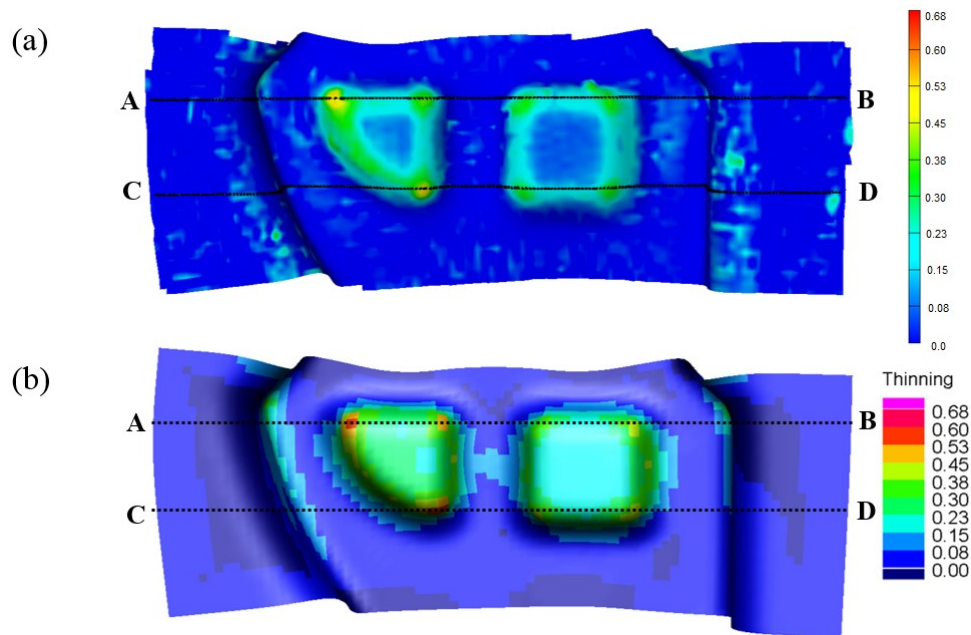
Figure 4-8. Thinning distributions (a) measured from the experimental forming test using ARGUS software and (b) predicted from the PAM-STAMP FE simulation

As seen in Figure 4-8, the numerical and the experimental results for the thinning distribution showed that the largest deformation occurred at the corner region of the central features of the part, with a maximum thinning level of 0.68. The thinning values of the part were compared along sections A–B and section C–D, shown in the figure. A good agreement between the simulated and experimental thinning results was achieved as shown in Figure 4-9 and Figure 4-10, thus verifying the FE model.
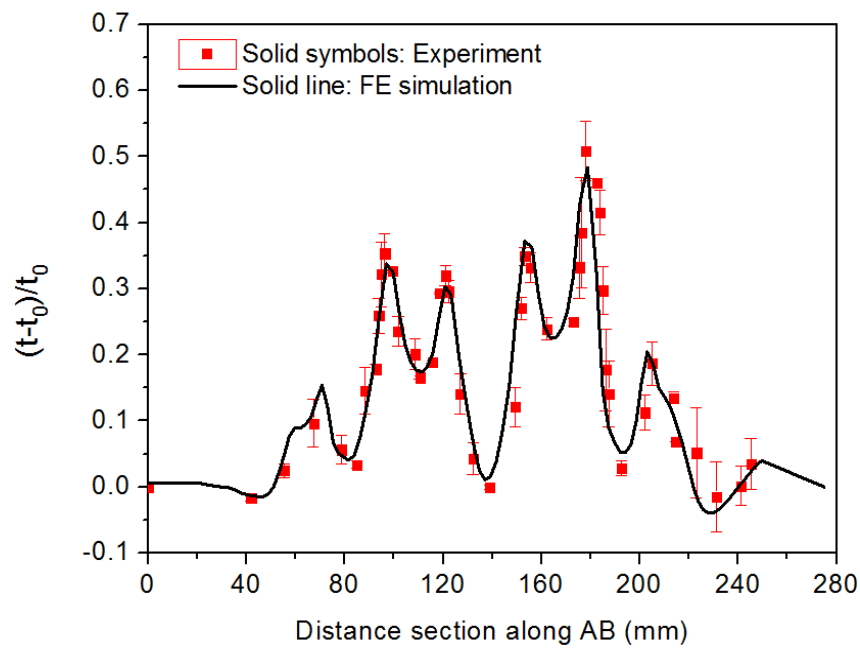
Figure 4-9. Comparison of experimental (solid symbols) and prediction results in thinning (solid curve) through section AB
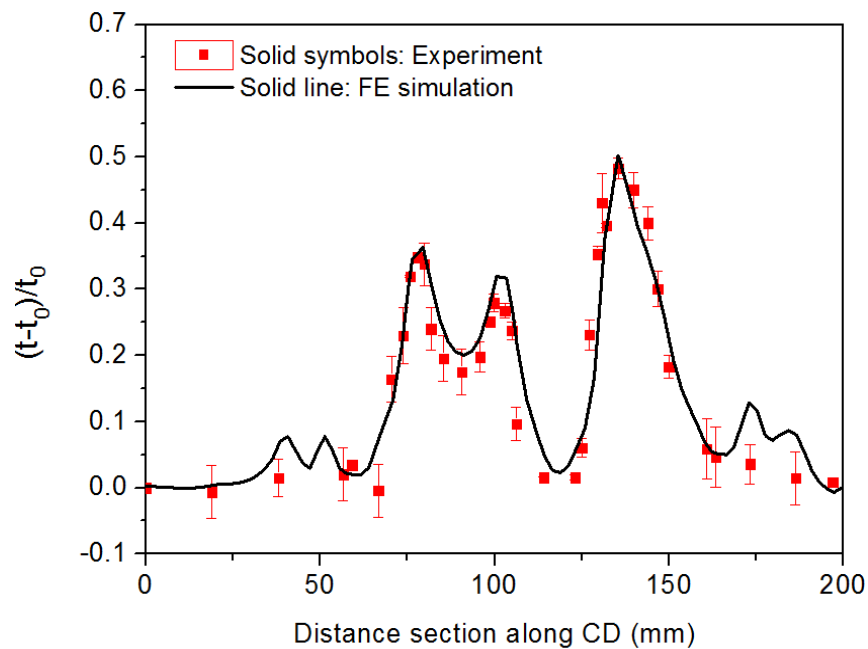
Figure 4-10. Comparison of experimental (solid symbols) and prediction results in thinning (solid curve) through section CD

4.3.2 FE simulation results

After calibration, the FE results in thinning from different regions (representing different geometrical features) were studied by selecting four elements in the formed part as shown in Figure 4-11. The results of thinning for these elements are listed in Table 4-5 and illustrated by Figure 4-12.

In Figure 4-12, it can be seen that the most thinning occurred at Element 4, which was located at one of the corners of the central part of the wing stiffener component. This high degree of thinning occurred at this location because of the complex geomerical features. Element 1 was located at the flat region of the formed part, and hence minimal plastic deformation occurred. The values in the thinning of Element 2, located at side walls, was relatively smaller than Element 4, but much higher than Elements 3 which were located at one of edges of the formed part.
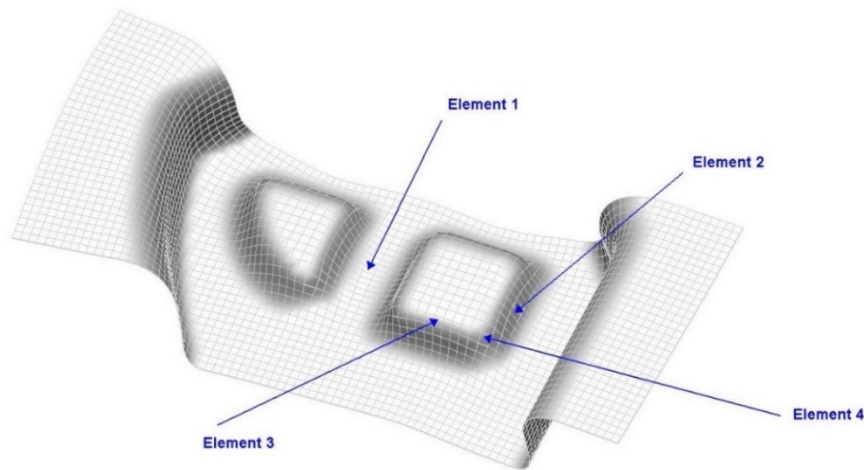
Figure 4-11. Selected elements from the wing stiffener component

Table 4-5. Selected elements from wing stiffener component and their thinning results

Element	Location	Thinning
Element 1	Flat region	0.102
Element 2	Thin wall region	0.449
Element 3	Edge region	0.227
Element 4	Corner region	0.466
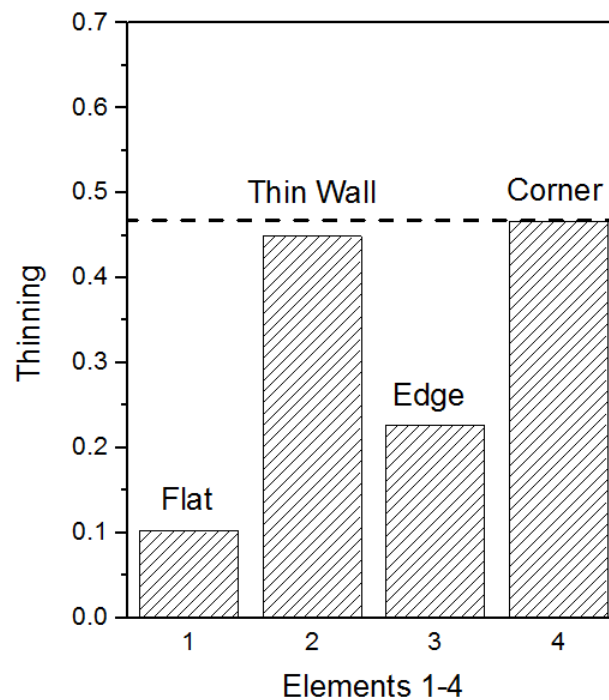
Figure 4-12. Comparison of selected elements in terms of thinning

Based on the Figure 4-12, it was predicted that the localised necking may occur at the corner region (element 4) or thin wall region (element 2) dut to their high levels of thinning. To evaluate the formability of the formed part, especially for both elements, the forming conditions were studied including temperature, strain rate and loading part.

Figure 4-13(a)–(d) show the stamping process of the AA2060 wing stiffener component with a forming stroke of 29.2 cm in more detail. Figure 4-13(a) shows the initial state, 'State 1'. As the strokes increased from 9.93 mm to 19.9 mm, most of the material was drawn into the die cavity (in 'State 2') as shown in Figure 4-13(b). In Figure 4-13(c), the second press action was activated when the bottom punches start to contact with blank at 'State 3'. When the forming stroke reaches 29.2 mm, the central features of the wing stiffener component are formed, as shown in Figure 4-13(d).

(a)

State 1

BHF

BHF
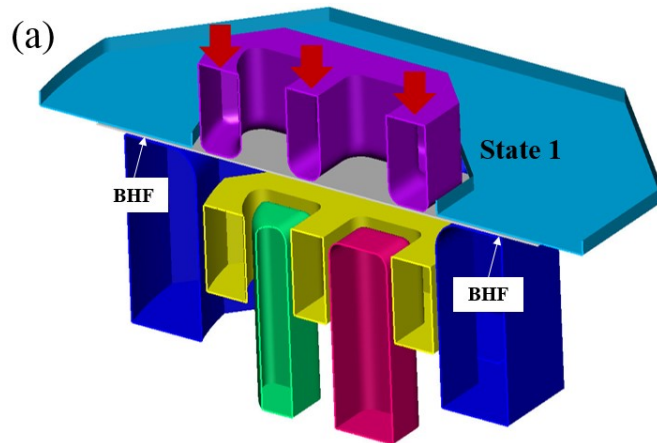
State 1:
Stroke: 0.00mm
No deformation

(b)

State 2

Deep drawing
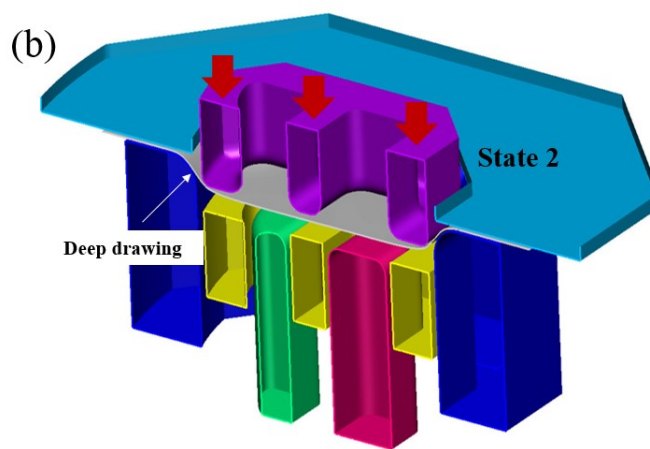
State 2
Stroke: 9.93mm
Material drawn in die cavity

(c)

State 3

Contact with
bottom central
punches

GSF

GSF

GSF
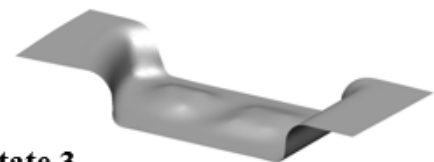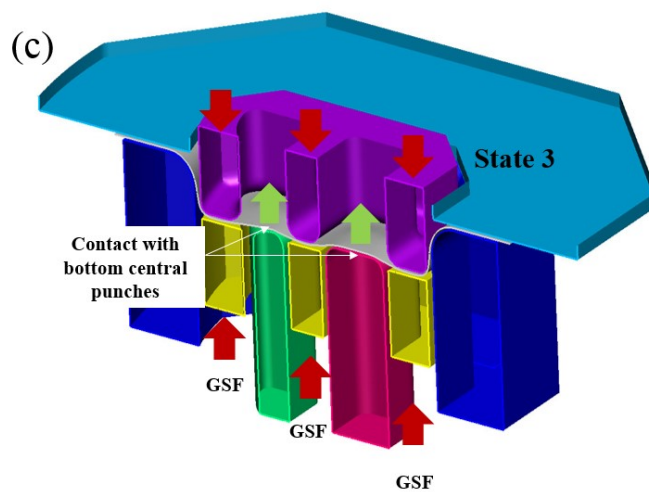
State 3
Stroke: 19.9 mm
Make contact with two bottom
central punch
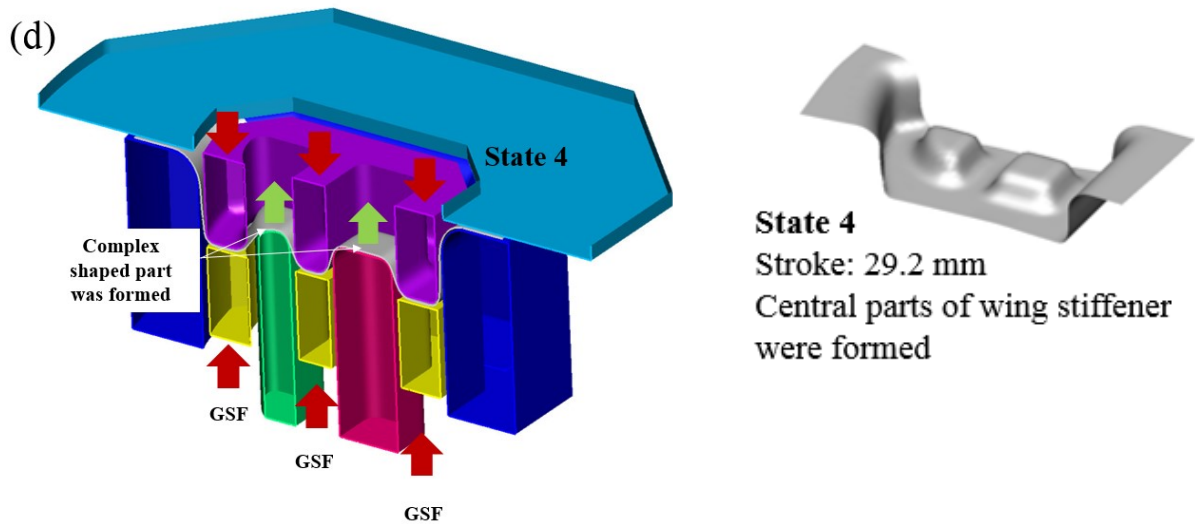
Figure 4-13. Stamping process of AA2060 wing stiffener component with forming limits.
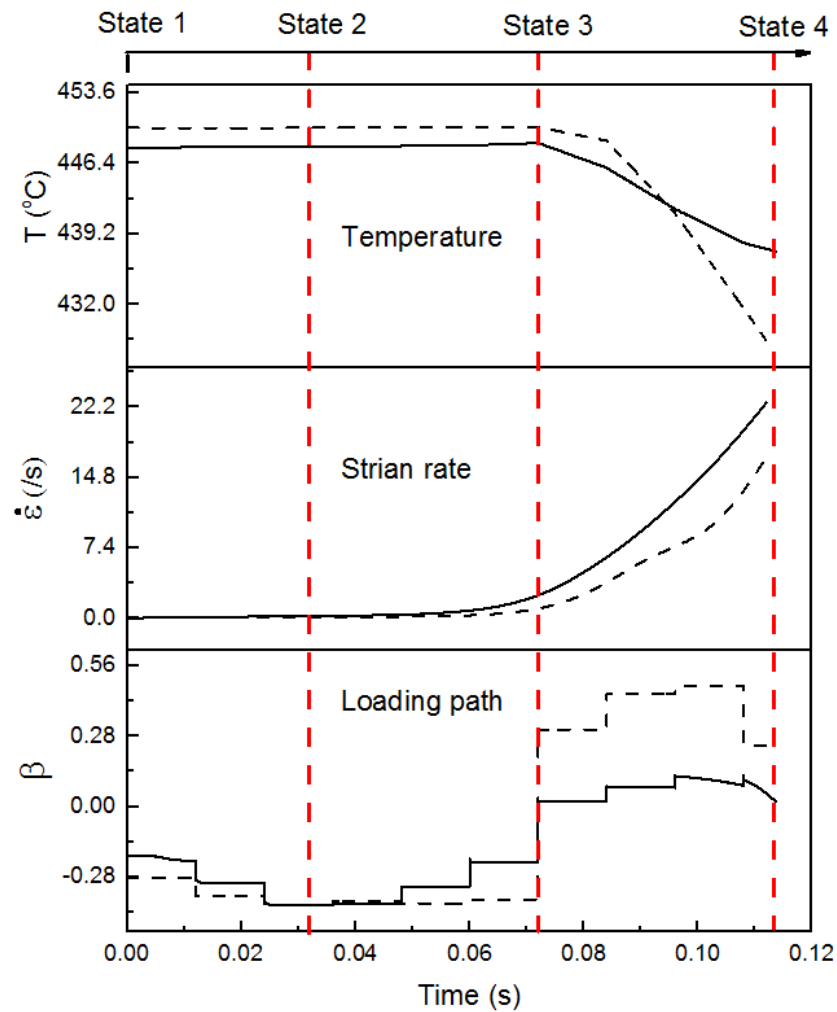
Figure 4-14. Histories of temperature, strain rate and loading path for Elements 2 and 4 throughout hot stamping process. (Solid line: Element 2 and Dash line: Element 4)

During the hot stamping process from 'State 1' to 'State 4', the hot blank experienced comprehensive changes in strain rate, quenching rate and loading path. The distributions of temperature, strain rate and loading path on the formed part are presented in Appendix 4C. The histories of temperature, strain rate and loading path throughout the forming process for Elements 2 and 4 are presented in Figure 4-14.

In Figure 4-14, it was found that the changes in strain rate, temperature and loading path in element 2 and 4 were different. In comparison to the corner region, the initial temperature was higher at the thin part region, formability of material may be enhanced due to high temperature. However, after "state 3", the quenching rate in the thin wall part become smaller than that in corner region. In addition to temperature history effect on the formability, the different strain rates with their different correspnding changes to loading path result in difficulties in evaluating the formability of a formed part. In order to evaluate the forming limit under such complex forming conditions, a forming limit prediction model was required, which enables the capture of such features by considering the comprehensive effects of changes in strain rate, temperature and loading path. The detailed analysis of these changes in strain rate, temperature and loading path are presented in Chapter 5.

4.4 Conclusion

In the present chapter, PAMSTAMP-FE simulations of the HFQ forming processes for forming wing stiffener components and its forming limit study were successfully made and verified by comparing the material thinning results from the forming tests. Good agreements were obtained between the simulation results and the experimental results. The thinning results of the formed part at different locations were compared and it was found that the localised necking may occur at corner regions or thin wall regions due to their high levels of thinning. The corresponding forming conditions of the thinned areas were studied by plotting histories of temperature, strain rate and loading path throughout the forming process. It was concluded that a forming limit prediction model is required which enables the effect of change in strain rate, temperature and loading path to be modelled in detail.

Chapter 5

Forming limit prediction of AA2060 under hot stamping conditions[2]

In Chapter 5, the flow stress and forming limits of AA2060 under hot stamping conditions were predicted using developed model, called viscoplastic-Hosford-MK model. The developed model was validated using fundamental experiments (uniaxial tensile and formability tests) The capability of the developed model was assessed by analyzing the effects of changes in the loading path (loading history), temperature (quenching rate) and strain rate on the FLD numerically. The accuracy of the developed model was verified by applying it to the hot stamping of an AA2060 component to predict the regions where necking and failure would occur.

5.1 Introduction of forming limit prediction model

In metal forming processes conducted at elevated temperatures, materials deform viscoplastically, and their microstructure changes with time. Therefore, the use of time integration based constitutive equations to model the evolution of physical phenomena during plastic deformation is essential. The effects of strain hardening and recovery on the flow stress evolution were modelled via dislocation-based hardening laws, in which the generation of dislocations due to plastic strain and the annihilation of dislocations (recovery) under hot forming conditions were taken into account. These temperature dependent viscoplastic constitutive equations were combined with a Hosford yield function to model the anisotropic nature of plastic deformation in sheet metals, and the M-K model. The latter represented the inherent nature of the imperfection in the material, which physically exists due to any non-uniformity, such as a thickness non-uniformity or pre-existing micro-defect. Consequently, fracture under different stress and strain conditions could be predicted.

---

[2] Chapter 5 is based on paper work "Gao, H., El Fakir, O., Wang, L., Politis, D.J., Li, Z., (2017) Forming limit prediction for hot stamping processes featuring non-isothermal and complex loading conditions, International Journal of Mechanical Sciences, in press."

5.1.1 A viscoplastic material model for an aluminum-lithium alloy

In most of the previous research on FLD prediction, two major types of material models have been employed (Khan and Baig, 2011), namely physics-based models and phenomenological models. Under most circumstances, the stress-strain behaviors of the workpiece material were modelled phenomenologically as a function of strain and strain rate (Schwindt et al., 2015; Khan and Baig 2011; Min et al., 2010), for example $\sigma = K\varepsilon_p^n$ and $\sigma = K\varepsilon_p^n \dot{\varepsilon}_p^m$. The material constants in these equations are normally not temperature dependent. Therefore, each flow stress curve requires a unique set of fitting parameters, which are determined based on experimental data. Most recently, this issue was addressed by Khan and Baig (Khan and Baig, 2011), who combined their sophisticated phenomenological KHL model with the M-K model to predict FLCs by considering the effects of strain rate and temperature. On the other hand, physically based viscoplastic constitutive models have not been used for FLD prediction, due to the difficulties in determining the material constants (Khan and Baig, 2011).

Such mechanistic-based constitutive equations (Lin and Liu, 2003) have been developed by considering the generation and annihilation of dislocations due to plastic strain and annealing under hot forming conditions. At elevated temperatures, it is assumed that the flow stress (σ) of the material obeys the power law $\sigma = K\varepsilon_p^n \dot{\varepsilon}_p^m$. The power law equation then can be modified as shown in Eq. (5.1) to obtain the plastic strain rate ($\dot{\varepsilon}_p$) as a function of the initial yield stress (k) and hardening of the material (R). Since the material in both the defect (Zone b) and non-defect (Zone a) zones are deformed under the same set of given constitutive equations (Eqs. 5.1 to 5.11), the subscripts a and b represent constitutive equations for the calculation of strain and stress in both Zones a and b respectively (El Fakir et al., 2014).

$$\dot{\varepsilon}_{Pa,b} = \left(\frac{\sigma_{a,b} - R_{a,b} - k}{K} \right)^{n_1} \tag{5.1}$$

$$\sigma_{a,b} = E\left(\varepsilon_{Ta,b} - \varepsilon_{Pa,b} \right) \tag{5.2}$$

where ε_T is the major strain and ε_P is the major plastic strain.

The hardening parameter $R_{a,b}$ is directly related to the normalised dislocation density shown in Eq. (5.3)(Gao et al., 2014), which varies with plastic strain and recovery as shown in Eq. (5.4)(Mohamed et al., 2012).

$$R_{A,B} = B\bar{\rho}_{A,B}{}^{0.5} \tag{5.3}$$

$$\dot{\bar{\rho}}_{A,B} = A(1 - \bar{\rho}_{A,B})\dot{\varepsilon}_{PA,B} - C\bar{\rho}_{A,B}{}^{n_2} \tag{5.4}$$

where $\bar{\rho}$ is the normalised dislocation density (Gao *et al.*, 2014), the parameters K, k, B, C, A, n and E are temperature-dependent material constants, while n_2 is a temperature-independent material constant.

Eqs. (5.55.) to (5.11) represent the Arrhenius equations for the temperature-dependent parameters.

$$K = K_0 \exp\left(Q_K/R_g T\right) \tag{5.5}$$

$$k = k_0 \exp\left(Q_k/R_g T\right) \tag{5.6}$$

$$B = B_0 \exp\left(Q_B/R_g T\right) \tag{5.7}$$

$$C = C_0 \exp\left(-Q_C/R_g T\right) \tag{5.8}$$

$$E = E_0 \exp\left(Q_E/R_g T\right) \tag{5.9}$$

$$A = A_0 \exp\left(Q_A/R_g T\right) \tag{5.10}$$

$$n_1 = n_{10} \exp\left(Q_{n_1}/R_g T\right) \tag{5.11}$$

The values of the temperature independent constants were determined by calibrating the above equations with the uniaxial tensile test results. From Eqs. (5.5) to (5.11), these values include K_0, k_0, B_0, C_0, A_0, n_{10}, E_0 and Q_{K_0}, Q_{B_0}, Q_{C_0}, Q_{A_0}, Q_{n_0}, Q_{E_0}. The term Q represents the activation energy, R_g is universal gas constant and T is the temperature.

5.1.2 Hosford Yield Criterion

Over the years, great efforts have been made to develop yield functions representing the anisotropic behaviour of sheet metals (Stoughton and Yoon, 2009; Yoon et al. 2006; Barlat et al., 2005; Barlat et al., 2003; Hill, 1993; Karafillis and Boyce, 1993; Hill, 1990; Graf and Hosford, 1990; Barlat and Lian 1989; Hosford, 1985). The Hosford anisotropic yield function (Hosford, 1985) is used in the present research because of its verified accuracy for the

description of high temperature yield loci (Wu et al., 2016; Min et al., 2010; Naka et al., 2008). Eq. (5.12) shows the Hosford anisotropic yield criterion.

$$R_2 \sigma_{11a,b}{}^{l} + R_1 \sigma_{22a,b}{}^{l} + R_1 R_2 \left(\sigma_{11a,b} - \sigma_{22a,b} \right)^{l} = R_2 \left(R_1 + 1 \right) \bar{\sigma}_{a,b}{}^{l} \tag{5.12}$$

where l is the material constant, and σ_{11} and σ_{22} are the major and minor stress, respectively. R_1 and R_2 are the strain ratios (r-values) measured in the longitudinal and transverse directions respectively, i.e. $R_1 = r_0$ and $R_2 = r_{90}$, r_0 and r_{90} were obtained from uniaxial tensile tests for aluminium alloys at evaluated temperature, and were determined to be 0.69 and 0.73, respectively.

5.1.3 M-K model for the prediction of forming limit

During the loading process, strain increments are imposed on the material in Zone a at each time step, with stresses calculated according to the constitutive model. Zone a and zone b are interlinked by compatibility, where the minor strain in zone a (ε_{2a}) is equal to the minor strain in zone b (ε_{2b}) at their interfaces (Eq. (5.13)) and force equilibrium, where the force in zone a is equal to that in zone b (Eq. (5.14)). A schematic diagram of the M-K model in Figure 5-1.
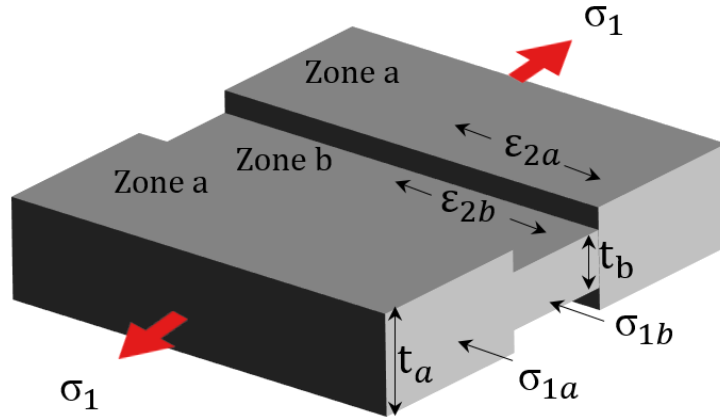
Figure 5-1. Schematic diagram of the M-K model

$$\varepsilon_{2a} = \varepsilon_{2b} \tag{5.13}$$

$$\sigma_{1a} = f \sigma_{1b} \tag{5.14}$$

where f is the instantaneous imperfection factor (thickness ratio between zone b and zone a), which is updated in each time step using Eq. (5.15).

$$f = f_0 \exp(\varepsilon_{3b} - \varepsilon_{3a}) \tag{5.15}$$

Experimental FLDs were used to calibrate the initial value of the imperfection factor f_0. The value of f decreases as deformation progresses and strain begins to localise at zone b. Necking occurs when the thickness strain increment ratio between Zone b and a approaches a critical value (Cao et al., 2000). Based on Barata and Hosford's researches, the accurate FLD prediction results were obtained using M-K model when the ratio between Zone b and a is over than 10 (Barata et al., 1985; Graf and Hosford, 1990), shown in Eq. (5.16).

$$\frac{d\varepsilon_{3b}}{d\varepsilon_{3a}} \geq 10 \tag{5.16}$$

when the critical value is reached, the final values of the major and minor strains become the forming limit strains. The equations presented above were developed into a new prediction model, the Viscoplastic-Hosford-MK model, and could be solved simultaneously using a time integration method to deduce the forming limit. This new model for the first time combines a viscoplastic material model, the Hosford anisotropic yield function and the M-K model together, to enable the prediction of the forming limit for a given temperature, forming speed, and ratio "β" between the minor and major strains (the loading path), under constant or varying conditions (El Fakir et al., 2014).

The following sections present the fundamental experimental methods and results from uniaxial tensile tests and forming limit tests used to calibrate the viscoplastic-Hosford-MK model.

5.1.4 Work-hardening behavior on strain localization

In addition to the consideration of temperature, strain rate and loading path on FLD predictions, recent studies have emphasized the effects of sheet thickness (Dilmec et al., 2013), lubrication (Karthik et al., 2002) and strain history (Yoshida et al., 2007). Yoshida et al. (2007) in particular demonstrated the effect of the work-hardening rate on the formability of an anisotropic material under a proportional loading path. These authors analysed the work hardening behaviour of a material under multiaxial stress paths using a crystal plasticity model, also indicating that the plastic work per unit volume was a significant parameter on the stress-dependent working behaviour of aluminium alloy. Similar analysis work by Khan et al. (1995; 2007) also took into account the incremental work per unit volume parameter in the calculation of the forming limit. The effect of plastic work on their failure prediction was concerned (Khan and Liu, 2012).

5.2 Verification of unified Viscoplastic-Hosford-MK model

The viscoplastic-Hosford-MK model was validated using the experimental results from the uniaxial tensile tests and forming limit tests. The calibration process consisted of two steps. The first step was to calibrate the viscoplastic equations with the flow stress data obtained at different temperatures and strain rates. The second step was to calibrate the viscoplastic-Hosford-MK model with experimentally obtained FLDs for different temperatures and forming speeds.

5.2.1 Prediction of flow stress curves at different temperatures and strain rates

The calibration of the material model was performed by determining the material model constants from the uniaxial tensile test data. The flow stress curves of AA2060 at different strain rates and temperatures are shown in Figure 5-2 and Figure 5-3. The symbols in the figures represent the experimental flow stress at strain rates ranging from 0.2 to 13s^{-1} and temperatures ranging from 400°C to 520°C, whereas the solid curves show the predictions of flow stress using the viscoplastic material model with the derived constants shown in Table 5-1. A detailed explanation of this phenomena on AA2060 is provided in Chapter 3. Additionally, the procedures of determination of material constants using viscoplastic material model are shown in Appendix 5A.

Table 5-1. Material parameters for viscoplastic material model (AA2060)

K_0 (MPa)	Q_K (J/mol)	k_0 (MPa)	Q_k (J/mol)	B_0 (MPa)	Q_B (J/mol)	C_0	n_2
0.510	29231.256	1.09E-10	98722.800	87.663	2892.790	31.171	3

Q_C (J/mol)	E_0 (MPa)	Q_E (J/mol)	A_0	Q_A (J/mol)	n_{10}	$Q_{n_{10}}$ (J/mol)
-2739.973	9917.930	9591.400	0.0304	1017.950	0.748	11644.803

To assess the effectiveness of the viscoplastic material model, experimental results from the strain rate and temperature variation tests are presented as symbols in Figure 5-4 and Figure 5-5 respectively, and compared with the model predictions under such conditions. The solid curves of Figure 5-4 and Figure 5-5 show that the developed viscoplastic material model was able to accurately predict the flow stress under complex loading conditions of changing strain

rate and temperature. A good agreement was achieved between the predicted and experimental results, with errors of less than 10%.
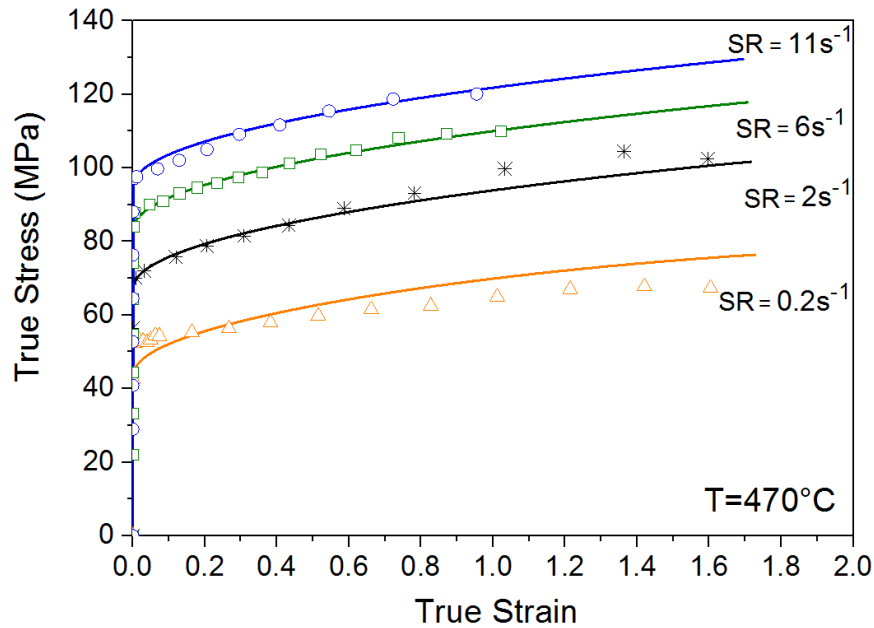
Figure 5-2. Comparison of the predicted (solid curves) and experimental flow stress curves (symbols) for AA2060 with different strain rates at 470 ºC
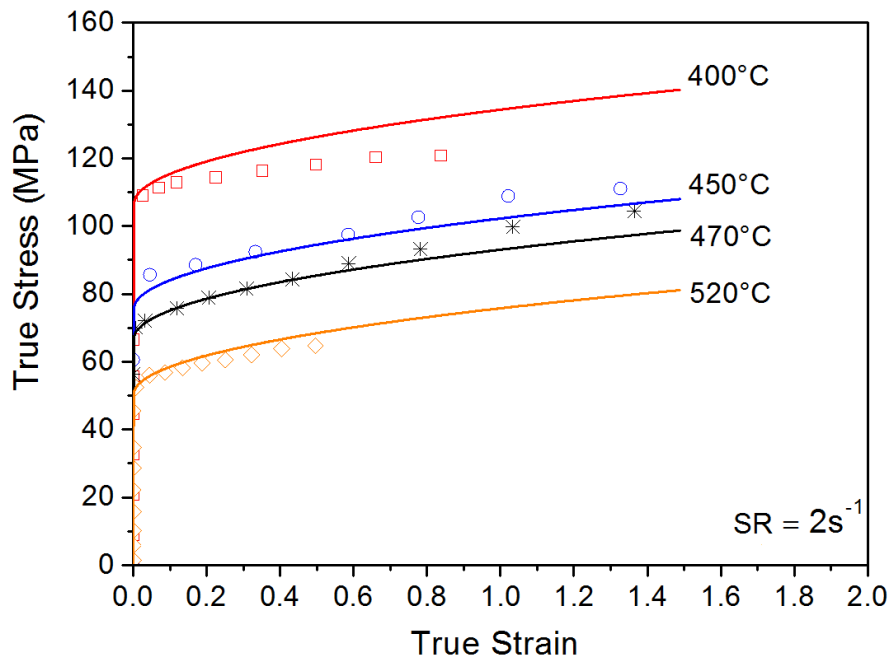
Figure 5-3. Comparison of the predicted (solid curves) and experimental flow stress curves (symbols) for AA2060 at different temperatures with a strain rate of 2/s
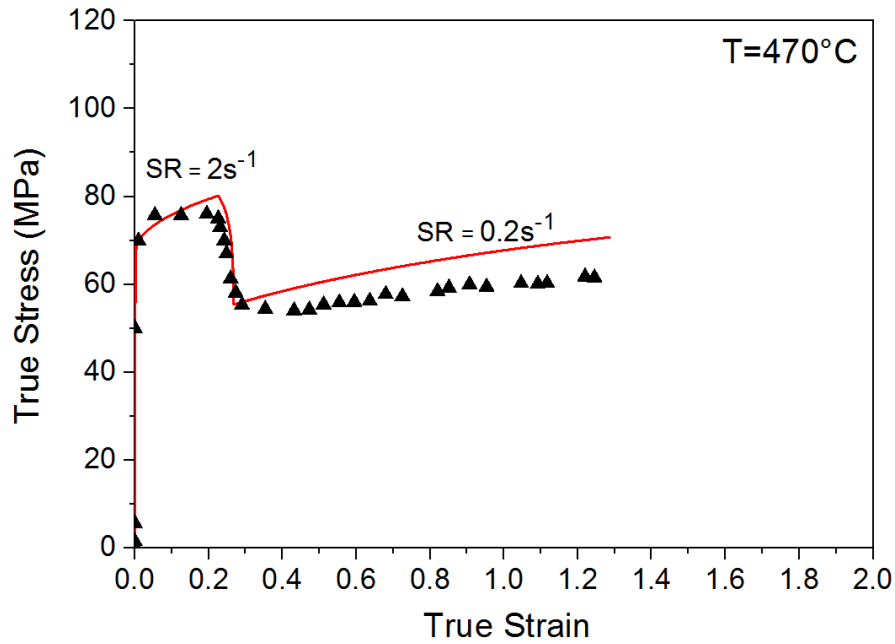
Figure 5-4. Comparison of the predicted (solid curves) and experimental flow stress curves (symbols) for AA2060 with strain rate change at constant temperature of 470 ºC
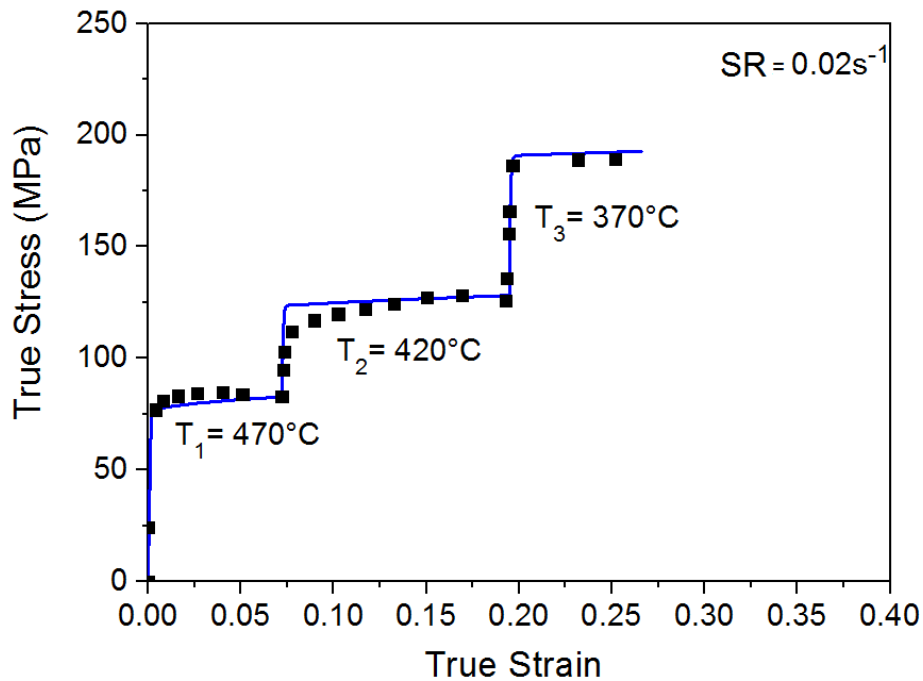
Figure 5-5. Comparison of the predicted (solid curves) and experimental flow stress curves (symbols) for AA2060 at temperature change at constant strain rate of 0.02/s.

5.2.2 Predictions of forming limit diagrams

Figure 5-6 and Figure 5-7 show the forming limit diagrams (FLDs) of AA2060, as a function of forming temperature (ranging from 300 to 450°C) and speed (ranging from 75 to 400mm/s). The symbols in both figures represent the experimental forming limit curves (FLCs) whereas the solid lines represent the FLD prediction results from the viscoplastic-Hosford-MK model. Based on the forming limit test, it was found that the formability of AA2060 increased with temperature, and decreased with forming speed. Small deviations between the experimental and prediction results can be found at 400°C and 450°C at 250mm/s under equi-biaxial loading. This was mainly due to the uncertainty in the level of localized necking detected during the strain measurement at these conditions. This uncertainty was the result of the degradation of the surface quality of the deformed specimen at high temperatures where larger strains were attained. The dashed line in Figure 5-6 represents the prediction of the FLD when the forming speed was increased from 250mm/s to 400mm/s at t=0.4s at a forming temperature of 400°C The dashed line in Figure 5-7 represents the prediction of the FLD with a quenching rate of 200°C/s at a forming speed of 250mm/s. Additionally, in order to predict the FLD with different forming speeds using viscoplastic-Hosford-MK model, the major strain rates were calculated from forming speeds as demonstrated in Appendix 5B.

The viscoplastic-Hosford-MK model was calibrated using the experimental FLDs from Figure 5-6 and Figure 5-7 by adjusting the imperfection factor, f_0. The predicted solid curves in the figures show that there was a good agreement between the predicted FLDs and experimental FLDs. From these curves, the imperfection factor of each FLC as a function of temperature and strain rate was determined, and the empirical function of f_0 was made and expressed by Eq. (5.17):

$$f_0 = 99.8449 \ln(\dot{\varepsilon}^2) - 199.7016 \ln(\dot{\varepsilon}) - 4.5111 \ln(T^2) + 9.0613 \ln(T) + 0.7551 \quad (5.17)$$

where in this equation, f_0 is the imperfection factor, $\dot{\varepsilon}$ is the strain rate and T is the temperature.

From the calibrated model, the FLD and failure criteria on AA2060 material can be predicted. The input variables required for the model are strain rate, temperature and strain path ratio. The failure criteria was defined as the onset of neck calculated by the ratio $d\varepsilon_{3b} / d\varepsilon_{3a}$. As mentioned as above, $d\varepsilon_{3b} / d\varepsilon_{3a}$ is calculated by the ratio of equivalent plastic strains between zones b and

a. The onset of necking can be defined when the $d\varepsilon_{3b}/d\varepsilon_{3a}$ ratio reaches a value greater than 10. The detailed calculation of $d\varepsilon_{3b}/d\varepsilon_{3a}$ can be found in Appendix 5C.
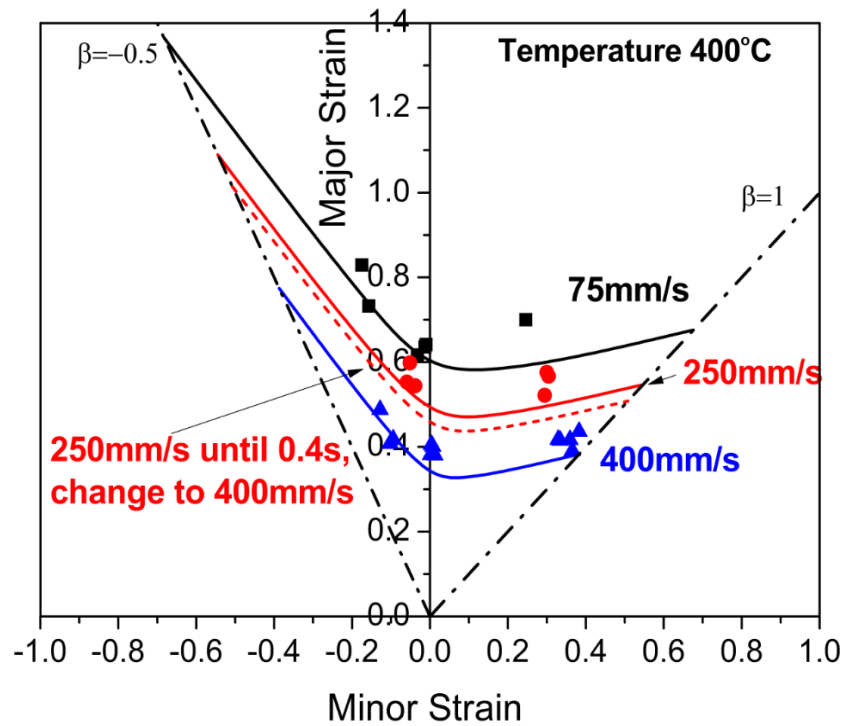
Figure 5-6. Comparison of the predicted (solid curves) and experimental forming limit curves (symbols) for AA2060 with different forming speeds at a constant temperature of 400°C.
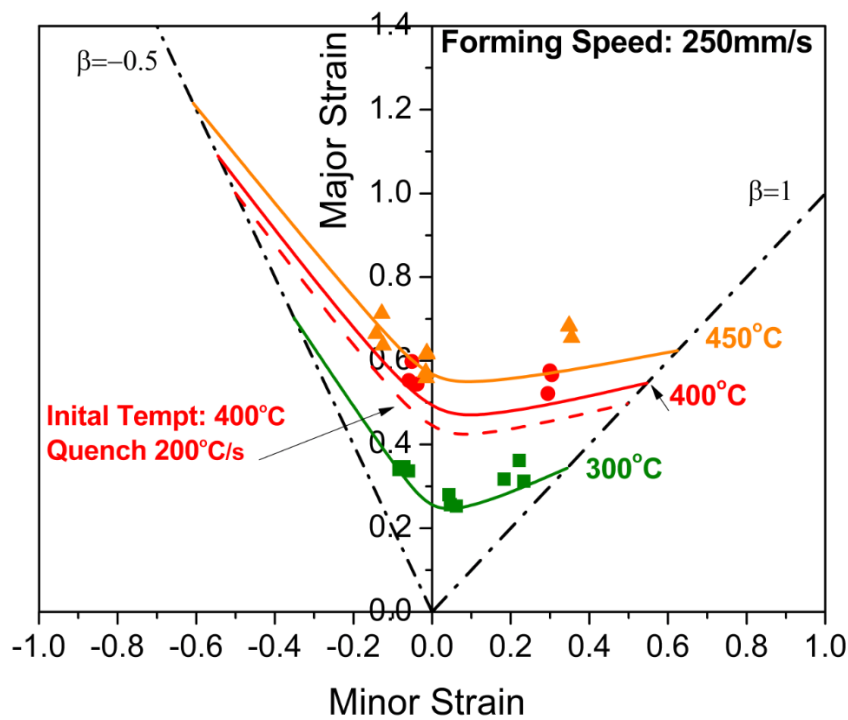
Figure 5-7. Comparison of the predicted (solid curves) and experimental forming limit curves (symbols) for AA2060 at different temperatures with a constant forming speed of 250mm/s

5.3 Validation of the model responses to strain rate changes, quenching rates and loading path changes

In this section, the responses of the developed model to complex loading histories are demonstrated and its intrinsic mechanisms revealed by analysing the evolution of the value $d\varepsilon_{3b}/d\varepsilon_{3a}$ against time. In the viscoplastic-Hosford-MK model, for a given constant temperature, strain rate and loading path, the development of necking is indicated by a sharp increase in $d\varepsilon_{3b}/d\varepsilon_{3a}$, as shown in Figure 5-8, at t=0.55s. This occurs due to more plastic straining occurring in Zone b than in Zone a as deformation progresses (Stoughton and Yoon, 2011); as the heterogeneous plastic flow develops further and becomes more severe, this eventually causes the onset of necking.
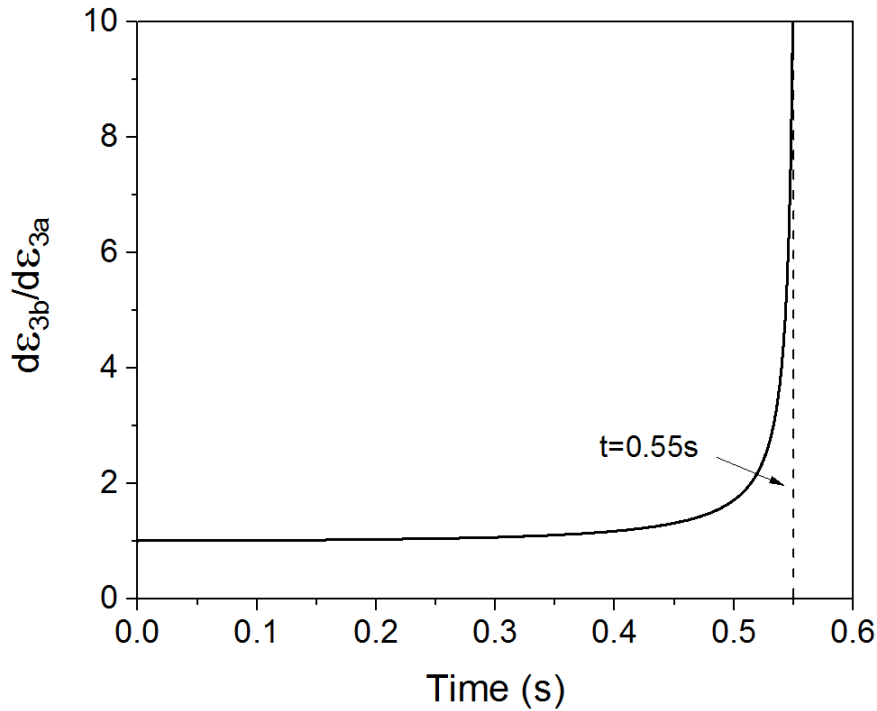
Figure 5-8. The development of a neck ($d\varepsilon_{3b}/d\varepsilon_{3a}$) against time at a constant temperature of 400°C, strain rate of 3s^{-1} and linear loading path of β=-0.5

To study the model's responses to strain rate, quenching rate and loading path variations, a mathematical decomposition was conducted (as shown in Appendix 5D, Eqs. 5.27 to 5.53) to distinguish between the effects of the individual terms in the model on the development of necking. Figure 5-9 clearly shows that the increment work per volume ratio between Zones a and b ('X') plays a significant role on the development of necking. Such an assumption was similarly made by Yoshida and Khan (Yoshida et al., 2014; Yoshida et al., 2007; Khan et al.,

2007), who analysed the effective stresses and effective strain increments during the deformation. The principle of increment work per unit volume (Khan and Huang, 1995; Khan et al., 2007) or plastic work per unit volume (Yoshida et al., 2014) was emphasised by considering anisotropic material responses under non-proportional loading (Yoshida et al., 2014), various strain rates and temperatures (Khan and Huang, 1995; Khan et al., 2007). Based on their pioneering work, a detailed mathematical analysis was conducted, associated with the increment work per unit volume ratio and accounting for the effects of strain rate changes, quenching rates and loading path changes on formability in a hot stamping process.

From the numerical study on strain localisation, the development of necking ($d\varepsilon_{3b}/d\varepsilon_{3a}$) can be expressed by Eq. (5.18).

$$\frac{d\varepsilon_{3b}}{d\varepsilon_{3a}} = \frac{\left(-R_2 - R_1\alpha_b^{l-1}\right)\left\{\left[R_2 + \alpha_a^{l}R_1 + \left(1-\alpha_a\right)^{l}R_1R_2\right]\right\}}{\left(-R_2 - R_1\alpha_a^{l-1}\right)\left\{\left[R_2 + \alpha_b^{l}R_1 + \left(1-\alpha_b\right)^{l}R_1R_2\right]\right\}} \cdot f_0 \exp\left(\varepsilon_{3b} - \varepsilon_{3a}\right) \cdot \frac{\bar{\sigma}_b d\bar{\varepsilon}_b}{\bar{\sigma}_a d\bar{\varepsilon}_a} \tag{5.18}$$

where α is the ratio between the minor stress and major stress.

Let:

$$X = \frac{\bar{\sigma}_b d\bar{\varepsilon}_b}{\bar{\sigma}_a d\bar{\varepsilon}_a} \tag{5.19}$$

$$Y = f_0 \exp\left(\varepsilon_{3b} - \varepsilon_{3a}\right) \tag{5.20}$$

$$Z = \frac{\left(-R_2 - R_1\alpha_b^{l-1}\right)\left\{\left[R_2 + \alpha_a^{l}R_1 + \left(1-\alpha_a\right)^{l}R_1R_2\right]\right\}}{\left(-R_2 - R_1\alpha_a^{l-1}\right)\left\{\left[R_2 + \alpha_b^{l}R_1 + \left(1-\alpha_b\right)^{l}R_1R_2\right]\right\}} \tag{5.21}$$

where $\bar{\sigma}_{a,b}$ is the equivalent stress, and $d\bar{\varepsilon}_{a,b}$ is the equivalent strain increment. These parameters all depend on the stress ratio (α), temperature (T), strain ratio (β) and strain rate ($\dot{\varepsilon}$).

From the numerical study on Eq. (5.25) to (5.51), the effect of Y and Z on $d\varepsilon_{3b}/d\varepsilon_{3a}$ can be considered to be negligible, and f_0 is the constant (0.9967), thus

$$\frac{d\varepsilon_{3b}}{d\varepsilon_{3a}} \propto \frac{\bar{\sigma}_b d\bar{\varepsilon}_b}{\bar{\sigma}_a d\bar{\varepsilon}_a} \tag{5.22}$$

Utilising the expression for the incremental work per unit volume ratio:

$$\dot{W}_{a,b} = \overline{\sigma}_{a,b} \cdot d\overline{\varepsilon}_{a,b} \tag{5.23}$$

$$\frac{d\varepsilon_{3b}}{d\varepsilon_{3a}} \propto \frac{\dot{W}_b}{\dot{W}_a} = \frac{\overline{\sigma}_{b(\alpha_b,T,\dot{\varepsilon}_b)} d\overline{\varepsilon}_{b(\alpha_b,T,\dot{\varepsilon}_b)}}{\overline{\sigma}_{a(\alpha_a,T,\dot{\varepsilon}_a)} d\overline{\varepsilon}_{a(\alpha_a,T,\dot{\varepsilon}_a)}} \tag{5.24}$$

Thus, $\dot{W}_b / \dot{W}_a$ can be regarded as a representative factor to evaluate the strain localisation under different strain rates, quenching rates and loading paths.
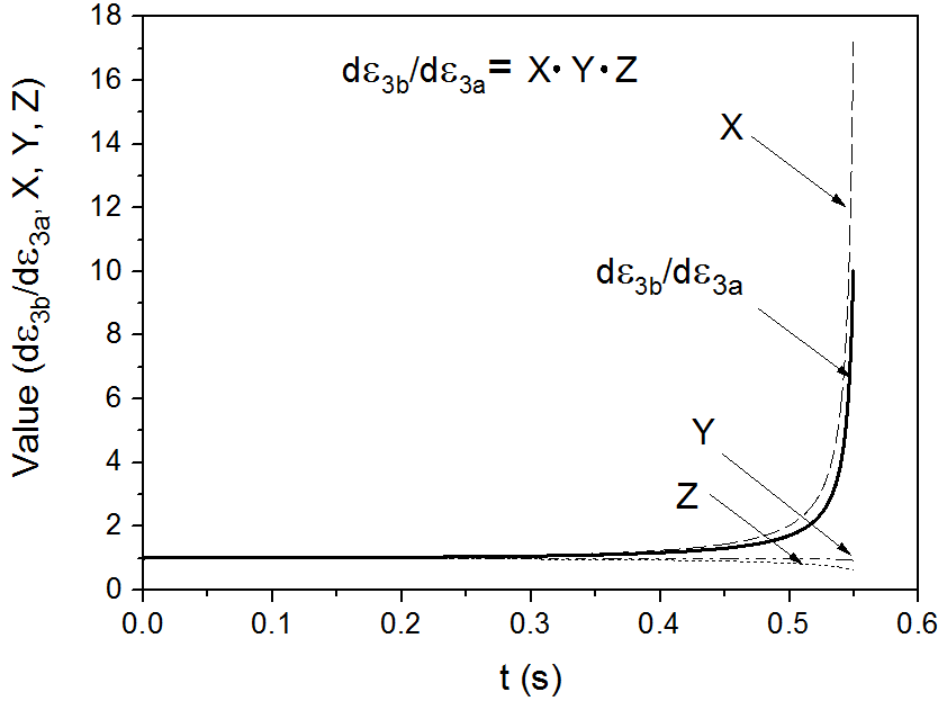
Figure 5-9. The calculated expression terms "X", "Y", "Z" and   against time using the viscoplastic-Hosford-MK model at a strain rate of 3/s, a temperature of 400°C, the loading path $\beta = -0.5$

In the viscoplastic-Hosford-MK model, the failure criterion was defined as a critical value of the thickness strain increment ratio between Zone *b* and Zone *a*. This criterion is an overall response to the evolutions of stress and strain states in all directions in the material with changing temperature, strain rate and loading path. In Figure 5-10 and Figure 5-11, the equivalent stress and strain increments are plotted, and it is shown that initially $d\overline{\varepsilon}_b$ and $\overline{\sigma}_b$ are almost equivalent to $d\overline{\varepsilon}_a$ and $\overline{\sigma}_a$ respectively. Eventually, compared to Zone *a*, $d\overline{\varepsilon}_b$ and $\overline{\sigma}_b$ reach such large values that localisation and failure occurs.
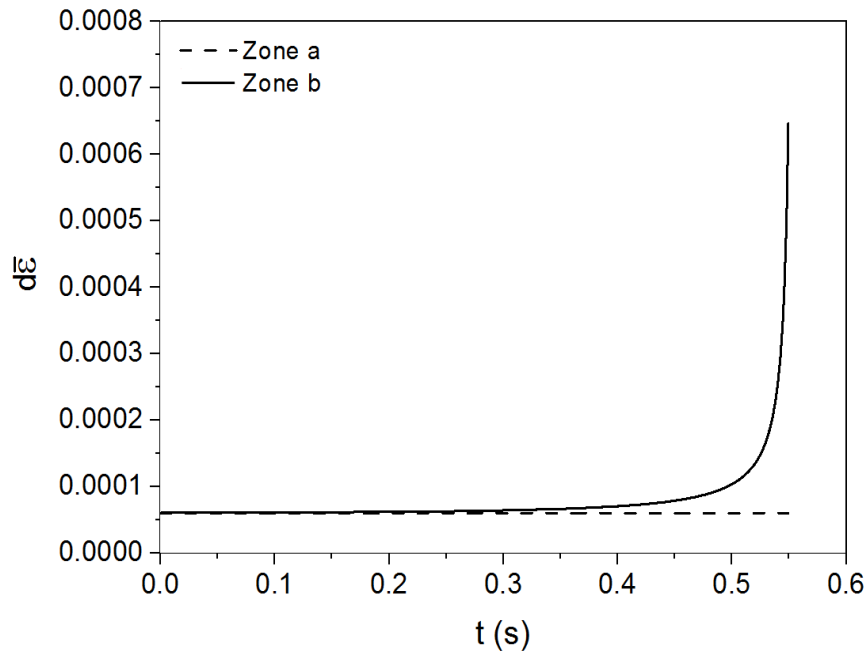
Figure 5-10. Calculations of (a) strain increment and (b) equivalent stress in Zone *a* and Zone *b* using the viscoplastic-Hosford-MK model under the same conditions as in Figure 5-8.
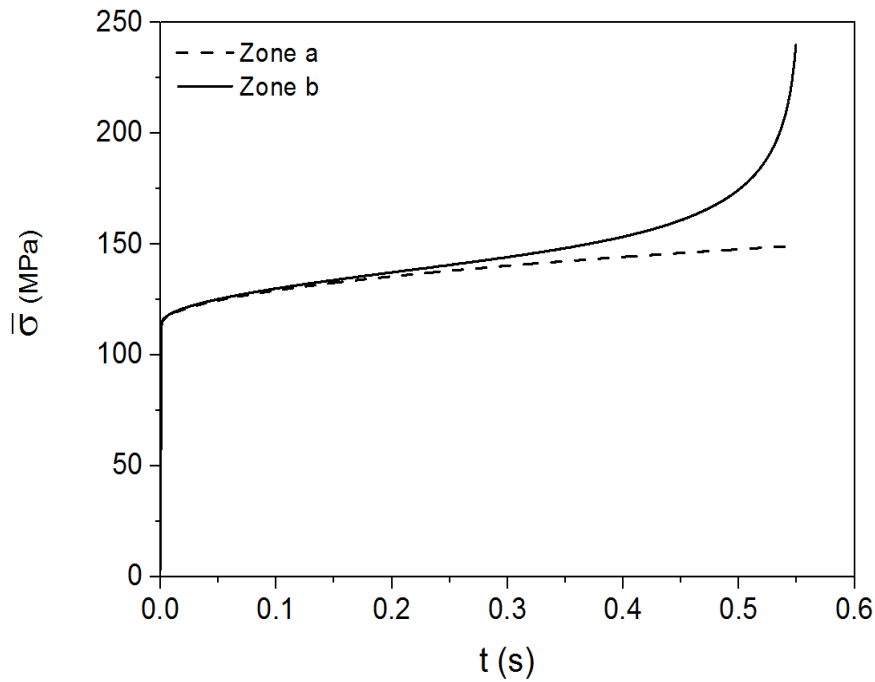
Figure 5-11. Calculations of (a) strain increment and (b) equivalent stress in Zone *a* and Zone *b* using the viscoplastic-Hosford-MK model under the same conditions as in Figure 5-8.

5.3.1 Effect of strain rates on necking development

For the following set of model constants: imperfection factor ($f_0 = 0.9967$), temperature (400°C) and loading path (β=-0.5) applied to the viscoplastic-Hosford-MK model, the various strain rate histories shown in Figure 5-12(a) were applied to the developed model. Figure 5-12(b) shows the model response to various strain rates, and in general, it could be deduced that the development of a neck is strain-rate dependent: as the strain rate increases, necking development is accelerated. Namely, the formability of AA2060 would decrease when forming takes place at higher rates. In a forming process, higher forming rates would normally lead to higher overall strain rates, which makes the material less formable. The reduced formability at higher strain rates would compete with the increased drawability at higher forming speeds typically achieved in forming processes. As indicated by from Eqs. 5.17 to 5.23, the development of necking represents the overall responses of a blank material to external loadings. In fact, the complex response of the blank material to strain rates might be more explicitly revealed by the incremental work, i.e. the joint effects of the strain increment (Figure 5-12(c)) and stress evolution (Figure 5-12(d)). Figure 5-12(c) shows the evolution of strain increments with loading. The dashed lines show the strain increments in Zone *a*, loaded at constant strain rates of 3, 5 or 7/s. In Zone *b*, the strain increments were rather stable at the initial stages and their magnitudes only slightly higher than those in Zone *a*, due to the thickness differences induced by the initial defects. The strain increments grow dramatically when necking starts to occur, due to the fact that a more severe stress concentration occurs when excessive plastic strain induced thinning takes place in Zone *b*. Therefore, the material in Zone *b* is deformed at a higher rate, as indicated by Figure 5-12(c).

The equivalent stress values in Zone *b* (the dashed lines) are also fairly close to those found in Zone *a* at the initial stages of loading and increase gradually, which reflects the strain hardening behaviour of the blank material, as indicated by Figure 5-12(d). When the blank material is continuously loaded with different strain rates, the dominant factor in the development of the neck is the strain rate hardening. The increase of strain rate not only leads to the acceleration of the plastic strain difference between Zone *a* and Zone *b*, but also results in a more pronounced difference in their strength. Consequently, a greater ratio in the incremental work per unit volume (Eq. 5.23) was obtained, resulting in premature fractures at lower strain levels, as shown in Figure 5-12(b).
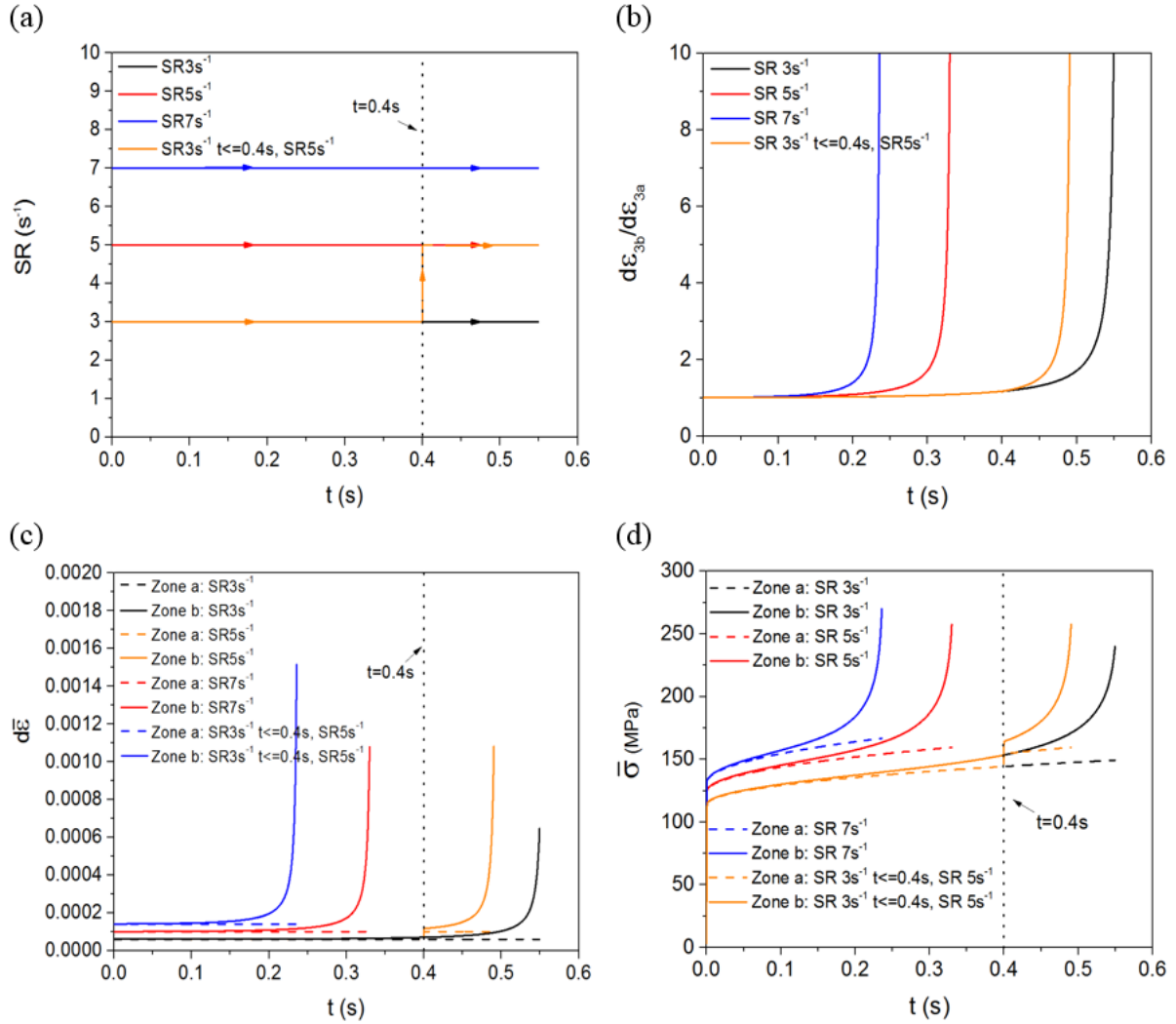
Figure 5-12. Evolution of: (a) $\dot{\varepsilon}$ profiles against time applied into model, (b) Predictions of developments of necks with different strain rates and strain rate changes using linear loading path (β =-0.5) and constant temperature of 400°C, (c) $d\bar{\varepsilon}$ and (d) $\bar{\sigma}$ against time in Zone a and Zone b under the conditions corresponding to (a).

When the blank material is subject to an abrupt strain rate increase, *e.g.* from 3 to 5 s^{-1}, at 0.4s, as shown in Figure 5-12(a), the model is able to immediately respond to the strain rate increase and the necking development is accelerated correspondingly, as indicated by Figure 5-12(b). As a result of the abrupt strain rate increase applied in Zone *a*, the strain increment in Zone *b* showed a simultaneous steep increase (Figure 5-12(c)). Since the strain rate change is introduced to Zone *a* at a late stage, when a neck has started to develop, an obvious deviation in the strain increment (Zone *b*) can be observed from Figure 5-12(c), leading to the occurrence of fracture rather rapidly. The abrupt increase in strain rate brings step-changes in the equivalent stresses in both Zone *a* and Zone *b*, as shown in Figure 5-12(d). The magnitude of the instant stress increase is determined by the strain rate hardening of the blank material:

higher strain rate hardening leads to a greater stress increase as a response to the abrupt strain increase. During the necking development stage following the strain rate increase, Figure 5-12 (d) shows that there is a more rapid deviation of the equivalent stress in Zone *b* from that of Zone *a*, and subsequently necking occurs at a lower failure strain.

5.3.2 Effects of temperature and quenching rate changes on necking development

In a hot stamping process, the hot blank is formed and quenched simultaneously by water cooled forming tools. The effect of the quenching rate on the forming limit was therefore modelled. As shown in Figure 5-13(a), the hot blank is formed and quenched from 400°C at a constant quenching rate of 30 or 150°C/s. The formability at isothermal conditions at contact temperatures of 300 and 400°C is also presented and analysed. For the following set of model constants: imperfection factor (f_0 =0.9967), strain rate (3/s) and loading path (β = -0.5) applied to the viscoplastic-Hosford-MK model, as shown in Figure 5-13(b), the development of necking is forming temperature and quenching-rate dependent; a temperature increase would enhance the formability of the hot blank, while a higher quenching rate would accelerate the development of necking. The predicted results suggest that, in light of formability, hot stamping performed at higher blank temperatures and lower quenching rates would be more favourable.

The material response to the quenching rate was revealed by analysing the incremental work per unit volume ratio, *i.e.* the corresponding joint effects of the strain increment (Figure 5-13(c)) and equivalent stress (Figure 5-13(d)). A constant strain rate ($3s^{-1}$) was assigned in Zone *a*, while the strain increment in Zone *b* was fairly stable in the initial stages, until necking started to occur. The different increasing gradients of the strain increment were mainly induced from the corresponding changes in the flow stress, as shown Figure 5-13(c) and (d). In the application of a quenching rate, the material response is reflected by the flow stress of the material. Temperatures in both Zones *a* and *b* drop more quickly, and results in greater strain hardening. Thus, strain localisation occurred earlier due to the excessive stress concentration induced from strain hardening at Zone *b*. The higher the quenching rate in the quenching process, the more the strain localisation would be accelerated.

When an abrupt quenching rate increase from 30 °C /s to 150 °C /s was applied, *e.g.* at 0.4s, as shown in Figure 5-13(a), the model was able to immediately respond to the increase, and the necking development was accelerated correspondingly, as indicated by Figure 5-13(b). The

increase in the quenching rate brings step changes in the equivalent stresses in both Zone *a* and Zone *b*, as shown in Figure 5-13(d). The magnitude of the sharp stress increase is determined by the instant increase in the strain increment (Figure 5-13(c)) and subsequent strain hardening of the blank material; higher strain hardening leads to greater stress localisation. During the necking development stage following the quenching rate increase, the deviation of the equivalent stress in Zone *b* from that of Zone *a* is accelerated by the increase in strain hardening, causing an earlier onset of necking.
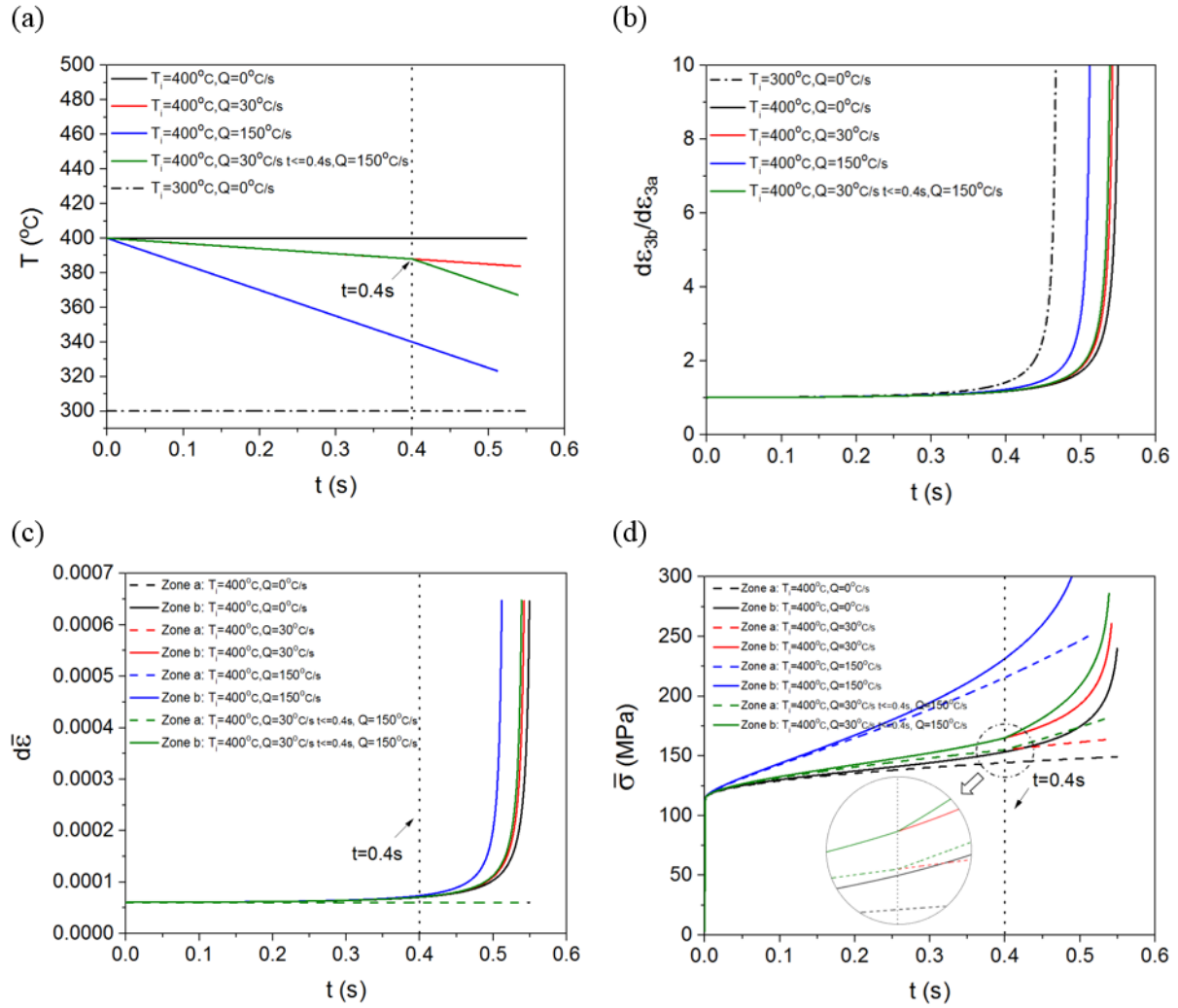
Figure 5-13. (a) Temperature profiles against time with different quenching rates (b) Predictions of developments of necks ($d\varepsilon_{3b}/d\varepsilon_{3a}$) with different quenching rates using linear loading path (β =-0.5) and strain rate of 3s^{-1}. The developments of (c) $d\bar{\varepsilon}$ and (d) $d\bar{\sigma}$ against time (T$_i$ is the initial temperature, Q is the quenching rate)

5.3.3 Effect of changes in loading path on necking development

To form the wing stiffener component with its complex geometrical features required the forming process to be performed in two stages within a single pressing operation. Each region of the part was deformed in either a linear or non-linear loading path. The effect of one-stage straining (linear loading path) and two-stage straining (non-linear loading path) on the forming limit was therefore demonstrated by plotting their corresponding FLCs. For the following set of model constants: imperfection factor f_0 =0.9967, a temperature of 400 °C and an average strain rate of 3s^{-1}, applied to the viscoplastic-Hosford-MK model, FLCs with changes in loading paths were predicted and shown in Figure 5-14.
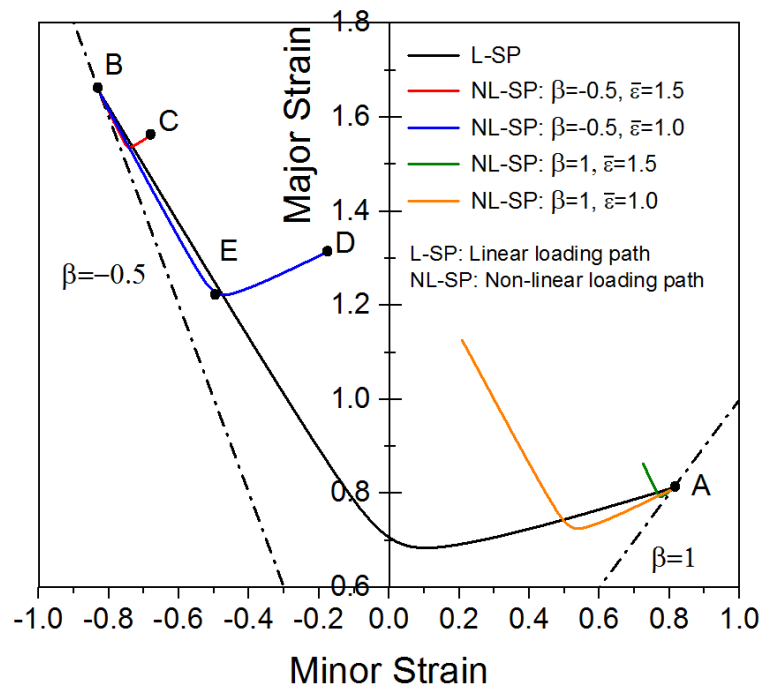
Figure 5-14. shows the predicted FLCs with different changes in loading path

In Figure 5-14, the black line represents the predicted FLC under a linear loading path. NL-SP are the predicted FLCs under non-linear loading paths, where the material was pre-stretched under one type of loading path up to a specified equivalent strain level, and then stretched under a different type of loading path. As the loading path changes from linear to non-linear, the new FLCs shift towards different directions as indicated by the blue, green, red, yellow and green lines, thus revealing the loading path dependence of the developed model. To investigate the effect of non-linear loading paths on the formability of sheet metal, the development of the neck against time was analyzed. The loading path conditions corresponding to the forming limit strains in points A, B, C, D, and E in Figure 5-14 are listed in Table 5-2.

Table 5-2. List of different loading path applied into developed model

Loading path (LP)		Point
LP1	β=1, equi-biaxial tension	A
LP2	β=-0.5, uniaxial tension	B
LP3	β=-0.5 to β=1, uniaxial tension for $\bar{\varepsilon}$=1.0 followed by equi-biaxial stretching	C
LP4	β=-0.5 to β=1, uniaxial tension for $\bar{\varepsilon}$=1.5 followed by equi-biaxial stretching	D
LP5	β=-0.5 to β=-0.05, uniaxial tension for $\bar{\varepsilon}$=1.0 followed by plane strain stretching	E
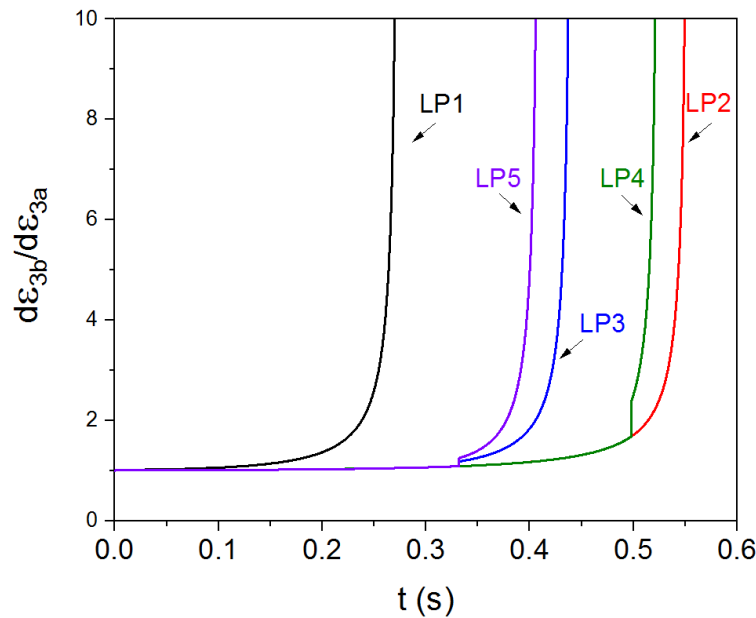
Figure 5-15. Prediction of developments of necks ($d\varepsilon_{3b} / d\varepsilon_{3a}$) under different changes in loading path at an average strain rate of 3/s and constant temperature of 400ºC

Figure 5-15 shows the model responses to changes in loading path at the conditions listed in Table 5-2. In comparison to the failure strains under linear loading paths (LP1 and LP2), the failure strains under the non-linear loading paths LP3, LP4 and LP5, which each have different loading path conditions, were higher than LP1 (equi-biaxial tension), but lower than LP2 (uniaxial tension). In Figure 5-15, it was predicted that the type of loading path and the amount of first-stage straining applied were two major factors that could have great effects on the forming limit strains.

Effects of different types of loading path

LP2: β=-0.5, uniaxial tension;

LP3: β=-0.5 to β=1, uniaxial stretching ($\bar{\varepsilon}$=1.0) and followed by biaxial tension until failure;

LP5: β=-0.5 to β=-0.05, biaxial stretching ($\bar{\varepsilon}$=1.0) and followed by plane strain stretching until failure;
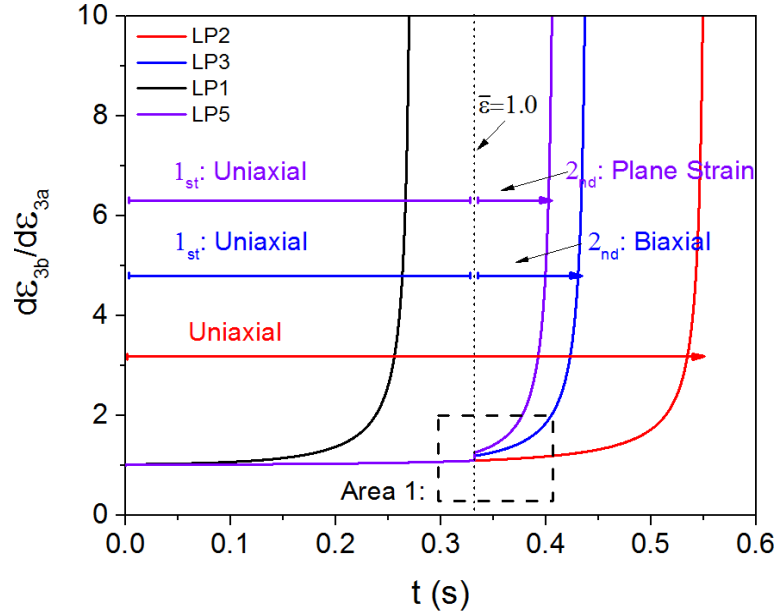
Figure 5-16. Prediction of developments ($d\varepsilon_{3b}/d\varepsilon_{3a}$) of necks with the same amount of equivalent strain but different loading path sequences at an average strain rate of 3/s and constant temperature of 400°C
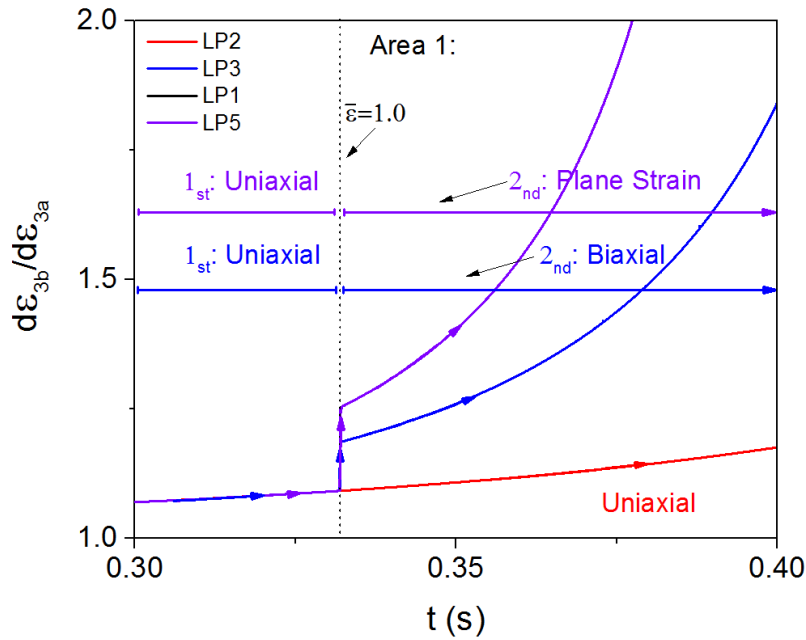
Figure 5-17. Detailed view of Area 1 in corresponding to Figure 5-16

The HFQ forming process for the wing stiffener component occurred in two stages, the details of which are described, in the paper (El Fakir et al., 2014). From the FE model anaylsis, it was deduced that in the first stage of the process where the material was drawn into the die cavity, the loading was linear and uniaxial. In the second stage where the central geometrical features (Appendix 5E) were formed, the material in the side wall was mostly stretched under plane strain conditions, whereas the material in the corner region was mostly strectched under biaxial conditions. Thus, capturing the effect of the loading path change and the amount of first-stage straining applied was critical.

Figure 5-16 shows the model responses to different types of loading paths during second stage straining. The development of a neck under LP2 shows a higher failure strain than that under LP3 and LP5. The prediction results suggest that the formability under LP2 (a-linear loading path) is higher than that under LP3 (a non-linear loading path) and LP5 (also a non-linear loading path). It was also predicted that the formability under LP3 is higher than that under LP5. At $\bar{\varepsilon}=1.0$, the evolutions of the development of the neck under LP3 and LP5 show instant step increases in the value of $d\varepsilon_{3b}/d\varepsilon_{3a}$, the details of which are shown in Figure 5-17. The instant increase with different magnitudes induced by different types of loading path (biaxial & plane strain) can be explained by the incremental work per unit volume, *i.e.* the corresponding joint effects of the strain increment (Figure 5-18) and equivalent stress (Figure 5-19).

In Figure 5-18, it is shown that the same amount of uniaxial straining was applied until $\bar{\varepsilon}=1.0$ for LP2, 3 and 5, and hence their strain increment evolutions up to this point were identical. When the loading path switched from the initial loading path (β=-0.5) to the new loading path (β=-0.05 or β=1), the strain increments under LP3 and LP5 begin to increase faster than that under LP2. This is due to the resulting instant changes in the equivalent strain rate, which would induce additional work hardening of the material, as shown by the subsequent increase in the equivalent stress evolutions. Although the initial increase in the strain increment and equivalent stress (Figure 5-19) is larger for LP3 at $\bar{\varepsilon}=1.0$, failure occurs earlier in LP5. This is because the resulting difference in equivalent stress and strain increment between Zone *a* and Zone *b* for LP3 when the loading changes to plane strain conditions. Consequently, the incremental work per unit volume ratio for LP5 was larger than that in LP3. Strain localization under plane

strain conditions would therefore occur more rapidly, leading to a faster evolution of the equivalent strain increment and equivalent stress, and hence failure.
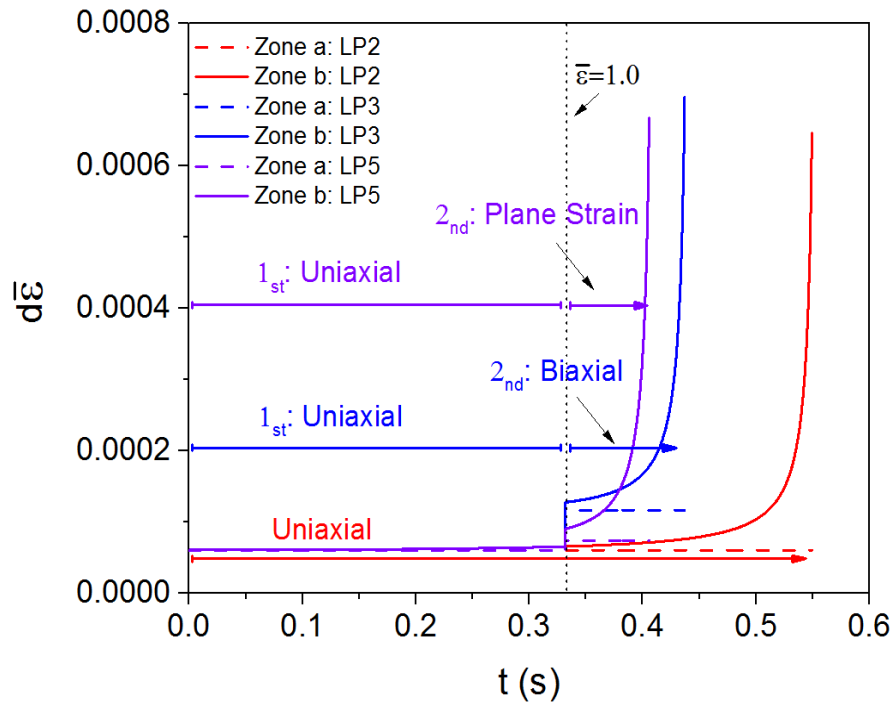
Figure 5-18. Evolution curves of $d\bar{\varepsilon}$ in Zone a and Zone b under the conditions corresponding to Figure 5-16.
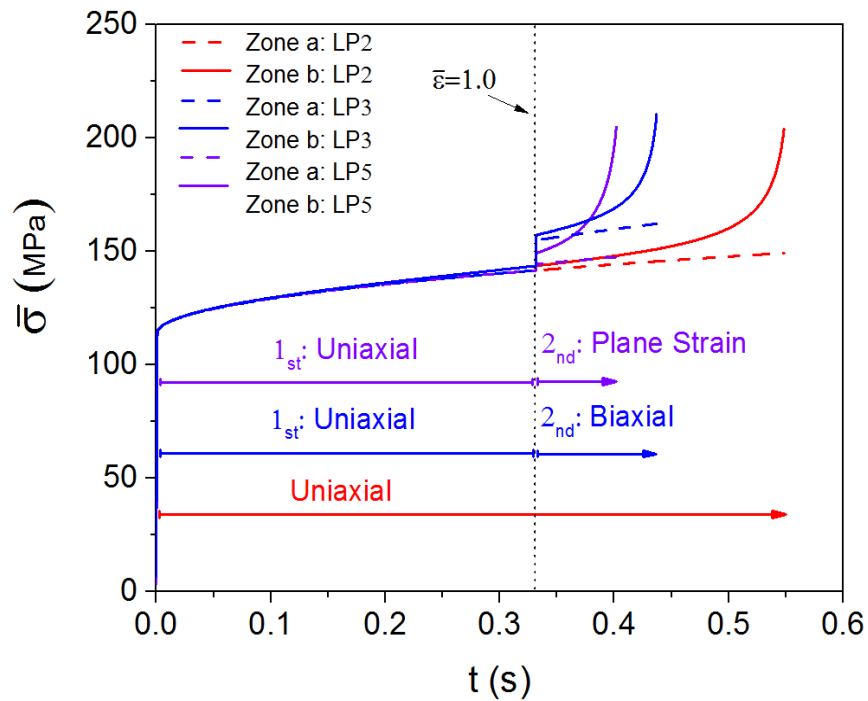
Figure 5-19. Evolution curves of $\bar{\sigma}$ in Zone a and Zone b under the conditions corresponding to Figure 5-16.

Effects of the amount of strain in the first-stage straining

LP1: $\beta=1$, biaxial tension;

LP3: $\beta=-0.5$ to $\beta=1$, uniaxial stretching ($\bar{\varepsilon}=1$) and followed by biaxial tension until failure;

LP4: $\beta=-0.5$ to $\beta=1$, uniaxial stretching ($\bar{\varepsilon}=1.5$) and followed by biaxial tension until failure;
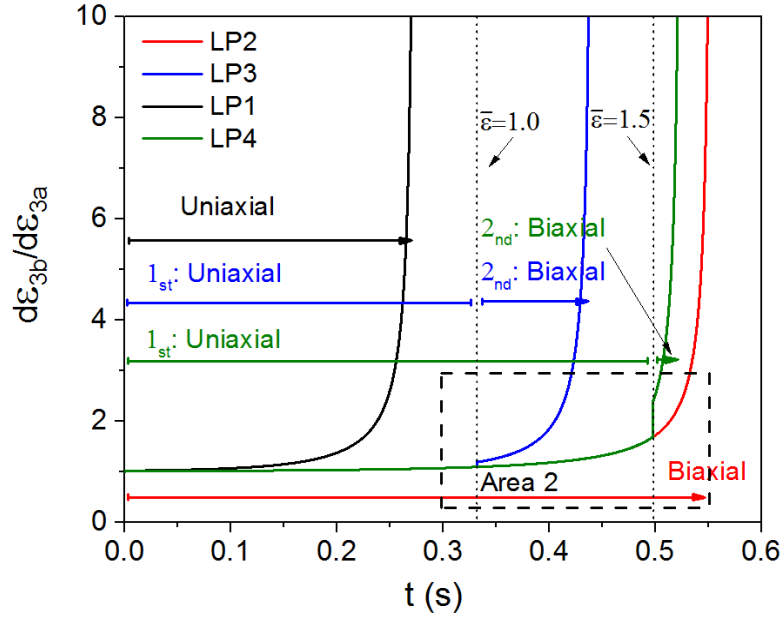
Figure 5-20. Prediction of developments of necks ($d\varepsilon_{3b}/d\varepsilon_{3a}$) with different amounts of equivalent strain in the first stage but the same loading path sequences at an average strain rate of 3/s and constant temperature of 400°C
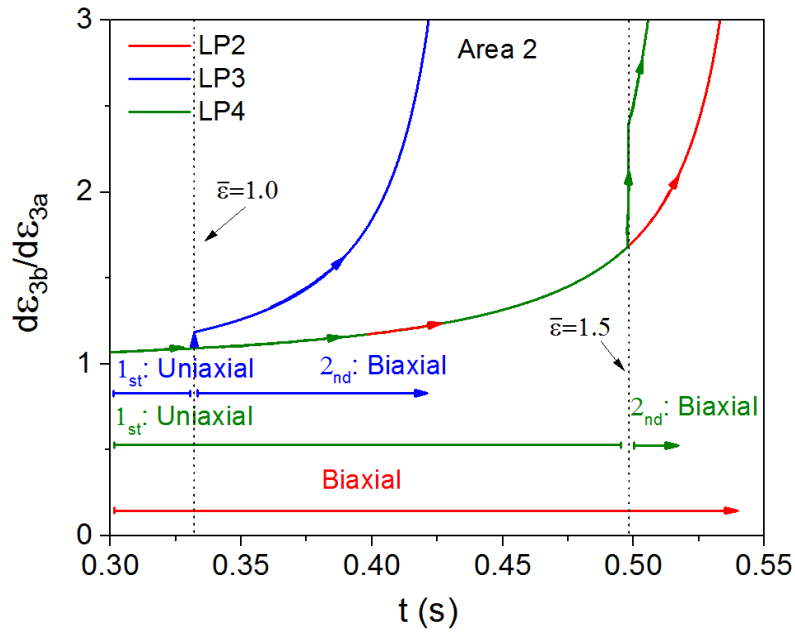
Figure 5-21. Detailed view of Area 1 in corresponding to Figure 5-20

In Figure 5-20, the development of a neck under LP4 shows a relatively higher failure strain than that under LP3. The prediction results suggest that the formability under LP4 is higher than that under LP3(a non-linear loading path) and LP1 (a linear loading path, with $\beta=1$). In the evolution of the development of the necks under LP1, LP3 and LP4, the onset of necking occurred during biaxial stretching. The differences in their corresponding formability were mainly due to the amount of first-stage uniaxial straining. The formability was enhanced when the amount of first-stage uniaxial straining was increased. Without any uniaxial straining, such as under LP1 (linear loading path), the formability was the lowest. Under the loading paths LP3 and LP4, the step increases in the values of $d\varepsilon_{3b}/d\varepsilon_{3a}$ were at $\bar{\varepsilon}=1.0$ and $\bar{\varepsilon}=1.5$, the details of which can be seen in Figure 5-21. In Figure 5-21, when the loading path changed from uniaxial to biaxial at $\bar{\varepsilon}=1.0$ and at $\bar{\varepsilon}=1.5$ for LP3 and LP4 respectively, the gradient of the curves under LP3 tended to be increasingly higher than that under LP4, which accelerates the occurrence of strain localization; hence the failure strain under LP3 was lower.

The material response to different amounts of first-stage straining was analysed in terms of the incremental work per unit volume ratio, *i.e.* the corresponding joint effects of strain increment (Figure 5-22) and equivalent stress (Figure 5-23). In Figure 5-22, the strain increment evolution in Zone *a* and Zone *b* under LP1 was initially higher than that under LP3 and LP4 due to the relatively higher equivalent strain rate under LP1. Under the linear loading path LP1, the differences in strain increments between Zone *a* and Zone *b* increase at a higher rate than that of the non-linear paths LP3 and LP4. With the increasing level of uniaxial pre-straining from LP3 to LP4, the strain localisation was delayed. In Figure 5-23, the stress evolution in Zone *b* under LP1, LP3 and LP4 shows different levels of strain hardening induced by the different strain levels. As the amount of first-stage uniaxial straining increases, the additional straining hardening induced from biaxial straining is delayed, resulting in the retardation of strain localisation.
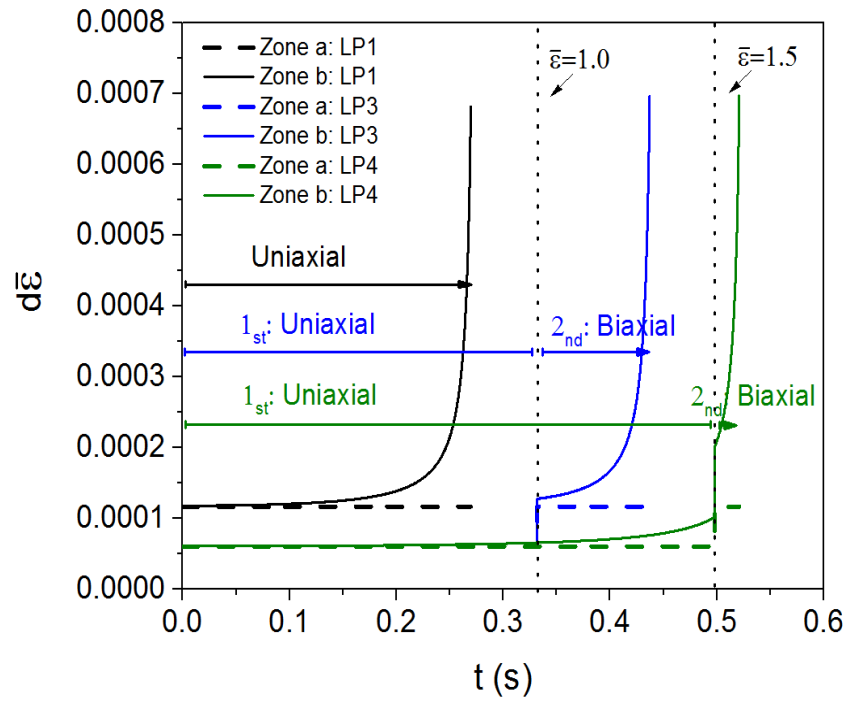
Figure 5-22. Evolution curves of $d\bar{\varepsilon}$ in Zone a and Zone b under the same conditions as in Figure 5-20.
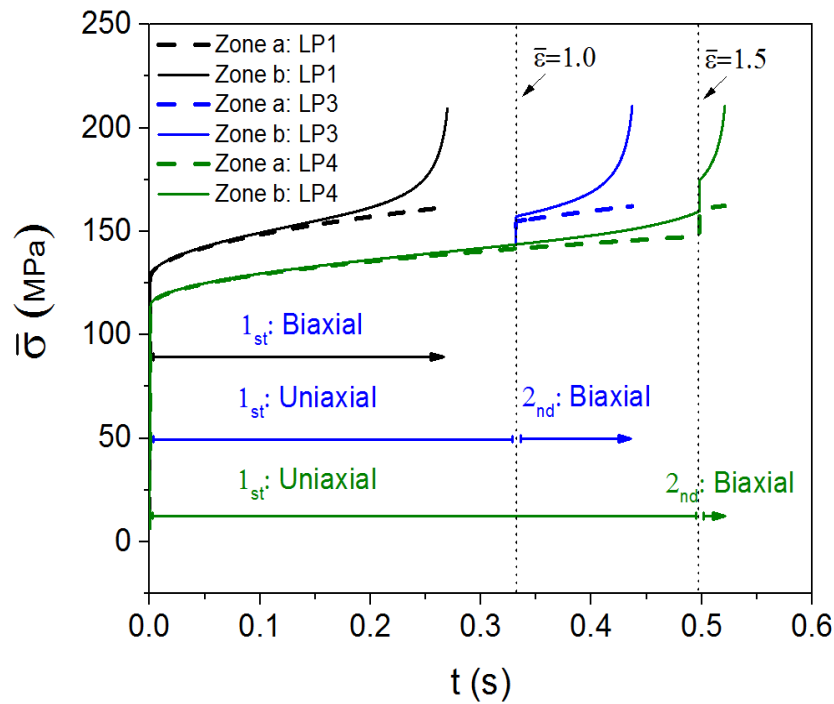
Figure 5-23. Evolution curves of $\bar{\sigma}$ in Zone a and Zone b under the same conditions as in Figure 5-20.

5.4 Application of the forming limit prediction model in the forming of the AA2060 complex-shaped component

Having verified the capabilities of the model for the range of loading conditions discussed previously, the model was experimentally validated using the results obtained from the forming of a practical component. The following section discusses the results obtained by utilizing the viscoplastic-Hosford-MK with a Finite Element simulation of the process and the comparisons made with a formed wing stiffener component.

5.4.1 Forming limit prediction for the AA2060 wing stiffener component

As the FE simulation was verified in Chapter 4, the forming limit of the AA2060 sheet wing stiffener component was predicted using the developed forming limit prediction model (viscoplastic-Hosford-MK model) and the PAM-STAMP FE simulation. The full procedures of the forming limit prediction using developed model and PAM-STAMP simulation were shown in Appendix 5F and Chapter 4, respectively. In Figure 5-24, the final formed part with localized necking and the corresponding prediction of the forming limit is shown. In the experiment, the localized necking occurred at the side wall region rather than the corner region of the central feature of the part. The same failure location for forming wing stiffener component on AA5754 and AA6082 were found at the side wall region in Appendix 5G. Thus, the localized necking did not occur at the region with the greatest thinning. However, the location of necking could be determined correctly by the model developed, which predicted that the forming limit was exceeded in the region as expected. Based on the simulation results in Figure 5-25, the FE simulation results in the corner region (Region 2) and side wall region (Region 1) were analyzed by considering the thinning values and $d\varepsilon_{3b}/d\varepsilon_{3a}$ values. In Figure 5-25, the elements selected for analysis in Regions 1 and 2 are highlighted (10 elements and 5 elements, respectively), and the thinning and corresponding $d\varepsilon_{3b}/d\varepsilon_{3a}$ values plotted for each as shown in Figure 5-26.

Based on the results from Figure 5-26, in the forming of the AA2060 wing stiffener component, the localised necking may not occur at the region of maximum thinning. The onset of localised necking is strongly affected by many factors, such as the quenching rates and forming speed and loading path variations that occur in hot stamping processes; using the developed forming

limit prediction model, the localised necking was predicted based on the combined effects of these factors, as shown in Figure 5-27.
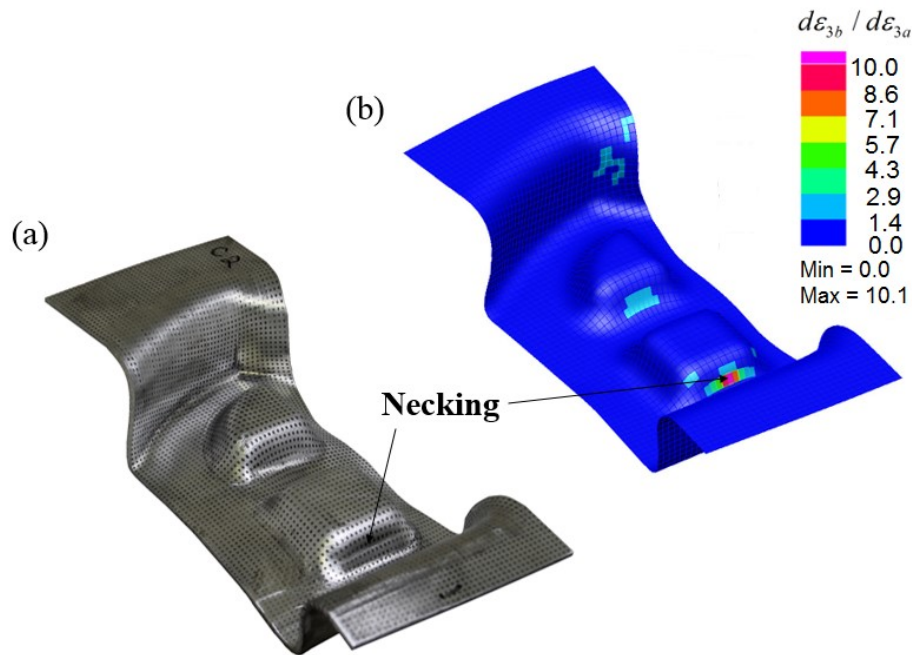
Figure 5-24. Formed component: (a) Observation of localised necking located at side wall and (b) Prediction of localised necking using the developed model
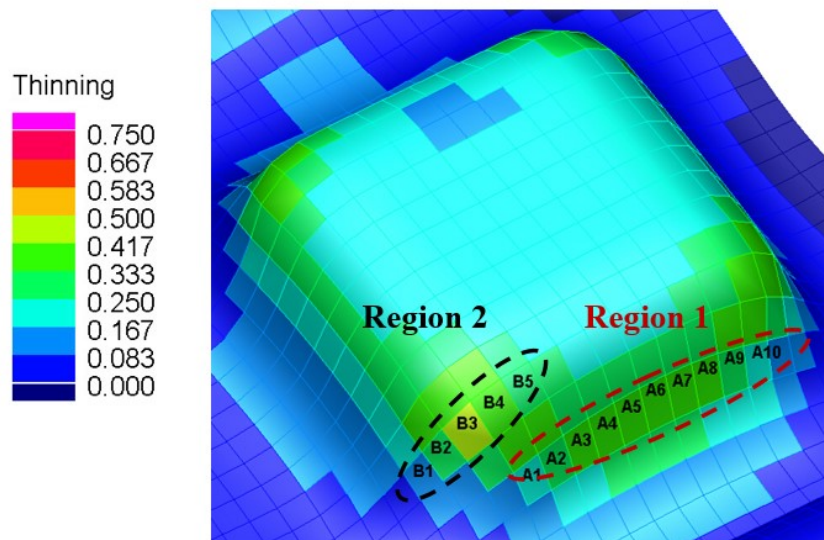
Figure 5-25. Analysis of selected elements from region 1 and region 2
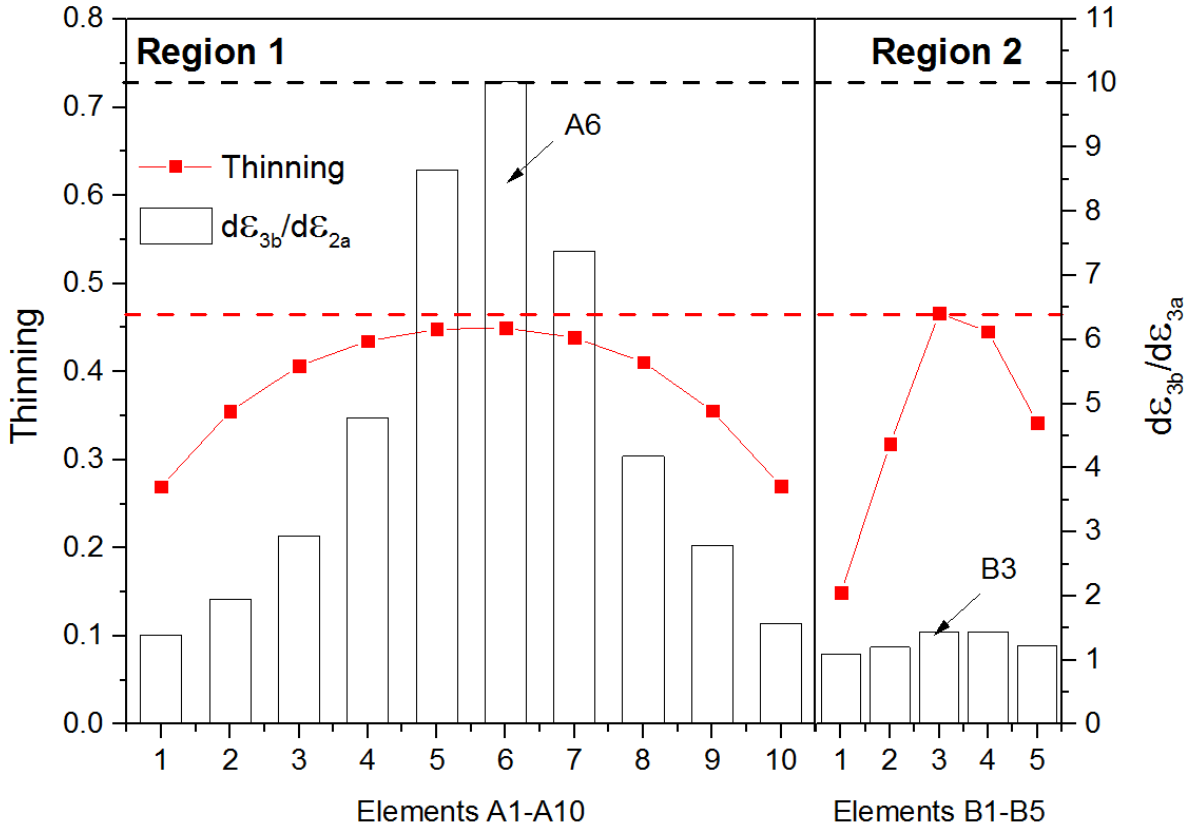
Figure 5-26. Development of a neck and thinning for element: (a) A1-A9 and (b) B1-B5 of the FE simulation.

In the predicted localised necking region and maximum thinning region, two elements (A6 and B3) were selected. The evolutions of the development of the neck, temperature, strain rate and loading path were all plotted in Figure 5-27. In Figure 5-27(a), the development of a neck curve ($d\varepsilon_{3b}/d\varepsilon_{3a}$) against time is shown. Along this curve for element A6, numerous spikes are observed at different times, which were the combined result of the simultaneous changes in the strain rate, temperature and loading path. For example, at t=0.72 in the hot stamping process for the wing stiffener component, the central parts of the component were formed, which involved changes in the strain rate and loading path. Meanwhile, the central part was quenched, causing a change in temperature. Regarding the loading path change at t=0.72s shown in Figure 5-27(d), it was found that the loading on the side wall (A6) changes from a uniaxial tensile mode to a plane strain mode when the central regions were started to be formed, whereas the loading on the corner region (B3) changes from a uniaxial tensile mode to a biaxial mode. In Figure 5-27(b), at t=0.72, the temperature changes from approximately 451 ºC to 423 ºC for both elements. Figure 5-27(c) also shows that the strain rate also increased dramatically when the central region was formed for both elements. Based on the detailed analysis of the viscoplastic-Hosford-MK model, the poor predicted formability of element A6, where the

failure point was observed, was due to a high strain rate, a high quenching rate to a low temperature, and a change in the loading path from a uniaxial mode to a plane strain mode.
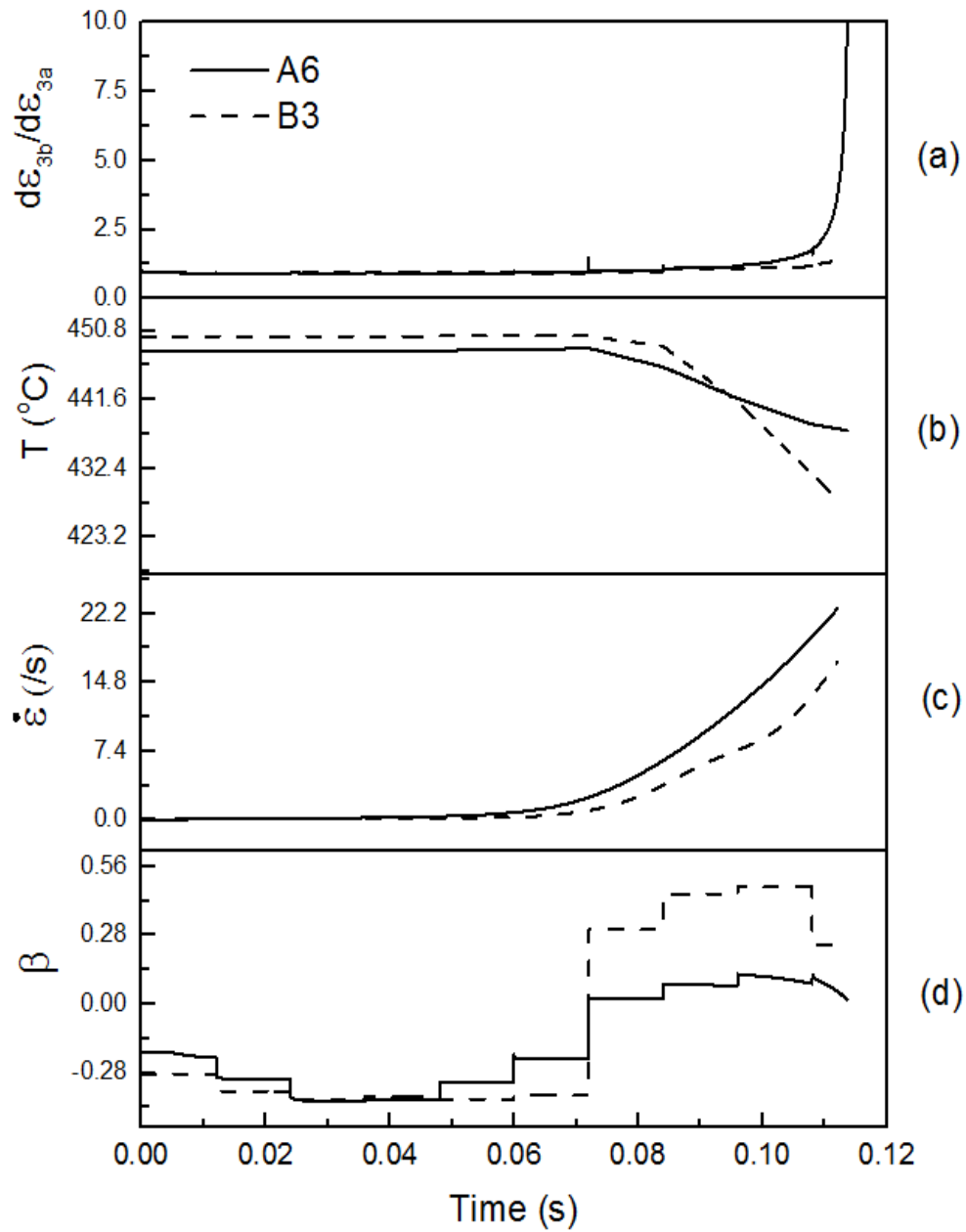
Figure 5-27. (a) Development of a neck for selected elements (A6 & B3) against time. The corresponding histories of (b) temperature against time (c) strain rates against time and (d) loading path against time of the selected elements

5.5 Conclusion

The visocoplastic-Hosford-MK model was used to predict forming limit of the hot-stamped AA2060 wing stiffener component. The location of onset of necking was accurately predicted, and makes a good agreement with the results obtained from experimental forming tests. It was indicated that the onset of necking occurred at the thin wall rather than corner region as expected. It was concluded that the onset of necking may not necessarily occur at the maximum thinning region. The forming limit prediction for the hot stamping process featuring non-isothermal and non-linear loading conditions were successfully achieved on AA2060 alloy. The onset of necking under such complex forming conditions mainly relies on the comprehensive effect of changes in strain rate, temperature and loading paths. Due to the detailed numerical analysis of the developed model, two significant features were found: it was concluded that the viscoplastic-Hosford-MK gives accurate model response in the variation of temperature, strain rate and loading path, even with the instantaneous change of those parameters. Additionally, it was concluded that the work hardening behaviour and its parameter "incremental work per unit volume ratio" plays an important role in the forming limit prediction of AA2060 under hot stamping conditions.

<div align="right">**Chapter 6**</div>

Forming limit prediction of AA7075 alloy under hot stamping conditions[3]

In this chapter, the optimized initial blank shape for a hot-stamped AA7075 component was determined using a trial-and-error simulation procedure through the application of the viscoplastic-Hosford-MK model. By applying the developed model to the hot stamping of a trial AA7075 component, the accuracy of the model was successfully validated. Finally, the optimal initial blank shape was determined using the developed model by predicting the forming limits of AA7075 alloy for different initial blank shape designs.

6.1 Introduction

Numerical simulations of sheet metal forming processes are used extensively in the stamping industry where numerical and Finite Element (FE) simulations are conducted as cost-effective ways to optimize forming parameters and evaluate forming defects before experimental forming. More importantly, the determination of an optimal initial blank shape is a key requirement in the success of a forming process to improve the product quality and formability, and also minimize the costs of material and overall production (Fazli and Arezoo, 2012; Azaouzi et al., 2011). Traditional methods to determine the geometry of optimal blank rely on experimental trial-and-error experimentation, requiring a series of trials and blanks to examine the effects of different geometries. The determination of optimum blank shape with these means results in low efficiency and high cost. In order to improve the production efficiency, the FE simulation aided trial-and-error methods are used.

Many approaches including numerical simulation have been studied (Mole et al., 2013) to determine the optimal blank shape. The first is the development of numerical models to

---

determine geometrical features of edges. Several associated studies in the literature have been made for a range of numerical models, such as slip line field (Chen and Sowerby, 1992; Vogel and Lee, 1990; Gloeckl and Lange, 1983), geometrical mapping (Sowerby, Duncan and Chu, 1986), sensitivity analysis method (Son and Shim, 2003; Shim et al., 2000), inverse approach (Guo et al., 2000; Park et al., 1999; Lee and Huh, 1998) and trial-and-error method based on finite element analysis (Guo et al., 1990; Kim and Kobayashi, 1986). Those models have focused on the geometry design of the blank shape. Another has been the development of advanced constitutive models to predict accurate material response under complex forming conditions (Padmanabhan et al., 2009; Pegada et al., 2002). The plasticity of deformation and specific material behaviour is crucial in the study of optimising the initial blank shape. Vijay et al. (Pegada et al., 2002), Hu et al. (Hu et al., 2001) and Padmanabhan et al. (Padmanabhan et al., 2009) considered the effect of anisotropic material behavior on the initial blank designs during the deep drawing process. In Padmanabham's research, the isotropic work hardening proposed by Swift (Swift, 1952), and the Hill's 1948 (Hill, 1948) and Cazacu & Barlat (Cazacu and Barlat, 2001) anisotropic yield criterions were utilized in their numerical models. It was stated that the initial anisotropy has a great effect on the material flow characteristics, giving a direct impact on the blank shape design and final quality of production. Park et al. (Park et al., 1999) used Hill's 1979 yield criterion (Hill, 1979), rigid plastic material model in the numerical model. Good formability of the formed part with optimum blank shape was obtained, based on the ideal forming theory, minimizing plastic work. It was demonstrated that the development of advanced constitutive equations plays a significant role for initial blank shape optimization.

In the hot stamping processes, it is difficult to model the material behaviour under non-isothermal and non-proportional loading conditions. The combined influences of change in strain rate, temperature and loading path throughout the hot stamping process occur due to the hot blank being deformed and quenched between cold tools. Moreover, the traditional method of assessing forming quality of the initial blank shape design has focused on the thinning and accuracy of geometry rather than defects. The prediction of thinning is an indirect way to assess the quality of formed components and the prediction of forming limit is more effective in identifying defects of the formed part.

To predict the forming limit of complex-shaped parts under hot stamping conditions, the initial blank shape design in the present study was determined by employing the viscoplastic-

Hosford-MK model. The application and validation of this model to predict the forming limit of a formed demonstrator component is presented in this chapter. This study focuses on determining the formability of an AA7075 formed part using three different initial blank shape designs, with their success in forming predicted using the viscoplastic-Hosford-MK model. The accuracy of the forming limit prediction model was validated through experimentation. Moreover, the optimization of the initial blank shape was achieved by comparing the formability of the formed components with different initial blank shapes. The effect of initial blank shape on the formability under hot stamping conditions is also concluded in this present chapter.

6.1 Experimental tests of AA7075 alloy

6.1.1 Uniaxial tensile test and isothermal forming limit test of AA7075 alloy

The viscoplastic material responses and forming limits of AA7075 alloy over a range of strain rates and temperatures were evaluated by conducting uniaxial tensile tests and isothermal forming limit tests. The uniaxial tensile test was conducted by Mr Kang Ji and isothermal forming limit test was conducted by Mr Xi Luan. For both tests, the 2mm thick AA7075 blanks were supplied by Schuler Pressen GmbH, in the T6 condition (Solution heat treatment, cold worked and artificially aged). The same experimental procedures were used in uniaxial tensile test and isothermal forming limit test, which were fully demonstrated in Chapter 3. The test matrixes for the uniaxial tensile tests and isothermal forming limit tests are shown in Table 6-1 and Table 6-2.

Table 6-1. Test Matrix of uniaxial tensile test on AA7075 alloy

Strain rate \ Temperature (°C)	300	350	400	420
1/s			√	
2/s	√	√	√	√
5/s			√	

Table 6-2. Forming speed and temperatures used in the forming limit tests

Forming speed \ Temperature (°C)	300	400	420
75 mm/s			√
250 mm/s	√	√	√
400 mm/s			√

6.1.2 HFQ^TM forming of AA7075 L-shape component

The proposed viscoplastic-Hosford-MK model was validated using a hot-stamped AA7075 L-shape component. The test-pieces with different initial blank shapes were prepared using laser cutting. Forming trail was conducted at Schuler Pressen GmbH, Goppingen. In the forming process, the furnace was heated to a target temperature of 490°C, and the specimen was subsequently placed into a furnace. After the specimens were soaked at 490 °C in the furnace for 10-15 minutes, the specimen was then transferred to the forming tool and formed at a temperature of approximately 480°C and a forming speed of 250 mm/s.

6.2 Validation of unified viscoplastic-Hosford-MK model

The viscoplastic-Hosford-MK model on AA7075 alloy was first validated using uniaxial tensile test and forming limit tests. Based on uniaxial tensile test results, the viscoplastic constitutive equations were calibrated to the flow stress data obtained at different temperatures and strain rates. From the results of the forming limit tests, the viscoplastic-Hosford-MK model was subsequently calibrated for different temperatures and forming speeds.

6.2.1 Prediction of flow stress at different temperatures and strain rates

By calibrating the viscoplastic material model with experimental flow stress data obtained from uniaxial tensile tests, the optimal material constants for viscoplastic constitutive equations were determined as listed in Table 6-3. The experimental (symbols) and predicted (solid) flow stress curves of AA7075 alloy at temperatures ranging from 350°C to 420°C and at strain rates ranging from 1 to 5s^{-1} are presented in Figure 6-1 and Figure 6-2. In both figures, a good agreement between predicted and experimental results was achieved, with the deviation between experimental and prediction results found to be within 5%.

Table 6-3. Material parameters for AA7075 alloy using viscoplastic material model

K_0 (MPa)	Q_K (J/mol)	k_0 (MPa)	Q_k (J/mol)	B_0 (MPa)	Q_B (J/mol)	C_0	n_2
0.0563	38268.400	0.716	1091.435	6.917	10287.800	64.780	5

Q_C (J/mol)	E_0 (MPa)	Q_E (J/mol)	A_0	Q_A (J/mol)	n_{10}	$Q_{n_{10}}$ (J/mol)	
-16875.948	29584.300	2402.250	125.080	-2501.970	3.408	2382.062	
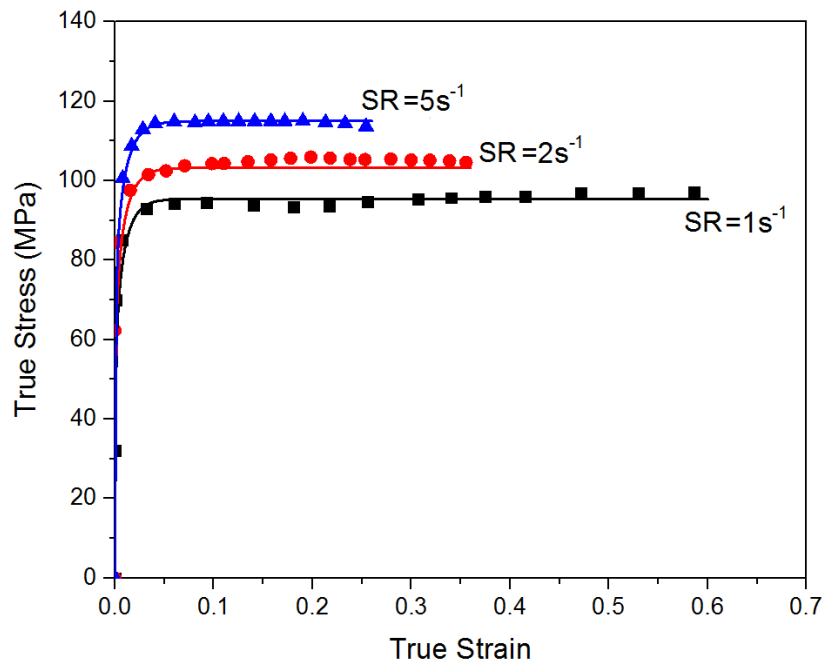
Figure 6-1. Comparison of the predicted (solid curves) and experimental flow stress curves (symbols) for AA7075 alloy with different strain rates at 400°C
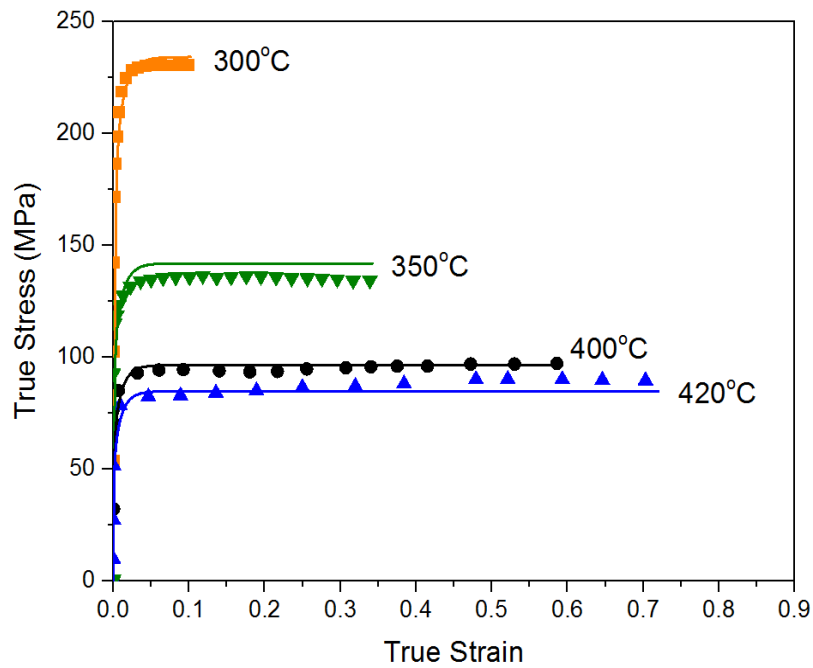
Figure 6-2. Comparison of the predicted (solid curves) and experimental flow stress curves (symbols) for AA7075 alloy at different temperatures with a strain rate of 2s^{-1}

6.2.2 Prediction of forming limit diagram of AA7075 alloy

By calibrating the viscoplastic-Hosford-MK model with the experimental FLDs obtained from forming limit tests at different temperatures and strain rates, each imperfection factor was calibrated. Figure 6-3 and Figure 6-4 show the forming limit diagrams (FLDs) of AA7075 alloy as a function of temperatures and forming speeds. Symbols in Figure 6-3 and Figure 6-4 represent the experimental forming limit curves (FLCs) with different forming temperatures ranging from 300°C to 420°C and forming speeds ranging from 75mm/s to 400mm/s. The corresponding solid curves in both figures represent the prediction of FLCs, in which the numerical results obtained by viscoplastic material model agree well with the experimental results. Based on experimental FLCs over a range of temperatures and strain rates, it was found that the formability of AA7075 alloy increases with increased forming temperature and decreases at higher forming speed.

Small deviations from experimental and simulation results can be found at 75mm/s, 250mm/s and 400mm/s formed at 420°C by equal-biaxial loading. This is mainly due to the presence of unclear localized necking detected from the strain measurement under equal-biaxial tension and poor surface quality. The same issue was also found in AA2060 alloy as mentioned in Chapter 3.
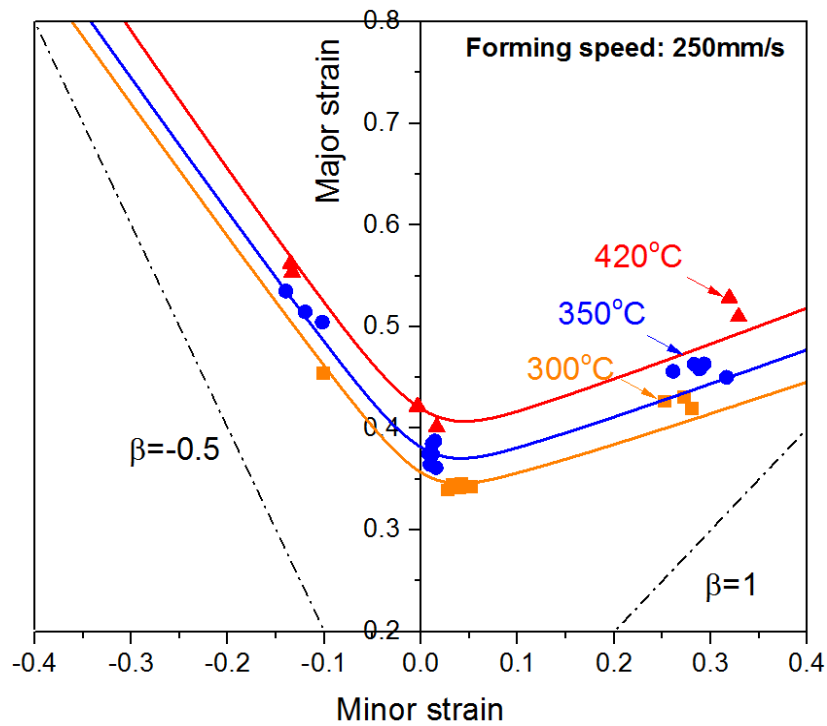
Figure 6-3. Experimental forming limit curves for AA7075 alloy at different temperature with a constant forming speed of 250mm/s
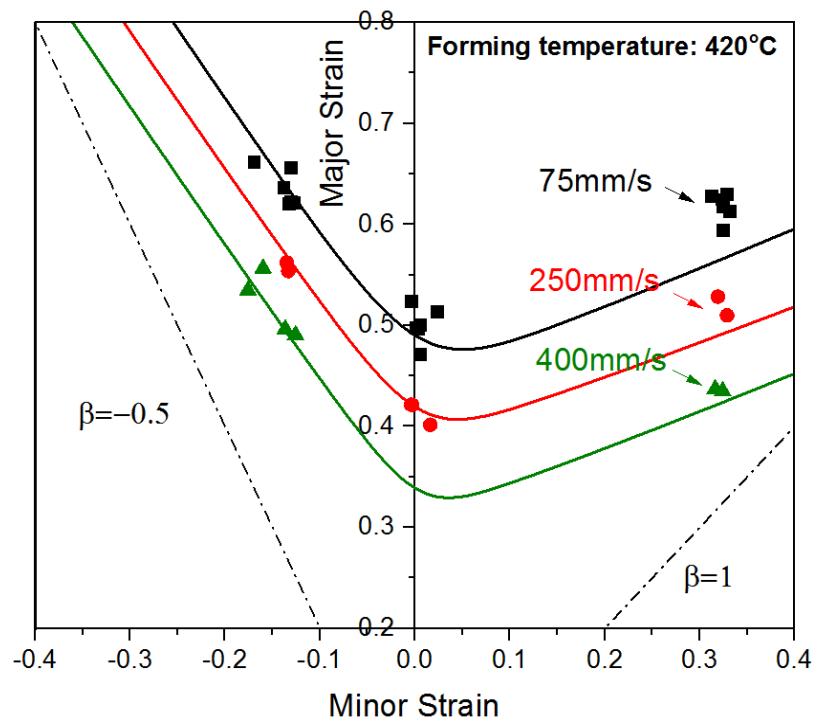
Figure 6-4. Experimental forming limit curves for AA7075 alloy with different forming speeds at a constant temperature of 420°C

6.3 Application of the forming limit prediction for hot stamped L-shape component

Finite element (FE) simulation for the forming of an AA7075 L-shape component under hot stamping conditions was conducted using the sheet forming software PAM-STAMP. Optimisation of the initial blank was achieved by predicting the forming limit of the formed part using viscoplastic-Hosford-MK model and FE PAM-STAMP simulation. In this study, three different initial blank shape designs were demonstrated through trial-and-error simulation procedures. The forming limits of the formed parts were studied and predicted for different initial blank shape designs. The optimal blank shape design lying within the forming limit of the material was selected and produced for experimental forming tests. Finally, the accuracy of the model was verified.

6.3.1 FE simulation setup

The geometries of the tool models and the position of the blank on the die were simulated as the real experimental setup. The FE model set up for the forming tool and blank are shown in Figure 6-5. Apart from assembly of forming tools, the position of blank on the tool is also shown in Figure 6-6. In real forming tests, the AA7075 work-piece was positioned relative to the three positioning pins. In Figure 6-6, the locations of those three pins were indicated by three circle lines.
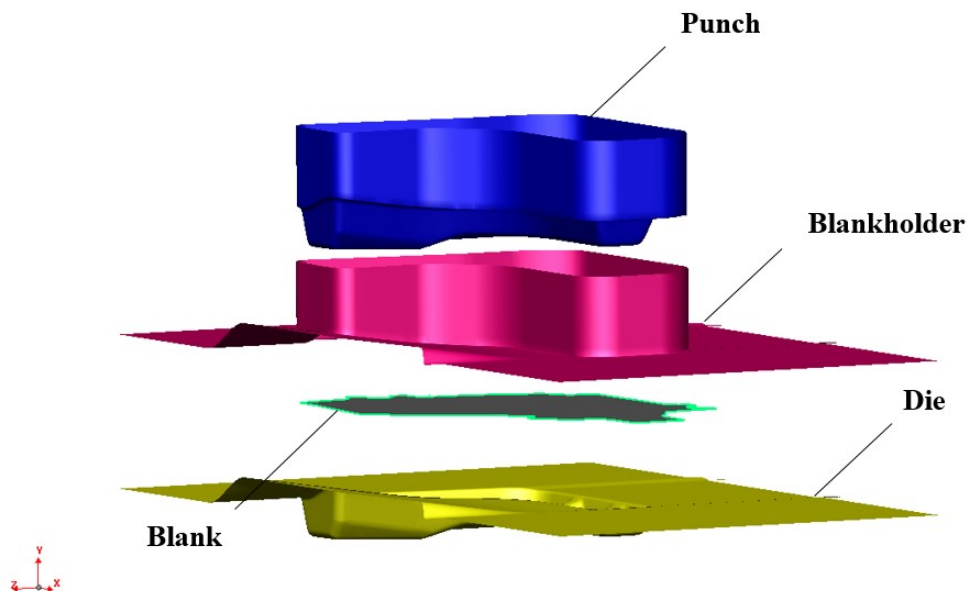
Figure 6-5. Section view of assembled forming tools for forming AA7075 L-shape component
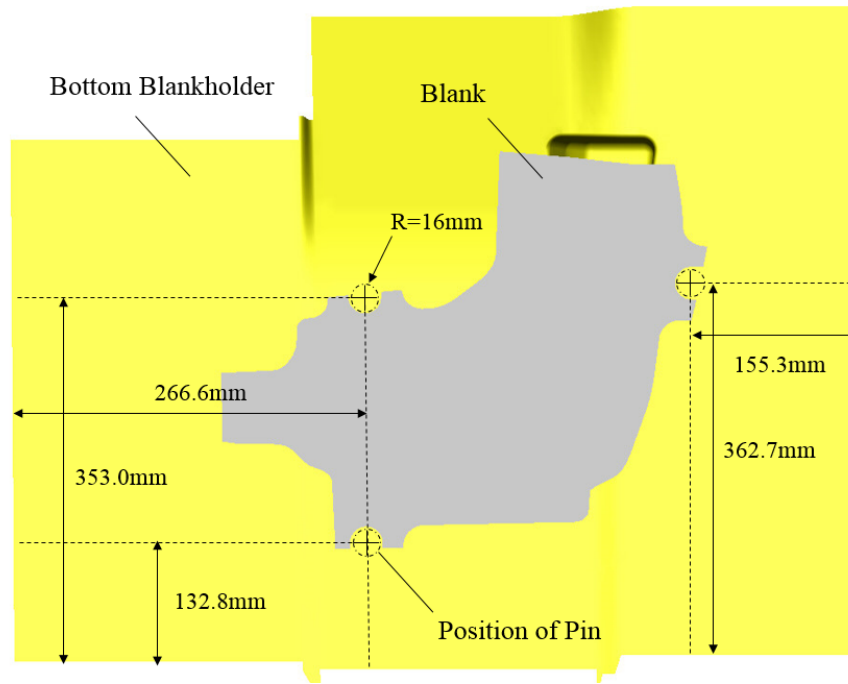
Figure 6-6. Position of blank on the tool (Top view)

In the simulations, the forming tools and blank were meshed using shell element with a mesh size of 2 mm. Punch, blankholder and die tools were implemented as rigid bodies with the material properties of H13 tool steel shown in Table 6-4. In addition to the forming tools, the material properties such as the stress-strain behaviour of AA7075 blank were imported from the viscoplastic-Hosford-MK model.

The FE simulation process was subdivided into three main stages, namely: gravity stage, holding stage and stamping stage. In the "gravity stage", the blank was first positioned on the bottom die with the effect of gravity considered. The blank-holder was subsequently applied and made contact with the blank by applying the blank-holding force in the "holding stage". In the "stamping" stage, the work-piece was formed by activating the punch. The parameters of the stamping FE simulation are shown in Table 6-5.

Table 6-4. Material properties of forming tools in PAM-STAMP simulation

Property	Tool steel
Thermal conductivity (kW/mm K)	20
Specific heat (mJ/tonne K)	6.5×10^8
Density (tonne/mm^3)	7.8×10^{-9}
Poisson's ratio	0.3
Young's modulus (GPa)	210

Table 6-5. Parameters used for forming AA7075 component in PAM-STAMP simulation

Process parameter	Value
Initial blank temperature (°C)	480
Initial tooling temperature (°C)	20
Forming speed (mm/s)	250
Friction coefficient	0.2
Blankholding force (kN)	15
Gas spring stiffness (kN/mm)	1

Table 6-6. Initial blank shape designs

Initial blank shape	Area (mm^2)
Design I	153362.62
Design II	121206.34
Design III	102014.65
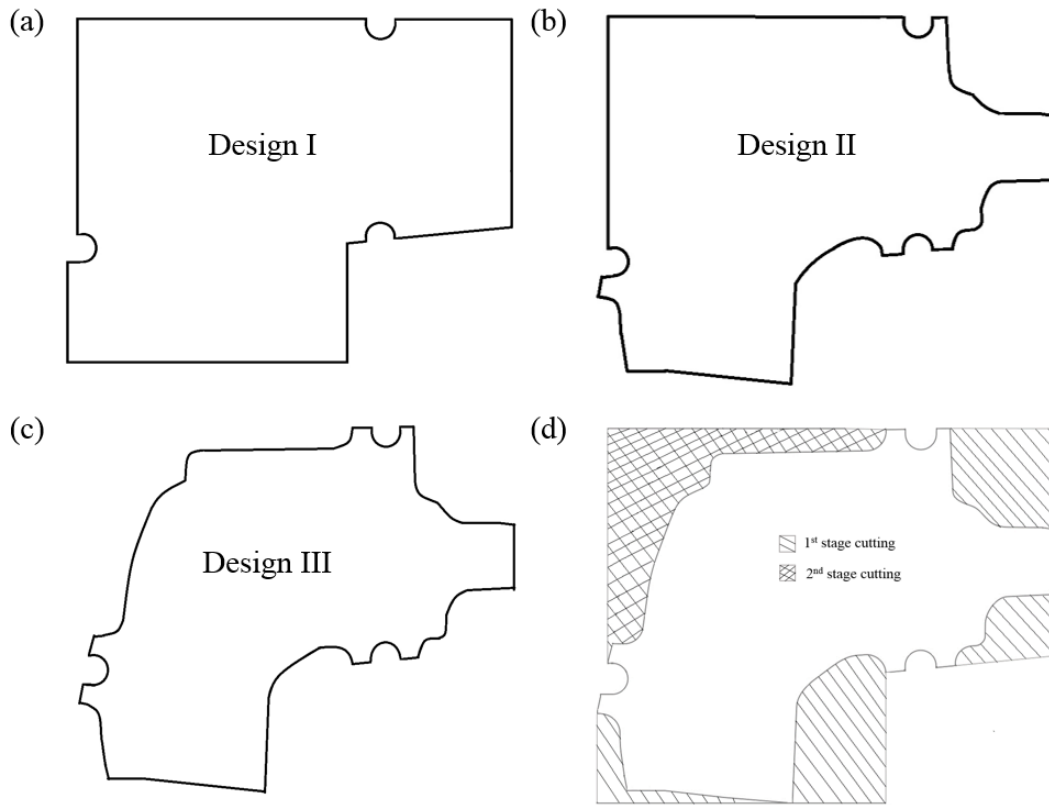
Figure 6-7. Initial blank shape designs a) Design I b) Design II c) Design III d) initial blank shape designs procedures from Design I to Design III
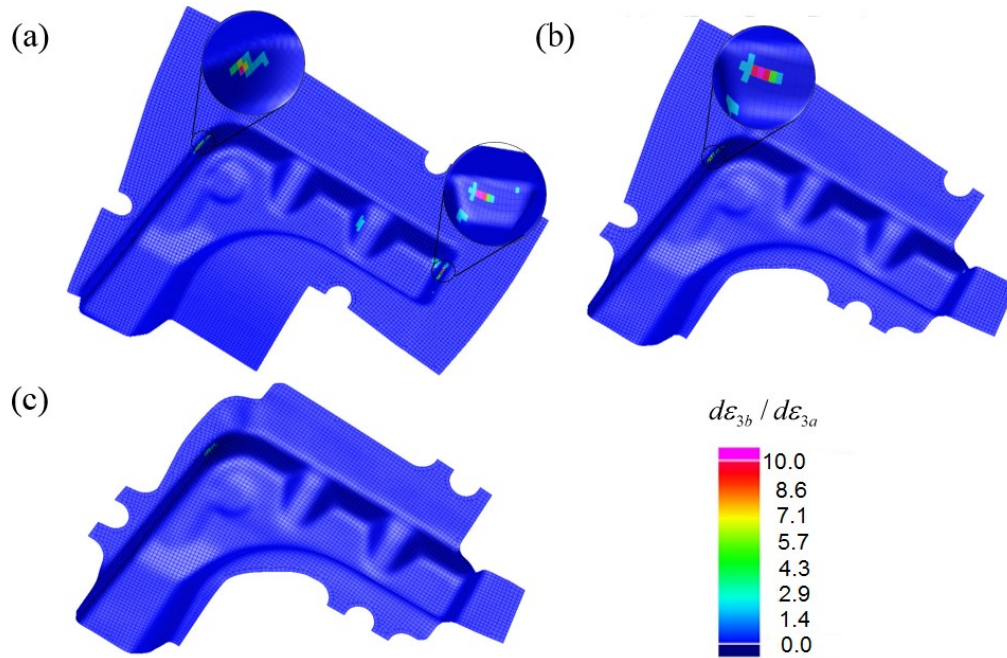
Figure 6-8. Prediction of localised necking of formed part using the developed model with different initial blank shape designs: a) Design I, b) Design II and c) Design III

The trial-and-error simulation method was utilised to achieve the optimisation of initial blank shape for the hot stamping process. With different initial blank shape designs, the forming limits of the formed parts were predicted using the forming limit prediction model. After a series of simulation trials, the optimal blank shape was finally selected using trial-and-error simulation procedures. In this study, three initial blank shape designs were demonstrated to show the optimisation procedure for an initial blank shape using the forming limit prediction model under hot stamping as shown in Figure 6-7. In Figure 6-7(d), the blank shape design III was edited after a two-stage cutting process, where the areas of those cutting phases are indicated by the shaded areas. The blank areas of initial blank shape design I, II, III are identified as listed in Table 6-6. It was evaluated that the usage of material using initial blank shape II and III could save 20.79% and 33.48% in comparison to that using initial blank shape I.

After each FE simulation, the numerical data associated with temperature, strain rate, and loading path from PAM-STAMP were imported into the Viscoplastic-Hosford-MK model. The forming limit predictions of the formed parts with three different initial blank shape designs were made and visualised by PAMSTAMP software as presented in Figure 6-8. In Figure 6-8, it was predicted that the optimal initial blank shape design to form the L-shape component is "Design III" with negligible predicted failure and minimal material usage as shown in Figure 6-8(c). As can be seen for the initial blank shape Designs I and II (Figure 6-8(a) and (b)), the onset of necking was predicted to occur at the side wall of their formed parts as indicated by the enhanced circles.

6.3.2 Accuracy of numerical model

To assess the accuracy of the numerical model, the optimal initial blank shape (Design III) was produced and experimentally tested. Based on practical forming tests, the part was successfully formed without any fracture being evident as shown in Figure 6-9. The forming conditions used were fully consistent with the ones used in FE simulation. The forming temperature (480 ºC), forming speed (250mm/s) and forming stroke (55.89mm) were applied.

Figure 6-9. AA7075 L-shape part with determined optimal blank shape was formed at forming temperature of 480ᵒC and forming speed 250mm/s.

In the forming test, thickness measurements were taken from different locations on the formed part as shown in Figure 6-10. The accuracy of the FE model was made by comparing to the thinning results from the experimental forming tests. A good agreement of thinning results between the simulations and experiments was achieved as shown in Figure 6-11, demonstrating a deviation of less than 5%.
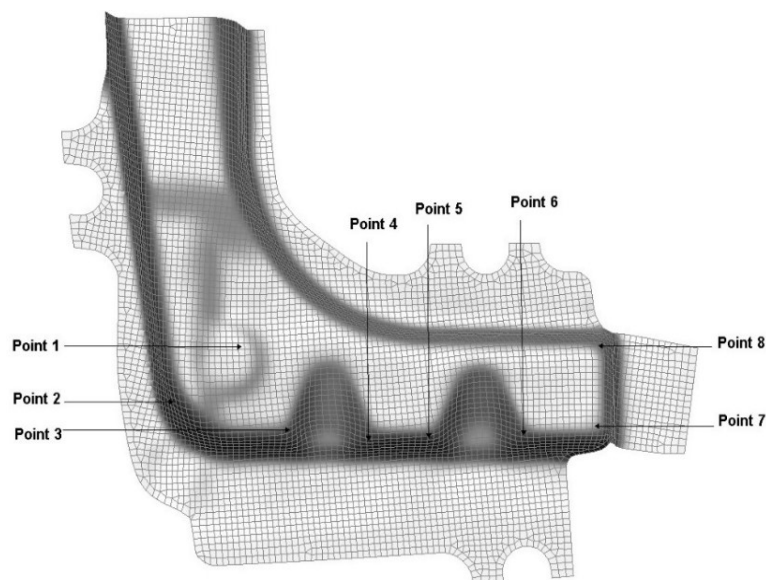
Figure 6-10. Thickness measurement from the selected elements from FE simulation
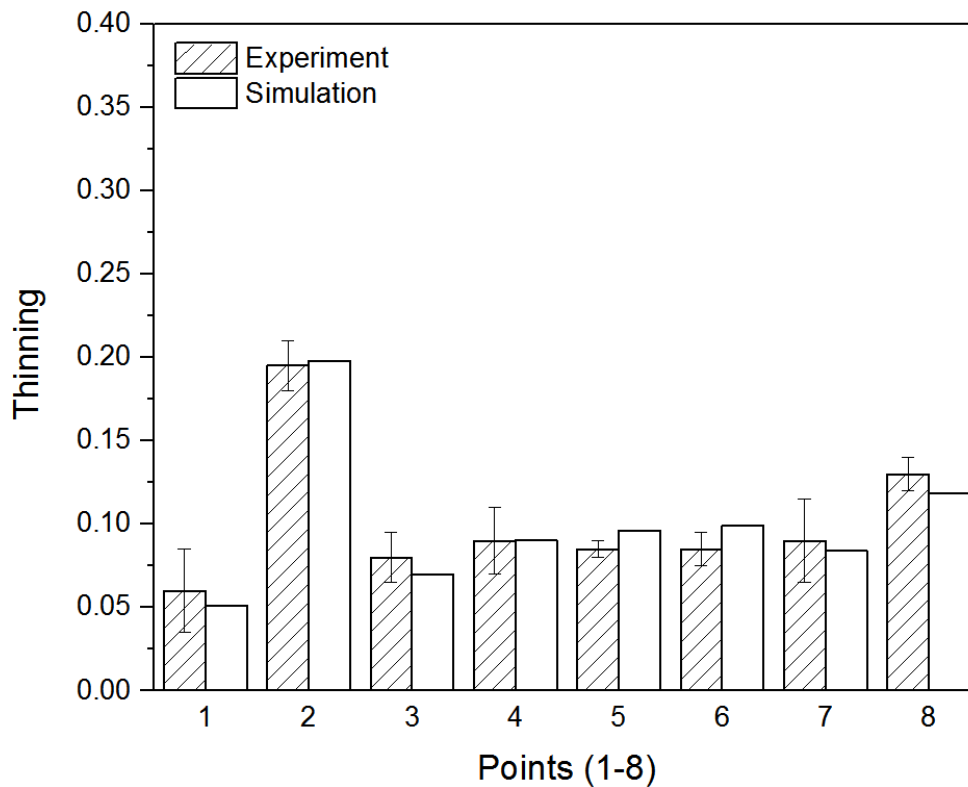
Figure 6-11. Comparison of experimental (shaded bars) and prediction results (clear bars) in thinning from selected elements

In Figure 6-12, the maximum thinning of the formed parts was located at the corner region for all initial blank shape designs, as indicated by the red dashed circle. The localised necking of the formed part was predicted at the side walls in Figure 6-16 and Figure 6-17 rather than the corner regions as expected. This phenomenon can be explained as follows: As the initial blank shape is fixed, the onset of localised necking is strongly affected by combined effects including strain rate, quenching rate and loading path variations under hot stamping conditions. The localised necking might not necessarily occur at the region with the maximum thinning, which can be proved from similar phenomenon occurring from experimental forming tests of a formed wing stiffener component from AA2060, AA6082 and AA5754 under hot stamping conditions as shown in Chapter 5 Appendix 5F. Consequently, the quality of the formed part might not necessarily rely solely on the thinning parameter. Using the advanced material constitutive equations and comprehensive analysis of hot stamping conditions, the optimisation of initial blank shape was obtained by predicting the forming limits of the AA7075 component.
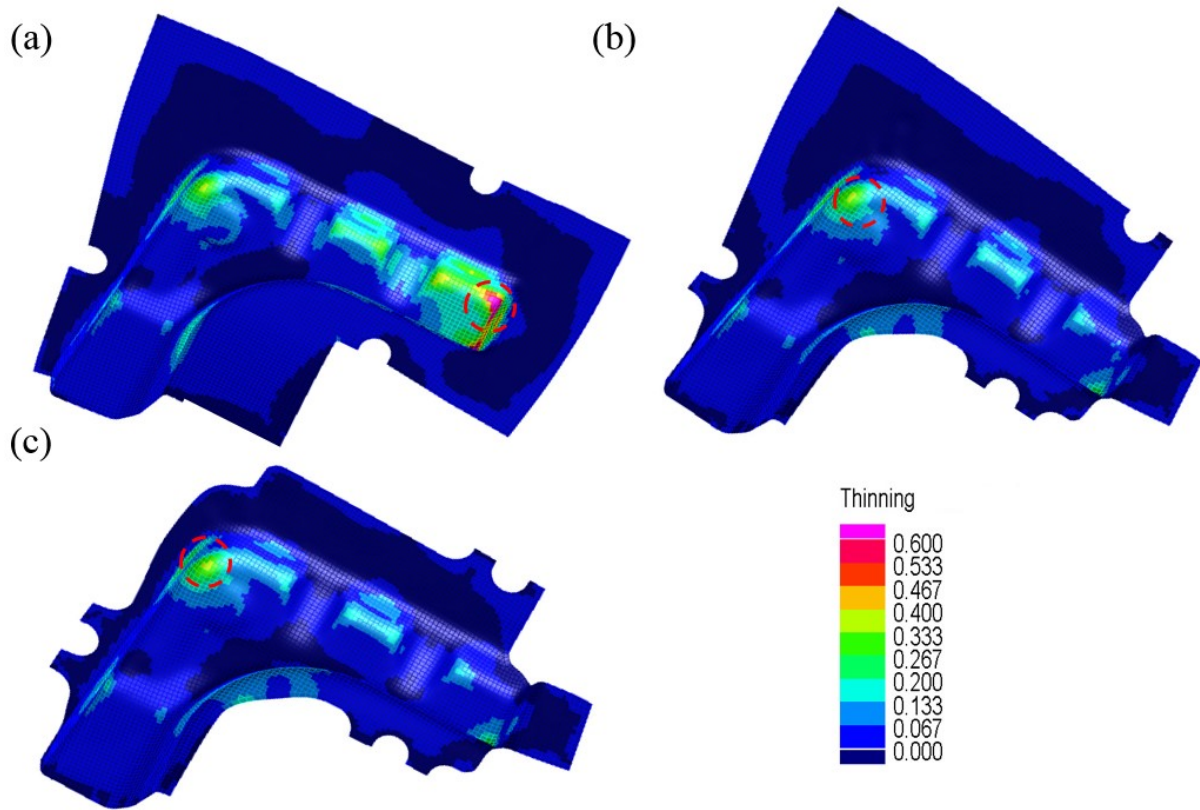
Figure 6-12. Prediction of thinning of formed part using the developed model with different initial blank shape designs: a) Design I b) Design II c) Design III

6.3.3 Effect of initial blank shapes on the forming limit prediction

As shown in Figure 6-8, the formability of formed parts was improved when the initial blank shape was changed from "Design I" to "Design III". Using Pam-stamp software, the "follower lines" were used to describe the drawability of material during the stamping process. In Figure 6-13 and Figure 6-14, blue and red lines were defined as two follower lines in FE simulation. When the forming stroke increased from 29.4mm to 55.89mm, two follower lines were located at different regions, indicating the changes in material flow drawn into the die cavity. Based on Figure 6-8, two specific regions on failure were recognised, which were defined as region A (indicated by the dashed red circle) and region B (indicated by the dashed blue circle) in Figure 6-13 and Figure 6-14. In both regions, three equal-spaced lines were taken which were used to measure the distances between two follower lines. Those distance measurements from region A and region B were used to demonstrate the level of element draw into die cavity with each initial blank shape designs, as listed in Table 6-7 and presented in Figure 6-15. In Figure 6-15, it was found that the average drawing distance of elements generally increases as the initial blank shape changes from design I to III. In hot stamping processes, material flow is strongly influenced by the initial blank shape designs. A larger initial blank design would usually reduce the drawability and thus reduce the overall formability of the blank due to the

following three factors. (1) The blank in the blank holding area undergoes a tensile stress (σ_r) in the radius direction; and a compressive stress (σ_θ) in the hoop direction; σ_r decreases with increasing radial distance from die entrance, whilst σ_θ increases with increasing radius radial distance. Therefore, the larger radial distance from the die entrance would lead to a greater tendency of wrinkling (Zheng *et al.*, 2017). Ironing of the wrinkles (localised thickening) in the blank holding area and the die entrance would inevitably result in a higher resistant force for the blank to be drawn into the die cavity. (2) The localised thickening (tendency of wrinkling) would lead to an increase in contact pressure in such local areas, thus a more pronounced cold die quenching effect (Liu *et al.*, 2017) and lower blank temperature, which could reduce the drawability of the hot blank. (3) In addition, during the forming process, a higher local contact pressure may also lead to the premature breakdown of lubricant (Hu *et al.*, 2017) and direct contacts between the hot aluminium blank and tool steel would cause a higher friction coefficient resulting a decreased drawability. During a hot stamping process, the initial blank shape design plays a dominant role in the formability of the hot blank, due to the fact that the hot blank makes contact with the cold blank holders prior to the start of plastic deformation. Therefore, the resistance to the plastic deformation in this region is extremely sensitive to the initial blank shape design. Consequently, when the size of the initial blank shape was reduced from "Design I" to "Design III", the drawability of material in region B was much higher than material in region A.

Table 6-7. Drawing distance between two identified follower lines from corner and side wall regions

Corner Part	d1	d2	d3	Average
Design I	8.82	7.84	8.45	8.37
Design II	8.66	7.89	8.65	8.40
Design III	8.66	8.23	8.41	8.43
Side Wall	d4	d5	d6	Average
Design I	6.82	7.83	8.26	7.63
Design II	20.20	19.84	19.32	19.78
Design III	21.08	20.66	19.41	20.38
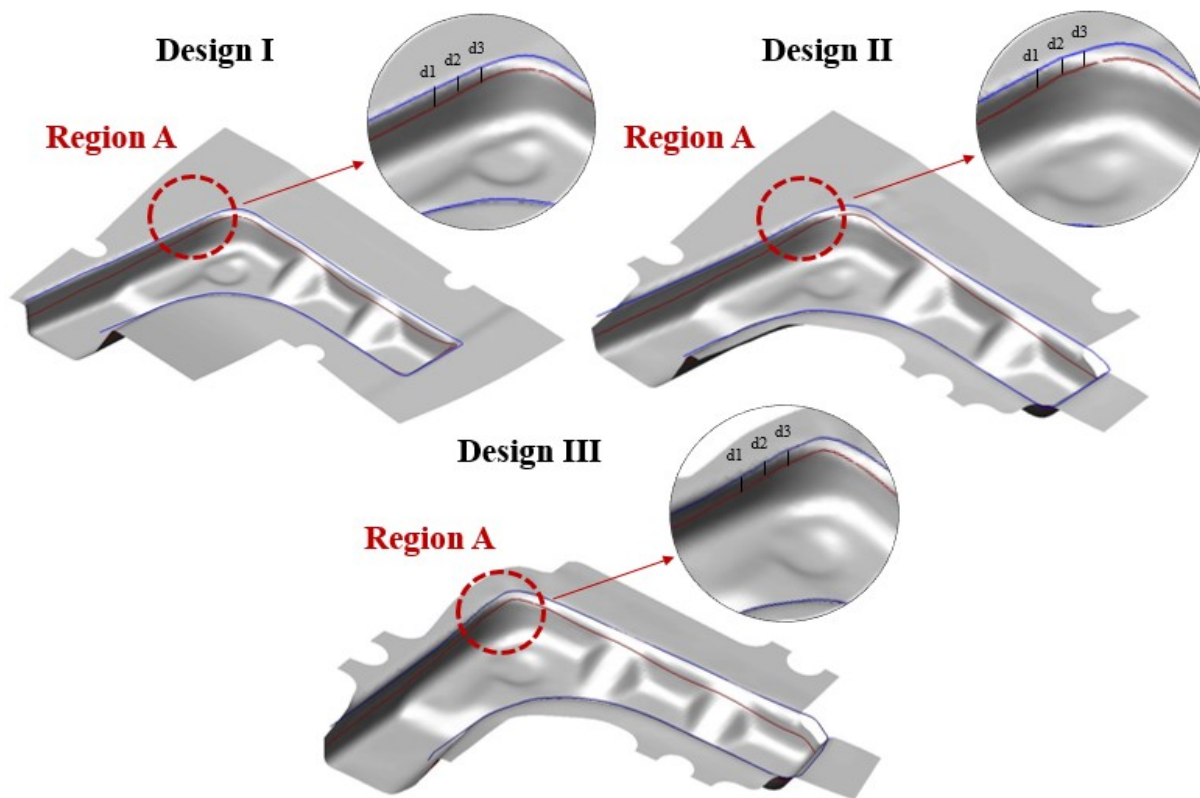
Figure 6-13. Drawability obtained from region A (red dash circle line) with initial blank shape design I, II and III using follower lines from PAM-STAMP simulation
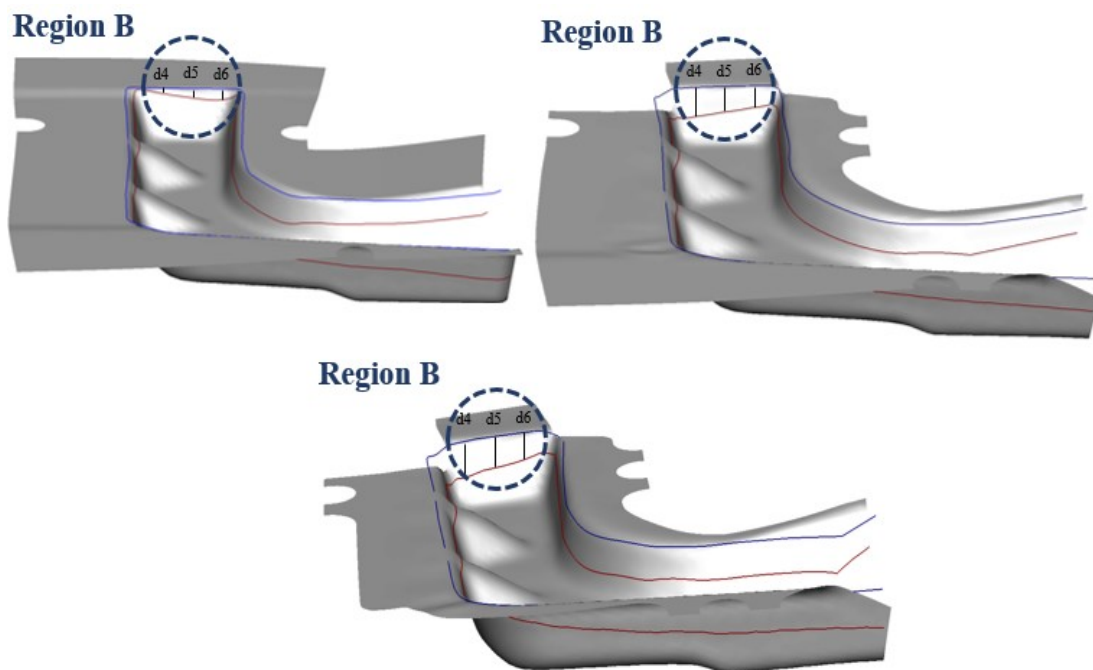
Figure 6-14. Drawability obtained from region B (blue dash circle line) different regions with initial blank shape design I, II and III using follower lines from PAM-STAMP simulation
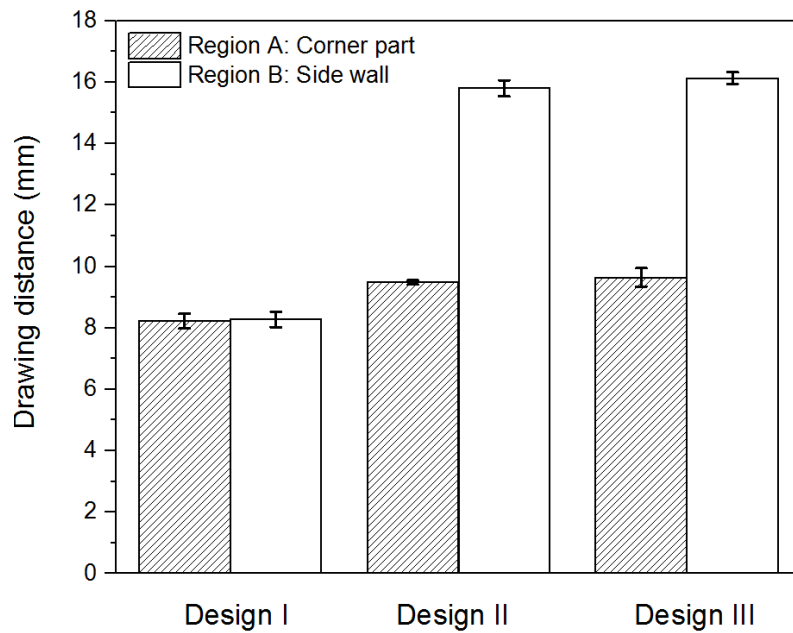
Figure 6-15. Comparison of drawing distances obtained from region A and B with initial blank shape design I, II and III

Therefore, it can be seen from the results that different equivalent plastic strains of deformed parts were obtained, especially at the failure regions. The plastic strain and forming limit of the failure regions were analysed for Designs I and II, with 14 elements selected from "region A" as shown in Figure 6-16. To investigate the effect of initial blank shape on the forming limit, the same regions on the formed part using initial blank shape design II and III were selected, as indicated by "region B", as shown in Figure 6-17. Their equivalent plastic strains and forming limits were analysed as listed in Table 6-8.
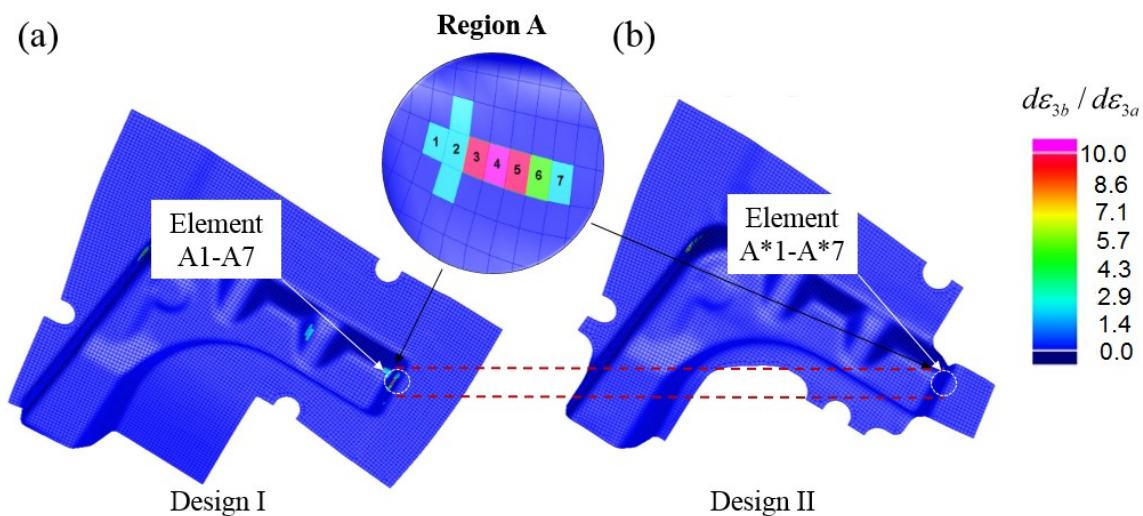
Figure 6-16. Analysis of selected elements from region A using initial blank shape design I and initial blank shape design II
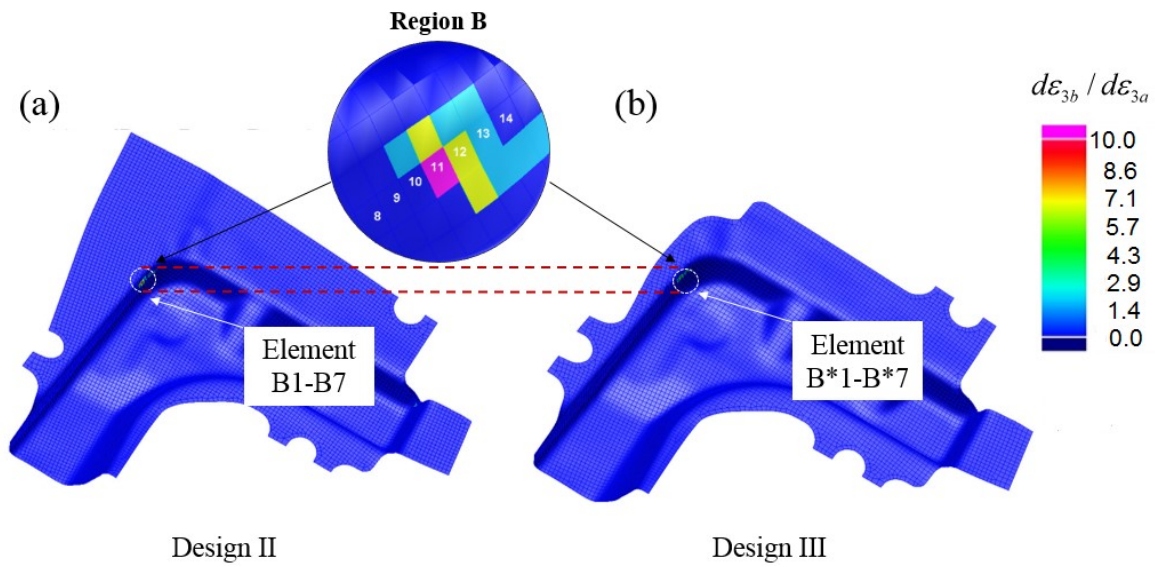
Figure 6-17. Analysis of selected elements from region B using initial blank shape design II and initial blank shape design III

Table 6-8. Comparisons of strain and forming limit with different initial blank shape designs

Comparison 1	Initial blank shape "Design I"	Initial blank shape "Design II"
	Elements A1-7	Elements A*1-7
Comparison 2	Initial blank shape "Design II"	Initial blank shape "Design III"
	Elements B1-7	Elements B*1-7

In Figure 6-18, equivalent strains of Design I elements (A1-7) were generally much larger than the ones from Design II (A*1- A*7). It was found that the onset of necking did not occur at the element located on the "corner region" with maximum plastic straining. It occurred at element A4 with equivalent strain of 0.457. In comparison to element A*4 (same position), the $d\varepsilon_{3b}/d\varepsilon_{3a}$ of element A*4 was zero with equivalent strain of 0.101, indicating good formability due to large strain reduction. Consequently, as the initial blank shape changed from Design I to Design II with removal of material due to the 1st cutting stage (Figure 6-7), the equivalent strain at A4 was largely reduced by 78%, the formability was enhanced due to reduction of strain, which finally reduce strain localisation at region A.
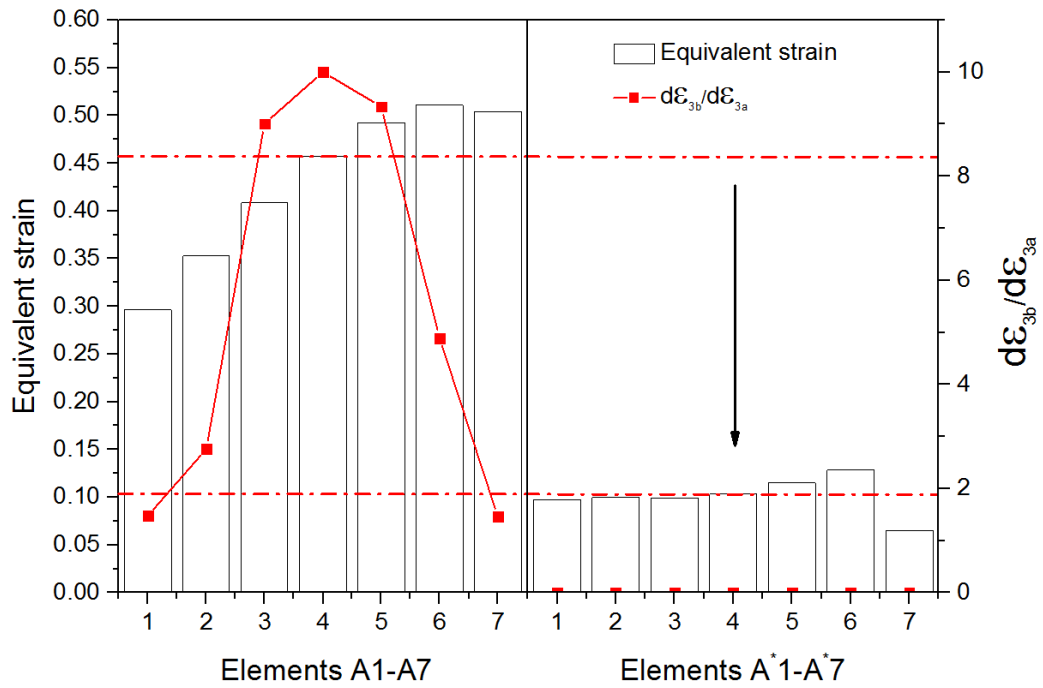
Figure 6-18. Equivalent strain and development of a neck ($d\varepsilon_{3b}/d\varepsilon_{3a}$) for element: (a) A1-A7 and (b) A*1-7 shown in Figure 6-16
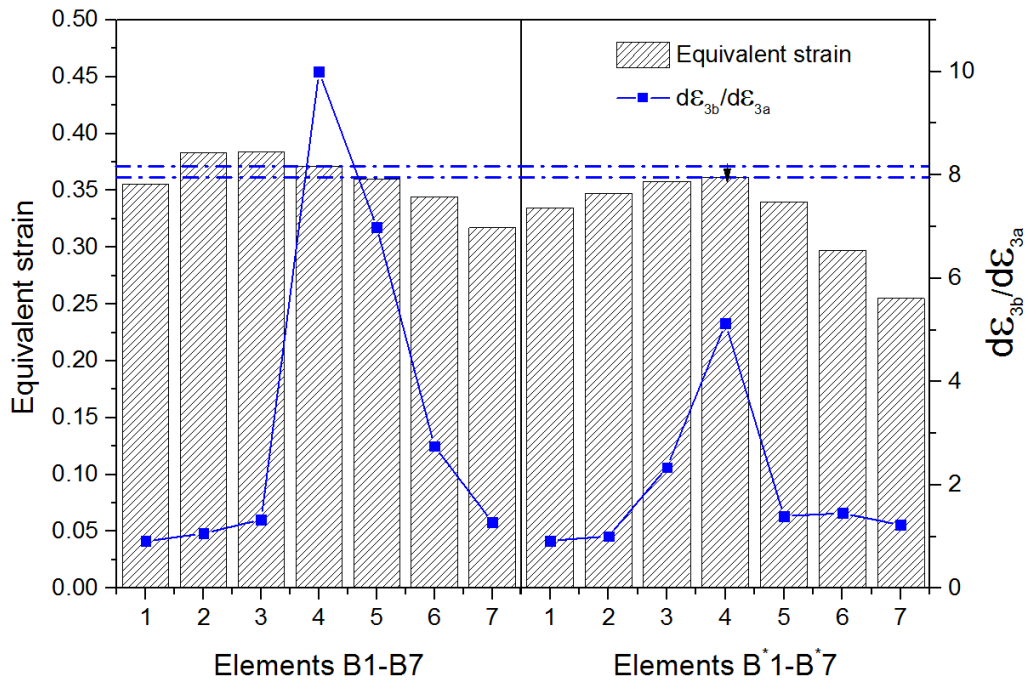
Figure 6-19. Equivalent strain and development of a neck ($d\varepsilon_{3b}/d\varepsilon_{3a}$) for element: (a) B1-7 and (b) B*1-7 shown in Figure 6-17

In Figure 6-19, a slight difference (2%) in equivalent strains between elements B1-7 and B*1-7 was obtained when the initial blank shape was changed from Design II to Design III. The onset of necking was found at element B4 with equivalent strain of 0.372. In comparison to element B*4, the equivalent strain of B4 was almost at the similar straining level, with a deviation of 3% due to removal of material from the 2nd cutting stage. In this case, for elements B1-7 and B*1-7, equivalent strains of those elements were identified to be high and slight differences were found in equivalent strain. However, the formability at the elements from B*1-7 were much higher than the elements from B1-7 after the 2nd stage cutting stage.

In Figure 6-18 and Figure 6-19, the onset of necking occurred at A4 and B4, while good formability was identified at A*4 and B*4, respectively. For elements A4 and A*4, the strain hardening and strain rate hardening of both elements were different. Based on research work from Yoshida (Yoshida et al., 2014), it was found that work hardening behaviour played an important role on the formability of the part. Many factors could affect the work hardening behaviour under hot stamping conditions including variations of temperature, forming speeds and loading paths. The variation of temperature, strain rate and loading path were influenced by the variation of initial blank shape. The evolutions of element A4, A*4, B4 and B*4 in temperature, strain rate and loading path were demonstrated in Figure 6-20 and Figure 6-21.

The development of the neck at A4 and A*4 are plotted in Figure 6-20(a). The onset of necking was induced from the combined effects of changes in strain rate, temperature and loading path. In Figure 6-20, the differences in evolutions of temperature, strain rate and loading path between A4 and B4 were compared. It has been deduced that: the histories of temperature at A4 were similar with the ones at B4, the differences in temperature for both elements in each increment was quite small in comparison to strain rate and loading paths. In Figure 6-20(b), much larger strain rate was obtained at A4 after t=0.12s, resulting in much larger equivalent strain. Thus, the strain and strain rate hardening of A4 was much higher than B4, accelerating the strain localisation at A4. In Figure 6-20(d), different types of loading path for both elements were found from different initial blank shape. In terms of β values, much larger changes occur at A4 than B4. Based on the strain-path dependent viscoplastic-Hosford-MK model, the effect of different loading path on the formability were evaluated.
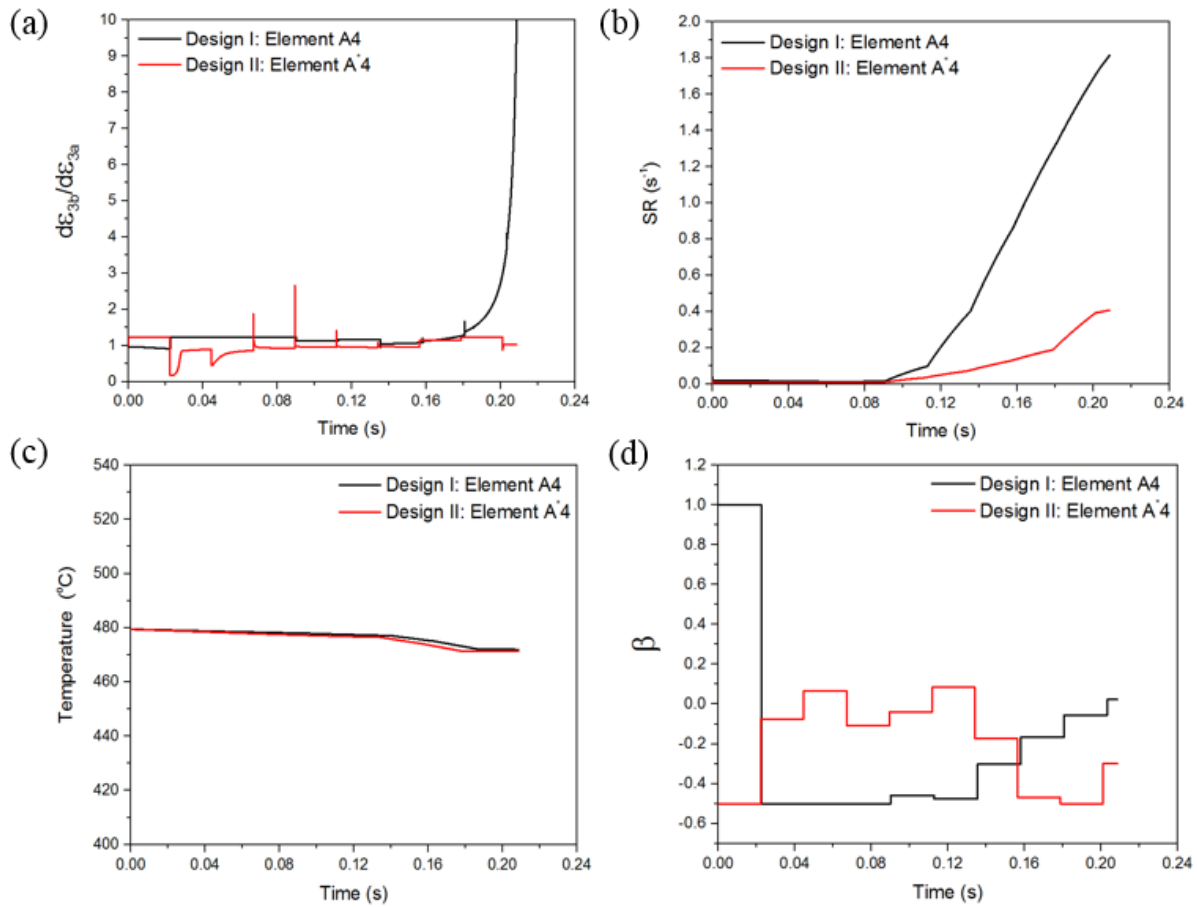
Figure 6-20. Comparison of development of necks against time for selected elements (Design I: A4, Design II: A*4) with blank design I and II. The comparison of the corresponding histories of (a) loading path against time (b) strain rates against time of (c) temperature against time (d) loading path against time of selected elements

The development of a neck, histories of strain rate, temperature, loading path for element B4 and B*4 were plotted in Figure 6-21. The evolutions of strain rate and temperature between both elements were similar as shown in Figure 6-21(b) and Figure 6-21(c). Large differences were found at their loading paths. In Figure 6-21(d), different loading path were found at the beginning of deformation. The near plane strain loading path was applied at B4, while the uniaxial loading path was applied at B*4. Using the viscoplastic-Hosford-MK model, the near plane straining at the beginning lead to the strain localisation occurring earlier than that of uniaxial loading path.
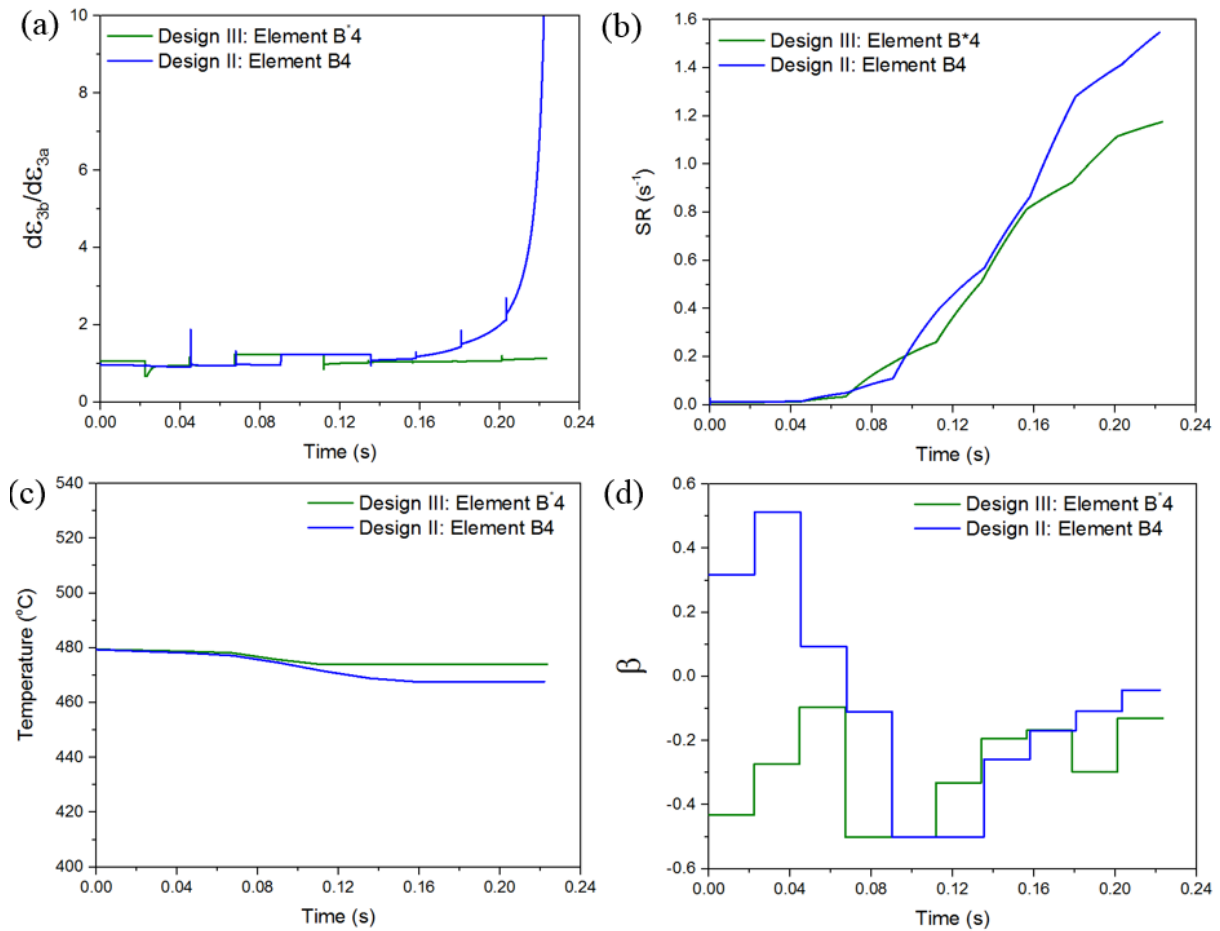
Figure 6-21. Comparison of development of necks against time for selected elements (Design II: B4, Design III: B*4) with blank design II and III. The comparison of the corresponding histories of (a) loading path against time (b) strain rates against time of (c) temperature against time (d) loading path against time of selected elements

Although the thinning was a significant parameter that can assess the quality of a formed part, the forming limit prediction did not fully rely only on thinning, especially under complex forming conditions, such as hot stamping conditions. Due to changes of initial blank shapes, different drawability of material could influence the uniformity of thinning and have a great effect on variation of loading path, strain rate and temperatures. Those effects involving the histories of temperature, strain rate, loading might finally lead to the onset of a neck on the formed part.

6.4 Conclusion

The forming limit prediction for the hot stamping of an AA7075 L-shape component was successfully made using the developed viscoplastic-Hosford-MK model with different initial blank shape designs. It was found that for the formed component, Design III exhibited negligible predicted failure and minimal material usage. Moreover, in contrast to expectations, the localised necking of the formed component was predicted to occur at the side walls rather than the corner regions. Additionally, the determination of optimal initial blank shape design is a function of the influences of changes in strain rate, temperature and loading path and the numerical prediction of these effects enables the accurate determination of the onset of necking in a formed component. Finally, based on the results of the study, it is determined that the prediction of part quality should not only focus on thinning as is currently performed in simulation studies, and should also incorporate failure limit criteria.

<div align="right">

Chapter 7

</div>

Final conclusions and future work

7.1 Conclusions

In this research project, the HFQ forming and modelling of AA2060 and AA7075 alloys were studied and a forming limit model (viscoplastic-Hosford-MK model) was developed to predict the onset of necking for AA2060 and AA7075 alloys. It was concluded that HFQ forming technology shows good feasibility to enable the forming of complex-shape AA2060 and AA7075 components without necking or fracture. The forming limit predictions for hot stamping of AA2060 and AA7075 alloys were successfully made using the developed viscoplastic-Hosford-MK model. The onset of necking under complex loading conditions is mainly due to the combined influences of changes in temperature, strain rate and loading path changes, which are typical intrinsic features of hot stamping processes.

The key findings from the project are summarised below:

(1) The optimum forming temperature for AA2060 material is 450-470°C at strain rates of 1/s. However, poor ductility was found at the temperature which is above the solution heat treatment temperature of AA2060 (520°C). This was proven with tensile tests and forming tests. It has been concluded that a AA2060 wing stiffener component was successfully formed without any failure or necking using forming temperatures from 450 to 470°C.

(2) The age hardening behaviour of AA2060 is heavily influenced by temperature, heat treatment time and multi-stage heat treatment such as two-stage aging. Artificial aging using a one-stage process at an aging temperature of 170°C and aging time of 19.5 hours gave a peak hardness of 161.5HV, which is 97% of the full mechanical strength of the as-received material. The two-stage artificial aging route (First-stage aging: 170°C, second-stage aging: 190°C) was found to be the most effective as 97% of the full mechanical strength of AA2060-T6 was maintained with the total artificial aging time reduced by 65% to 7 hours.

(3) FE simulations were conducted using PAMSTAMP-FE commercial software to replicate the HFQ forming of the wing stiffener component. This enabled a forming limit study to be conducted and verified by comparing the material thinning results to experimental forming tests. As expected, significant thinning was found to occur at the corner regions. The corresponding forming conditions of the thinned areas were studied via simulation by analysing the histories of temperature, strain rate and loading path throughout the forming process. It was concluded that a new forming limit prediction model is required to enable the effects of change in strain rate, temperature and loading path to be modelled in detail as these complex features could not be replicated with existing models.

(4) A new model, named the visocoplastic-Hosford-MK model was developed and used to successfully predict the forming limit of a hot-stamped AA2060 wing stiffener component. The model enables the prediction of necking for non-isothermal and non-linear loading conditions such as complex forming conditions involving changes in strain rate, temperature and loading path. The location of the failure regions in the AA2060 wing stiffener component was accurately predicted, showing good agreement with results obtained from experimental forming tests. It was concluded that the position of the onset of the neck does not necessarily coincide with the region of maximum thinning. Additionally, two significant features of the developed model were found: accurate model responses could be obtained when forming parameters were varied, such as the forming temperature, strain rate and loading path. Particularly, the instantaneous change of strain rate, quenching rate and loading path could be captured. Furthermore, the incremental work per unit volume ratio plays a dominant role in the prediction of necking in the developed model, and the temperature, strain rate and loading path all have great effects on the hardening behavior of the materials.

(5) To demonstrate the versatility of the developed viscoplastic-Hosford-MK model, the forming prediction was made for an L-shape geometry component manufactured from AA7075 alloys. Different blank design interactions were studied with the model and it was found once again that localised necking of the formed component was predicted to occur at the side walls rather than the corner regions as expected. Based on the location of these necking sites and their dependence on changes in strain rate, temperature and loading path, as predicted by the model, a new blank design (Design III) was determined that exhibited

no predicted failure and a reduction in material usage by 33.5% in comparison of initial blank shape design I. It was concluded that the prediction of failure should not only focus on thinning, as is currently performed in simulation studies of forming processes, but should also incorporate a failure limit criterion.

7.2 Future work

Since the forming limit predictions of AA2060 and AA7075 under HFQ forming conditions were studied, the future work may focus on two major tasks. 1) Prediction of post-form strength of AA2060 and AA7075 under HFQ forming conditions. HFQ forming is a non-isothermal forming process involving solution heat treatment, in-die quenching and artificial aging. In order to predict the final strength of HFQ-formed components, the strengthening mechanisms of AA2060 and AA7075 need to be studied. Knowledge of the precipitation hardening sequence during the heating process would be insufficient. To identify the formed precipitates during the HFQ forming process, microstructural investigation of AA2060 and AA7075 will be required, such as conducting Scanning Electron Microscopy (SEM) or Transmission electron microscopy (TEM) tests. 2) Prediction of friction coefficient during the forming of AA2060 and AA7075 under HFQ conditions. In hot forming process, the friction between die and blank depends on the contact pressure and sliding speed. In traditional FE simulations, the coefficient of friction is input as a constant value. A model associating friction with the effects of contact pressure and sliding speed are necessary to improve the accuracy of the forming limit prediction model.

References

Abedrabbo, N., Pourboghrat, F. and Carsley, J. (2006a) 'Forming of aluminium alloys at elevated temperatures - Part 1: Material characterization', *International Journal of Plasticity*, 22(2), pp. 314–341. doi: 10.1016/j.ijplas.2005.03.005.

Abedrabbo, N., Pourboghrat, F. and Carsley, J. (2006b) 'Forming of aluminium alloys at elevated temperatures - Part 2: Numerical modeling and experimental verification', *International Journal of Plasticity*, 22(2), pp. 342–373. doi: 10.1016/j.ijplas.2005.03.006.

Abedrabbo, N., Pourboghrat, F. and Carsley, J. (2007) 'Forming of AA5182-O and AA5754-O at elevated temperatures using coupled thermo-mechanical finite element models', *International Journal of Plasticity*, 23(5), pp. 841–875. doi: 10.1016/j.ijplas.2006.10.005.

Abovyan, T. *et al.* (2014) 'Formability prediction of aluminium sheet alloys under isothermal forming conditions', *Journal of Manufacturing Processes*. The Society of Manufacturing Engineers, 20, pp. 406–413. doi: 10.1016/j.jmapro.2014.08.003.

Adeeb, S. (2017) *Introduction to Solid Mechanics & Finite Element Analysis*. Available at: http://sameradeeb.srv.ualberta.ca (Accessed: 25 April 2017).

Allwood, J. M. and Shouler, D. R. (2009) 'Generalised forming limit diagrams showing increased forming limits with non-planar stress states', *International Journal of Plasticity*. Elsevier Ltd, 25(7), pp. 1207–1230. doi: 10.1016/j.ijplas.2008.11.001.

Ashby, M. F. (2006) *Engineering Materials 2: An Introduction to Microstructures, Processing and Design*. Oxford: Elsevier Butteworth-Heinemann.

Azaouzi, M., Belouettar, S. and Rauchs, G. (2011) 'A numerical method for the optimal blank shape design', *Materials and Design*. Elsevier Ltd, 32(2), pp. 756–765. doi: 10.1016/j.matdes.2010.07.027.

Balmuth, E. S. and Schmidt, R. (1980) *A perspective on the development of aluminium-lithium alloys*. Edited by S. Jr.

Banabic, D. (2010) 'A review on recent developments of Marciniak-Kuczynski model', *Computer Methods in Materials Science*, 10(1952), pp. 1–24. Available at: http://comod.utcluj.ro/documents/articles/Banabic_CMMS 2010.pdf.

Banabic, D. (2010) *Sheet Metal Forming Processes*, *Springer*. Berlin: Springer Berlin Heidelberg. doi: 10.1007/978-3-540-88113-1.

Barata, .R. A., Barlat, F., & and Jalinier, J. M. (1985) 'Prediction of the forming limit diagrams of anisotropic sheets in linear and non-linear loading', *Materials Science and Engineering*, 68(2), pp. 151–164. doi: 10.1016/0025-5416(85)90404-5.

Barlat, F., Aretz, H., Yoon, J.W., Karabin, M.E., Brem, J.C., Dick, R. E. (2005) 'Linear transfomation-based anisotropic yield functions', *International journal of plasticity*, 21(5), pp. 1009–1039.

Barlat, F., Brem, J. C., Yoon, J. W., Chung, K., Dick, R. E., Lege, D. J., Pourboghrat, F., Choi, S. H., Chu, E. (2003) 'Plane stress yield function for aluminum alloy sheets - Part 1: Theory', *International Journal of Plasticity*, 19(9), pp. 1297–1319. doi: 10.1016/S0749-6419(02)00019-0.

Barlat, F., Lian, K. (1989) 'Plastic behavior and stretchability of sheet metals. Part I: A yield function for orthotropic sheets under plane stress conditions', *International Journal of Plasticity*, 5(1), pp. 51–66. doi: 10.1016/0749-6419(89)90019-3.

Barlat, F. *et al.* (1997) 'Yield function development for aluminum alloy sheets', *Journal of the Mechanics and Physics of Solids*, 45(11–12), pp. 1727–1763. doi: 10.1016/S0022-5096(97)00034-3.

Barlat, F. *et al.* (1997) 'Yielding description for solution strengthened aluminum alloys', *International Journal of Plasticity*, 13(4), pp. 385–401. doi: http://dx.doi.org/10.1016/S0749-6419(97)80005-8.

Barnes, A. J. (2007) 'Superplastic Forming 40 Years and Still Growing', *Journal of Materials Engineering and Performance*, 16(4), pp. 440–454. doi: 10.1007/s11665-007-9076-5.

Battelle Memorial Institute (2012) *Metallic Materials Properties Development and Standardization (MMPDS)*. Columbus, OH.

Bishop, J. F. W., Hill, R. (1951) 'Philosophical Magazine', pp. 414–427 & 1298–1307.

Bressan, J. D. and Williams, J. A. (1983) 'The use of a shear instability criterion to predict local necking in sheet metal deformation', *International Journal of Mechanical Sciences*, 25(3), pp. 155–168. doi: 10.1016/0020-7403(83)90089-9.

Brünig, M. and Gerke, S. (2011) 'Simulation of damage evolution in ductile metals undergoing dynamic loading conditions', *International Journal of Plasticity*, 27(10), pp. 1598–1617. doi: 10.1016/j.ijplas.2011.02.003.

Campbell, F. C. (2006) *Manufacturing technology for aerospace structural materials*. Amsterdam: Elsevier.

Cao, J., Yao, H., Karafillis, A., Boyce, M. C. (2000) 'Prediction of localized thinning in sheet metal using a general anisotropic yield criterion', *International journal of plasticity*, 16(9), pp. 1105–1129. doi: 10.1016/S0749-6419(99)00091-1.

Cazacu, O. and Barlat, F. (2001) 'Generalization of drucker's yield criterion to orthotropy', *Mathematics and Mechanics of Solids*, pp. 613–630. doi: 10.1177/108128650100600603.

Chaboche, J. L. (2008) 'A review of some plasticity and viscoplasticity constitutive theories', *International Journal of Plasticity*, 24(10), pp. 1642–1693. doi: 10.1016/j.ijplas.2008.03.009.

Chen, X. and Sowerby, R. (1992) 'The development of ideal blank shapes by the method of plane stress characteristics', *International Journal of Mechanical Sciences*, 34(2), pp. 159–166.

Cheong, B.H., Lin, J., Ball, A. A. (2000) 'Modelling of the hardening characteristics for superplastic materials', *The Journal of Strain Analysis for Engineering Design*, 35(3), pp. 149–157. doi: 10.1243/0309324001514314.

Chiba, R., Takeuchi, H., Mitsutoshi, K., Tomoyuki, H., Toshihiko, K. (2013) 'Theoretical and experimental study of forming-limit strain of half-hard AA1100 aluminium alloy sheet', *Computational Materials Science*. Elsevier B.V., 77, pp. 61–71. doi: 10.1016/j.commatsci.2013.04.025.

Davis, J. R. (2004) 'Tensile testing', in *Tensile testing*. 2nd edn, p. 131. Available at: http://www.books24x7.com/marc.asp?bookid=42684.

Denzer, D.K., Rioja, R.J., Bray, G.H., Venema, G.B., Colvin, E. L. (2012) 'The evolution of plate and extruded products with high strength and toughness', in Weiland, H., Rollette, A.D., Cassada, W. A. (ed.) *Proceedings of the 13th International Conference on Aluminium alloys (ICAA13)*. The Minerals, Metals and Materials Society (TMS) and John Wiley & Sons, pp. 587–592.

Dilmec, M. *et al.* (2013) 'Effects of sheet thickness and anisotropy on forming limit curves of AA2024-T4', *International Journal of Advanced Manufacturing Technology*, 67(9–12), pp. 2689–2700. doi: 10.1007/s00170-012-4684-0.

Dorward, R. C. and Pritchett, T. R. (1988) 'Advanced Aluminium Alloys for Aircraft and Aerospace Applications', 9(2), pp. 63–69.

Dursun, T. and Soutis, C. (2014) 'Recent developments in advanced aircraft aluminium

alloys', *Materials and Design*. Elsevier Ltd, 56, pp. 862–871. doi: 10.1016/j.matdes.2013.12.002.

Emani, S.V., Benedyk, J., Nash, P., Chen, D. (2009) 'Double aging and thermomechanical heat treatment of AA7075 aluminum alloy extrusions', *Journal of Materials Science*, 44(23), pp. 6384–6391. doi: 10.1007/s10853-009-3879-8.

ESI (2015) *PAM-STAMP SIMULATION*. Available at: https://www.esi-group.com/software-solutions/virtual-manufacturing/sheet-metal-forming/pam-stamp-stamping-simulation-solution.

Eyckens, P., Van Bael, A., Van Houtte, P. (2011) 'An extended Marciniak-Kuczynski model for anisotropic sheet subjected to monotonic strain paths with through-thickness shear', *International Journal of Plasticity*, 27(10), pp. 1577–1597. doi: 10.1016/j.ijplas.2011.03.008.

El Fakir, O., Wang, L., *et al.* (2014) 'Numerical study of the solution heat treatment, forming, and in-die quenching (HFQ) process on AA5754', *International Journal of Machine Tools and Manufacture*. Elsevier, 87, pp. 39–48. doi: 10.1016/j.ijmachtools.2014.07.008.

El Fakir, O., Wang, L., *et al.* (2014) 'Predicting Effect of Temperature, Strain Rate and Strain Path Changes on Forming Limit of Lightweight Sheet Metal Alloys', *Procedia Engineering*. Elsevier B.V., 81(October), pp. 736–741. doi: 10.1016/j.proeng.2014.10.069.

El Fakir, O. (2015) *Studies on the solution heat treatment, forming and in-die quenching process in the production of light weight alloy components*. Imperial College London.

El Fakir O, Wang L, Balint D, Dear, J. (2014) 'Solution Heat Treatment, Forming and In-Die Quenching of a Commercial Sheet Magnesium Alloy into a Complex-Shaped Component: Experimentation and FE Simulation', *Key Engineering Materials*, 622–623, pp. 596–602.

Fazli, A. and Arezoo, B. (2012) 'A comparison of numerical iteration based algorithms in blank optimization', *Finite Elements in Analysis and Design*. Elsevier, 50, pp. 207–216. doi: 10.1016/j.finel.2011.09.011.

Friedman, P. A. and Pan, J. (2000) 'Effects of plastic anisotropy and yield criteria on prediction of forming limit curves', *International Journal of Mechanical Sciences*, 42(1), pp. 29–48. doi: 10.1016/S0020-7403(98)00114-3.

Gao, H. *et al.* (2014) 'Determination of a set of constitutive equations for an Al -Li alloy at SPF conditions', *Materialstoday*, 0.

Gao, H. *et al.* (2016) 'Hot stamping of an Al-Li alloy: A feasibility study', *Manufacturing Rev*, 3, p. 9. doi: 10.1051/matecconf/20152105007.

Gao, H., Wang, L. and Lin, J. (2014) 'Study of new set of constitutive equations for modelling microstructural evolution in Superplastic forming', in *3rd UK-China steel research forum & 15th CMA-UK conference on Materials Science and Engineering*.

Garrett, R. P., Lin, J. and Dean, T. (2005) 'An investigation of the effects of solution heat treatment on mechanical properties for AA 6xxx alloys: experimentation and modelling', *International Journal of Plasticity*, 21(8), pp. 1640–1657. doi: 10.1016/j.ijplas.2004.11.002.

Garrett, R. P., Lin, J. and Dean, T. A. (2005) 'Solution Heat Treatment and Cold Die Quenching in Forming AA 6xxx Sheet Components: Feasibility Study', *Advanced Materials Research*, 6–8, pp. 673–680. doi: 10.4028/www.scientific.net/AMR.6-8.673.

Gloeckl, H. and Lange, K. (1983) 'Computer aided design of blanks for deep drawn irregular shaped components', in *Proceedings of the 11th NAMRC*, pp. 243–251.

Graf, A. and Hosford, W. F. (1990) 'Calculations of forming limit diagrams', *Metallurgical Transactions A*, 21(1), pp. 87–94. doi: 10.1007/BF02656427.

Gregson, P.J., McDarmaid, D.S., Hunt, E. (1988) 'Post-yield deformation characteristics in Al-Li alloys', *Materials Science and Technology*, 4, pp. 713–718. doi: doi:10.1179/mst.1988.4.8.713.

Gregson, P. J. and Flower, H. M. (1985) 'Microstructural control of toughness in aluminium-lithium alloys', *Acta Metallurgica*, 33(3), pp. 527–537. doi: 10.1016/0001-6160(85)90095-1.

Grimes, R. and Butler, R. G. (1988) 'The forming behaviour of commerically available superplastic aluminium alloys', *Superplasticity in aerospace*, (Warrendale, PA, USA), pp. 97–114.

Guo, Y *et al.* (1990) 'Finite Element Procedures for Strain Estimations of Sheet Metal Forming Parts', *International Journal for Numerical Methods in Engineering*, 30, pp. 1385–1401.

Guo, Y. Q. *et al.* (2000) 'Recent developments on the analysis and optimum design of sheet metal forming parts using a simplified inverse approach', *Computers & Structures*, 78(1–3), pp. 133–148. doi: 10.1016/S0045-7949(00)00095-X.

Heinimann, M. *et al.* (2007) *Validation of advanced metallic hybird concept with improved damage tolerance capabilities for nex generation lower wing and fuselage applications*. Edited by A. Lazzeri, L, Salvetti.

Heinz, A. *et al.* (2000) 'Recent development in aluminium alloys for aerospace applications', *Materials Science and Engineering A*, 280(1), pp. 102–107. doi: 10.1016/S0921-5093(99)00674-7.

Hill, R. (1948) 'A Theory of the Yielding and Plastic Flow of Anisotropic Metals', *Proc. Roy. Soc. London A*, 193, pp. 281–297.

Hill, R. (1952) 'On discontinuous plastic states, with special reference to localized necking in thin sheets', *Journal of the Mechanics and Physics of Solids*, 1(1), pp. 19–30. doi: 10.1016/0022-5096(52)90003-3.

Hill, R. (1979) 'Theoretical plasticity of textured aggregates', *Mathematical Proceedings of the Cambridge Philosophical Society*, 85(1), pp. 179–191. doi: 10.1017/S0305004100055596.

Hill, R. (1990) 'Constitutive modelling of orthotropic plasticity in sheet metals', *Journal of the Mechanics and Physics of Solids*, 38(3), pp. 405–417. doi: 10.1016/0022-5096(90)90006-P.

Hill, R. (1993) 'A user-friendly theory of orthotropic plasticity in sheet metals', *International Journal of Mechanical Sciences*, 35(1), pp. 19–25. doi: 10.1016/0020-7403(93)90061-X.

Hiwatashi, S. *et al.* (1998) 'Prediction of forming limit strains under strain-path changes: Application of an anisotropic model based on texture and dislocation structure', *International Journal of Plasticity*, 14(7), pp. 647–669. doi: 10.1016/S0749-6419(98)00031-X.

Hosford, W. F. (1972) 'A Generalized Isotropic Yield Criterion', *Journal of Applied Mechanics*, 39, pp. 607–609.

Hosford, W. F. (1985) 'Comments on anisotropic yield criteria', *International Journal of Mechanical Sciences*, 27(7–8), pp. 423–427. doi: 10.1016/0020-7403(85)90032-3.

Hu, P., Liu, Y. Q. and Wang, J. C. (2001) 'Numerical study of the flange earring of deep-drawing sheets with stronger anisotropy', *International Journal of Mechanical Sciences*, 43(1), pp. 279–296. doi: 10.1016/S0020-7403(99)00119-8.

Hu, Y. *et al.* (2017) 'Development of an interactive friction model for the prediction of lubricant breakdown behaviour during sliding wear', *Tribology International*, 110(October 2016), pp. 370–377. doi: 10.1016/j.triboint.2016.11.005.

Hutchinson J.W. (1968) 'Singular behaviour at the end of a tensile crack in a hardening material', *Journal of the Mechanics and Physics of Solids*, 16, pp. 13–31.

Hwang, Y. M. *et al.* (1997) 'Analysis of superplastic sheet metal forming in a circular closed-die considering non-uniform thinning', *Journal of Materials Processing Technology*, 65, pp. 215–227.

Ibijola, E. A. (2002) 'On some fundamental concepts of Continuum Damage Mechanics', *Computer Methods in Applied Mechanics and Engineering*, 191, pp. 1505–1520. doi: 10.1016/S0045-7825(99)90187-1.

Imperial College London (2017) *Metal forming and materials modelling*. Available at:

http://www.imperial.ac.uk/metal-forming/ (Accessed: 16 June 2017).

Karabin, L. M. *et al.* (2012) 'Al-Li-Cu-Mg-(Ag) products for lower wing skin applications', in Weiland, H., Rollett, A.D., Cassada, W. A. (ed.) *Proceedings of the 13th International Conference on Aluminium Alloys (ICAA13)*. Metals and Materials Society (TMS) and John Wiley & Sons, Hoboken, NJ, pp. 529–534.

Karafillis, A. P. and Boyce, M. C. (1993) 'A general anisotropic yield criterion using bounds and a transformation weighting tensor', *Journal of the Mechanics and Physics of Solids*, 41(12), pp. 1859–1886. doi: 10.1016/0022-5096(93)90073-O.

Karthik, V. *et al.* (2002) 'Variability of sheet formability and formability testing', *Journal of Materials Processing Technology*, 121(2–3), pp. 350–362. doi: 10.1016/S0924-0136(01)01219-5.

Keeler, S. P. (1961) *Plastic Instability and fracture in sheets stretched over rigid punches*. Cambridge: MIT.

Khan, A.S. and Huang, S. (1995) *Continuum Theory of Plasticity*. New York: John Wiley & Sons. doi: 10.1021/jp108806v.

Khan, A. S. and Baig, M. (2011) 'Anisotropic responses, constitutive modeling and the effects of strain-rate and temperature on the formability of an aluminum alloy', *International Journal of Plasticity*. Elsevier Ltd, 27(4), pp. 522–538. doi: 10.1016/j.ijplas.2010.08.001.

Khan, A. S., Kazmi, R. and Farrokh, B. (2007) 'Multiaxial and non-proportional loading responses, anisotropy and modeling of Ti-6Al-4V titanium alloy over wide ranges of strain rates and temperatures', *International Journal of Plasticity*, 23(6), pp. 931–950. doi: 10.1016/j.ijplas.2006.08.006.

Khan, A. S. and Liu, H. (2012) 'A new approach for ductile fracture prediction on Al 2024-T351 alloy', *International Journal of Plasticity*. Elsevier Ltd, 35, pp. 1–12. doi: 10.1016/j.ijplas.2012.01.003.

Kim, J. H. *et al.* (2013) 'Numerical procedures for predicting localization in sheet metals using crystal plasticity', *Computational Materials Science*. Elsevier B.V., 72, pp. 107–115. doi: 10.1016/j.commatsci.2013.02.008.

Kim, N. and Kobayashi, S. (1986) 'Blank design in rectangular cup drawing by an approximate method', *International Journal of Machine Tool Design and Research*, 26(2), pp. 125–135. doi: 10.1016/0020-7357(86)90213-1.

Kim, T. W. and Dunne, F. P. E. (1999) 'Modelling heterogeneous microstructures in superplasticity', *Proceedings of the Royal Society A: Mathematical, Physical and Engineering Sciences*, 455(1982), pp. 701–718. doi: 10.1098/rspa.1999.0330.

Kim, Y. H. *et al.* (1996) 'Processing Technology', *Journal of Material Processing Technology*, 62, pp. 90–99.

Krajcinovic, D. (2000) 'Damage mechanics: accomplishments, trends and needs', *International Journal of Solids and Structures*, 37(1–2), pp. 267–277. doi: 10.1016/S0020-7683(99)00081-5.

Lee, C. H. and Huh, H. (1998) 'Blank design and strain estimates for sheet metal forming processes by a finite element inverse approach with initial guess of linear deformation', *Journal of Materials Processing Technology*, 82(1–3), pp. 145–155. doi: 10.1016/S0924-0136(98)00034-X.

Lemaitre, J. (1985) 'A Continuous Damage Mechanics Model for Ductile Fracture', *Journal of Engineering Materials and Technology*, 107(January 1985), pp. 83–89. doi: 10.1115/1.3225775.

Li, J. *et al.* (2013) 'Forming limit analysis for two-stage forming of 5182-O aluminum sheet with intermediate annealing', *International Journal of Plasticity*, 45, pp. 21–43. doi: 10.1016/j.ijplas.2012.10.004.

Li, X. Q., Song, N. and Guo, G. Q. (2012) 'Experimental measurement and theoretical

prediction of forming limit curve for aluminum alloy 2B06', *Transactions of Nonferrous Metals Society of China (English Edition)*, 22(SUPPL.2), pp. 335–342. doi: 10.1016/S1003-6326(12)61728-2.

Lin, J. *et al.* (2005) 'Development of dislocation-based unified material model for simulating microstructure evolution in multipass hot rolling', *Philosophical Magazine*, 85(18), pp. 1967–1987. doi: 10.1080/14786430412331305285.

Lin, J. *et al.* (2009) 'Method for forming component of complex shape from aluminum-alloy sheet, involves quenching heated sheets between cold dies in solution and maintaining shape of sheet'.

Lin, J. *et al.* (2011) 'A method of forming a component of complex shape from aluminium alloy sheet'.

Lin, J. *et al.* (2013) 'The development of continuum damage mechanics-based theories for predicting forming limit diagrams for hot stamping applications', *International Journal of Damage Mechanics*, 23(5), pp. 684–701. doi: 10.1177/1056789513507731.

Lin, J., Cheong, B. H. and Yao, X. (2002) 'Universal multi-objective function for optimising superplastic-damage constitutive equations', *Journal of Materials Processing Technology*, 125–126, pp. 199–205. doi: 10.1016/S0924-0136(02)00311-4.

Lin, J. and Liu, Y. (2003) 'A set of unified constitutive equations for modelling microstructure evolution in hot deformation', *Journal of Materials Processing Technology*, 143–144(1), pp. 281–285. doi: 10.1016/S0924-0136(03)00472-2.

Lin, J. and Yang, J. (1999) 'GA-based multiple objective optimisation for determining viscoplastic constitutive equations for superplastic alloys', *International Journal of Plasticity*, 15(11), pp. 1181–1196. doi: 10.1016/S0749-6419(99)00031-5.

Liu, X. *et al.* (2015) 'Determination of the interfacial heat transfer coefficient in the hot stamping of AA7075', in *MATEC Web of Conferences 21*, pp. 1–8.

Liu, X. *et al.* (2017) 'Determination of the interfacial heat transfer coefficient for a hot aluminium stamping process', *Journal of Materials Processing Technology*, 247(April), pp. 158–170. doi: 10.1016/j.jmatprotec.2017.04.005.

Lockheed Martin (2012) *Lockheed Martin*. Available at: http://www.lockheedmartin.com/data/assets/12742.pdf (Accessed: 7 July 2017).

Luan, X. *et al.* (2016) 'Formability of AA6082-T6 at warm and hot stamping conditions', *Key Engineering Materials*, 716, pp. 107–113. doi: 10.4028/www.scientific.net/KEM.716.107.

Mabuchi, M. and Higashi, K. (2001) 'An experimental investigation of a superplastic constitutive equation in Al–Mg–Si alloy composites reinforced with Si3N4 whiskers', *International Journal of Plasticity*, 17(3), pp. 399–407. doi: 10.1016/S0749-6419(00)00043-7.

Magnusen, P. E. *et al.* (2012) 'Development of high toughness sheet and extruded products for airplane fuselage structures', in Weiland, H., Rollette, A.D., Cassada, W. A. (ed.) *Proceedings of the 13th International Conference on Aluminium alloys (ICAA13)*. The Minerals, Metals and Materials Society (TMS) and John Wiley & Sons, pp. 535–540.

Maier, C. (2013) 'Failure Prediction in Sheet Metal Forming Using Fea of Nakazima Test', *Machines, Technologies, Materials*, (7), pp. 9–12.

Marciniak, Z. and Kuczyński, K. (1967) 'Limit strains in the processes of stretch-forming sheet metal', *International Journal of Mechanical Sciences*, 9(9), pp. 609–620. doi: 10.1016/0020-7403(67)90066-5.

Mechanicatech (2014) *Mechanica Technical Solution*. Available at: http://www.mechanicatech.com/Forming/superplasticforming.html (Accessed: 3 May 2017).

Messerschmidt, U. and Bartsch, M. (2003) 'Generation of dislocations during plastic deformation', *Materials Chemistry and Physics*, 81(2–3), pp. 518–523. doi: 10.1016/S0254-

0584(03)00064-6.

Min, J. *et al.* (2010) 'Investigation on hot forming limits of high strength steel 22MnB5', *Computational Materials Science*. Elsevier B.V., 49(2), pp. 326–332. doi: 10.1016/j.commatsci.2010.05.018.

Mohamed, F. (2011) 'Micrograin superplasticity: characteristics and utilization', *Materials*, pp. 1194–1223. doi: 10.3390/ma4071194.

Mohamed, M. S. *et al.* (2012) 'Investigation of deformation and failure features in hot stamping of AA6082: Experimentation and modelling', *International Journal of Machine Tools and Manufacture*. Elsevier, 53(1), pp. 27–38. doi: 10.1016/j.ijmachtools.2011.07.005.

Mole, N., Cafuta, G. and Štok, B. (2013) 'A method for optimal blank shape determination in sheet metal forming based on numerical simulations', *Strojniski Vestnik/Journal of Mechanical Engineering*, 59(4), pp. 237–250. doi: 10.5545/sv-jme.2012.989.

Mukherjee, A. K. (1979) 'Deformation Mechanisms', *Materials Science and Engineering*, 9, pp. 191–217.

Naka, T. *et al.* (2008) 'Effects of strain rate, temperature and sheet thickness on yield locus of AZ31 magnesium alloy sheet', *Journal of Materials Processing Technology*, 201(1–3), pp. 395–400. doi: 10.1016/j.jmatprotec.2007.11.189.

Nakazima, K., Kikuma, T. and Hasuka, K. (1968) 'Study on the formability of steel sheets', *YAWATA TECH REP SEPT.*, 264, pp. 8517–8530.

Nes, E., Ryum, N. (1971) 'The ageing characteristics of an Al2 Pct Li-3 Pct Cu0.12 Pct Zr alloy at 190oC', *Scr. Metall.*, 5, pp. 987–990.

Padmanabhan, R. *et al.* (2009) 'Numerical study on the influence of initial anisotropy on optimal blank shape', *Finite Elements in Analysis and Design*, 45(2), pp. 71–80. doi: 10.1016/j.finel.2008.07.012.

Padwal, S. B. and Chaturvedi, R. C. (1992) 'Prediction of forming limits using Hosford's modified yield criterion', *International Journal of Mechanical Sciences*, 34(7), pp. 541–547. doi: 10.1016/0020-7403(92)90029-G.

Park, S. H. *et al.* (1999) 'Optimum blank design in sheet metal forming by the deformation path iteration method', *International Journal of Mechanical Sciences*, 41(10), pp. 1217–1232. doi: 10.1016/S0020-7403(98)00084-8.

Paul, S. K. (2013) 'Theoretical analysis of strain- and stress-based forming limit diagrams', *The Journal of Strain Analysis for Engineering Design*, 48(3), pp. 177–188. doi: 10.1177/0309324712468524.

Pedersen, K. O., Børvik, T. and Hopperstad, O. S. (2011) 'Fracture mechanisms of aluminium alloy AA7075-T651 under various loading conditions', *Materials and Design*. Elsevier Ltd, 32(1), pp. 97–107. doi: 10.1016/j.matdes.2010.06.029.

Pegada, V., Chun, Y. and Santhanam, S. (2002) 'An algorithm for determining the optimal blank shape for the deep drawing of aluminum cups', *Journal of Materials Processing Technology*, 125–126, pp. 743–750. doi: 10.1016/S0924-0136(02)00382-5.

Pickens, J. R. (1985) 'Review The weldability of lithium-containing aluminium alloys', *Review The weldability of lithium-containing aluminium alloys*, 20.

Poole, W. J., Wells, M. A. and Lloyd, D. J. (2006) 'Recently-Developed Aluminium Solutions for Aerospace Applications', *Materials Science Forum*, 519–521, pp. 1271–1278. doi: 10.4028/www.scientific.net/MSF.519-521.1271.

Prasad, N. E., Gokhale, A. A. and Wanhill, R. J. . (2014) *Aerospace Application of Aluminium-Lithium*, *Aluminium-Lithium Alloys Processing, Properties, and Appications*.

Prasad, N. E. and Ramachandran, T. R. (2013) *Phase Diagrams and Phase Reactions in Al-Li Alloys*, *Aluminum-Lithium Alloys: Processing, Properties, and Applications*. Elsevier Inc. doi: 10.1016/B978-0-12-401698-9.00003-3.

Ram Prabhu, T. (2015) 'An overview of high-performance aircraft structural al alloy-

AA7085', *Acta Metallurgica Sinica (English Letters)*. The Chinese Society for Metals, 28(7), pp. 909–921. doi: 10.1007/s40195-015-0275-z.

Reuleaux, O. (1924) 'Scleron alloys', *Journal of the Institute of Metals*, 33, p. 346.

Rioja, R. J. and Liu, J. (2012) 'The evolution of Al-Li base products for aerospace and space applications', *Metallurgical and Materials Transactions A: Physical Metallurgy and Materials Science*, 43(9), pp. 3325–3337. doi: 10.1007/s11661-012-1155-z.

Di Russo, E. (1964) 'Microstructures, tensle properties, fatigue crack growth behaiour of the zirconium modified 2024 alloys processed by liquid dynamic compaction', *Alluminio e Nuova Metall.*, 33, p. 505.

Schwindt, C. *et al.* (2015) 'Experimental and Visco-Plastic Self-Consistent evaluation of forming limit diagrams for anisotropic sheet metals: An efficient and robust implementation of the M-K model', *International Journal of Plasticity*. Elsevier Ltd, 73, pp. 62–99. doi: 10.1016/j.ijplas.2015.01.005.

Shim, H., Son, K. and Kim, K. (2000) 'Optimum blank shape design by sensitivity analysis', *Journal of Materials Processing Technology*, 104(3), pp. 191–199. doi: 10.1016/S0924-0136(00)00556-2.

Signorelli, J. W., Bertinetti, M. A. and Turner, P. A. (2009) 'Predictions of forming limit diagrams using a rate-dependent polycrystal self-consistent plasticity model', *International Journal of Plasticity*, 25(1), pp. 1–25. doi: 10.1016/j.ijplas.2008.01.005.

Son, K. and Shim, H. (2003) 'Optimal blank shape design using the initial velocity of boundary nodes', *Journal of Materials Processing Technology*, 134(1), pp. 92–98. doi: 10.1016/S0924-0136(02)00927-5.

Sovereign (2017) *Omega*. Available at: http://sovereign-omega.co.uk/omega-35-ultimate-high-temperature-grease/.

Sowerby, R., Duncan, J. L. and Chu, E. (1986) 'The modelling of sheet metal stampings', *International Journal of Mechanical Sciences*, 28(7), pp. 415–430. doi: 10.1016/0020-7403(86)90062-7.

Srivatsan, T. *et al.* (1994) *Quasi-Static Strength, Deformation, and Fracture Behavior of Aluminum-Lithium Alloys*, *Advanced Materials and Processes*. Elsevier Inc. doi: 10.1016/B978-0-12-401698-9.00010-0.

Starke, E. A. (2013) *Historical Development and Present Status of Aluminum-Lithium Alloys*, *Aluminum-Lithium Alloys: Processing, Properties, and Applications*. Elsevier Inc. doi: 10.1016/B978-0-12-401698-9.00001-X.

Stören, S. and Rice, J. R. (1975) 'Localized necking in thin sheets', *Journal of the Mechanics and Physics of Solids*, 23(6), pp. 421–441. doi: 10.1016/0022-5096(75)90004-6.

Stoughton, T. B. and Yoon, J. W. (2005) 'Sheet metal formability analysis for anisotropic materials under non-proportional loading', *International Journal of Mechanical Sciences*, 47(12), pp. 1972–2002. doi: 10.1016/j.ijmecsci.2005.06.005.

Stoughton, T. B. and Yoon, J. W. (2009) 'Anisotropic hardening and non-associated flow in proportional loading of sheet metals', *International Journal of Plasticity*. Elsevier Ltd, 25(9), pp. 1777–1817. doi: 10.1016/j.ijplas.2009.02.003.

Stoughton, T. B. and Yoon, J. W. (2011) 'A new approach for failure criterion for sheet metals', *International Journal of Plasticity*. Elsevier Ltd, 27(3), pp. 440–459. doi: 10.1016/j.ijplas.2010.07.004.

Sugamata, M., Blankenship, C. P. and Starke, E. A. (1993) 'Predicting plane strain fracture toughness of AlLiCuMg alloys', *Materials Science and Engineering A*, 163(1), pp. 1–10. doi: 10.1016/0921-5093(93)90572-V.

Swift, H. W. (1952) 'Plastic instability under plane stress', *Journal of the Mechanics and Physics of Solids*, 1(1), pp. 1–18. doi: 10.1016/0022-5096(52)90002-1.

Tadano, Y., Yoshida, K. and Kuroda, M. (2013) 'Plastic flow localization analysis of

heterogeneous materials using homogenization-based finite element method', *International Journal of Mechanical Sciences*. Elsevier, 72, pp. 63–74. doi: 10.1016/j.ijmecsci.2013.03.015.

The Aluminum Association, I. (2001) *Aluminium 7075-T6*. Available at: http://asm.matweb.com/search/GetReference.asp?bassnum=MA7075T6 (Accessed: 7 June 2017).

Vasudévan, A. K. and Doherty, R. D. (1987) 'Grain boundary ductile fracture in precipitation hardened aluminum alloys', *Acta Metallurgica*, 35(6), pp. 1193–1219. doi: 10.1016/0001-6160(87)90001-0.

Vogel, J. H. and Lee, D. (1990) 'An Analysis Method for Deep Drawing Process Design', *International Journal of Mechanical Sciences*, 32(11).

Wang, L., Strangwood, M., Balint, D., Lin, J., Dean, T. A. (2011) 'Formability and failure mechanisms of AA2024 under hot forming conditions', *Materials Science and Engineering A*. Elsevier B.V., 528(6), pp. 2648–2656. doi: 10.1016/j.msea.2010.11.084.

Wang, H. *et al.* (2011) 'On crystal plasticity formability analysis for magnesium alloy sheets', *International Journal of Solids and Structures*, 48(6), pp. 1000–1010. doi: 10.1016/j.ijsolstr.2010.12.004.

Wanhill, R.J.H., Prasad, N.E., Gokhale, A. A. (2014) *Aerospace Applications of Aluminum-Lithium Alloys*, *Aluminum-Lithium Alloys: Processing, Properties, and Applications*. doi: 10.1016/B978-0-12-401698-9.00015-X.

Weng, T. (2015) *Forming Limit of Light Alloy at Warm/hot Forming Conditions*.

Wilm, A. (1911) *Physical-metallurgical experiments on aluminium alloys containing magnesium*.

Wu, Y. *et al.* (2016) 'Formability and microstructure of Ti22Al24.5Nb0.5Mo rolled sheet within hot gas bulging tests at constant equivalent strain rate', *Materials & Design*. Elsevier Ltd, 108, pp. 298–307. doi: 10.1016/j.matdes.2016.06.109.

Yoon, J. W. *et al.* (1999) 'General elasto-plastic finite element formulation based on incremental deformation theory for planar anisotropy and its application to sheet metal forming', *International journal of plasticity*, 15(1), pp. 35–67. doi: 10.1016/S0749-6419(98)00059-X.

Yoon, J. W. *et al.* (2006) 'Prediction of six or eight ears in a drawn cup based on a new anisotropic yield function', *International Journal of Plasticity*, 22(1), pp. 174–193. doi: 10.1016/j.ijplas.2005.03.013.

Yoshida, K., Ishii, A. and Tadano, Y. (2014) 'Work-hardening behavior of polycrystalline aluminum alloy under multiaxial stress paths', *International Journal of Plasticity*. Elsevier Ltd, 53, pp. 17–39. doi: 10.1016/j.ijplas.2013.07.003.

Yoshida, K., Kuwabara, T. and Kuroda, M. (2007) 'Path-dependence of the forming limit stresses in a sheet metal', *International Journal of Plasticity*, 23(3), pp. 361–384. doi: 10.1016/j.ijplas.2006.05.005.

Zadpoor, A. A., Sinke, J. and Benedictus, R. (2009) 'Formability prediction of high strength aluminum sheets', *International Journal of Plasticity*. Elsevier Ltd, 25(12), pp. 2269–2297. doi: 10.1016/j.ijplas.2009.02.005.

Zhai, J. *et al.* (2016) 'Modeling the ductile damage process in commercially pure titanium', *International Journal of Solids and Structures*. Elsevier Ltd, 91, pp. 26–45. doi: 10.1016/j.ijsolstr.2016.04.031.

Zhang, L. and Wang, J. (2012) 'Modeling the localized necking in anisotropic sheet metals', *International Journal of Plasticity*. Elsevier Ltd, 39, pp. 103–118. doi: 10.1016/j.ijplas.2012.05.005.

Zhang, Y. and Ma, M. (2015) 'International conference on advanced high strength steel and press hardening', in *Proceedings of the 2nd international conference (ICHSU2015)*, p. 94.

Zheng, K. *et al.* (2017) 'A buckling model for flange wrinkling in hot deep drawing aluminium alloys with macro-textured tool surfaces', *International Journal of Machine Tools and Manufacture*. Elsevier, 114(March), pp. 21–34. doi: 10.1016/j.ijmachtools.2016.12.008.

Zhou, M., Dunne, F. P. E. (1996) 'Mechanisms-based constitutive equations for the superplastic behaviour of a titanium alloy', *The Journal of Strain Analysis for Engineering Design*, 31, pp. 181–196.

Appendices

Appendix – Chapter 3

3A. Isothermal zone measurement

To measure the length of isothermal zone of tensile speicmen in the Gleeble tensile test, five sets of thermocouples were spot welded (Figure 3-37 (a)) and positioned on the tensile specimen at different locations (as defined in Figure 3-37 (b)) on the AA2060 tensile test specimen.
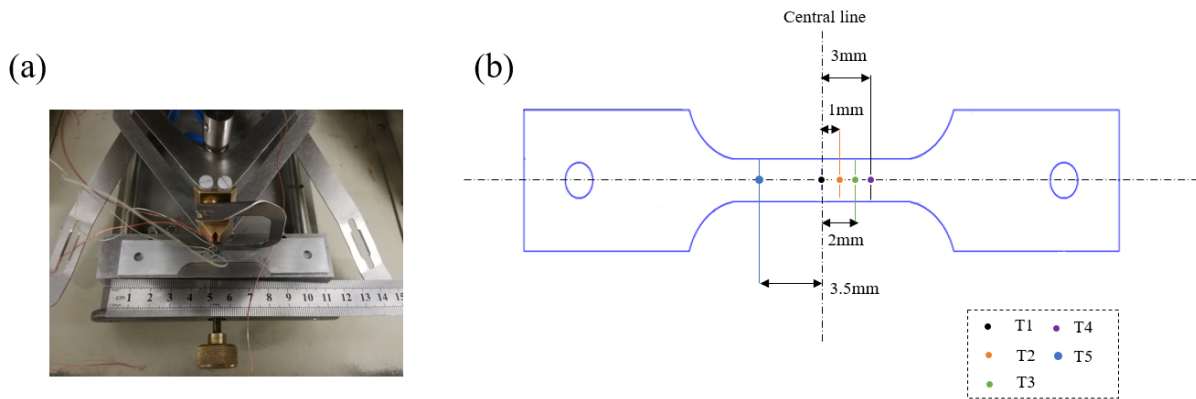
Figure 3-37. (a) Spot welding on the AA2060 tensile test with thermocouples (b) Positions of temperature measurement on the tensile test specimen

In the Gleeble heating test, the target temperature set to be 520°C. The temperatures of five defined positions in each time were recorded by Gleeble. The temperature profiles against time were shown in Figure 3-38. In Figure 3-38, as the distance is more than 3cm away from central line, the temperature in T5 was lower than the ones in T1-4. Consequently, the length of isothermal zone in the half part of tensile speciemn was defined as 3mm. The isothermal zone in the whole tensile specimen was measured to be 6mm.
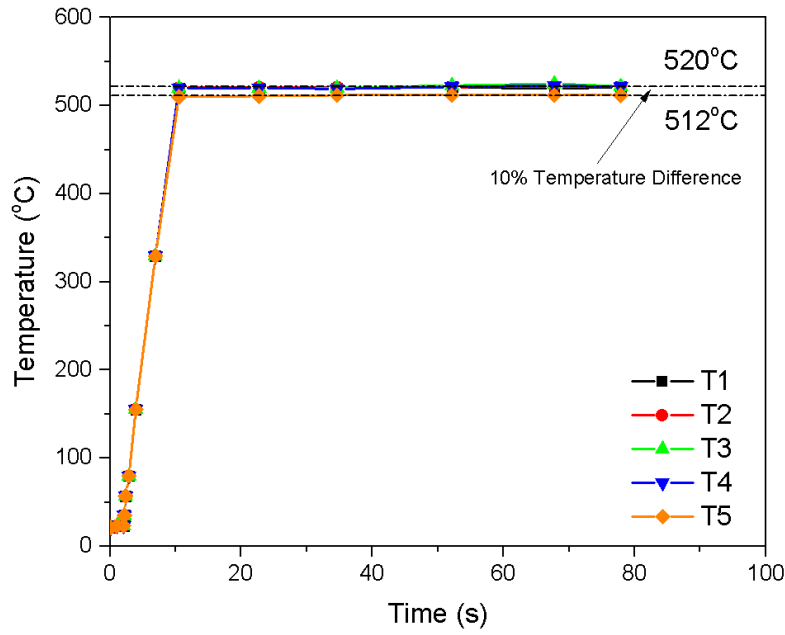
Figure 3-38. Temperature histories of T1-5 positions through tensile test specimen during the heating process

3B. Measterment of limit dome height for AA2060

To measure the limit dome height of the specimens, two measurements were taken for each sample: one (T: total height) was measured from ground to the top of the dome, the other one was from top edge of specimen to ground (B: Basial thickness) as presented in Figure 3-39. Limit dome height was identified to be the difference between those two measurements as expressed by Eq. (3.1):

$$H = T - B \tag{3.1}$$

Where T is the total height of formed part, B is the basal thickness and H is the dome height.
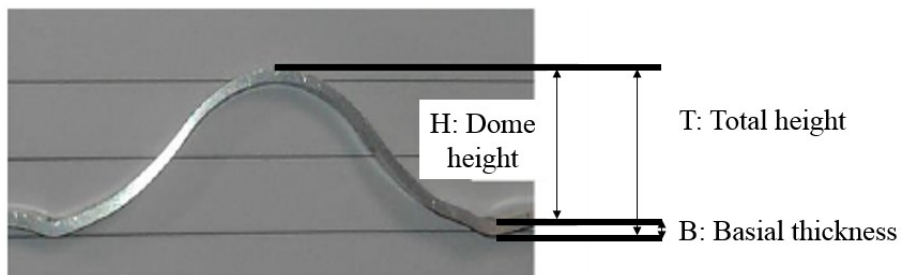
Figure 3-39. Limit dome height measurement of formed part (Weng, 2015)

Table **3-7** and Table 3-18 show that the measured limit dome heights were recorded at different forming speeds and temperatures.

Table 3-7. Effect of forming temperature on limit dome height on AA2060 alloy

	B1	B2	B3	T1	T2	T3	H1	H2	H3	Average	STD
Limit dome height of formability specimen at 300 °C with a forming speed of 250mm/s (in mm)											
Uniaxial	4.20	4.03	4.02	15.73	15.77	15.74	11.53	11.40	11.27	11.40	0.130
Plane strain	4.11	4.06	4.07	15.09	15.09	15.04	10.98	10.72	10.57	10.76	0.207
Biaxial	4.29	4.37	4.47	14.02	14.01	14.02	9.73	9.64	9.55	9.64	0.090
Limit dome height of formability specimen at 400 °C with a forming speed of 250mm/s (in mm)											
Uniaxial	4.13	4.19	4.01	20.61	20.59	20.61	16.58	16.50	16.70	16.99	0.101
Plane strain	4.09	4.04	4.06	20.90	20.86	20.80	16.81	16.82	16.74	16.79	0.044
Biaxial	3.98	3.91	3.90	19.97	19.96	19.96	15.99	16.05	16.06	16.03	0.038
Limit dome height of formability specimen at 450 °C with a forming speed of 250mm/s (in mm)											
Uniaxial	3.98	3.91	3.90	21.97	21.00	20.96	17.99	17.09	17.06	17.38	0.528
Plane strain	4.09	4.04	4.06	21.35	21.50	21.28	17.26	17.46	17.22	17.31	0.129
Biaxial	4.13	4.19	4.01	20.72	21.40	21.20	16.59	17.21	17.19	17.00	0.352

Table 3-8. Effect of forming speeds on limit dome height on AA2060 alloy

	B1	B2	B3	T1	T2	T3	H1	H2	H3	Average	STD
Limit dome height of formability specimen at 400 °C with a forming speed of 75mm/s (in mm)											
Uniaxial	3.93	3.93	3.89	20.9	20.95	20.71	16.97	17.02	16.82	16.94	0.104
Plane strain	4.35	4.03	4.01	20.98	20.98	20.91	16.63	16.95	16.90	16.83	0.172
Biaxial	4.17	4.09	4.08	20.61	20.59	20.61	16.44	16.50	16.53	16.49	0.045
Limit dome height of formability specimen at 400 °C with a forming speed of 250mm/s (in mm)											
Uniaxial	4.13	4.19	4.01	20.81	21.03	20.61	16.48	16.40	16.60	16.83	0.101
Plane strain	4.09	4.04	4.06	20.90	20.86	20.80	16.81	16.82	16.74	16.79	0.044
Biaxial	3.98	3.91	3.90	19.90	19.93	19.01	15.99	16.05	16.06	15.59	0.038
Limited dome height of formability specimen at 400 °C with a forming speed of 400mm/s (in mm)											
Uniaxial	4.09	4.15	4.13	20.06	20.88	20.86	14.81	14.73	14.77	16.49	0.040
Plane strain	4.06	4.16	4.07	20.31	20.08	19.98	15.63	15.52	15.62	16.03	0.061
Biaxial	3.94	3.94	3.92	18.26	18.25	19.62	16.32	16.31	16.33	14.77	0.010

3C. Hardness measurement of age hardening behaviour of AA2060

Table 3-9. Determination of optimum soaking time on solution-heat-treated AA2060 at 520°C

Aging time (minutes)	1 (HV)	2 (HV)	3 (HV)	4 (HV)	5 (HV)	Average (HV)	Standard deviation (STD) (HV)
1	79.5	81.5	79.5	82.7	82.9	81.22	1.66
5	80.3	80.8	79.3	80.0	80.9	80.8	0.65
10	80.8	81.1	80.8	80.8	81.1	81.1	0.16
13	80.8	79.3	79.2	81.9	81.9	80.08	1.22
30	78.8	82.3	82.2	82.6	82.5	81.68	1.62
60	78.4	78.3	80.7	80.7	79.4	79.50	1.18

Table 3-10. Hardness of solution-heat-treated AA2060 with different natural aging time

Aging time (minutes)	1 (HV)	2 (HV)	3 (HV)	4 (HV)	5 (HV)	Average (HV)	Standard deviation (STD) (HV)
0	81.1	76.8	80.3	81.7	82.8	80.54	2.28
33	81.8	84.1	83.4	82.1	84.1	83.10	1.09
105	98.6	98	97.9	97.6	97.9	98.00	0.37
190	106.2	108.2	105.9	105	107	106.46	1.21
390	118.2	114.9	116.3	113.6	114.5	115.5	0.05
720	116.6	122.8	125.8	123.3	124.9	122.68	3.61
1600	128.3	127	129.5	129	128	128.36	0.1
2300	131.6	129.8	128.6	132	128	130	1.77
2912	129.0	131.0	131.0	132.7	130.5	130.4	1.32

Table 3-11. Hardness measurement of one-stage artificially aged AA2060 at aging temperature 160°C with different variable aging time

Aging time (hours)	1 (HV)	2 (HV)	3 (HV)	Average (HV)	Standard deviation (STD) (HV)
0.0	80.8	80.8	80.1	80.6	0.4
1.0	111.0	110.0	111.0	110.7	0.6
4.0	129.0	128.0	130.0	129.0	1.0
16.0	152.0	150.0	150.0	150.7	1.2
17.5	152.0	152.0	151.0	151.7	0.6
18.5	152.0	154.0	153.0	153.0	1.0
19.5	154.0	154.0	155.0	154.3	0.6
20.0	156.0	154.0	156.0	155.3	1.2
20.5	156.0	155.0	155.0	155.3	0.6
21.0	155.0	157.0	155.0	155.7	1.2
21.5	156.5	155.5	157.0	156.3	0.8
22.0	157.0	158.0	158.0	157.7	0.6
22.5	156.0	156.5	156.5	156.3	0.3
23.0	155.0	156.0	155.5	155.5	0.5
25.0	153.0	153.0	154.0	153.3	0.6

Table 3-12. Hardness measurement of one-stage artificially aged AA2060 at aging temperature 170°C with different variable aging time

Aging time (hours)	1 (HV)	2 (HV)	3 (HV)	Average (HV)	Standard deviation (STD) (HV)
0.0	80.8	80.8	80.1	80.6	0.0
1.0	115.0	114.0	114.0	114.3	0.6
5.0	132.0	134.0	130.0	132	0.5
8.0	143.5	142.0	145.0	143.5	1.5
11.0	149.5	149.0	150.0	149.5	0.5
13.0	151.5	152.0	151.0	151.5	0.5
15.0	155.0	154.0	156.0	155.0	1.0
17.0	156.5	156.0	157.0	156.5	0.5
18.0	158.5	158.0	159.0	158.5	0.5
19.0	160.0	160.0	160.0	160.0	0.0
19.5	161.4	160.5	162.0	161.3	0.8
20.0	160.0	160.5	159.5	160.0	0.5
20.5	158.40	158.5	158.0	158.3	0.3
21.0	156.5	157.0	156.0	156.5	0.5
21.5	155.0	155.0	155.0	155.0	0.0
22.0	152.5	152.0	153.0	152.5	0.5
23.0	151.5	152.0	151.0	150.5	0.5
25.0	147.5	148.0	147.0	147.5	0.5

Table 3-13. Hardness measurement of one-stage artificially aged AA2060 at aging temperature 180°C with different variable aging time

Aging time (hours)	1 (HV)	2 (HV)	3 (HV)	Average (HV)	Standard deviation (STD) (HV)
0.0	80.8	80.8	80.1	80.6	0.0
1.0	115.0	114.0	114.0	114.3	0.6
5.0	132.0	134.0	130.0	132	0.5
8.0	143.5	142.0	145.0	143.5	1.5
11.0	149.5	149.0	150.0	149.5	0.5
13.0	151.5	152.0	151.0	151.5	0.5
15.0	155.0	154.0	156.0	155.0	1.0
17.0	156.5	156.0	157.0	156.5	0.5
18.0	161.5	158.0	159.0	159.5	1.8
19.0	160.0	160.0	160.0	160.0	0.0
19.5	158.4	160.5	162.0	160.3	1.8
20.0	160.0	160.5	159.5	160.0	0.5
20.5	158.40	158.5	158.0	158.3	0.3
21.0	156.5	157.0	156.0	156.5	0.5
21.5	155.0	155.0	155.0	155.0	0.0
22.0	152.5	152.0	153.0	152.5	0.5
23.0	158.7	155.3	155.3	156.5	2.0
25.0	147.5	148.0	147.0	147.5	0.5

Table 3-14. Hardness measurement of one-stage artificially aged AA2060 at aging temperature 190°C with different variable aging time

Aging time (hours)	1 (HV)	2 (HV)	3 (HV)	Average (HV)	Standard deviation (STD) (HV)
0.0	81.1	80.8	80.1	80.7	0.41
1.0	122.0	123.0	123.0	122.7	0.58
3.0	134.0	135.0	132.0	133.7	1.26
5.0	143.0	142.0	142.0	142.3	0.58
7.0	143.0	144.0	144.0	143.7	0.58
8.5	145.0	144.0	145.0	144.7	0.50
10.5	147.0	147.0	148.0	147.3	0.50
12.5	148.3	149.3	149.3	149.7	0.58
15.0	151.0	152.0	150.0	151.0	0.82
16.5	154.0	154.0	155.0	154.3	0.50
17.0	154.0	155.0	155.0	154.7	0.58
17.3	155.0	156.0	155.5	155.5	0.48
17.7	154.0	154.0	154.5	154.2	0.25
18.0	154.0	154.0	153.5	153.8	0.25
20.0	150.0	152.0	152.0	151.3	1.15
21.5	146.0	148.0	149.0	147.7	1.50

Table 3-15. Hardness measurement of one-stage artificially aged AA2060 at aging temperature 200°C with different variable aging time

Aging time (hours)	1 (HV)	2 (HV)	3 (HV)	Average (HV)	Standard deviation (STD) (HV)
0.0	80.8	80.8	80.1	80.6	0.4
2.0	111.0	110.0	111.0	110.7	0.6
5.0	129.0	128.0	130.0	129.0	1.0
7.0	145.1	142.0	144.0	143.7	1.2
9.0	152.0	152.0	151.0	151.7	0.6
11.0	152.0	154.0	153.0	153.0	1.0
12.0	154.0	154.5	155.0	154.5	0.5
13.0	157.7	155.0	155.0	155.9	1.6
13.5	155.0	157.0	155.0	155.7	1.2
14.0	156.5	155.5	157.0	156.3	0.8
14.5	157.0	158.0	158.0	157.7	0.6
15.0	156.0	156.5	156.5	156.3	0.3
16.0	156.5	158.0	157.5	157.5	0.5
18.0	153.0	153.0	154.0	153.3	0.6
20.0	148.1	148.0	144.0	146.7	0.5
23.0	137.0	137.0	136.0	136.7	0.5

Table 3-16. Two-stage artificial aging of AA2060: First-stage aging (170°C), Second-stage aging (190°C) with variable time

Aging time (hours)	1 (HV)	2 (HV)	3 (HV)	Average (HV)	Standard deviation (STD) (HV)
0.0	80.8	80.8	80.1	80.6	0.4
1.0	130.1	130.0	132.0	130.7	1.1
3.0	138.0	138.0	139.0	138.3	0.6
5.0	141.0	141.0	140.0	140.7	0.6
7.0	141.0	142.0	143.0	142.0	1.0
8.5	144.0	143.0	142.0	143.0	1.0
10.0	144.0	144.0	144	144	0.0
10.5	145.0	144.5	144.0	144.5	0.5
11.0	146.0	147.0	142.6	145.2	2.3
11.5	145.5	142.5	145.5	144.5	1.7
12.0	140.0	141.0	141.0	140.7	0.6
13.0	136.0	135.0	137.0	136.0	1.0
14.0	143	143.5	144	143.5	0.5
15.0	132.0	129.0	130.0	130.3	1.5
16.0	127.0	126.0	128.0	127.0	1.0
17.0	128.0	126.0	125.0	126.3	1.5
19.0	125.0	126.0	125.0	125.3	0.6
21.0	123.0	125.0	124.0	124.0	1.0

Table 3-17. Two-stage artificial aging of AA2060: First stage aging (170°C), Second stage aging (200°C) with variable time

1st stage artificial aging			2nd stage artificial aging		Total hours (h)		Hardness Testing: HV 5/10						
							1	2	3	4	5	Average (HV)	Standard Deviation
Start T	End T	Length	Start T	End T	Length	Total Length							
1st stage artificial aging (170°C, 1hour), 2nd stage artificial aging 190°C with variable time													
170.2	171.1	1	190.5	191.3	2	3	123	122	125	125.5	126	124.3	1.72
170.2	171.1	1	190.5	189.7	3	4	137	136.3	138	138	137.2	137.2	0.77
170.2	171.1	1	190.5	190	4	5	145.2	144	148	143	145.4	145.4	2.03
170.2	171.1	1	190.5	190	5	6	153	152	152	152	153.4	153.4	2.61
170.2	171.1	1	190.5	189.8	6	7	150	150	150	152	152.6	152.6	4.77
170.2	171.1	1	190.5	189	7	8	148	149	150	150	150.8	150.8	3.56
170.2	171.1	1	190.5	189	8	9	148	150	148	149	149.1	149.1	1.14
1st stage artificial aging (170°C, 2hour), 2nd stage artificial aging 190°C with variable time													
169.5	170.8	2	190	190.3	1.5	3.5	124	128	127	125	127	126.2	1.64
169.5	170.8	2	190	190.6	2	4	136	134	137	136	136	132.8	1.10
171.1	170.6	2	192.2	191.5	2.5	4.5	142	139	139	140	139	137.8	1.30
171.1	170.6	2	192.2	186.5	3	5	150	148	148	150	150	146.2	1.10
171.1	170.6	2	192.2	191.5	4	7	155	154	155	155	156	156	0.71
171.1	170.6	2	192.2	186.5	5	8	154	153	151	152	152	152.4	1.14
1st stage artificial aging (170°C, 4hour), 2nd stage artificial aging 190°C with variable time													
170.9	170.3	4	190.8	190.7	0.7	4.0	127	132	130	126	125	128	2.92
170.9	170.3	4	190.8	191	1.5	5.5	139	142	140	135	142	139.6	2.88
170.9	170.5	4	190.8	188.1	2.3	6.3	149	149	149	148	148	148.6	0.55
170.9	170.3	4	190.8	191.2	3.0	7.0	153	154	154	153	153	153.4	0.55
170.9	170.3	4	190.8	191.6	3.7	7.7	148	150	150	150	149	149.4	0.89
170.9	170.2	4	190.8	191.6	4.4	8.4	145	146	144	145	146	145.2	0.84
1st stage artificial aging (170°C, 5hour), 2nd stage artificial aging 190°C with variable time													
170.5	170.2	5	190.6	191	1.2	6.2	134	136	137	136	135	135.6	1.14
170.5	170.8	5	190.6	189.6	2.0	7.0	148	146	146	145	148	146.6	1.34
170.8	170.9	5	190.6	190.1	2.7	7.7	152	150	153	151	152	151.6	1.14
170.9	170.9	5	190.6	190.6	3.3	8.3	148	150	151	151	150	150	1.22

Table 3-18. Two-stage artificial aging of AA2060: First stage aging (170°C), Second stage aging (220°C) with variable time

1st artificial aging			2nd stage artificial aging			Total hours (h)	Hardness Testing: HV 5/10						
							1	2	3	4	5	Average (HV)	Standard Deviation
Start T	End T	Length	Start T	End T	Length	Total Length							
1st stage artificial aging (170°C, 1hour), 2nd stage artificial aging 200°C with variable time													
169.7	169.8	1	200.3	200.2	1	2	118	117	120	121	121	119.4	1.14
170.2	171.1	1	200	199.6	2	3	143	145	143	144	143	143.6	1.34
170.2	171.1	1	200	199	3	4	150	148	150	150	149	149.4	1.14
170.2	171.1	1	200	199.7	4	5	152	154	150	152	151	151.8	1.22
170.2	171.1	1	200	202	5	6	152	153	150	150	150	151.0	1.14
170.2	171.1	1	200	198.6	6	7	149	148	154	149	150	150.0	1.34
170.2	171.1	1	200	198.9	7	8	148	148	150	147	150	148.6	1.14
1st stage artificial aging (170°C, 5hour), 2nd stage artificial aging 200°C with variable time													
165.9	169.7	5	198	200	0.5	5.5	134	136	135	134	136	135.0	1.00
165.9	169.7	5	198	200.3	1	6	139	140	141	142	140	140.4	1.14
165.9	169.7	5	198	200.5	1.5	6.5	144	145	145	144	146	144.8	0.83
165.9	169.7	5	198	200.5	2	7	152	150	150	150	151	150.6	0.89
165.9	169.7	5	198	200.5	2.5	7.5	152	148	149	149	147	149.0	1.87
165.9	169.7	5	198	200.6	3	8	147	146	146	145	148	146.4	1.14
165.9	169.7	5	198	200.8	3.5	8.5	146	145	144	145	144	144.8	0.83
165.9	169.7	5	198	200.8	4	9	142	143	143	144	142	142.8	0.83
165.9	169.7	5	198	200.6	4.5	9.5	143	141	142	140	143	141.8	1.30
1st stage artificial aging (170°C, 2hour), 2nd stage artificial aging 200°C with variable time													
169.5	166	2	202	201.8	1	3	127	124.1	125.2	125	126.7	125.8	1.22
169.5	166	2	202	199.5	2	4	146	145	144	146	144	145	1.00
169.5	166	2	202	199.5	2.5	4.5	149	150	148	150	149.5	149.3	0.84
169.5	166	2	202	199.2	3	5	153	155	153	155	154.5	154.1	1.02
169.5	166	2	202	200	4	6	150	151	148	152	151	150.4	1.52
169.5	166	2	202	200.1	5	7	145	146	146	147	146	146	0.71
169.5	166	2	202	200.4	6	8	142	142	142	143	143	142.4	0.55
1st stage artificial aging (170°C, 3hour), 2nd stage artificial aging 200°C with variable time													
169.5	172.3	3	201.8	199.5	1	4	132	132	129	128	133	130.8	2.17
169.5	172.3	3	201.8	199.2	2	5	148	148	148	147	147	147.6	0.55
169.5	172.3	3	201.8	200	3	6	152	154	152	152	152	152.4	0.89
169.5	172.3	3	201.8	200.1	4	7	147	148	148	148	147	147.6	0.55
169.5	172.3	3	201.8	200.4	5	8	142	142	143	142	143	142.4	0.55
169.5	172.3	3	201.8	200	6	9	136	138	138	137	138	137.4	0.89

Appendix – Chapter 4

4A. Flow stress curves of AA2060 at different strain rates and temperatures imported in PAM-STAMP FE simulation
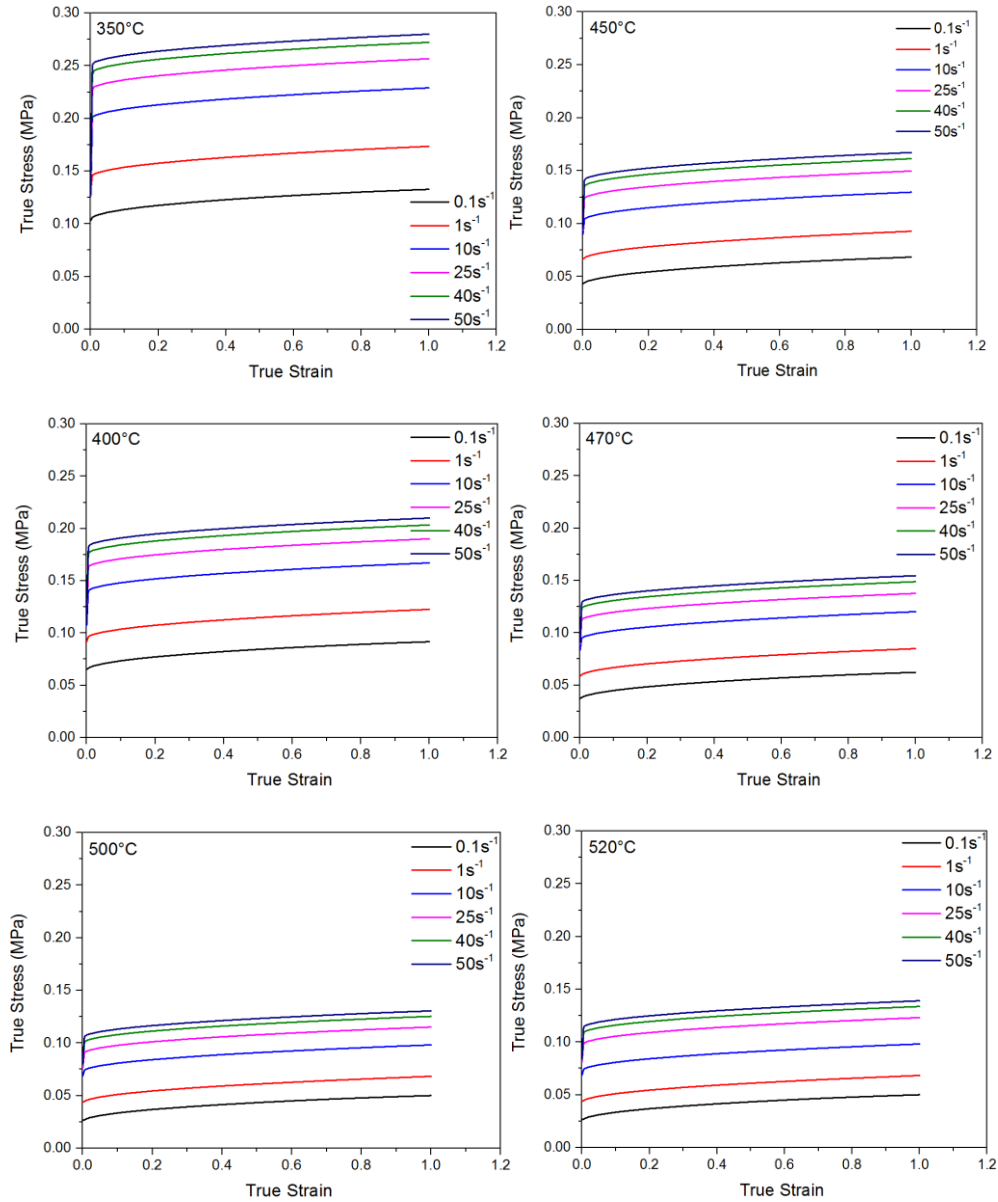
Figure 4-15. Flow stress curves of AA2060 under different strain rates and temperatures

4B. Material Packages of AA2060 for PAM-STAMP FE simulation

Table 4-6. Matrix of PAM-STAMP material package defined for Al-Li alloy

Temperature (°C) Strain rate (s⁻¹)	350	400	450	470	500	520
0.1	√	√	√	√	√	√
1	√	√	√	√	√	√
10	√	√	√	√	√	√
25	√	√	√	√	√	√
40	√	√	√	√	√	√
50	√	√	√	√	√	√

4C. Temperature, strain rate and strain path of AA2060 during the HFQ forming process

State	Temperature distribution of AA2060 formed part
State 1	Nodal temperature - Membrane 450.00000 442.85715 435.71429 428.57144 421.42856 414.28571 407.14285 400.00000 Min = 450.00000 Max = 450.00000
State 2	Nodal temperature - Membrane 450.00000 442.85715 435.71429 428.57144 421.42856 414.28571 407.14285 400.00000 Min = 366.84296 Max = 451.22992
State 3	Nodal temperature - Membrane 450.00000 442.85715 435.71429 428.57144 421.42856 414.28571 407.14285 400.00000 Min = 312.94131 Max = 451.52948
State 4	Nodal temperature - Membrane 450.00000 442.85715 435.71429 428.57144 421.42856 414.28571 407.14285 400.00000 Min = 292.83960 Max = 462.25781

State	Loading path distribution of AA2060 formed part
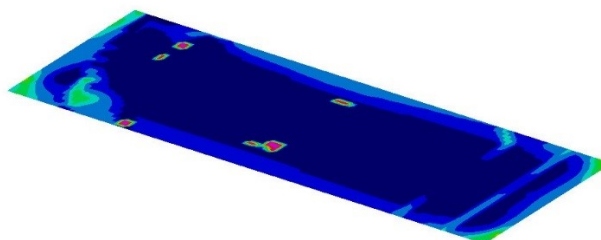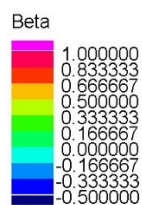
State 1

State 2
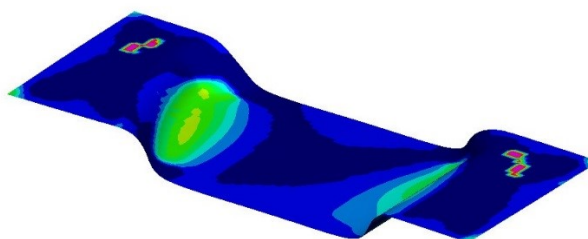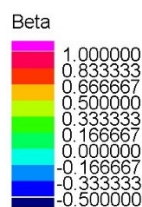
State 3
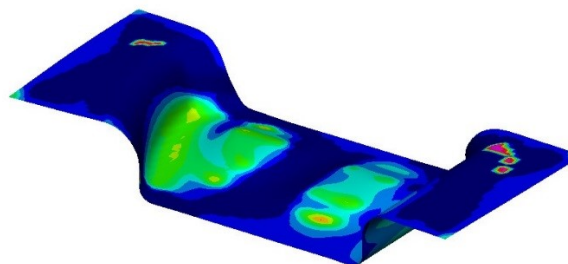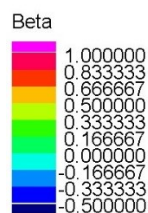
State 4
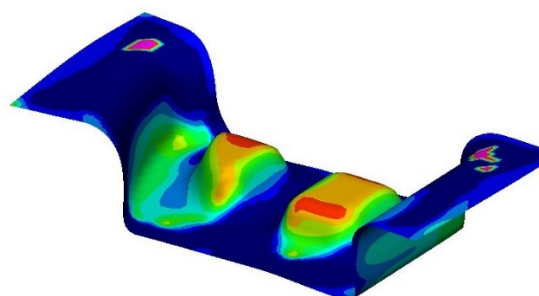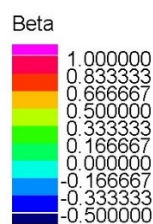
State	Strain rate distribution of AA2060 formed part

State 1

Strain rate - Membrane
0.040000
0.034286
0.028571
0.022857
0.017143
0.011429
0.005714
0.000000
Min = 0.000000
Max = 0.000000

State 2

Strain rate - Membrane
0.040000
0.034286
0.028571
0.022857
0.017143
0.011429
0.005714
0.000000
Min = 0.000000
Max = 0.006406

State 3

Strain rate - Membrane
0.040000
0.034286
0.028571
0.022857
0.017143
0.011429
0.005714
0.000000
Min = 0.000000
Max = 0.010764

State 4

Strain rate - Membrane
0.040000
0.034286
0.028571
0.022857
0.017143
0.011429
0.005714
0.000000
Min = 0.000000
Max = 0.039691

Appendix – Chapter 5

5A. Flow chart for the determination of material constants using viscoplastic material model

START

Input Variables:
Strain rate: $\dot{\varepsilon}_1$
Temperature: T
Time step: Δt

Select material constants:
K, k, B, C, A, n_1, E, n_2, Q_K, Q_k, Q_B, Q_C, Q_A, Q_{n_1} and Q_E

Calculate:

$\dot{\varepsilon}_P$ by Eq. (5.1)

$\dot{\bar{\rho}}$ by Eq. (5.4)

Euler method: Numerical Integration

$t_{(i+1)} = t_{(i)} + \Delta t$

$\bar{\varepsilon}_T = \dot{\bar{\varepsilon}} \cdot t$

Calculate: $\bar{\rho}$, $\bar{\varepsilon}_p$, R

$\bar{\varepsilon}_T = \dot{\bar{\varepsilon}} \cdot t$

$\bar{\sigma}$ by Eq. (5.2)

If $\bar{\sigma} - R - k < 0$,
Yes, $\bar{\sigma} = 0$
NO

If No

Plot the graph: $\bar{\sigma}$ against $\bar{\varepsilon}_T$
Compare with experimental flow stress curves

Optimization?
(Material constants)

END
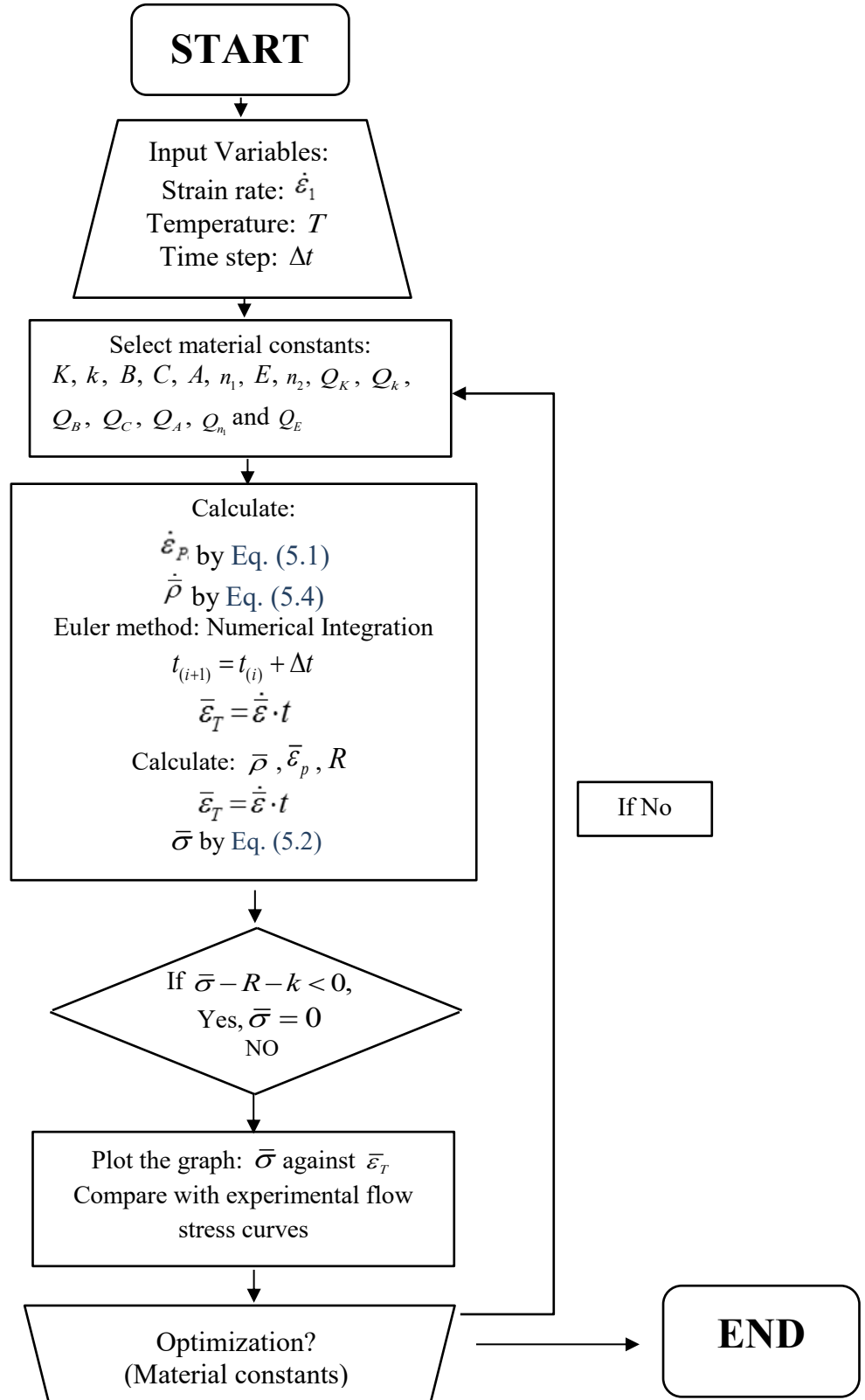
5B. Calculation of major strain rate in viscoplastic-Hosford-MK model

In FLD prediction using viscoplastic-Hosford-MK model, the stroke of each deformed element was known, the forming time of formed part can be calculated as below:

$$t = \frac{D}{v}$$
(5.25)

when t is the forming time, D is the stroke required in each formed element, v is the forming speed.

The strain rate of each deformed element is expressed as that:

$$\dot{\varepsilon} = \frac{\varepsilon}{t}$$
(5.26)

when $\dot{\varepsilon}$ is the strain rate, ε is the major strain, t is the forming time.

5C. Flow chart for the FLD prediction using viscoplastic-Hosford-MK model

START

Input Variables:
Strain rate: $\dot{\varepsilon}_1$, Temperature: T
Time step: Δt,
Strain ratio: β

Input Material constants in viscoplastic material model
K, k, B, C, A, n_1, E, n_2, Q_K, Q_k, Q_B, Q_C, Q_A, Q_{n_1} and Q_E

Input Material constants in Hosford yield function:
R_1, R_2, l,

Select f_0 in M-K Model

Zone a:

$d\varepsilon_{1a} = \dot{\varepsilon}_{1a} \cdot \Delta t$, $d\varepsilon_{2a} = d\varepsilon_{1a} \cdot \beta_a$
$d\varepsilon_{3a} = -(d\varepsilon_{1a} + d\varepsilon_{2a})$

Calculate: $d\bar{\varepsilon}_a$
Update $\bar{\sigma}_a$ by viscoplastic material model
Using Hosford yield function and Euler integration function
Calculate:
σ_{1a}, σ_{2a}, σ_{3a}, α_a

Compatibility law:
$d\varepsilon_{2a} = d\varepsilon_{2b}$
$f\sigma_{1b} = \sigma_{1a}$

Zone b:

$d\varepsilon_{2a} = d\varepsilon_{2b}$
$f = f_0 \exp(\varepsilon_{3b} - \varepsilon_{3a})$
$\sigma_{1b} = \psi_b \bar{\sigma}_b$, $\sigma_{2b} = \alpha_b \sigma_{1b}$
$f\sigma_{1b} = \sigma_{1a}$, $\sigma_{1b} = \psi_b \bar{\sigma}_b$
$\delta\varepsilon_{3b} = -(\delta\varepsilon_{1b} + \delta\varepsilon_{2b})$

Solve α_b in
$\beta_b = f(\alpha_b)$

Calculate:
If $\dfrac{d\varepsilon_{3b}}{d\varepsilon_{3a}} > 10$

Update σ_{1b}, σ_{2b}, σ_{3b} and $\delta\varepsilon_{3b}$ in each time increment
(by Viscoplastic-Hosford-MK model)

Calculate forming limit major and minor strains and plot FLD
Compare with experimental FLD

Optimisation?

If no, then

END

5D. Development of viscoplastic-Hosford-MK model

The Hosford anisotropic yield function can be expressed as:

$$R_2\sigma_1^l + R_1\sigma_2^l + R_1R_2(\sigma_1 - \sigma_2)^l = R_2(R_1 + 1)\bar{\sigma}^l \tag{5.27}$$

According to the Hosford anisotropic yield function, the equivalent stress in Zones a and b were calculated as following:

$$\bar{\sigma}_{a,b} = \left\{ \frac{1}{R_2(R_1 + 1)} \left[R_2\sigma_{1a,b}^l + R_1\sigma_{2a,b}^l + R_1R_2(\sigma_{1a,b} - \sigma_{2a,b})^l \right] \right\}^{\frac{1}{l}} \tag{5.28}$$

In thin sheet metals, it is assumed that $\sigma_3 = 0$. Let $\sigma_2 = \alpha\sigma_1$,

$$\bar{\sigma}_{a,b} = \sigma_{1a,b} \left\{ \frac{1}{R_2(R_1 + 1)} \left[R_2 + \alpha_{a,b}^l R_1 + (1 - \alpha_{a,b})^l R_1R_2 \right] \right\}^{\frac{1}{l}} \tag{5.29}$$

Let,

$$\sigma_{1a,b} = \varphi_{a,b}\bar{\sigma}_{a,b} \tag{5.30}$$

$$\varphi_{a,b} = \left\{ \frac{1}{R_2(R_1 + 1)} \left[R_2 + \alpha_{a,b}^l R_1 + (1 - \alpha_{a,b})^l R_1R_2 \right] \right\}^{-\frac{1}{l}} \tag{5.31}$$

Let $d\varepsilon_2 = \beta d\varepsilon_1$,

$$d\varepsilon_3 = -(1 + \beta)d\varepsilon_1 \tag{5.32}$$

According to the associated flow rule,

$$d\varepsilon_{ij} = d\lambda\frac{\partial f}{\partial\sigma_{ij}} = d\lambda\frac{\partial\bar{\sigma}}{\partial\sigma_{ij}} \rightarrow d\lambda = d\varepsilon_{ij} \bigg/ \frac{\partial\bar{\sigma}}{\partial\sigma_{ij}} \tag{5.33}$$

$$\frac{d\varepsilon_{1a,b}}{R_2\sigma_{1a,b}^{l-1} + R_1R_2(\sigma_{1a,b} - \sigma_{2a,b})^{l-1}} = \frac{d\varepsilon_{2a,b}}{R_1\sigma_{2a,b}^{l-1} - R_1R_2(\sigma_{1a,b} - \sigma_{2a,b})^{l-1}} = \frac{d\varepsilon_{3a,b}}{-R_2\sigma_{1a,b}^{l-1} - R_1\sigma_{2a,b}^{l-1}} = \frac{d\bar{\varepsilon}_{a,b}}{R_2(R_1 + 1)\bar{\sigma}_{a,b}^{l-1}} \tag{5.34}$$

Thus,

$$\frac{d\varepsilon_3}{-R_2 - R_1 \alpha^{a-1}} = \frac{d\overline{\varepsilon}}{R_2\left(R_1+1\right)\left\{\frac{1}{R_2\left(R_1+1\right)}\left[R_2 + \alpha^a R_1 + \left(1-\alpha\right)^a R_1 R_2\right]\right\}^{\frac{a-1}{a}}} \tag{5.35}$$

$$d\varepsilon_{3a,b} = \frac{-R_2 - R_1 \alpha_{a,b}{}^{l-1}}{R_2\left(R_1+1\right)\left\{\frac{1}{R_2\left(R_1+1\right)}\left[R_2 + \alpha_{a,b}{}^l R_1 + \left(1-\alpha_{a,b}\right)^l R_1 R_2\right]\right\}^{\frac{l-1}{l}}} d\overline{\varepsilon}_{a,b} \tag{5.36}$$

According to Eq. (5.36), $d\varepsilon_{3a}$ and $d\varepsilon_{3b}$ can be expressed as:

$$d\varepsilon_{3a} = \frac{-R_2 - R_1 \alpha_a{}^{l-1}}{R_2\left(R_1+1\right)\left\{\frac{1}{R_2\left(R_1+1\right)}\left[R_2 + \alpha_a{}^l R_1 + \left(1-\alpha_a\right)^l R_1 R_2\right]\right\}^{\frac{l-1}{l}}} d\overline{\varepsilon}_a \tag{5.37}$$

$$d\varepsilon_{3b} = \frac{-R_2 - R_1 \alpha_b{}^{l-1}}{R_2\left(R_1+1\right)\left\{\frac{1}{R_2\left(R_1+1\right)}\left[R_2 + \alpha_b{}^l R_1 + \left(1-\alpha_b\right)^l R_1 R_2\right]\right\}^{\frac{l-1}{l}}} d\overline{\varepsilon}_b \tag{5.38}$$

Eq. (5.38) divided by Eq. (5.37) gives

$$\frac{d\varepsilon_{3b}}{d\varepsilon_{3a}} = \frac{\left(-R_2 - R_1\alpha_b{}^{l-1}\right)R_2\left(R_1+1\right)\left\{\frac{1}{R_2\left(R_1+1\right)}\left[R_2 + \alpha_a{}^l R_1 + \left(1-\alpha_a\right)^l R_1 R_2\right]\right\}^{\frac{l-1}{l}} d\overline{\varepsilon}_b}{\left(-R_2 - R_1\alpha_a{}^{l-1}\right)R_2\left(R_1+1\right)\left\{\frac{1}{R_2\left(R_1+1\right)}\left[R_2 + \alpha_b{}^l R_1 + \left(1-\alpha_b\right)^l R_1 R_2\right]\right\}^{\frac{l-1}{l}} d\overline{\varepsilon}_a} \tag{5.39}$$

$$\frac{d\varepsilon_{3b}}{d\varepsilon_{3a}} = \frac{\left(-R_2 - R_1\alpha_b{}^{l-1}\right)R_2\left(R_1+1\right)\left\{\frac{1}{R_2\left(R_1+1\right)}\left[R_2 + \alpha_a{}^l R_1 + \left(1-\alpha_a\right)^l R_1 R_2\right]\right\}^{1}\left\{\frac{1}{R_2\left(R_1+1\right)}\left[R_2 + \alpha_a{}^l R_1 + \left(1-\alpha_a\right)^l R_1 R_2\right]\right\}^{-\frac{1}{l}} d\overline{\varepsilon}_b}{\left(-R_2 - R_1\alpha_a{}^{l-1}\right)R_2\left(R_1+1\right)\left\{\frac{1}{R_2\left(R_1+1\right)}\left[R_2 + \alpha_b{}^l R_1 + \left(1-\alpha_b\right)^l R_1 R_2\right]\right\}^{1}\left\{\frac{1}{R_2\left(R_1+1\right)}\left[R_2 + \alpha_b{}^l R_1 + \left(1-\alpha_b\right)^l R_1 R_2\right]\right\}^{-\frac{1}{l}} d\overline{\varepsilon}_a} \tag{5.40}$$

Substitute $\varphi_{a,b} = \left\{\frac{1}{R_2\left(R_1+1\right)}\left[R_2 + \alpha_{a,b}{}^l R_1 + \left(1-\alpha_{a,b}\right)^l R_1 R_2\right]\right\}^{-\frac{1}{l}}$ into Eq. (5.40),

$$\frac{d\varepsilon_{3b}}{d\varepsilon_{3a}} = \frac{\left(-R_2 - R_1\alpha_b{}^{l-1}\right)\left\{\left[R_2 + \alpha_a{}^l R_1 + \left(1-\alpha_a\right)^l R_1 R_2\right]\right\}\varphi_a d\overline{\varepsilon}_b}{\left(-R_2 - R_1\alpha_a{}^{l-1}\right)\left\{\left[R_2 + \alpha_b{}^l R_1 + \left(1-\alpha_b\right)^l R_1 R_2\right]\right\}\varphi_b d\overline{\varepsilon}_a} \tag{5.41}$$

In the M-K model, the initial imperfect factor:

$$f_0 = \frac{t_{b_0}}{t_{a_0}}$$ (5.42)

Where t_a and t_b are the thickness in Zone a and Zone b.

The imperfect factor is expressed as:

$$f = \frac{t_b}{t_a}$$ (5.43)

$$\varepsilon_{3b} = \ln\left(\frac{t_b}{t_{b_0}}\right) \Rightarrow t_b = t_{b_0} \exp(\varepsilon_{3b})$$ (5.44)

$$\varepsilon_{3a} = \ln\left(\frac{t_a}{t_{a_0}}\right) \Rightarrow t_a = t_{a_0} \exp(\varepsilon_{3a})$$ (5.45)

$$f = \frac{t_b}{t_a} = f_0 \exp(\varepsilon_{3b} - \varepsilon_{3a})$$ (5.46)

The assumption of the M-K model is that:

$$\varepsilon_{2a} = \varepsilon_{2b}$$ (5.47)

$$\sigma_{1a} = f\sigma_{1b}$$ (5.48)

Thus, based on Eq. (5.30) and Eq. (5.48),

$$\bar{\sigma}_a \varphi_a = f\bar{\sigma}_b \varphi_b$$ (5.49)

$$\varphi_a \bar{\sigma}_a = f_0 \exp(\varepsilon_{3b} - \varepsilon_{3a})\bar{\sigma}_b \varphi_b$$ (5.50)

$$\frac{\varphi_a}{\varphi_b} = f_0 \exp(\varepsilon_{3b} - \varepsilon_{3a})\frac{\bar{\sigma}_b}{\bar{\sigma}_a}$$ (5.51)

Finally, substitute Eq. (5.51) into Eq. (5.41),

$$\frac{d\varepsilon_{3b}}{d\varepsilon_{3a}} = \frac{\left(-R_2 - R_1\alpha_b^{l-1}\right)\left\{\left[R_2 + \alpha_a^{l}R_1 + \left(1-\alpha_a\right)^{l}R_1R_2\right]\right\}}{\left(-R_2 - R_1\alpha_a^{l-1}\right)\left\{\left[R_2 + \alpha_b^{l}R_1 + \left(1-\alpha_b\right)^{l}R_1R_2\right]\right\}} \cdot f_0 \exp\left(\varepsilon_{3b} - \varepsilon_{3a}\right) \cdot \frac{\bar{\sigma}_b d\bar{\varepsilon}_b}{\bar{\sigma}_a d\bar{\varepsilon}_a} \qquad (5.52)$$
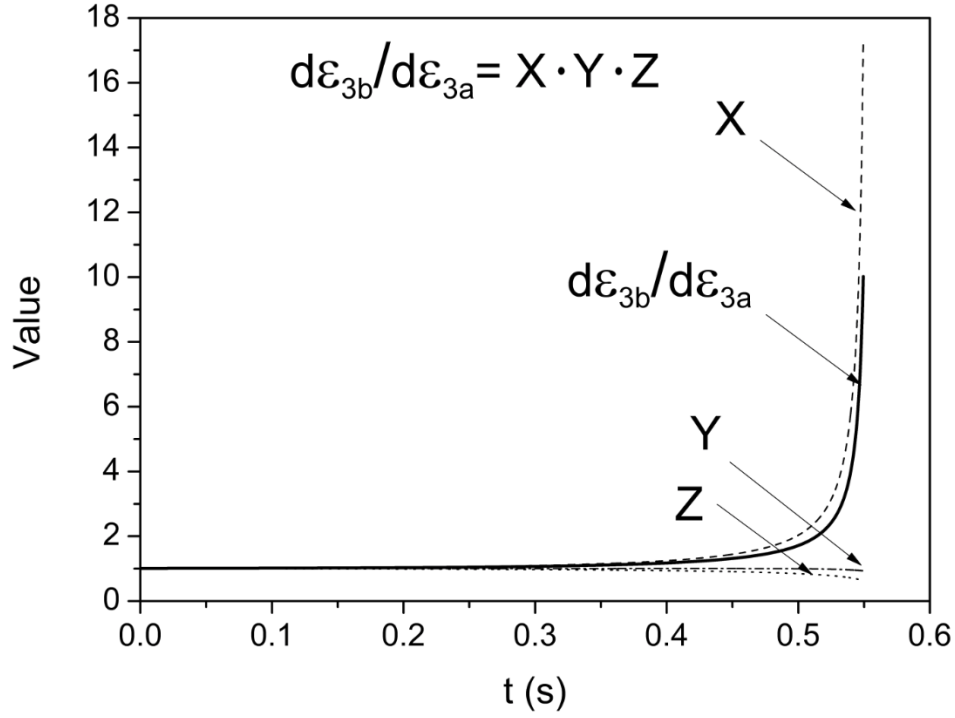

Figure 5-28. The calculated expression terms "X", "Y", "Z" and $d\varepsilon_{3b}/d\varepsilon_{3a}$ against time using viscoplastic-Hosford-MK model at strain rate 3/s, temperature 400°C, strain path $\beta = -0.5$.

Due to the numerical study by Eq. (5.50), the effect of X and Y expressions on the $\dfrac{d\varepsilon_{3b}}{d\varepsilon_{3a}}$ is neglected and f_0 is the constant, thus

$$\frac{d\varepsilon_{3b}}{d\varepsilon_{3a}} \propto \frac{\bar{\sigma}_b d\bar{\varepsilon}_b}{\bar{\sigma}_a d\bar{\varepsilon}_a} \qquad (5.53)$$

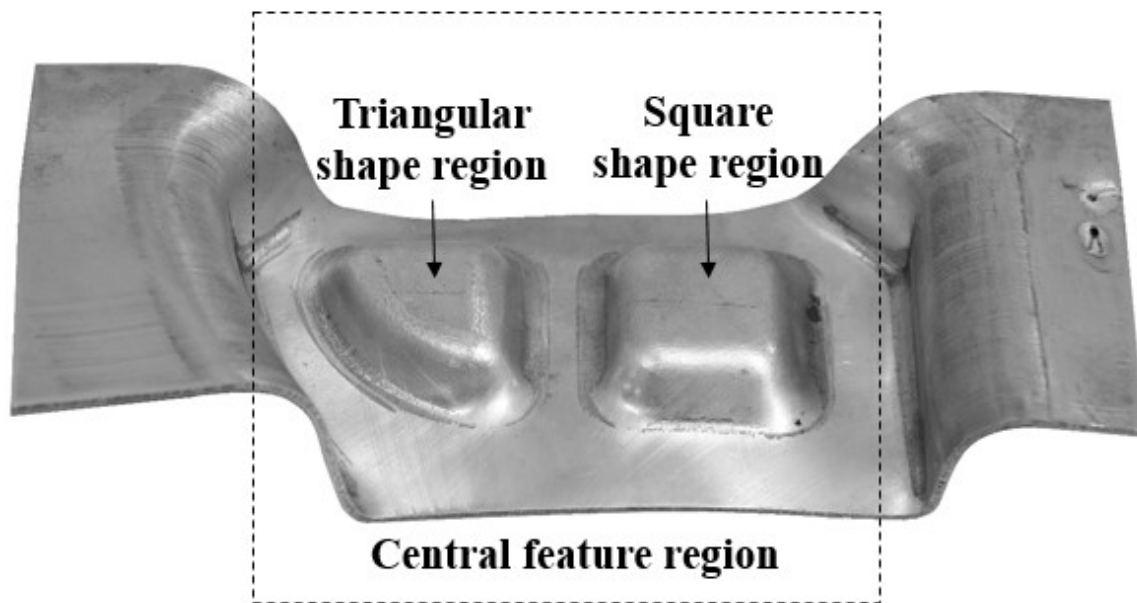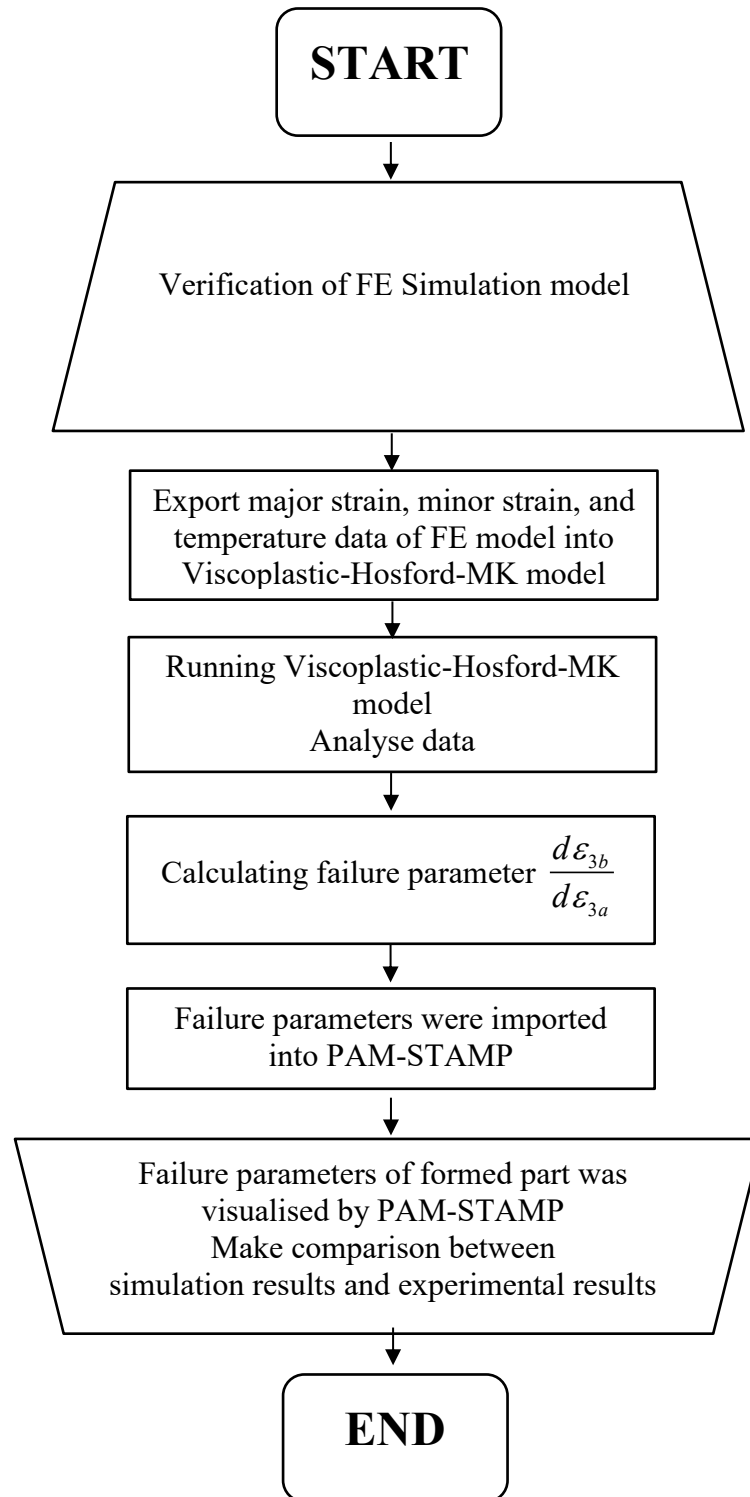**5E. Photo of formed wing stiffener component**

Figure 5-29. Demonstration of central features in formed wing stiffener component

5F. Flow chart of the forming limit prediction for hot stamped wing stiffener component

START

Verification of FE Simulation model

Export major strain, minor strain, and temperature data of FE model into Viscoplastic-Hosford-MK model

Running Viscoplastic-Hosford-MK model
Analyse data

Calculating failure parameter $\dfrac{d\varepsilon_{3b}}{d\varepsilon_{3a}}$

Failure parameters were imported into PAM-STAMP

Failure parameters of formed part was visualised by PAM-STAMP
Make comparison between simulation results and experimental results

END

5G. Forming tests on AA2060, AA6082 & AA5754

The same failure locations (failure in the side wall) were observed on different aluminium alloys for forming wing stiffener component under hot stamping conditions.
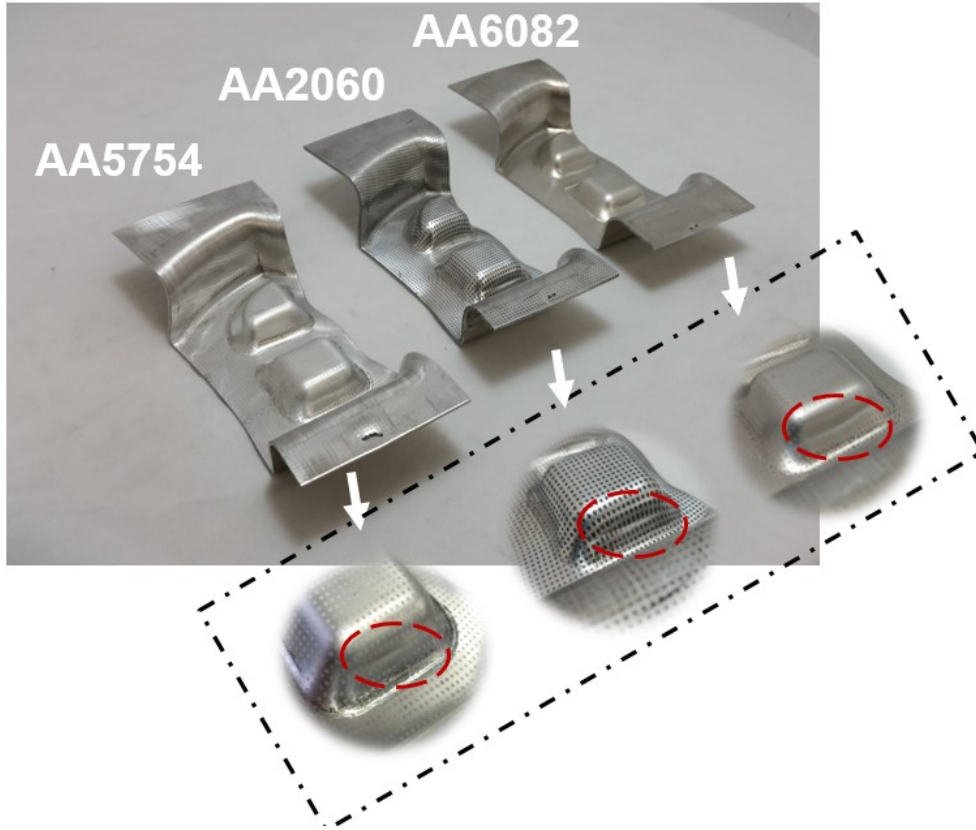

Figure 5-30. shows the failure positions of formed wing stiffener component on AA5754 (Left), AA2060 (middle) and AA6082 (Right) alloys under the hot stamping conditions with different forming strokes.

Table 5-3. Forming conditions for forming wing stiffener component on AA5754, AA2060 & AA6082

Material	Forming Temperature	Forming Speed
AA5754	450 °C	250mm/s
AA2060	450 °C	250mm/s
AA6082	450 °C	250mm/s